Medida de la masa del quark top en eventos de topología $t\bar{t}$ + 1-jet en el experimento ATLAS de LHC

Davide Melini

bajo la supervisión de
Roberto Pittau y Juan Fuster Verdú

Tesis presentada por el título de
Doctor en Física

UNIVERSIDAD
DE GRANADA

Departamento de Física Teórica y del Cosmos
Universidad de Granada, España
Noviembre 2018

Editor: Universidad de Granada. Tesis Doctorales
Autor: Davide Melini
ISBN: 978-84-1306-067-5
URI: http://hdl.handle.net/10481/54635

Measuring the top-quark mass in $t\bar{t}+1$-jet topologies with the ATLAS detector at the LHC

Davide Melini

under the supervision of
Roberto Pittau and Juan Fuster Verdú

A thesis presented for the degree of
Doctor of Philosophy

UNIVERSIDAD DE GRANADA

Departamento de Física Teórica y del Cosmos
University of Granada, Spain
November 2018

But if there is no solace in the fruits of our research, there is at least some consolation in the research itself. Men and women are not content to comfort themselves with tales of gods and giants, or to confine their thoughts to the daily affairs of life; they also build telescopes and satellites and accelerators, and sit at their desks for endless hours working out the meaning of the data they gather. The effort to understand the universe is one of the very few things that lifts human life a little above the level of farce, and gives it some of the grace of tragedy.

Steven Weinberg
"The first three minutes"

On the cover page:

D'oú Venons Nous / Que Sommes Nous / Oú Allons Nous
(Where Do We Come From / What Are We / Where Are We Going)

by Paul Gauguin

Contents

Chapter 1

Introduction

The understanding of the world we live in has always fascinated the human being, from the early philosophers to the modern scientists, and can be summarised in three questions: where do we come from? what are we? where are we going?[1]. The second question in particluar, has been succesfully answered in the last centruy in the context of high energy particle physics. It has been proven that matter is made of elementary particles, which properties and interactions can be described in the theoretical framework of the so-called Standard Model (SM).

The SM model describes matter and three of the four fundamental forces of Nature: electromagnetic, weak force and strong force. Gravity is not described by the SM and one of the biggest challenges in theoretical physics is in fact to incorporate it into the SM in a unified model.

Elementary particles are dimension-less particles and their properties are defined by a set of quantum numbers, defining their quantum state. For each particle an anti-particle exists, which has the same quantum numbers, but with opposite sign. Particles can be divided into two groups:fermions and bosons. The difference between the two groups is that identical fermions at same energy cannot have the same quantum states, while there can be an infinite number of bosons sharing the same quantum numbers and energy.

Fermions are the matter building blocks and they always have semi-integer spin value. They can be divided in lepton and quarks. While the formers only feel the electroweak force, the latters are also sensitive to the strong interaction. There are six types (or *flavours*) of leptons, organised in three generations, each one formed by an electromagnetic charged lepton and a neutral one called neutrino. Leptons can be directly observed in detectors as free particles The first lepton to be discovered was a fermion, called *electron*, in 1897 [1]. Its discovery was followed by the one of the second generation fermion, the *muon*, in 1937 [2] and their respective charge-less neutrinos, ν_e in 1956 [3] and ν_μ in 1962 [4]. The third generation was discovered later, with the τ lepton discovered in 1975 [5] and the tau neutrino ν_τ found in 2000 [6], which was the last SM fermion to be discovered. The quarks can also be of six different flavours, organised in three generations. The first family is formed by the *up* (u) and *down* (d) quarks, the second by the *charm* (c) and *strange* (s) ones, while the third by

[1] '*Where Do We Come From, What Are We, Where Are We Going* by P. Gauguin is the painting used as backgrounf of the cover page.

the *beauty* or *bottom* (b) and *top* (t) ones. Quarks cannot be directly observed, since strong force only allows their existence in nature as bounded systems called hadrons. In fact their existence was postulated by theorists [7, 8] as an explanation to the large number of hadrons discovered in the first collider experiments. Studies performed in 1969 of the internal structure of the proton via deep inelastic scattering [9, 10] confirmed the existence of point-like particles inside the proton, which were the first generation quarks. The strange quark existence was a consequence of the previous experiment, being the first strange composed particle observed much earlier (1947 [11]). The charm quark was introduced ,to explain the suppression of flavour changing currents [12] and was found in 1974 [13, 14] with the discovery of the J/ψ resonance, a hadron made of $c\bar{c}$ pair. The presence of a third generation of quarks, made of the bottom and the top quarks, was introduced to explain the observation of processes violating the CP-simmetry [15]. The bottom quark existence was confirmed shortly after, in 1977 [16], while only in 1995 the top-quark was found [17, 18].

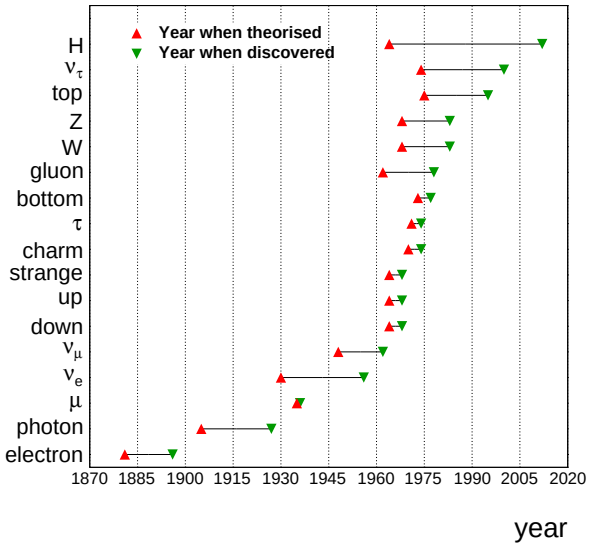

Figure 1.1: The elementary particles discovered so far.

In the SM, fundamental interactions between fermions happen through the exchange of quanta of vector bosons, which are particles with spin one. The electromagnetic force is mediated by photons, the electroweak by W and Z bosons and the strong force by gluons. The interpretation of the photons as light quanta is at the base of the quantum mechanic revolution which took place in the first half of the 1900 thanks to scientists like Einstein, Plank and Compton [19]. Photon quanta were experimentally measured in 1923 [20]. The gluons existence was confirmed indirectly after the quarks discovery, and directly 1978 [21, 22]. The electroweak vector bosons W and Z were more difficult to discover, since due to their large mass, colliders with enough energy to produce them were needed. Finally they were observed directly in 1983 [23–26],

An additional boson with zero spin was introduced [27–32] to explain the mechanism through which elementary particles and electroweak mediators can

acquire mass. Such a boson was finally found at the LHC by the ATLAS and CMS experiments in 2012 [33, 34], completing the list of the SM theorised particles to be discovered.

One could think that knowing all the elementary particles of the SM and their interactions, all the phenomena in the universe can be described. Nevertheless there are a few which cannot be explained in the context of the SM. Apart from gravity and its connection to the quantum world, the SM gives no explanation for neutrino oscillations, the absence of strong CP violation, the Baryon asymmetry and the nature of dark matter and dark energy. It is of course possible to think about extensions of the SM which describe the aforementioned phenomena, but so far no direct evidence of the existence of new particles or mechanisms different from the one predicted by the SM has been found and all the measurements of the theory parameters agrees with the SM theoretical expectations within their errors.

Since no big deviation from SM predictions has been observed, more precise measurements and more refined theoretical calculations are needed in order to look for possible small unexpected effects and to reduce the possibilities of beyond the Standard Model (BSM) scenarios as strongly as possible. In this context, the top-quark plays an important role. Firstly, there are BSM models which predicts deviations in the top-quark sector [35–37]. Secondly, being the top-quark the heaviest between all the SM particles, it has been postulated that it could play a special role in the spontaneous breaking of the electroweak symmetry which gives mass to the fermions [38]. Thirdly, an accurate and precise determination of all its properties (and of the SM parameters in general) is useful to stress the consistency of the SM [39].

Since deep inelastic scattering experiments in the 60's, the most successful method to study the properties of elementary particles at high energy has been the use of particle colliders. At the moment, the most powerful particle collider in the world is the Large Hadron Collider (LHC), which collides protons as well as heavy ions in a circular ring. The LHC produced proton-proton (pp) collisions at energies of the centre of mass of the pp system of $\sqrt{s} = 7$ TeV in 2011 and $\sqrt{s} = 8$ TeV in 2012 and, after a shutdown period to upgrade the detectors, is now colliding protons at $\sqrt{s} = 13$ TeV. There are four main experiments collecting data produced by the LHC collisions: ALICE, ATLAS, CMS and LHCb. ALICE has been designed to study a particular state of matter, the quark-gluon plasma, which is believed to have existed between 10^{-12} and 10^{-6} seconds after the Big Bang, when temperature and densities were so high to allow quarks and gluons to move freely without being confined in hadrons. LHCb's main purpose is to study the parameters of CP violation in hadrons containing b-quarks, which are important to understand why the universe universe we live in is mostly made of matter, instead of antimatter. ATLAS and CMS are general purpose experiments which have been designed to take advantage of the high energy of pp collisions to look for new particles and evidence for BSM theories, as well as measuring precisely the parameters of the SM.

In this thesis, data collected by the ATLAS experiment in pp collisions at $\sqrt{s} = 8$ TeV are used to measure the top-quark mass, in the context of the SM. Since quarks do not exist as free particles in nature, their mass is not directly measurable. Hence observables which depend on it have to be measured and then compared to theoretical predictions, checking which value of the top-quark

mass better describe data. The observable which have been chosen in this work is the normalised differential $t\bar{t}$ + 1-jet cross section, which was firstly proposed in [40]. A first measurement of the top-quark mass using this method was performed by the ATLAS collaboration using $\sqrt{s} = 7$ TeV collisions [41], resulting in the most precise measurement of the top-quark pole mass at that time. In this thesis the measurement has been repeated using the same observable, optimising the analysis to the data collected by ATLAS during 2012.

The thesis has the following structure. In Chapter 2 the formalism of the SM and the main theoretical aspects needed to describe the physics happening at the LHC are introduced. After a short explanation of the basic concepts of quantum field theory in Section 2.1, Section 2.2 introduces the SM and Section 2.3 explains how fermions like the top-quark can gain mass through the breaking of the electroweak symmetry. In Section 2.4 the physics of pp collisions is presented and in Section 2.5 it is explained how theoretical knowledge is in practice implemented in tools so that predictions can be computed for a variety of measurements. In Chapter 3 the physics of the top-quark at the LHC is introduced, with a particular focus on the role its mass has in the SM and beyond (Section 3.2). Section 3.3 shows how the top-quark mass is measured by the LHC experiments, highlighting the limitations of the current methods used and shortly explaining what the future prospects are. In Chapter 4 the experimental setup of the ATLAS experiment is described, including a short digression on the calibration of jet of large radius in Section 4.3, which was the topic I worked on during my qualification period within the ATLAS collaboration. In Chapter 5 the experimental strategy of the top-quark mass measurement is presented, which details the event selection and $t\bar{t}$ + 1-jet system reconstruction.To extract the top-quark mass, data and theoretical predictions must be compared at the same level. It is hence possible to correct data to the level where theoretical predictions exist, as it has been done in Chapter 6, or to fold theoretical predictions (or both), as explained in Chapter 7. Differences in the various approaches are commented in Chapter 8, where topics such as off-shell effects are discussed. Chapter 9 finally is a discussion of the results obtained and the prospects for the future.

Chapter 2

The Standard Model of particle physics

The Standard Model (SM) of particle physics is a gauge quantum field theory which describes three of the four forces of nature (gravity is not included) and all the elementary particle observed so far. All the information of the theory is encoded in a scalar function of quantum fields representing the elementary particles, called the SM Lagrangian, $\mathcal{L}^{\rm SM}$.

In Section 2.1 an introduction to the basic concepts of quantum field theories is given. Then, in Section 2.2, the $\mathcal{L}^{\rm SM}$ is built assuming the SM symmetries, and the physical fields measured in experiments are presented. One problem of the SM model described in Section 2.2 is the fact that its fields are massless due to the gauge symmetries assumed. In Section 2.3 such a problem is solved by mean of the electroweak symmetry breaking (EWSB) and the introduction of the Higgs field. Theoretical aspects of computing observables in the context of hadron collisions, such as the pp collisions which take place at the LHC, are discussed in Section 2.4. Sections 2.1 to 2.4 are mainly a personal recompilation of information available in Refs. [42–44]. A review on how the SM model has been implemented into software tools and how such tools can be used as a link between theoretical calculations and experimental measurements is presented in Section 2.5. It mainly use the information contained in manuals of the most common Monte Carlo programs used by experiments [45–49] and in the HiggsTools ITN network report [50], to which I directly contributed.

2.1 Basics of quantum field theory

Relativistic Quantum field theories (QFTs) combine field theory, quantum mechanics and relativity to describe elementary particle dynamics. In this contenxt, it is useful to use natural units, setting the speed of light and the Planck constant dimensionless and with unitary value: $c = \hbar = 1$.

As in classical field theory, the equation of the dynamics of a system are obtained by requiring that the action of a Lagrangian $\mathcal{L}(\Psi_i(x_i))$, function of some fields $\Psi_i(x_i)$, is stationary, i.e. $\delta \int \mathcal{L}(\Psi_i(x_i) = 0$. In order for the theory to be re-normalizable and hence a predictive theory, the Lagrangian must have dimensions of energy fourth power.

In quantum mechanics, all the significant features of a particle are contained in a quantum state $|\phi\rangle$, excitation of a vacuum field $|0\rangle$ (in classical mechanics, the important information is instead specified by spacial coordinates x and momenta p). Hence, a field quantization is obtained by promoting the classical particle fields to be creation and annihilation operators, making a field $\phi_a(x)$ to create a particle of type a at position x from the vacuum $|0\rangle$ state. The probability $P[\phi_a(x)]$ of the ϕ_a quantum state is then given by

$$P[\phi_a(x)] = \left| \int \phi_a(x)\phi_a^+(x)\mathrm{d}x \right|^2 =: |\langle \phi_a|\phi_a\rangle|^2 \tag{2.1}$$

being $\phi_a^+(x)$ the conjugate field of $\phi_a(x)$, and the evolution of a quantum state follows the Schroedinger's equation

$$i\frac{\partial}{\partial t}|\phi(\vec{x},t)\rangle = \hat{H}|\phi(\vec{x},t)\rangle \tag{2.2}$$

$\hat{H}$ in Eq. (2.2) is the Hamiltonian operator, defined as

$$\hat{H} = \sum_{i=1}^{n} T_i + V(\phi_1,\ldots,\phi_n) \tag{2.3}$$

for a system $|\phi\rangle = |\phi_1 \otimes \phi_2 \otimes \cdots \otimes \phi_n\rangle$ composed by n particles of type i, where T_i is the kinetic energy operator of particle ϕ_i.

Special relativity enters in the choice of the kinetic terms T_i and interacting term V, which have to be locally gauge invariant. Because any Lorentz invariant local quantum field theory with a hermitian Hamiltonian must have CPT symmetry[51], particle and anti-particle fields have to be taken into account into one single field together. A fermionic field f is then a superposition of four states: a matter fermion with two spin components[1] (f_L and f_R) and an anti-matter part also with two spin components ($\bar{f}_L$ and $\bar{f}_R$):

$$f(x) = \int \frac{\mathrm{d}\vec{p}}{(2\pi)^3\sqrt{2p_0}} \left[\begin{pmatrix} f_L(p) \\ f_R(p) \end{pmatrix} e^{ixp} + \begin{pmatrix} \bar{f}_L(p) \\ \bar{f}_R(p) \end{pmatrix} e^{ixp} \right] \tag{2.5}$$

Particles with spin-1 have three spin degrees of freedom, which can be described by polarization vectors $\epsilon_\mu(p)$ such that $\epsilon_\mu(p)p^\mu = 0$. The spin-1 particle field hence can be written as:

$$A_\mu(x) = \int \frac{\mathrm{d}\vec{p}}{(2\pi)^3\sqrt{2p_0}} \left[\epsilon_\mu(p)e^{ixp} + \bar{\epsilon}_\mu(p)e^{ixp} \right] \tag{2.6}$$

Since scalar particle have no spin-components, they are described by scalar operators:

$$\phi(x) = \int \frac{\mathrm{d}\vec{p}}{(2\pi)^3\sqrt{2p_0}} \left[\phi(p)e^{ixp} + \bar{\phi}(p)e^{ixp} \right] \tag{2.7}$$

[1] It is convenient to define helicity as the projection of the spin along the direction of the fermion four-momentum. Helicity is defined as

$$\xi_{L/R} = \frac{1 \pm \gamma^5}{2} \tag{2.4}$$

, being $\gamma^5 = i\gamma_0\gamma_1\gamma_2\gamma_3$ and γ_μ the Dirac matrices.

Kinetic terms T_i are chosen such that, after requiring the action of the Lagrangian to be stationary, free-particle fields satisfy Eq. (2.2). For scalar particles ϕ of mass m, it correspond to choose the kinetic term

$$T_\phi = \partial_\mu \phi \partial^\mu \bar{\phi} - m^2 \phi \bar{\phi} \tag{2.8}$$

while for a vector boson A_μ of mass m (defining the tensor $F_{\mu\nu} = \partial_\mu A_\nu - \partial_\nu A_\mu$)

$$T_A = -\frac{1}{2} F_{\mu\nu} \bar{F}^{\mu\nu} + m^2 \bar{A}_\mu A^\nu \tag{2.9}$$

and for a fermionic filed f of mass m

$$T_f = i \bar{f} \cdot \gamma^\mu \partial_\mu f - m \bar{f} \bar{f} \tag{2.10}$$

With these choices, the resulting equation of motions of non-interacting fermions follow the Dirac equation $(i\gamma^\mu \partial_\mu - m) f(x) = 0$, while every component of the vector boson fields, as well the scalar bosons, follows the Klein-Gordon equation.

In high energy particle collisions, relativistic QFT is used to compute the probability of an initial state $|\Psi_i\rangle$ formed by two particles non-interacting at long distances, which after interaction produce a certain final state $|\Psi_f\rangle$ of free particles. A fundamental role in this calculation is played by the S matrix, which is related to the probability that the initial state Ψ_i evolves after interaction into the final state Ψ_f by the equation

$$P_{i \to f} = \left[\langle \Psi_i | \, S \, | \Psi_f \rangle \right]^2 \tag{2.11}$$

The S matrix, to conserve the quantum probability, must be unitary.

Using Schroedinger equation to determine the evolution of the colliding system, the S-matrix can be computed from a given Lagrangian. Using a Dyson series, it can be written in the form:

$$S = \sum_{n=0}^{\infty} \frac{i^n}{n!} \int \prod_{j=1}^{n} \mathrm{d}^4 x_j \mathcal{T} \left[\prod_{j=1}^{n} \mathcal{L}_{\text{int}} \left(\Psi_j(x_j) \right) \right] \tag{2.12}$$

where $\mathcal{L}_{\text{int}}$ includes the terms of the Lagrangian where fields interact between each others, while $\mathcal{T}$ stands for a time-ordered product. Here $\Psi_j(x_j)$ define a certain field Ψ_j, which value depend on its coordinate x_j. The usual approach to compute the S-matrix is via the so-called Feynman diagrams[2], which allows to calculate the time ordered product $\mathcal{T}\left[\prod_{j=1}^{n} \mathcal{L}_{\text{int}} \left(\Psi_j(x_j) \right)\right]$ in a diagrammatic way, as it is shown in Fig. 2.1.

To summarise, once a Lagrangian is defined, transition probabilities can be computed and theoretical values for cross sections and decay widths can be obtained. Such values can then be compared to the ones measured by experiments. The Lagrangian which best describes experimental observations is the SM lagrangian, which is introduced in the next section, Section 2.2.

[2]The time ordered product of Eq. (2.12) can be rewritten by means of a Wick expansion.

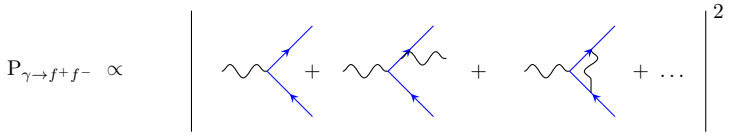

Figure 2.1: Types of Feynman diagrams which contribute to the calculation of the probability P of a photon decaying into a fermion-antifermion pair,$\gamma \to f^+f^-$. The terms contributing to $P_{\gamma\to f^+f^-}$ up to second order in the $\gamma - f$ coupling are shown. First diagram only contains one $\gamma - f$ vertex and, if the coupling value is smaller than 1, it is the leading contribution, being the second and third terms sub-leading. The second diagram is often referred to as real-radiation contribution, while the third one is the so-called virtual radiation.

2.2 Introduction to the Standard Model

The three forces described by the SM are represented by a local gauge symmetry which is $\mathcal{SU}(3)_C \otimes \mathcal{SU}(2)_L \otimes \mathcal{U}(1)_Y$. The strong force is represented by the $\mathcal{SU}(3)_C$ group, i.e. the group of unitary 3×3 matrices, and its conserved quantum number is called *colour*. It has 8 generators $C_a, a \in \{1, \ldots, 8\}$ in its fundamental representation, which can be identified with the Murray-Gellman matrices λ_a. A transformation from this group acts on an field $\Psi(x)$ as $e^{ig_s \vec{C}\cdot\vec{g}(x)}\Psi(x)$, where $\vec{C} = \{C_1, C_2, \ldots, C_8\}$. The $\mathcal{SU}(2)_L$ group only acts on the left-handed[3] fermions and has conserved charge the *weak isospin*, T. Its fundamental representation is the group of unitary 2×2 matrices, and has three generators $T_i, i \in \{1, 2, 3\}$, which are proportional to the Pauli matrices σ_i. A field $\Psi(x)$ is transformed under the action of a $\mathcal{SU}(2)_L$ transformation as $e^{ig_w \vec{T}\cdot\vec{w}(x)}\Psi(x)$, with $\vec{T} = \{\frac{\sigma_1}{2}, \frac{\sigma_2}{2}, \frac{\sigma_3}{2}\}$. The last group $\mathcal{U}(1)_Y$ is the group of complex numbers with unitary module, which have one generator usually defined as $\frac{Y}{2}$, the *weak hypercharge*, acting on fields as $e^{ig\frac{Y}{2}b(x)}\Psi(x)$. The first derivatives of the functions $g^a(x)$, $w^i(x)$ and $b(x)$ are also fields. Hence , it is possible to define fields such as $G^a_\mu = \partial_\mu g^a(x)$.They are the so-called gauge fields and they will be called G^a_μ, W^i_μ and B^i_μ, for their respective simmetries, in the following. When quantised, they create/annihilate spin-1 gauge bosons from the vacuum. In the following the dependence of all the fields on the spatial coordinates is omitted, as well as sum over repeated indices. For the indices relative to the $\mathcal{SU}(3)_C$ group letters $a, b, c, \ldots$ has been used, while for $\mathcal{SU}(2)_L$ indices $i, j, k, \ldots$. were used. The Lorentz indices instead are denoted by Greek letters $\mu, \nu, \ldots$.

As already mentioned in Chapter 1, six leptons $(e, \mu, \tau, \nu_e, \nu_\mu, \nu_\tau)$ have been discovered which does not feel the strong force and other six (u, d, c, s, b, t) which instead do. They can be divided into generations, based on their relation through weak isospin. It is possible to rearrange the physical fermions

[3]The left handed part of a fermion is obtained by acting on the fermion field with the operator $\frac{(1-\gamma^5)}{2}$, whereγ^5 here is the product of the four Dirac matrices: $\gamma^5 = i\gamma^0\gamma^1\gamma^2\gamma^3$. The same procedure applies to get the right handed part of a fermion. In this latter case the chirality-right projector would be $\frac{(1+\gamma^5)}{2}$.

into a multi dimensional fermionic field, for each generation i:

$$\begin{aligned} l^i &= \left\{ \begin{pmatrix} \nu_L^i \\ e_L^i \end{pmatrix}, \nu_R^i, e_R^i \right\} \\ q^{a,i} &= \left\{ \begin{pmatrix} u_L^{i,a} \\ d_L^{i,a} \end{pmatrix}, u_R^{i,a}, d_R^{i,a} \right\} \end{aligned} \tag{2.13}$$

where the left and right hand components of each fermion have been separated, $u(d)$ denotes the $up(down)$-type quark with their respective colour charge α, while e and ν represent the electron-type and neutrino-type fermions. A generic $\mathcal{SU}(2)_L$ transformation would hence only affect the first component of the vectors of Eq. (2.13). A common choice is to take e_L and ν_L as autostate of the third component of the weak isospin operator, i.e. $T_3 e_L = -\frac{1}{2} e_L$ and $T_3 \nu_L = +\frac{1}{2}\nu_L$. Since $\mathcal{SU}(2)_L$ does not affect right handed fermions, $T_i \nu_R = T_i e_R = 0, \forall i \in 1,2,3$. The quark fields are affected by a $\mathcal{SU}(2)_L$ exactly in the same way. $\mathcal{SU}(3)_C$ only acts on the quark fields $q^{i,\alpha}$, which means that, making explicit the color indices, $[C_a]_{bc}\, q^c = c_{abc} q^b$. $\mathcal{U}(1)_Y$ acts differently on l^i and $q^{\alpha,i}$. The typical choice is $Y l_L^i = -2 l_L^i$ and $Y e_R^i = -1 e_R^i$ for leptons and $Y q_L^{a,i} = \frac{1}{3} q_L^{a,i}$, $Y u_R^{a,i} = \frac{4}{3} u_R^{a,i}$, $Y d_R^{a,i} = -\frac{2}{3} d_R^{a,i}$ for quarks, in order to recover the correct value of each field electric charge, as it will be clear in the follwing.

The most general dimension-4 Lagrangian which can be written, invariant under the $\mathcal{SU}(3)_C \otimes \mathcal{SU}(2)_L \otimes \mathcal{U}(1)_Y$ symmetry is:

$$\mathcal{L}^{\mathrm{SM}} = \sum_{f \in \left\{ \substack{\text{leptons} \\ \text{quarks} } \right\}} i \bar{f} \gamma^\mu D_\mu f - \frac{1}{4} W_{\mu\nu}^i W_i^{\mu\nu} - \frac{1}{4} B^{\mu\nu} B_{\mu\nu} - \frac{1}{4} G_a^{\mu\nu} G_{\mu\nu}^a \tag{2.14}$$

where it has been introduced the covariant derivative

$$D_\mu = \partial_\mu - i g_w T_i W_\mu^i - i g \frac{Y}{2} B_\mu - i g_s \left(C^a\right) \gamma_{\mu\nu} G_{ab}^\nu \tag{2.15}$$

at first order in the coupling constants $g, g_w$and g_s; and the tensor fields

$$\begin{aligned} B_{\mu\nu} &= \partial_\mu B_\nu - \partial_\nu B_\mu \\ W_{\mu\nu}^i &= \partial_\mu W_\nu^i - \partial_\nu W_\mu^i + g_w \epsilon^{ijk} W_\mu^j W_\nu^k \\ G_{\mu\nu}^a &= \partial_\mu G_\nu^a - \partial_\nu G_\mu^a - g_s \epsilon'^{abc} G_\mu^b G_\nu^c \end{aligned} \tag{2.16}$$

where ϵ^{ijk} and ϵ'^{abc} are the structure constants[4] of the $\mathcal{SU}(2)_L$ and $\mathcal{SU}(3)_C$ respectively.

In order to make explicit the electromagnetic force and the weak charged currents, it is possible to define:

$$\begin{aligned} W_\mu^\pm &= \frac{1}{\sqrt{2}} \left(W_\mu^1 \mp i W_\nu^2 \right) \\ Z_\mu &= \cos\theta_W W_\mu^3 - \sin\theta_W B_\mu \\ A_\mu &= \sin\theta_W W_\mu^3 + \cos\theta_W B_\mu \end{aligned} \tag{2.17}$$

[4] Structure constants are defined by commutation laws of the group generators. For example $[T_i, T_j] = i\epsilon^{ijk} T_k$ for $\mathcal{SU}(2)_L$ group and $[C_i, C_j] = i\epsilon'^{abc} C^c$ for $\mathcal{SU}(3)_C$.

Performing such field rotation, one could define[5] $T^{\pm} = \frac{1}{\sqrt{2}}(T^1 \pm T^2)$and write the covariant derivative Eq. (2.15) as :

$$D_\mu = \partial_\mu - ig_w T^+ W_\mu^+ - ig_w T^- W_\mu^- - ieQ_Z Z_\mu - ieQA_\mu - ig_s\,(C^a)\,G_\nu^a \quad (2.18)$$

where the operators

$$\begin{aligned} eQ_Z &= g_w \cos\theta_W T^3 - g \sin\theta_W \frac{Y}{2} \\ eQ &= g_w \sin\theta_W T^3 + g \cos\theta_W \frac{Y}{2} \end{aligned} \quad (2.19)$$

have been introduced, being e the electric charge of the proton.

The operator Q can be identified with the electromagnetic charge operator if $eQ[\nu_e]_{L/R} = 0$ and $eQ[l_e]_{L/R} = -e$, i.e the neutrino has no electric charge, while the electron is negatively charged. Similarly for quarks, $eQ[u]_{L/R} = \frac{2}{3}e$ and $eQ[d]_{L/R} = -\frac{1}{3}e$. These conditions imply:

$$\begin{aligned} g_w \sin\theta_W &= g\cos\theta_W = e \\ Q &= T^3 - \frac{Y}{2} \end{aligned} \quad (2.20)$$

Using Eqs. (2.17) to (2.19) the SM Lagrangian can then be written at the first order in g, g_s, g_w as

$$\begin{aligned} \mathcal{L}^{\mathrm{SM}} = & \sum_{\text{fermions}} \left[i\bar{f}\gamma^\mu \partial_\mu f\right] - \frac{1}{2}W^{+\mu\nu}W^-_{\mu\nu} - \frac{1}{4}Z^{\mu\nu}Z_{\mu\nu} - \frac{1}{4}A^{\mu\nu}A_{\mu\nu} - \frac{1}{4}G_a^{\mu\nu}G^a_{\mu\nu} + \\ & + \sum_{\text{fermions}} \left[\frac{g_w}{\sqrt{2}}\bar{f}\left(\gamma^\mu T^+ W_\mu^+ + \gamma^\mu T^- W_\mu^-\right) f + e\bar{f}\gamma^\mu Q_Z Z_\mu f + e\bar{f}\gamma^\mu Q A_\mu f\right] + \\ & + \sum_{\text{quarks}} g_s \bar{f}\gamma_\mu C^a f G_a^\mu + \\ & + \quad \text{three- and four- bosons interaction terms} \end{aligned} \quad (2.21)$$

The term involving the Z and fermions fields in particular refers to weak neutral currents, predicted by the SM model and then discovered in 1973 [52], which at the time were a strong confirmation that the theory was in fact working.

First line of Eq. (2.21) describes the kinematic energy of free massless fermioninc and bosonic fields, as it was shown in Eqs. (2.9) and (2.10) . The second line containes the electro-weak interaction terms between fermions and bosons, as a function of the physical vector boson oberved in experiments: two oppositely EM charged W bosons and one neutral EM charged Z boson, as well as the photon field A_μ. Third line contains the information on the interaction between quarks and gluons. The lines describing vector bosons self-interactions and interaction between three and four vector bosons have not been reporte and can be found in [44].

In order to quantize such a Lagrangian, one can use the approach introduced in Section 2.1, and obtain the equation of motion for the free fields by requiring

[5] $T^{\pm}$ acts on a $\mathcal{SU}(2)_L$ doublet as $T^+ \begin{pmatrix} \nu_L^i \\ e_L^i \end{pmatrix} = \begin{pmatrix} e_L^i \\ 0 \end{pmatrix}$ and $T^- \begin{pmatrix} \nu_L^i \\ e_L^i \end{pmatrix} = \begin{pmatrix} 0 \\ \nu_L^i \end{pmatrix}$

the action of $\mathcal{L}^{\mathrm{SM}}$to be stationary. When gauge symmetries are involved though, the equation of motions do not uniquely determine the evolution of the fields, and there is no a priori procedure to select one of multiple equivalent physical solutions. In order to not over-count such solutions, which could breakdown unitarity of the S-matrix, a gauge choice has to be made to cancel the additional degrees of freedom which comes from the local invariance of the theory. This can be done by adding additional terms to the Lagrangian [53]. For abelian group symmetries, such as $\mathcal{U}(1)_Y$, it is enough to add terms which are functions of the gauge fields. For non abelian ones, like $\mathcal{SU}(3)_C$ and $\mathcal{SU}(2)_L$, additional non-physical anti-commuting fields have to be introduced . Such fields are usually called *ghost*, and do not affect explicitly any obseravble which can be computed within the SM. For this reason, ghost-fields are not taken into account in the next sections. One possible choice for the gauge fixing terms is the so-called Lorentz gauge:

$$\begin{aligned}\mathcal{L}^{\text{g.f.}} =& \frac{1}{2\xi}\left(\partial^\mu B_\mu\right)\left(\partial^\mu B_\mu\right) + \frac{1}{2\xi}\left(\partial^\mu W_\mu^i\right)\left(\partial_\mu W_i^\mu\right) + \frac{1}{2\xi}\left(\partial^\mu G_\mu^a\right)\left(\partial_\mu G_a^\mu\right) + \\ &+ \bar{c}^a\left(\partial_\mu\partial^\mu c^a\right) + ig_s\left(\partial_\mu \bar{c}^a\right)\epsilon'^{abc}A^{c,\mu}c^b + ig_w\left(\partial_\mu \bar{b}^i\right)\epsilon'^{ijk}W^{j,\mu}b^k + \bar{b}^i\left(\partial_\mu\partial^\mu b^i\right)\end{aligned} \tag{2.22}$$

where c^a are the ghost fields of the $\mathcal{SU}(3)_C$ group, and b^i the ones of the $\mathcal{SU}(2)_L$ one. The choice of the value of ξ is arbitrary. For $\xi \to \infty$ the chosen gauge is called Feynman gauge and the gauge bosons, such as the photon and the gluons, are massless.

In the picture of the SM Lagrangian depicted so far, fermions are massless and gauge bosons masses are not defined because of gauge freedom (massless in the Feynman gauge). In fact, explicit mass terms, like the ones shown in Eqs. (2.9) and (2.10), would violate the gauge symmetry of the Lagrangian. Still, it is possible to generate fermion and boson masses through the Brout-Englert-Higgs (BEH) mechanism [27–32] and the spontaneous breaking of the electroweak symmetry, as it is explained in the following.

2.3 Electroweak simmetry breaking and elementary particles masses

Fermion and electroweak boson masses can be generated when and additional field is added to the theory. Such a particle has to be a doublet under $\mathcal{SU}(2)_L$ and it is usually chosen to have a hypercharge value $Y(\Phi) = -Y(f_L) = 1$. Such particle was in fact found at the LHC by the ATLAS and CMS experiments[33, 34] and was finally denominated Higgs boson.

Given the new scalar field Φ, additional terms which are invariant under the SM symmetry can be added to $\mathcal{L}^{\mathrm{SM}}$:

$$\mathcal{L}^{\Phi} = \left(D_\mu\Phi\right)^\dagger\left(D^\mu\Phi\right) - V(\Phi) + \sum_{\text{fermions}}\left[\bar{f}_L Y_f \Phi f_R + h.c.\right] \tag{2.23}$$

where D_μ is the covariant derivative defined in Eq. (2.15), $V(\Phi)$ is the Higgs potential and the last term is the so-called Yukawa term [54] which contains the interaction of the Φ field with fermions, proportional to the $\mathcal{SU}(2)_L \otimes \mathcal{U}(1)_Y$ matrix Y_f.

In the standard approach to EWSB, it is supposed that just after the Big Bang, the Higgs potential had its minimum value for $\Phi = 0$. This can happen for shapes of $V(\Phi)$ as:

$$V(\Phi) = +\mu^2(\Phi\Phi^\dagger) + \lambda(\Phi\Phi^\dagger)^2 \quad , \tag{2.24}$$

with $\mu^2 > 0$ and $\lambda > 0$, which is shown in Fig. 2.2. In this condition, all the SM fermions and bosons still are massless. Then, with the expansion and cooling of the universe, a phase transition could have occurred, as it happens for instance in ferromagnetic systems below the Curie temperature [55]. This phase transition modified the Higgs potential giving it a shape which can be described by crefeq:HiggsPot, but with $\mu^2 < 0$ and $\lambda > 0$. In this case the potential of Eq. (2.24), the minimum potential configuration is obtained for values of the Φ field satisfying

$$\|\Phi\|^2 = -\frac{\mu^2}{\lambda} = \frac{v}{2} \tag{2.25}$$

where the vacuum expectation value v has been introduced. Eq. (2.25) only fixes the magnitude of the Φ field, giving infinite possible minimum configurations which are connected by $\mathcal{SU}(2)_L$ gauge transformations. Since gauge choices do

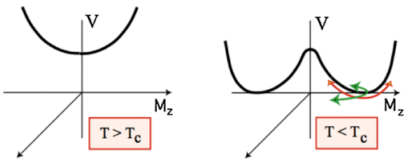

Figure 2.2: Behaviour of the Higgs potential above (left) and below (right) a critical temperature T_c. Figure from Ref [55].

not change the physical result in the end of the calculations, it is convenient to expand the Φ field around one of these minimum potential configurations. It is possible to chooseΦ to have definite value of weak isospin, for instance choosing in the $\mathcal{SU}(2)_L$ space $\Phi(x) = \frac{1}{\sqrt{2}}\begin{pmatrix}0\\ v+H(x)\end{pmatrix}$, where the field H and the constant v are both real and $\|H\|^2 = 0$.

The total Lagrangian of the SM would hence gain new terms. Firstly, the Higgs potential can be rewritten as:

$$V(\Phi)|_{\Phi\sim\Phi^{\min}} = -\mu^2 H^2 + \lambda v H^3 + \frac{\lambda}{4}H^4 + \text{const.} \tag{2.26}$$

where the first term introduces a mass term for the H field ($-\mu^2 > 0$, $m_H = \sqrt{2\lambda v^2}$ from Eqs. (2.24) and (2.25)) and the other terms contains the H field self-interactions. Secondly, the first term of 2.23 can also be expanded in terms

of the H field:

$$\begin{aligned}(D_\mu\Phi)^\dagger (D^\mu\Phi) =& \frac{1}{2}\partial_\mu H\partial^\mu H + \lambda v H^3 + \frac{\lambda}{4}H^4 + \\ &+ \frac{g_w^2 v^2}{4} W_\mu^+ W^{-\mu} + \frac{g_w^2}{4} W_\mu^+ W^{-\mu} H^2 + \\ &+ \frac{\left(g_w\cos\theta_w - g\sin\theta_w\right)^2 v^2}{4} Z_\mu Z^\mu + \frac{\left(g_w\cos\theta_w - g\sin\theta_w\right)^2}{4} Z_\mu Z^\mu H^2 + \\ &+ \frac{\left(g_w\sin\theta_w + g\cos\theta_w\right)^2 v^2}{4} A_\mu A^\mu + \frac{\left(g_w\sin\theta_w + g\cos\theta_w\right)^2}{4} A_\mu A^\mu H^2 + \\ &+ \frac{g_s^2 v^2}{2} G_\mu^a G_a^\mu + \frac{g_s^2}{2} G_\mu^a G_a^\mu H^2\end{aligned} \tag{2.27}$$

Using the results of Eq. (2.20) and choosing the gauge in which vector bosons are massless, the H-induced mass terms for the gauge bosons become:

- $m_\gamma = 0$
- $m_{\text{gluon}} = 0$
- $m_Z = \frac{(g_w\cos\theta_w - g\sin\theta_w)v}{2}$
- $m_W = \frac{g_w v}{2}$

As far it regards the Yukawa term of Eq. (2.23), at the minimum of the Higgs potential it becomes

$$\begin{aligned}\mathcal{L}^{\text{Yuk}}|_{V(\Phi)_{\min}} =& -\sum_{\text{fermions}} \left(\bar{f} Y_f (v+H) f_R + h.c.\right) = \\ =& -\sum_{\text{generations}} \frac{(v+H)}{\sqrt{2}} \left(y_{l_e}\bar{l_e} l_e + y_d \bar{q_d} q_d + y_u \bar{q_u} q_u\right)\end{aligned} \tag{2.28}$$

where $f = \begin{pmatrix} f_L \\ f_R \end{pmatrix}$ are the fermionic fields of electron-, up- and down-type of each generation. Neutrino-type fermions are not present, since right-handed neutrino have no interactions with any of the other SM fields and hence have not been observed so far. The fermion mass terms are defined as

$$m_f = \frac{v y_f}{\sqrt{2}} \tag{2.29}$$

and are fundamental parameters of the SM Lagrangian. Their value cannot be inferred from theory and must be determined experimentally. As already mentioned, quarks are not free particles as the leptons and can not be observed directly. Their mass is not an observable, though, but it can influence other observables measured in experiments. This topic will be discussed in more detail in Section 3.3.1. First of all, a short discussion on how SM can be used as a predictive theory has to be made. This is done in Section 2.4.

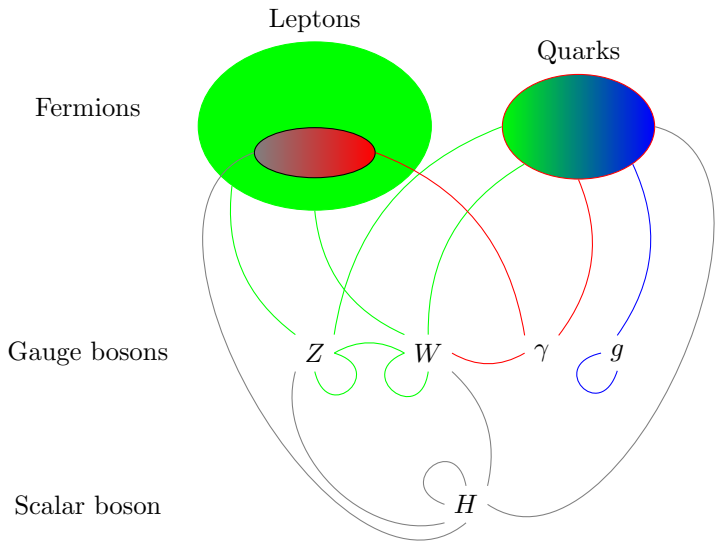

Figure 2.3: Observed SM particles and their interactions. Lines represent interactions: green lines for electroweak, red lines for electromagnetic and blue line for the strong one. The gray lines instead represente the interactions with the Higgs field. Also bosons self interactions are represented.

2.4 Quantum Chromo Dynamic at the Large Hadron Collider

The study of fundamental interactions and elementary particles benefit of particle colliders, since the very first project to build one [56]. By increasing the energy of the collisions and by varying the colliding beams and targets, ordinary matter has been studied at very small distances and a number of new particles and exotic states of matter has been discovered. In fact, by increasing the energy of the collisions, one can study deeply the structure of the colliding particles and eventually access region of the phase space were new particles can be produced.

The collider which at the moment produce collisions at the highest energy is the Large Hadron Collider (LHC). It produced proton-proton (pp) collisions at a centre of mass energy of the pp system of $\sqrt{s} = 7$ TeV and $\sqrt{s} = 8$ TeV and it is currently working at $\sqrt{s} = 13$ TeV. As it has been mentioned in Chapter 1, protons are made of quarks and gluons, which, all together, are called partons. When a high energy pp collision occur, the highest scale (*hard*) interaction happens between two partons of each proton, while the rest of the proton constituents either do not interact or interact with at lower scales. In general pp collisions are considered as a combination of high energy (short distance) and low energy (large distance) processes and factorisation theorems are used to separate these two behaviours. Factorisation has been proven mathematically for a number of processes, such as deep inelastic scattering and Drell-Yan, but

is elsewhere taken as an approximation [57].

If a parton a of an hadron A carries a fraction x_a^A of the hadron momentum, the cross-section of the collision of two protons A and B can be written as:

$$\sigma_{\mathrm{AB}} = \int \mathrm{d}x_a \mathrm{d}x_b f_A(x_a, \mu_F) f_B(x_b, \mu_F) \frac{\mathrm{d}\sigma_{ab}}{\mathrm{d}x_a \mathrm{d}x_b}(x_a, x_b, \mu_F) \tag{2.30}$$

where $f_A(x_a, \mu_F)$ is the probability of finding parton a in the proton A, carrying a fraction x_a of its four momentum, at an energy scale of μ_F. μ_F is the scale at which the separation between the short distance and long distance effects occur, and it is usually set to values at which the partonic collision happens. The $f_A(x_a, \mu_F)$ distributions are called parton distribution functions (PDF).

The computation of such functions involves non perturbative calculations which are difficult and often impossible to be made. Hence PDFs are extracted from data instead [58], with μ_F fixed by the experimental processes studied by the experiments. The dependence of the PDFs on the factorisation scale is described by the Dokshitzer-Gribov-Lipatov-Altarelli-Parisi (DGLAP) equations [59–61]:

$$\frac{\mathrm{d}f_A(x_a, \mu_F)}{d \log \mu_f^2} \propto P_{a,b}(z) \otimes f_A(x_b = x_a/z, \mu_F) \tag{2.31}$$

where $\otimes$ stands for convolution product. $P_{a,b}(z)$ are the splitting functions, i.e. the probability for a parton a to emit a parton b carrying a fraction z of his four momentum, which are general objects independent of the process under study. Hence, the typical procedure is to extract PDFs from experiments and then to use them at a generic μ_F using Eq. (2.31). Various methods exists to extract PDFs [62], but it is out of the scope of this thesis a more detailed discussion on PDFs. Only the proton PDF is shown in Fig. 2.4, at two different factorisation scales.

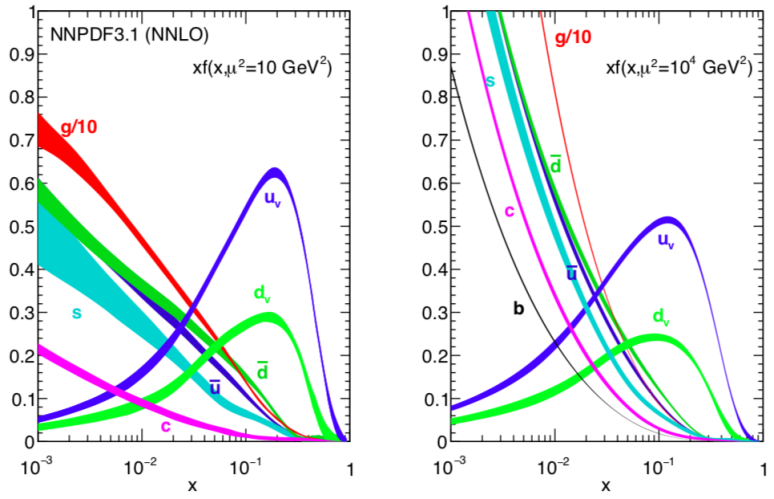

Figure 2.4: Distribution of the partons inside the proton at NNLO in QCD, according to the NNPDF group, evaluated at a scale $\mu_F^2 = 10\mathrm{GeV}^2$ (left) and $\mu_F^2 = 10^4\mathrm{GeV}^2$ (right). Figure from Ref. [63].

The second term of Eq. (2.30), $\frac{\mathrm{d}\sigma_{ab}}{\mathrm{d}x_a \mathrm{d}x_b}(x_a, x_b, \mu_F)$, is called the partonic cross section and includes the perturbative part of the calculation. The probability to produce a final state X from two colliding partons a and b ($ab \to X$) can be computed from $\mathcal{L}^{\mathrm{SM}}$, using the S matrix of Eq. (2.12), at the desired perturbative order in the coupling constants of the electromagnetic, weak and strong interactions.

2.4.1 Ultraviolet divergences and renormalisation

When computing cross sections including terms beyond the leading order (LO), the so called next-to-leading order (NLO) calculations, divergent terms come up in the calculation of the S matrix. Thanks to the renormalizability of the SM though, such divergences, called ultraviolet (UV) can be reabsorbed by redefining fields and coupling of the Lagrangian, using a finite number of parameters, by mean of the Ward-Takahashi identity [64, 65]. Various schemes can be used to reabsorb such infinities, such as the minimal subtraction scheme (MS) and its modified version ($\overline{MS}$), which introduces a parameter with mass dimensions, usually called the renormalisation scale μ_R. The choices of the renormalisation scheme and the renormalisation scale are both unphysical, hence any observable must be independent on such arbitrarierty. This fact leads to renormalisation group equations (RGE). For any observable O, function of the $\mathcal{L}^{\mathrm{SM}}$coupling g_i and fermion masses m_j, one has:

$$\begin{aligned} 0 &= \mu_R^2 \frac{\mathrm{d}}{\mathrm{d}\mu_R^2} O = \\ &= \left(\mu_R^2 \frac{\partial}{\partial \mu_R^2} + \sum_{i=1}^{n} \beta_i(g_1, \ldots, g_n) \frac{\partial}{\partial g_i} - \sum_{i=1}^{n} \gamma_i(g_1, \ldots, g_n) m_i \frac{\partial}{\partial m_i} \right) O \end{aligned} \tag{2.32}$$

where the β_i functions and the anomalous mass dimensions, γ_i, have been introduced:

$$\begin{aligned} \beta_i(g_1, \ldots, g_n) &= \mu_R^2 \frac{\partial g_i}{\partial \mu_R^2} \\ \gamma_i(g_1, \ldots, g_n) &= -\mu_R^2 \frac{1}{m_i} \frac{\partial m_i}{\partial \mu_R^2} \end{aligned} \tag{2.33}$$

Such functions are usually computed at a fixed perturbative order, and the differential equations of Eq. (2.33), solved for g_i, takes to the so called *running* of the couple constants, which is the dependence of the coupling constants on the renormalisation scale, shown for example in Fig. 2.5.

The standard interpretation of this effect is that fields and couplings appearing in the Lagrangian differ from the ones which are then seen by the experiments. The first ones are then called *bare*, while the latter are called *renormalised*, and their relation is controlled by the RGE equations Eq. (2.32). For instance, at NLO in pQCD, the strong coupling constant RGE in the $\overline{\mathrm{MS}}$ scheme reads[6]:

$$g_s(\mu_R^2) = g_s(\Lambda_{QCD}^2) \frac{1}{1 + 7 g_s(\Lambda_{QCD}^2) \log\left(\frac{\mu_R^2}{\Lambda_{QCD}^2}\right)} \tag{2.34}$$

[6] We used the six flavour scheme, where $n_f = 6$. For a generic number n_f of flavours the factor in the denominator of Eq. (2.34) would have been $\beta_0 = 11 - \frac{2 n_f}{3}$

where $\Lambda_{QCD} \approx 200$ MeV indicates the scale at which the renormalised coupling would diverge. The Λ_{QCD} scale is the limit at which pQCD theory can be used.

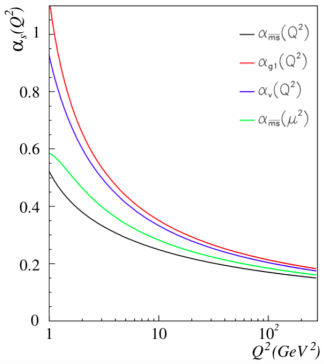

Figure 2.5: Running of the QCD strong coupling at NLO in QCD, in various renormalisation schemes. Figure from [66]. Translating to the notation used in this thesis, one has $g_s = 4\pi\alpha_s$, $\mu_R = Q$. Green line shows the choice $\mu = 0.708\mu_R$.

The running of the couplings is important in particular in the context of QCD, since allow to use perturbative QCD (pQCD) to compute partonic cross sections in high energy hadronic collisions. For such collisions, the typical scale at which partons collide are much larger than Λ_{QCD}, i.e. $\mu_R \gg \Lambda_{QCD}$. In this condition the strong force coupling is much smaller than 1, as can be seen in Fig. 2.5. Therefore it make sense to compute partonic cross sections using a perturbative approach. This phenomena is called *aymptotic freedom* of QCD.

Renormalisation of quarks masses Quarks masses also are renormalized in pQCD beyond the tree-level, and the γ_i functions of Eq. (2.33) control their renormalisation. One could solve for the mass m_i the γ_i equation, getting:

$$m_i(\mu_R^2) = m_i(\mu_0^2) e^{-2\int_{\mu_0}^{\mu_R} \gamma_i(g_1,\ldots,g_n) \mathrm{d}\mu_R} \tag{2.35}$$

At NLO in pQCD in the $\overline{\text{MS}}$ scheme, the γ_i functions are positive ($\gamma(\mu) = 4g_s(\mu)$ is the first and dominant term in g_s). It is then obvious from Eq. (2.35) that, in such renormalisation scheme, quark masses get smaller at higher scales. It possible though to define, at fixed order in the coupling constant, a constant mass term, which is the running mass at its scale $m_i^{\overline{\text{MS}}} = m_i(\mu_R = m_i)$.

Another renormalisation scheme which is often used for quark masses is the so called *pole mass* scheme. It is defined by requiring that the mass of the quark coincides with the pole of the quark propagator, and that the residue of such pole has a fixed value at any order in pQCD. The full propagator for a particle is inferred for example from Eq. (2.10) and has the typical structure is:

$$\Pi(p^2) \propto \frac{1}{p^2 - m_R^2 + \Sigma(p^2) + i0} \tag{2.36}$$

where p is the four momentum of the particle, m_R is the renormalised mass and $\Sigma(p^2)$ is the self-energy. At LO in pQCD, $\Sigma(p^2) = 0$, i.e. no self energy

correction exists to the propagator and the mass of the particle is the pole of the propagator, with residual given by the proportional constant of Eq. (2.36). These properties in the pole mass scheme are made valid at any order in pQCD, requiring:

$$\begin{aligned} \Sigma(p^2 = m_R^2) &= 0 \\ \left[\frac{\mathrm{d}\Sigma}{\mathrm{d}p^2}\right]_{p^2=m_R^2} &= 0. \end{aligned} \tag{2.37}$$

These equations are a possible alternative to the ones of Eq. (2.33), but for the pole mass scheme. The renormalised mass which satisfies the conditions of Eq. (2.37) is called the pole mass, m^{pole}. For heavy quark masses, the pole mass scheme has a non-perturbative ambiguity in its definition [67], which affects the pole mass by $\Delta m \approx \Lambda_{\text{QCD}}$. To solve this ambiguity new renormalisation schemes have been proposed [68, 69], but their discussion is outside of the scope of this thesis. Top quark mass definitions and their interpretation in experiments are discussed in more detail in Section 3.3.1

Of course, since m^{pole} and $m_i^{\overline{\text{MS}}}$ are renormalised quantities of the same $\mathcal{L}^{\text{SM}}$bare parameter, there is a connection between the two. Such relation is known to four loops in QCD [70, 71], and at first order in pQCD it reads:

$$m_i^{\text{pole}} = m_i^{\overline{\text{MS}}} \left(1 + \frac{16}{3} g_s(m_i^{\overline{\text{MS}}}) + \mathcal{O}(g_s^2)\right) \tag{2.38}$$

In general, equations relating two different renormalisation schemes exist for all the parameters of the Lagrangian.

2.4.2 Infrared divergences and jet physics

When performing calculations beyond the LO, another kind of divergences, called infrared (IR) may appear. They are typical of theories where massless particles are included, such as gluons and photons, but also other approximated theories, where light quarks are considered massless, suffer from it.

In the calculation of $S-$matrix elements beyond the LO, Feynman diagrams containing the exchange of virtual particles and the emission of additional real particles appear, as it has been shown in Fig. 2.1. Infrared divergences then arise from particular configurations of the momenta of the radiative particles. In particular IR divergences can be distinguished between collinear and soft. The collinear type arise when two four momenta p_1 and p_2 become parallel. The soft ones instead appear when the radiative particle energy is almost null. In both cases quantities such $\frac{1}{(p_1+p_2)^2} \xrightarrow{p_1^2=p_2^2=0} \frac{1}{2(|\vec{p}_1||\vec{p}_1|-\vec{p}_1\vec{p}_2)}$, which often appear in NLO calculations, diverge for massless particles.

For observables defined properly, these divergences cancel in the final result of the calculation, after integration over external particles four momenta is performed, thanks to the Kinoshita-Lee-Nauenberg (KLN) theorem [72, 73]. Observables which are non sensitive to the collinear or soft behaviour of the momenta of radiative particles are free of the IR divergences and are hence called IR safe observables. For them, the following properties hold:

$$\begin{aligned} &\mathcal{O}_{n+1}(p_1 \ldots, p_i, \ldots, p_j, \ldots p_{n+1}) \xrightarrow{p_i || p_j} \mathcal{O}_n(p_1 \ldots, p_i + p_j, \ldots p_n) \\ &\mathcal{O}_{n+1}(p_1 \ldots, p_i, \ldots, p_{n+1}) \xrightarrow{p_i \to 0} \mathcal{O}_n(p_1 \ldots, p_n) \end{aligned} \tag{2.39}$$

where n is the number of outgoing particles. Typically, observables which depends on the final state multiplicity are not IR safe. In fact, if one of the final particles momentum become soft, the multiplicity of the final state decrease, as it is shown in Eq. (2.39) ($n+1 \to n$).

For initial state partons soft/collinear radiation, the divergences are reabsorbed in the PDF definition, up to the factorisation scale. Hence, only real radiation with energy above μ_F enters the pQCD calculation. This is possible thanks to the fact that the probability of a parton to radiate, is process independent. For final state particles, it is possible to define objects, called *jets*, which is free of divergences coming from a soft/collinear emission

Jets Jets are clusters of final state partons, summed together in such a way that the resulting four momentum is an IR safe quantity. A number of algorithms exist [74–79] to define jets, and the most used share the same underlying idea.

Given a set of final state particles, the first step of the jet algorithms is to defined distances between each pair of final particles i and j (d_{ij}) and distances between each final state particle and the axis defined by the colliding initial partons (d_{iB}, B stands for beam). Typically, two parameters R and q are used in the definition of such distances:

$$\begin{aligned} d_{ij} &= \min({p_{\mathrm{T}}}_i^{2q}, {p_{\mathrm{T}}}_j^{2q}) \frac{\Delta R_{ij}^2}{R^2} \\ d_{iB} &= {p_{\mathrm{T}}}_i^{2q} \end{aligned} \tag{2.40}$$

where ΔR_{ij} is the angular distance between partons i and j [7], while p_{T} stands for transverse momentum. The parameter R naively gives the angular coverage of the formed jet and typically is chosen to be smaller than one. Parameter q is usually varied between $q=1$ (k_t algorithm), $q=0$ (Cambridge/Aachen, C/A, algorithm), $q=-1$ (anti-k_t algorithm).

Secondly, the minimum between all the d_{ij} and d_{iB} has to be found. If $d_{\min} = d_{ij}$, partons i and j are summed together, where the *sum* is defined by a proper algorithm. Else-way i is declared as a jet and removed from the list of partons. The procedure is then repeated until no particle from the intiali list is left.

Jets algorithm can be applied to whatever kind of set of four momenta. The four momenta could be associated to partons, stable particles, or energy deposits in calorimeters measured by a detector. This makes jets a very powerful objects when comparing theoretical prediction to experimental measurements.

2.4.3 Large logarithms and resummation

Even if divergences are reabsorbed in pQCD, there is another particular feature of perturbative calculation which could spoil the convergence of the S-matrix series expansion. In fact, at fixed order and after renormalization, terms containing logarithms of scale ratios may appear. Such logarithmic terms can take very large values in particular regions of the phase space, typically near the bounds

[7] $\Delta R = \sqrt{(\eta_i - \eta_j)^2 + (\phi_i - \phi_j)^2}$, where η_i and ϕ_i are the pseudo-rapidity and azimuthal angle of the parton i

of the collinear/soft regions. Writing a partonic observable at the N^nLO in pQCD :

$$\hat{O} = \sum_{i=0}^{n} c_i g_s^i \tag{2.41}$$

large logarithms (L) could appear in the coefficients c_i as:

$$c_i = \sum_{j=0}^{m} a_{ij} \log^j(y) = \sum_{j=0}^{m} a_{ij} L^j \tag{2.42}$$

where y depends on the observable under study and in ceratin phase space region could take very small absolute values. Hence, if the coefficients c_i misbehave, the series could still not converge. One possible way to mitigate this problem, which increases theoretical accuracy of the calculation as well as offers a better physic description of the process, is to interpret such logarithms as terms of a perturbative expansion in L. The large L terms can then be reorganised and resummed as [80]:

$$\begin{aligned}
\hat{O} &= \sum_{i=0}^{n}\sum_{j=0}^{m} a_{ij} g_s^i L^j = \\
&= L\left(a'_{10} + a'_{11} g_s L + a'_{12} g_s^2 L^2 + \dots\right) + \left(a'_{20} + a_{21} g_s^2 L + a_{22} g_s^2 L^2 + \dots\right) + \dots \\
&= C(g_s) \cdot \exp[L f_1(g_s L) + f_2(g_s L) + g_s f_3(g_s L) + \dots]
\end{aligned} \tag{2.43}$$

where $f_i(g_s L)$ are functions with a power series expansion in $g_s L$. The reorganisation of the large logarithms contributions of Eq. (2.43) is called large logarithms resummation. First term of the exponent of Eq. (2.43) is the so called leading logarithm (LL) expansion, the second the next-to-leading logarithm (NLL) and so on. The effects of these terms on a particular observable are shown in Fig. 2.6, where the benefits of calculations at higher orders in the coupling constant and in the leading logarithms are clear.

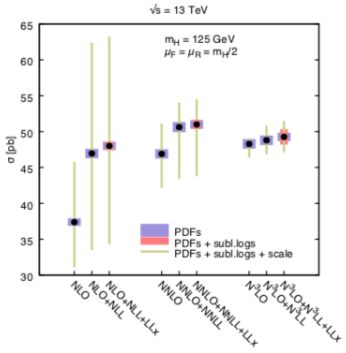

Figure 2.6: Effects of different perturbative expansion on the Higgs total cross section calculation. Plot from [81].

2.5 Tools for theoretical predictions at the LHC

Lagrangian models have been implemented in software tools to simplify the interface between the theory and experiments. These tools provide predictions for observables as a function of a set of input parameters, such as renormalisation and factorisation scales μ_R and μ_F or PDFs type, and also provide a way to estimate the uncertainty on the result. The standard way to implement these programs has been through the use of Monte Carlo (MC) event generators, each one with dedicated features to simulate various stages of the process.

When protons collide at the LHC at high energy a huge number of final state particles is produced. Such particles could have been produced in the hard scattering, from secondary scatterings at lower scales, as well as from radiation of charged particles in motion. When the protons beams are focused to produces the collsions, proton partons can be considered as moving charged particles which hence radiate. , only their constituent partons interact, as it has been explained in Section 2.4. The product of this partonic collision is a number of outgoing particles. Such particles are not the only product of the interaction though. The evolution of the remnants of the protons which did not participate into the hard collision have to be taken into account. Also, the evolution of all particles up to the energy scale at which detectors can measure them has to be modelled.

Typically, a MC event simulation of a pp collision contains the following steps:

- Computation of hard interaction

  The state of the art for general purpose tools is to have automated NLO QCD corrections implemented, for a two particle initial state into a two/three particles final state. For specific processes NNLO QCD [82, 83] and NLO EW predictions exist [84, 85].

- Parton shower

  High multiplicity final states are obtained from charged particles radiation. In automated calculation the radiation is usually computed at LO, and LL terms, which contain the main contribution of the soft/collinear radiation, are resummed via the so called parton shower (PS) algorithms. Since PSs describe same physics as higher order hard interaction calculations (i.e. emission of real radiation), the hard interaction part of the calculation and the PSs have to be combined properly to avoid radiation over/under counting. The combination procedure is usually referred to as matching and merging (M&M).

- Modelling of the protons remnants

  Interactions between partons not participating in the hardest interaction can occur. This is the so-called underlying event, or multiple parton interactions.

- Hadronization modelling

  After the hard interaction occur, partons start to radiate and progressively loose energy. When they reach an energy scale $\sim \Lambda_{\mathrm{QCD}}$, it is not possible to treat them as a free particles, because of the running of the strong

coupling constant. Hence they are recombined in hadrons, by algorithms which depend on the MC generator used.

- Decay of unstable particles

  Particles and hadrons can decay before they are measured by detectors, depending on their typical lifetime. In general purpose MC programs these decay are treated at LO.

- Simulation of the detector effects

  This is the last step of the simulation and connect the theoretical prediction to measured quantities. Stable particles interact with the material of which detectors are made, leaving a track. The modelling of the detector response is experiment based. General tools exist [86, 87] which gives the detector response of the main experiments at the LHC, but only each of the experiments has a fully detailed knowledge of how the detector works. It would be impossible to use all such information for people not belonging to the experiment, hence simplified versions of the detector response are usually implemented in the tools.

Simulations start from the process happening at the highest energy scale, the calculation of the hard interaction matrix element (ME), using pQCD. The structure of the UV and IR divergences is fixed by the Lagrangian and the perturbative order at which the calculation is made. This makes possible to define algorithms [88–90] which allows hard process MC generators to perform divergences cancellation internally. Then, an algorithm is used to generate events with four momenta of final state particles assigned by the probability distribution of the final state. The output of the hard process is then a set of events containing a list of particles with defined properties and four momenta, which has been agreed to be reported with a standard formatting(the LHE file format [91]). The renormalisation and factorisation scale values are input to the MC generator calculation and handle the infinities cancellation and renormalization which took place internally to the hard process generator. μ_R and μ_F are often chosen to have the same value, since they both give the scale at which perturbative calculation is spearated by other effects.

Initial and final state partons involved in the hard interaction are accelerated charged particle and hence they radiate. Because of the gluons interacting between themselves, the QCD radiation produces a shower of particles. Radiation coming from initial state partons is usually called initial state radiation (ISR), while if it comes from outgoing partons is called final state radiation (FSR). In the shower approach, a final state with high multiplicity is obtained as a succession of parton emissions, taking advantage of the factorisation of the differential cross section in the soft/collinear limit of an emitted particle:

$$\mathrm{d}\sigma_{p+1} \propto |M_{p+1}|^2 \,\mathrm{d}\Phi_{p+1} \propto |M_p|^2 \,\mathrm{d}\Phi_p \cdot \frac{\mathrm{d}t}{t} \frac{g_s(t)}{8\pi^2} P_{p\to p,1}(z)\mathrm{d}z \tag{2.44}$$

being $P_{p\to p,1}(z)$ the splitting function of emitting particle 1. The main contribution to this shower radiations is given by large logarithms produced in soft and collinear emissions of gluons is calculated by parton shower algorithms, i.e. the region of Eq. (2.44) where $t \to 0$. The differential probability of a parton a

to split into a couple of partons b and c carrying a z (and $1-z$) fraction of the original four momentum of a, at a scale t, at first order in QCD, is given by:

$$\mathrm{d}P_a(z,t) \propto \frac{\mathrm{d}t}{t}\frac{g_s}{8\pi^2}P_{a\to bc}(z)\mathrm{d}z \tag{2.45}$$

for every radiation of the shower algorithm. The process is then repeated, with subsequent emissions ordered following a scheme which can vary generator by generator. For instance PYTHIA [48] chooses to order the subsequent emissions by their p_{T}, choosing $t \sim p_{\mathrm{T}}^2$. HERWIG [47] instead uses angular ordering and sets $t \sim (1-\cos\theta)$, with θ the opening angle of the emitted particle. Different ordering schemes affect the behaviour of soft emission at large angle and could therefore have a strong impact on the calculation of observables which strongly depend on it. Resumming the soft contributions at LL, the probability of having a particle a not radiating between two scales t_i and t_f becomes:

$$\Delta_a(t_i,t_f) = \exp\left(-\int_{t_f}^{t_i}\frac{g_s(t)}{8\pi^2}\frac{\mathrm{d}t}{t}\sum_{bc}\int_z P_{a,bc}(z)\mathrm{d}z\right) \tag{2.46}$$

Since higher order ME calculations and PS both describe real radiation, it is important not to double count radiation when mixing the two approaches. This problem is solved by M&M methods which usually tackle the problem in one of the following ways:

- PS events are vetoed if they have already been counted in the ME calculation (the MLM scheme [92, 93], usually implemented in PYTHIA and HERWIG)
- events are assigned a weight to properly take into account certain phase space regions (the CKKW method [94], implemented in SHERPA [95])

To better clarify the M&M procedure, let us study a simplified example which is going to be useful in the following of this thesis, which is the matching of a NLO ME generator to a PS with a MLM algorithm.

Assuming a set of events has been computed using the POWHEG MC generator at NLO, the NLO real-radiation contribution is computed with an energy which depends on the scale which separates virtual from real effects. The POWHEG real radiations is p_{T} ordered, which means that if two gluons exist in the final state, the one with smaller p_{T} has been computed as a NLO contribution. Let us define the NLO real radiation certain transverse momentum ${p_{\mathrm{T}}}^{em}$. The real emission computed at NLO has the nice feature that it is properly described at that perturbative order in the whole phase space, in particular in the large-angle soft emission configuration which cannot be modelled in the PS algorithms. In order to save the best possible description of the hardest emission, PS emissions can be asked to only happen at a scale lower than ${p_{\mathrm{T}}}^{em}$. In the case the PS algorithm would produce an emission with transverse momentum harder than ${p_{\mathrm{T}}}^{em}$, the event is rejected from the shower, avoiding hardest emission double counting[8].

[8]This examples is simplified, since POWHEG and PYTHIA use the same ordering scheme by p_{T}. Things get more complicated when two generators havw different ordering scenarios, but such a discussion is out of the scope of this thesis.

After the shower has started, partons radiate and while the multiplicity of the final state increase, partons energy decrease until the regime at which strong force looses its perturbative behaviour. For energies of $\mathcal{O}(\Lambda_{\mathrm{QCD}})$ confinement forces become significant and hadronization occurs. In automated programs, the hadronization process is described via phenomenological models, such as the Lund model [96] or the cluster model [97]. The first hadrons produced can then be unstable and therefore decay shortly after. Models for hadrons decay exist and they are usually implemented at LO in the usual MC generators.

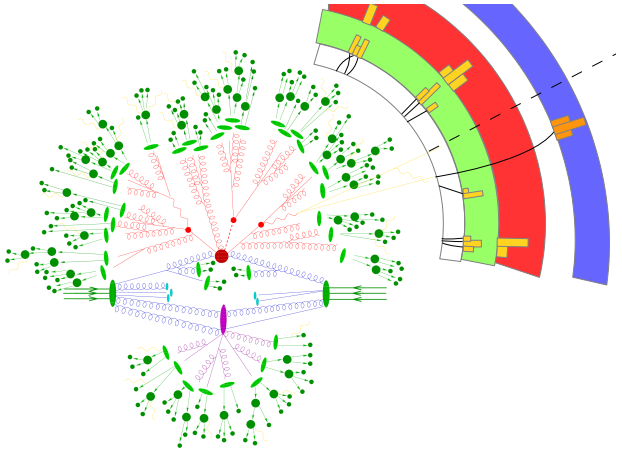

Figure 2.7: Schematic representation of a pp collision at the LHC. Different colors are associated to different phases of the MC simulation of the collision. The hard interaction is represented by the big red blob. Parton shower radiation is painted in red (final state radiation) and blue (initial state radiation). The underlying event produced by soft partons in the proton is depicted in violet instead. Primary hadrons, obtained by colored partons recombination, are drawn in light green. Their hadronic decay products, or secondary hadrons, are represented in dark green. Leptons and photons, which do not feel strong interaction, are painted in yellow instead. On the top-right corner, a typical detector for pp collisions and its interaction with the stable particles are sketched: the white part measure the tracks of charged particle (drawn as solid black lines), the green and red parts absorbe repsectively electron/photons and hadrons and measure their energies (yellow blocks), while the blue zone is dedicated to muons measurements. The dotted line refers to a neutrino escaping the detection. Figure ftaken rom Ref.[98] and subsequently modified.

Particles with a lifetime larger than 3 ns finally reach the detectors of the LHC experiments, which typically are placed starting from a distance of few centimetres from the beam axis. The details of the interaction between the particles and the detector, depend on the material of which the detector has been built and of course they vary experiment by experiment. Simplified models of the detector response are publicly available and implemented in general tools such as GEANT and DELPHI [86, 87]. Only hadrons, electrons, muons and photons interact with the detectors and are measured by the LHC experiments, since τ leptons have a lifetime ($10^{-13}s$) shorter than 3 ns, and neutrinos escape

detection because of their very small cross section. Typically four main sub-detectors are used to measure stable particles four momenta: a inner tracker which measure charged particles, a calorimeter which absorb all the electrons and photons, another calorimeter which absorb all the hadrons, and a muons spectrometer for tracking muons. Details on how experiments can measure such particles are given in Chapter 4, with a particular focus on the ATLAS detector.

Electrons and charged hadrons are reconstructed as energy deposit in their respective calorimeters, with an associated track in the inner tracker. If no associated track exists, then the signal can either come from a photon or a neutral hadron, depending on which calorimeter the signal come from. Muons are the only detectable particle which are not absorbed by the calorimeters, and their momenta are reconstructed from tracks left into the muon spectrometer. Of course, top-quarks are not measured directly by experiments, but top-quark-like events can be selected, by studying the particular signature of the top-quarks decay products. In the next chapter, Chapter 3, the phenomenology of top-quark production at the LHC is presented, focusing in particular on the determination of the top-quark mass.

Of course the four momenta of the physical objects reconstructed by the experiments could differ from the original ones, because of a multitude of experimental problems, but nevertheless they are everything one has to test theory predictions. Mainly two possibilities then exist to do so:

- Compute theoretically events up to the stable particle level, then add the specific experiment detector response and compare directly to the data measured by the respective experiment.
- Data collected by detectors are corrected by the experiments to the level at which they can be compared to a theoretical calculation, using the known detector response.

If the comparison between data and theory is performed via the first option, i.e. folding theoretical predictions to detector level, it relies on the available tools at the time the measurement is performed. Hence, if improvements are made on the modelling of the theoretical prediction, the analysis has to be repeated from the beginning, since theoretical calculation is fully entangled with the detector response modelling. This is not feasible, from the experiments point of view.

If data is corrected, a theory model has to be used to model the detector response, introducing a theory dependence on the data at the unfolded level. If the theory dependence is strong, the same problem as for the first option occur: theoretical and experimental modelling are so entangled that analysis has to be repeated. Such a dependence can be minimised though, unfolding data to a *truth* level well defined theoretically *fiducial volume*, which does not depend strongly on different underlying models. In general, a fiducial volume can be defined for different levels and selection cuts. For instance, the level formed by particles with a relatively long lifetime of nanoseconds is usually called *particle level*. It is also possible to define a level based on partons, the *parton level*, by considering particles before hadronization and/or top-quark decay, which describes elementary particles such as quarks and gluons not confined in hadrons. If an experiment corrects a measurement to parton level, it must assume a theoretical model for showering and hadronization, as well as a model for interaction of stable particles with the detector. At the particle level, only the

latter has to be assumed. Thus parton level descriptions in general depend more on theoretical assumptions than the particle level. The analysis presented in Chapters 5 to 7 study deeply the aforemetnioned arguments, in the context of the top-quark pole mass measurement. A more detailed discussion on such topic is therefore postponed to Section 6.1.

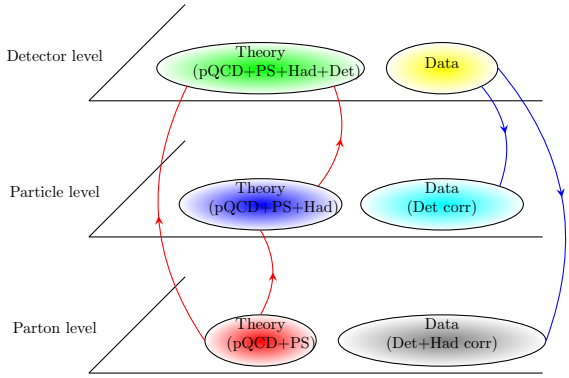

Figure 2.8: Different approaches in comparing theoretical predictions to measured data. The *particle* and *parton* truth levels are shown, as well as the level at which data is measured, the detector level. Comparsion between data and theory can be performed either by folding theoretical predictions to detector level, or by unfolding data to the level where theoretical calculation has been defined. Folding is represented by red lines while unfolding by blue ones. Ellipses represent the fiducial volumes defined for each level phase space.

Chapter 3

The top-quark and its mass

The top-quark is the heaviest particle discovered so far, with a mass of the order of 170 GeV. In the SM it has the strongest coupling to the Higgs field, with a Yukawa coupling $y_t \sim 1$. Precise measurements of the properties of the top-quark are important to better understand the SM and to put limit on the free parameters space of beyond the SM (BSM) theories. In this chapter top-quark physics and its phenomenology at the LHC are discussed, with a particular focus on the the top-quark mass. Firstly, an introduction to the physics of the top-quark is given in Section 3.1. The important role of the top-quark in the SM and its influence on BSM theories is explained in Section 3.2, where implications relative to the value of the top-quark mass are discussed. Measuring the top-quark mass is challenging in the very dense QCD environment of the LHC. Various methods have been developed to solve this difficult task and the most important ones are described in Section 3.3, in which also possible advantages of performing top-quark measurements in different conditions, such as the ones of a lepton collider, are also shortly discussed. Finally, the method which is used in the experimental analysis of Chapter 6 to extract the top-quark mass in the pole and $\overline{\text{MS}}$ scheme is reported in Section 3.3.2, which is a summary of Refs. [40, 99].

3.1 Top-quark physics

Production of top-quarks has only been observed at the Tevatron and LHC hadron colliders. Hence, most of the measurements of the top-quark proerties have been carried out by four collaborations: the D$\varnothing$ and CDF collaborations studied the top-quarks produced by $p\bar{p}$ interactons, while at the LHC the ATLAS and CMS collaborations are studying top-quarks coming from in pp collisions.

The top-quark belongs to the third generation of quarks of the SM, together with its weak isospin partner, the b-quark. Both quarks were introduced by Kobayashi and Maskawa [15], who generalised an existing work by Cabibbo [100] to explain the observation of CP-violation in the decay of kaon mesons [101]. Since the quarks mass eigenstates are not eigenstates of $\mathcal{SU}(2)_L$, the electroweak interaction term of $\mathcal{L}^{\text{SM}}$ mix the quarks flavours. The mixing can be described by a unitary matrix, which for two quarks generations is parametrised by only one free parameter, the Cabibbo angle. For three quark generations instead,

three angles and a complex phase are needed to parametrise it, the presence of the additional complex phase allowing CP-violation processes.The matrix in this case takes the name of Cabibbo-Kobayashi-Maskawa (CKM) matrix.

In the SM, the only t-quark free-parameters are its mass, m_t and the three CKM matrix elements which gives the strengths of the couplings of the top-quark to the other quarks, V_{tb}, V_{ts}, V_{td}. The magnitude of the CKM matrix parameters are precisely extracted from a global fit to all available measurements, imposing the existence of three quarks generations and matrix unitarity [102]:

$$V_{\mathrm{CKM}} = \begin{pmatrix} V_{ud} & V_{us} & V_{ub} \\ V_{cd} & V_{cs} & V_{cb} \\ V_{td} & V_{ts} & V_{tb} \end{pmatrix} = \begin{pmatrix} 0.974 & 0.224 & 0.004 \\ 0.224 & 0.974 & 0.0421 \\ 0.009 & 0.039(\pm 0.041) & 0.999 \end{pmatrix} \tag{3.1}$$

A precise measurement of m_t is a delicate topic which is discussed in detail in Section 3.3. In general though m_t is large, which implies a large decay width Γ_t, being $\Gamma_t \propto m_t^3$ in the SM.

The top width has been computed in the SM fully differentially at NNLO QCD plus NLO EW corrections [103, 104], and it has been measured at Tevatron and LHC [105–108], the most precise analysis giving

$$\Gamma_t = 1.36 \pm 0.02\ (\mathrm{stat})\ \pm {}^{0.14}_{0.11}\ (\mathrm{syst})\ \mathrm{GeV} \tag{3.2}$$

which is compatible within the errors with the theoretical expectation of 1.35 GeV. Such value for Γ_t implies that the top-quark is a very short living particle, being its lifetime of the order of $\tau_t \sim 1/\Gamma_t \sim 5 \cdot 10^{-25} s$. The t-quarks offer the unique chance of studying a quark free of confinement effects, since they decay before any hadronization effect occurs, being the time scale at which confinement effects become important $\tau_{\mathrm{QCD}} \sim 1/\Lambda_{\mathrm{QCD}} \sim 10^{-24} - 10^{-23} s$. Partial decay widths are proportional to the square of the CKM matrix elements, hence top-quarks decay into a b-quark and a W boson in $|V_{tb}|^2| \sim 99.8\%$ of the cases.

The top-quark electric charge Q_t is predicted to be $-2/3$ in the SM and can be determined in experiments by measuring the $t-\gamma$ interaction vertex or the charge of the top decay products. In the first case, the $t\bar{t}\gamma$ production processes should be studied, since its cross-section depends on Q_t. It has been studied both at Tevatron [109] and LHC [110], but a direct the interpretation of the measurement of the $t-\gamma$ vertex has not been attempted yet, since the photon in $t\bar{t}\gamma$ could come from other EM charged particles. A measurement of Q_t from t-quark decay products has been performed instead, giving a value [111]:

$$Q_t = 0.64 \pm 0.02\ (\mathrm{stat})\ \pm 0.08\ (\mathrm{syst}) \tag{3.3}$$

compatible with the SM expectation.

Spin can be measured from the angular distributions of the top-quark decay products. in fact, W bosons produced in top-quarks decay are polarized in the SM. The observable which is usually employed in spin measurements is the differential normalised cross section, function of the angle θ^* which the charged lepton (down-type quark) from the leptonic (hadronic) W boson form with the top-quark boost direction, in the W boson rest frame. Such cross section can

be written as a function of the fractions of left-handed (F_L), longitudinal (F_0) and right-handed (F_R) polarizations of the W boson:

$$\frac{1}{\sigma}\frac{\mathrm{d}\sigma}{\mathrm{d}\cos\theta^*} = \frac{3}{8}(1-\cos\theta^*)^2 F_L + \frac{6}{8}(1-\cos\theta^*)^2 F_0 + \frac{3}{8}(1+\cos\theta^*)^2 F_R \quad (3.4)$$

The measurements carried out at both Tevatron and LHC agree with the NNLO QCD SM expectation of $F_L \sim 0.3$, $F_R \sim 0$ and $F_0 \sim 0.7$ [112] within a 10% [113] and 5% [114] accuracy, confirming the top-quark is a fermion of spin $\frac{1}{2}$.

In the following, the physics of top-quarks produced in pp collisions is studied in more detail.

3.1.1 Top quark production at the LHC

Top-quarks are produced at the LHC either in quark-antiquark pairs ($t\bar{t}$ production) or as single quarks (single-t production). They can also be produced in association with other particles, like a Higgs boson or a Z boson, typically with cross sections smaller of few orders of magnitude.

For $pp \to t\bar{t}$ process, the most dominant production mode at LO in QCD is gluon fusion, accounting for 90% of $t\bar{t}$ events, with $q\bar{q}$ annihilation only contributing to a 10% of the total. At NLO in QCD additional production channels, such as (anti-)quark gluon production also become possible. The most precise calculation of the inclusive $t\bar{t}$ cross section to date is at NNLO+NNLL in QCD [115], while differential distributions have been computed at an approximate NNLO QCD. [116]. At such level of QCD precision, it has been showed that electroweak corrections begin to be relevant, and calculations at NNLO in QCD including NLO EW effects have been computed [117]. Since $t\bar{t}$ signature in ex-

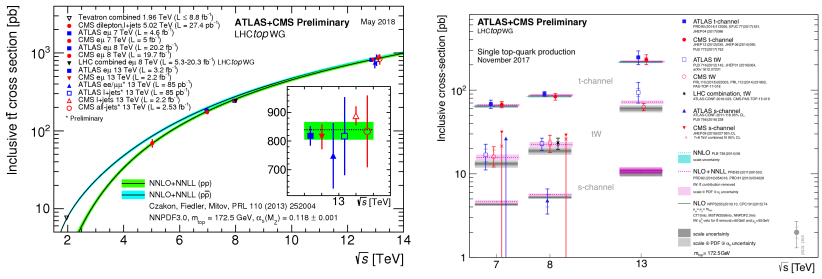

Figure 3.1: Summary of the $t\bar{t}$ and single-t inclusive cross sections measurements at the LHC. Figures from Refs. [118, 119].

periments are of the type $pp \to t\bar{t} \to W^+bW^-\bar{b}$, various calculations started including top-quark decay effects and off-shell top-quark contributions at fixed order in QCD, by computing directly the cross sections of $pp \to W^+bW^-\bar{b}$ [120–122].

Top-quark pair events are conveniently classified in experimental categories based on the number of leptons in their final state. The W boson decay hadronically into a $q'\bar{q}$ pair $\sim 67\%$ of the times or leptonically into a charged and neutral lepton pair with branching ratio $\sim 11\%$ for each fermion generation. The τ leptons also decay before interacting with the detector since they have $\sim 10^{-15}s$ lifetime, with branching ratios $\mathcal{B}(\tau \to \text{hadrons}) \sim 66\%$, $\mathcal{B}(\tau \to e\nu_e\nu_\tau) \sim 17\%$

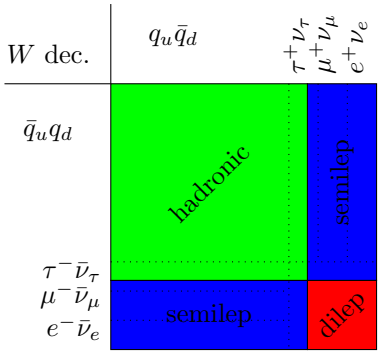

Figure 3.2: Branching ratio of $t\bar{t}$ events final states. If τ leptons are considered as stable particles (dotted lines), 44% of $t\bar{t}$ events are hadronic, 45% are semileptonic and 11% are dileptonic, while if τ are considered decayed (continuous line) the corresponding percentages are 55%, 38% and 7%.

and $\mathcal{B}(\tau \to \mu\nu_\mu\nu_\tau) \sim 17\%$. Hence 55% of $t\bar{t}$ events have no lepton in the final state and such decay channel is called *all hadronic*. The presence of one lepton only defines the *semileptonic* channel, which has a probability around the 38%, while the *dileptonic* final state (exactly two final state leptons) happens only the 7% of the times.

At high orders in pQCD, $t\bar{t}$ production in the SM is expected to have a small asymmetry under the exchange of top with anti-top quarks[123, 124]. At the LHC, the so-called *charge asymmetry* observable is used to measure $t\bar{t}$

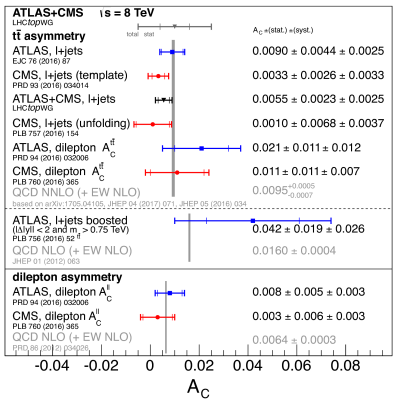

Figure 3.3: Summary of the $t\bar{t}$ charge asymmetries measurements performed at LHC at $\sqrt{s} = 8$ TeV. Figures from Refs. [118, 119].

production asymmetry. It is defined as the fraction of events with top-quarks with absolute pseudo-rapidity ($|\eta_t|$) higher than the anti-top-quark one ($|\eta_{\bar{t}}|$) minus the fraction of events with $|\eta_{\bar{t}}| > |\eta_t|$. So far, all the measurements performed by the ATLAS and CMS collaboration are not sensitive enough to confirm the SM asymmetry, but they all give results which are compatible with

no asymmetry, as it is shown in Fig. 3.1. Nevertheless, various BSM models predict large asymmetries in $t\bar{t}$ production and the measurements carried out at the LHC strongly exclude such models.

Top-quarks can also be produced singularly, via electro-weak processes called single-top production modes, as it is shown in Fig. 3.4. For instance, single tops are produced by a light quark and a b-quark interacting via the exchange of a space-like W boson $\sim 70\%$ of the times, via the so-called t-channel. If the exchanged W boson is time-like instead, the production mode is called s-channel and it contributes to $\sim 5\%$ of the total single top cross section. The remaining $\sim 25\%$ of single top-quarks is produced in association with a W boson (Wt channel). While the t-channel production has been calculated fully differentially at NNLO [125], the s-channel and Wt channel are available at approximate NNLO (NLO+NNLL) [126, 127]. Values of the inclusive single top production cross sections at the LHC are reported in Fig. 3.1.

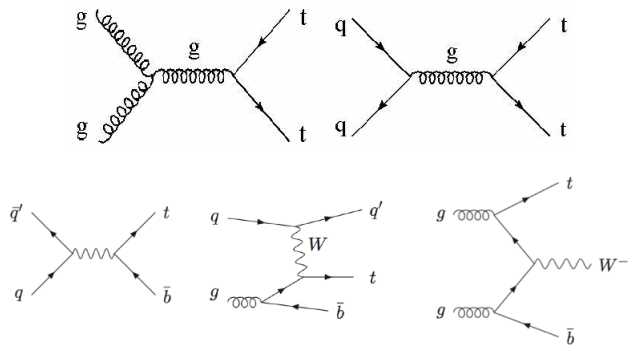

Figure 3.4: Examples of leading order Feynman graphs for top-quark production at the LHC. At the top, diagrams for $t\bar{t}$ pair production via gluon fusion (left) and quark annihilation (right). At the bottom, single-top production in the s-channel (left), t-channel (center) and in association with a W boson (right).

One particular production mode, which is interesting in the context of this thesis, is the associated production of top-quark pairs with a Higgs boson, $pp \to t\bar{t}H$. Such a process is the only one in which the top-Higgs vertex can be tested directly and it was observed for the first time only very recently by the ATLAS (and CMS?) experiment [128]. The observation confirmed that the top-quark couple to the Higgs field and hence gain its mass from the EWSB and the Higgs mechanism.

So far, the top-quark has been confirmed to have the characteristics predicted by the SM and top-quark cross sections measured by the experiments are compatible with the theoretical expectations, as it can be seen in Fig. 3.1. Nevertheless, new physics (NP) could be hiding in the top-quark sector, because of the relevant contribution of top-quark to the EWSB. The role of the top-quark mass in the EWSB and in BSM scenarios is discussed in the next Section 3.2.

3.2 The top-quark mass in the EWSB and BSM theories

The top-quark plays a special role in the SM and in new physics scenarios beacuse of the value of its Yukawa coupling, $y_t \sim 1$.

Firstly, top-quark strongly affect the Higgs and W bosons renormalimased masses, m_H and m_W. In fact, the running of the Higgs mass, ignoring fermions lighter than the top-quark, can be written at first order in QCD as [129]:

$$\frac{\mathrm{d}m_H^2}{\mathrm{d}\Lambda^2} \sim \frac{3g_s^2}{64\pi^2 m_W^2}\left(m_H^2 + m_Z^2 + 2m_W^2 - 4m_t^2\right) + \dots \tag{3.5}$$

being Λ^2 the scale of the renormalisation of the UV divergences, while for m_W:

$$m_W \sim m_W^{\text{bare}}\left(1 - \frac{3}{16v^2\pi^2\tan\theta_W}m_t^2 + \frac{11M_Z^2\cos\theta_W}{v^2 48\pi^2}\log\frac{m_H^2}{m_Z^2}\right) \tag{3.6}$$

Hence, the W boson, top-quark and Higgs masses are correlated between each other through their radiative corrections. By fixing θ_W and m_Z to their very precisely measured values, it is possible to check the consistency of the SM, as it is shown in Fig. 3.5. The relations between the masses change if new physics effects are taken into account [130] and hence mass measurements contribute to restrict the parameters space of BSM models, as it is shown in Fig. 3.5. The leading uncertainty in such tests come from the error with which the top-quark mass is measured, hence more precise measurements of it could show deviation from the SM expectation, or stronger constraints on BSM models.

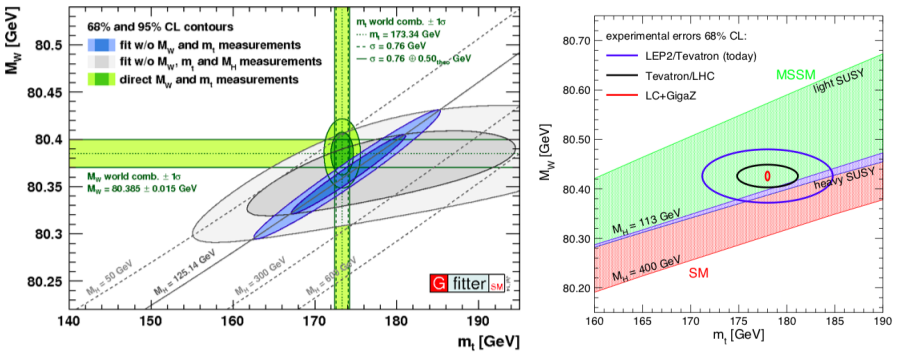

Figure 3.5: On the left, global fit of the SM masses of the W boson (m_W), Higgs boson (m_H) and top-quark m_t. The countours correspond to 68% (lighter colours) and 95% (darker coulours) confidence levels. Figure from Ref. [131]. On the right, the same fit is performed as consistency check of different BSM theories (Figure from Ref. [130]).

Secondly, from Eq. (3.5), the Higgs physical mass can be computed approximately as $m_H^2 \sim {m_H^{\text{bare}}}^2 + \left(m_H^2 + m_Z^2 + 2m_W^2 - 4m_t^2\right)\Lambda_{UV}^2$, with its value at the EW scale having been measured to be $m_H(m_Z) \sim 125$ GeV. To satisfy such condition, m_H^{bare} needs to have a very precise value to balance the radiative corrections to the Higgs self energy. Such corrections are dominated by the m_t

contribution coming from the top-quark loop correction, as shown in Fig. 3.6. Theories for which cancellations between large terms happen are called *fine tuned*. The corrections to the Higgs mass diverge at high Λ and there is no mechanism or symmetry in the SM which can avoid that. This originate the so-called *hierarchy* problem. In fact, one could imagine the corrections to the

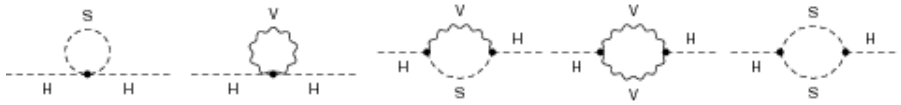

Figure 3.6: Example of quantum corrections to the SM bosons masses. F stands for a fermionic particle (such as the top-quark) while S for scalar and V for vector bosons. Figure from Ref. [132].

Higgs mass to be smaller than the mass itself, $\delta m_H^2 < m_H^2$, using arguments from *naturalness*[1], which imply the SM validity up to a scale $\Lambda_{UV} \sim 1$ TeV. Another option to solve the hierarchy problem is to define a BSM theory which introduce additional contributions to m_H which cancel the top-quark loop contribution. In supersymmetric (SUSY) models for instance, this is achieved by adding a bosonic field to the theory, associated to the top fermion field. Nevertheless up to now no evidence for any BSM model has been found, and the naturalness argument is just an aesthetic, not physical, criterion.

Another aspect in which top-quark plays an important role is the EW vacuum stability. To show that, it is convenient to write Eq. (3.5) as a function of the SM couplings instead that particles masses. Recalling Eq. (2.25) of Section 2.3, one obtains the running of the Higgs quartic coupling $\lambda^{\text{bare}}(= \frac{m_H^{\text{bare}\,2}}{2v^2})$ as a function of top-quark mass and strong coupling constant α_s, as shown in Fig. 3.7. For negative values of λ, the Higgs potential of Eq. (2.24) has no absolute minimum, making the electroweak vacuum unstable. Assuming the validity of the SM up to the Planck scale, the stability condition at NNLO in QCD reads [133]:

$$\frac{m_H - 125.14}{0.24}\ \text{GeV} \gtrsim +7.5 \left(\frac{m_t^{\text{pole}} - 173.2\ \text{GeV}}{0.9\ \text{GeV}} \right) - 2.1 \left(\frac{\alpha_s(m_Z) - 0.1184}{0.0007} \right) \tag{3.7}$$

and depends on three main parameters: the Higgs boson mass and the strong coupling constant α_s, which are well known at per-mille level, and the top-quark pole mass m_t^{pole}, which again has the largest uncertainty. The phase diagram of the EW vacuum is shown in Fig. 3.7.

It should be clear from the discussion of this section, that a precise measurement of the top-quark mass is interesting for many theoretical topics, from

[1] One practical definition of naturalness is that given any observable consisitng of n indipendent contributions, $\mathcal{O} = \mathcal{O}_1 + \mathcal{O}_2 + \cdots + \mathcal{O}_n$, each of the $\mathcal{O}_i$ should be comparable to or less than $\mathcal{O}$. If this condition is not satisifed, i.e. $\mathcal{O}_j \gg \mathcal{O}$, then another $\mathcal{O}_k$ should contribute to the observable in the opposite direction stabilizing the observable value. Then the cancellation of large contributions is considered "unnatural".

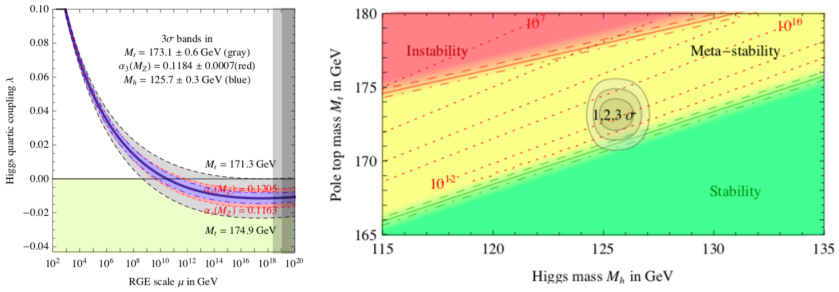

Figure 3.7: On the left, the running of the quartic coupling λ, with 3σ contours due to variations of α_s and m_t. On the right, the phase diagram of the EW vacuum, function of the physical masses of the Higgs boson and the top-quark. The plot is zoomed into the region of the measured values of m_t and m_H. Figures from Ref. [133].

naturalness to the stability of the universe. Various techniques have been developed to measure m_t in experiments, which are briefly discussed in the next Section 3.3.

3.3 Top-quark mass measurements

Two main kind of analyses have been developed to extract a value for the top-quark mass. Either m_t is inferred from the four momenta of its decay products, the so called *direct* or *kinematic* measurements, or the value is inferred from cross-sections which depend on it. An alternative possibility is to extract values of the top-quark from inclusive or differential cross sections. In both cases, the accuracy with which m_t has been measured is reaching the $\sim$ GeV precision, which makes relevant a number of theoretical aspects, such as [134]:

- what mass-scheme does the value measured refers to, as discussed in Section 2.4.1?
- is it possible to measure the mass of a colored particle with precision higher than $\Lambda_{\rm QCD}$?
- what is the connection between the measured m_t and the $\mathcal{L}^{\rm SM}$parameter?

Direct measurements do not completely answer to such questions and in fact for such measurements only experimental errors are reported by the experimental collaborations, while no theoretical extrapolation is performed. The top-quark mass in kinematical methods is defined from Monte Carlo simulations, where the top-quark is considered as a resonant particle with $p_t^2 \sim {m_t^{\rm MC}}^2$, Hence the mass which is reconstructed from the top-quark decay products which satisfy $\sum_{\rm products} p_i = p_t$ follows approximately a Breit-Weigner distribution centred in $m_t^{\rm MC}$. The resonant mass is extracted from data by comparing the reconstructed mass distribution to the one predicted by a set of MC produced with different input values of $m_t^{\rm MC}$. The mass extracted in this way does not have a theoretically rigorous definition, since no relation is known to relate $m_t^{\rm MC}$ to a well

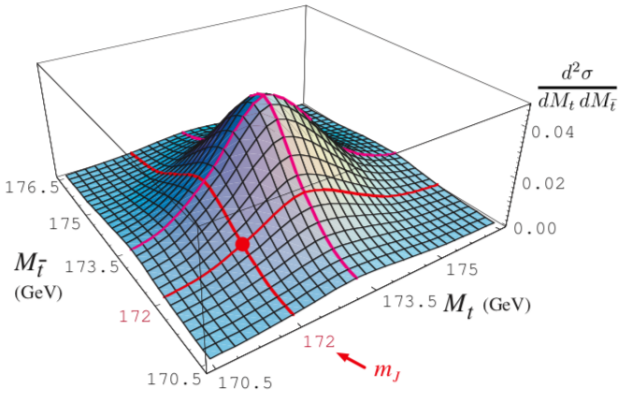

Figure 3.8: Plot of the double differential hemisphere invariant mass cross-section $\mathrm{d}\sigma/\mathrm{d}M_t^{\mathrm{reco}}\mathrm{d}M_{\bar{t}}^{\mathrm{reco}}$, where $M_{\bar{t}}^{\mathrm{reco}}$ is the mass reconstructed from top or antitop decay products. The observed peak position (intersection of the magenta lines) is not given by the true top-quark pole mass, which has been fixed to m_J = 172 GeV (red lines). Figure from Ref. [135].

defined $\mathcal{L}^{\mathrm{SM}}$parameter. Being m_t^{MC} close to the pole of the top-quark propagator, it has often been identified with m_t^{pole}. Nevertheless it has been shown that a theoretical error due to the misinterpretation of the mass in the pole scheme of the order of $|m_t^{\mathrm{MC}} - m_t^{\mathrm{pole}}| \sim \mathcal{O}(\mathrm{GeV})$ [135] exists, depending on the observable under study, as it is shown for example in Fig. 3.8. Measurements of m_t^{MC} hence, should contain a theoretical uncertainty to cover m_t^{MC} non rigorous definition. Such error is usually difficult to evaluate and is thus not included between the value reported by experiments, such as the ones of Fig. 3.9. With experimentally uncertainties getting lower an lower, $\Delta^{\mathrm{theory}} m_t$ is becoming the leading uncertainty for direct mass measurements.

On the other end, cross sections can be computed in well defined theoretical frame, and their values can depend on m_t. Hence top-quark mass values extracted from cross sections measurements can be directly related to the respective $\mathcal{L}^{\mathrm{SM}}$ parameter, in the renormalisation scheme in which the cross section is calculated. Sensitivities of cross sections to m_t are typically quite low, resulting in the end in a less precise m_t than m_t^{MC}, as can be seen from Fig. 3.9.

In the best possible scenario the top-quark mass would be inferred from observables which have high sensitivity to m_t, as in the case of direct measurements, and which are theoretically well defined (IR-safe, fixed mass scheme and theoretical errors under control), as in the case of the cross-sections. In the following, a summary of the techniques used in top-quark measurements performed so far is presented.

3.3.1 Review of top-quark mass measurements [136]

Various methods have been developed to measure the top-quark mass. Historically, the first methods measured m_t^{MC} in fully hadronic, semileptonic and dileptonic $t\bar{t}$ events.

In fully hadronic analyses [137], at least six jets come from $t\bar{t}$ decay, two of

them b-tagged. Hence, one can define m_{jjj} as the mass of the system made of three jets reconstructing the top-quark momentum. Such quantity strongly depend on how well jets four momenta are reconstructed, which is typically of the order of a few percent. To reduce such dependence, m_{jjj} can be divided by the mass of the di-jet system candidate of the W boson from the top-quark decay, m_{jj}, defining the observable $R_{\frac{3}{2}} = \frac{m_{jjj}}{m_{jj}}$. In a dense QCD environment such as the one of the LHC, the main difficulty of choosing fully hadronic final state is to reduce the overwhelming multi-jet background and describe it properly, typically using data driven techniques. In semileptonic events[138, 139], the presence of one neutrino does not allow to reconstruct the four momentum of the leptonic top-quark, since the projection of the neutrino four momentum along the beam axis cannot be inferred from the detectors. Hence, additional information has to be assumed to constrain the leptonic top reconstruction, which typically is a fixed value for the W boson mass. The m_t^{MC} value can then be identified with the mass of the lepton, neutrino and b-jet system, while the hadronically decaying top-quark that can be used to perform another measurement, for example constraining the scale of the jets energy, to reduce a particular systematic error.

Dileptonic final states instead [140, 141] have the advantage that leptons four momenta are very well reconstructed by detectors, while on the other hand they have a lower statistical precision. In the case of the dileptonic channel, two neutrinos are expected from $t\bar{t}$ events, which cannot be resolved without imposing constraints on m_t. Hence, observables which do not make use of neutrinos four momenta but are sensitive to m_t have been used, such as the the lepton and b-jet system invariant mass, or similar.

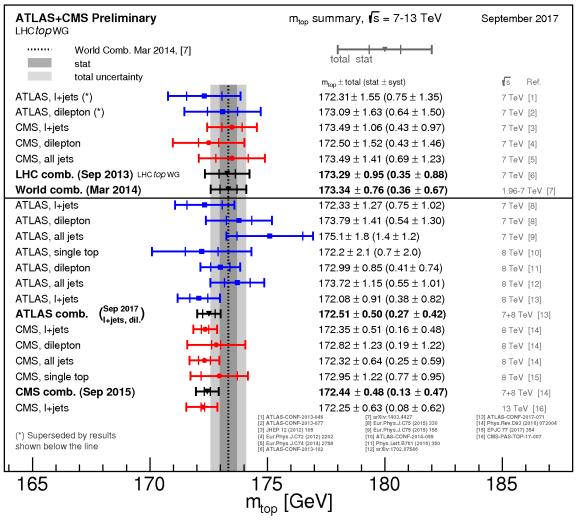

Figure 3.9: Measured top-quark mass values via kinematic reconstruction. Figure from Ref. [142].

In general, standard kinematic mass methods are limited by the detector precision on the determination of jets four momentum and/or by the modelling of the hadronization in the Monte Carlo program. Alternative methods were developed to reduce such systematic errors, for instance looking at the distributions of the charged particles [143] from top-quark decay, for which

the four momentum is reconstructed with higher accuracy; or studying leptons only distributions to reduce the impact of hadronization, such as in the case of $\mu^+\mu^-$ decay of J/ψ mesons produced in the hadronization of b-jets [144] from top-quark decay. Other methods extract instead extract $m_t^{\rm MC}$ from top-quarks produced with very large transverse momenta [145], or produced mainly via single-top production mode [146, 147], to explore phase space regions which are different to the standard ones. The advantage of having a multitude of different analyses measuring the same parameter with independent techniques or in independent phase space regions is that it becomes possible to combine all the measurements together to reduce the total error on the estimation of $m_t^{\rm MC}$. The latest combination[2] of the ATLAS and CMS results are reported in Fig. 3.9 and give:

$$\begin{aligned} m_t^{\rm MC}(\text{ATLAS comb.}) &= 172.51 \pm 0.50\,(\text{stat} \oplus \text{syst})\ \text{GeV} \\ m_t^{\rm MC}(\text{CMS comb.}) &= 172.44 \pm 0.48\,(\text{stat} \oplus \text{syst})\ \text{GeV} \end{aligned} \tag{3.8}$$

where no theoretical uncertainty is reported on $m_t^{\rm MC}$, since no extrapolation to the $\mathcal{L}^{\rm SM}$ parameter is performed. As it has already been mentioned, the dominant uncertainty on $m_t^{\rm MC}$ is becoming its theoretical interpretation, of the order of $\sim$ 1GeV.

Measurements of m_t via cross sections does not have such problem if the cross sections are calculated orders beyond the leading one, where a renormalisation scheme had to be fixed in order to reabsorb the UV divergences of the theory. $t\bar{t}$ and single-t cross sections have been calculated at NNLO in QCD, as it has anticipated in Section 3.1.1, and they do depend on the renormalised parameters of the $\mathcal{L}^{\rm SM}$, such as $m_t^{\rm pole}$ or $m_t(m_t)$. Typically, a good parametrisation for the inclusive $t\bar{t}$ cross section, $\sigma_{t\bar{t}}^{\rm incl.}$ is [115]

$$\sigma_{t\bar{t}}^{\rm incl.}(m_t^{\rm pole}) = \sigma_0 \left(\frac{m_0}{m_t^{\rm pole}}\right)^4 \left(1 + ax + bx^2\right) + \ldots \tag{3.9}$$

where m_0 is a reference value for the top-quark mass, around 170 GeV, $x = (m_t^{\rm pole} - m_0)/m_0$, while a, b and σ_0 are free parameters.

Top-quark mass extraction $\sigma_{t\bar{t}}^{\rm incl.}$ in the pole-mass scheme have been performed by both ATLAS and CMS, as reported in Fig. 3.10, yielding values which are not very competitive with the kinematic reconstruction methods, even if including the theoretical uncertainties. The main source of uncertainties in such measurements are the PDF uncertainties, which strongly affect $\sigma_{t\bar{t}}^{\rm incl.}$,. Also, sensitivity of $\sigma_{t\bar{t}}^{\rm incl.}$ to the top-quark pole mass is not very high. In fact, from Eq. (3.9), typically $\Delta\sigma/\sigma \sim 5\%\Delta m_t^{\rm pole}/m_t^{\rm pole}$, which means that a total error of 5% in the measurement of the cross section roughly imply a 1% error on $m_t^{\rm pole}$. To reduce the total uncertainty, normalised differential cross sections can be used. Nsormalisation reduce the impact of PDF uncertainties, which mostly simplify in the ratio, while differential distributions can have regions where they are more sensitive to the top-quark mass. $m_t^{\rm pole}$ has been measured by the ATLAS collaboration from the dileptonic differential distributions of $t\bar{t}$ events at 8 TeV[148] with a total error of $\sim$ 1.5 GeV and the normalised differential cross

[2]Not all of the measurements enter in the combination, since not all of them add useful information to the improvement of the result.

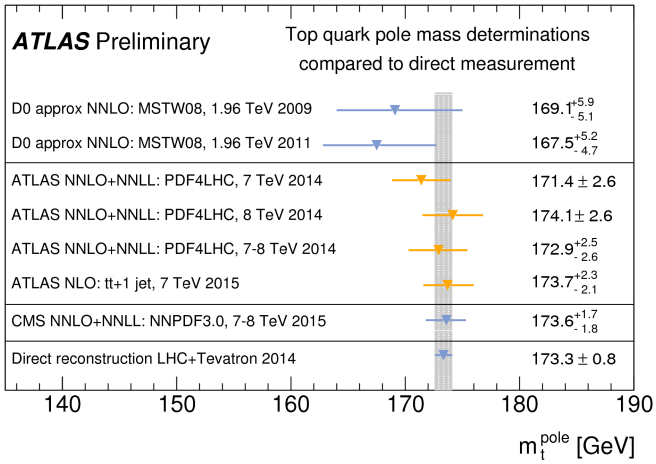

Figure 3.10: Measured top-quark mass values via cross section measurements. Figure from Ref. [142].

section as a function of $t\bar{t}+1$-jet system invariant mass has been used to extract m_t^{pole} from data at 7 TeV by ATLAS [41] and 8 TeV by CMS [149]. This last method has been used in this thesis to extract the top-quark mass using the 8 TeV data collected by the ATLAS detector, and is hence described in more detail in the following Section 3.3.2.

3.3.2 Top-quark mass measurement from $t\bar{t}+1$-jet tolopologies

The gluon emission from a radiating top-quark is sensitive to its mass, and it can be used to extract m_t^{pole} values with high accuracy, as it was proposed in [40]. One observable which is sensitive to this process is

$$\mathcal{R}(m_t^{\text{pole}}, \rho_s) = \frac{1}{\sigma_{t\bar{t}+1\text{-jet}}} \cdot \frac{\mathrm{d}\sigma_{t\bar{t}+1\text{-jet}}}{\mathrm{d}\rho_s}, \tag{3.10}$$

with

$$\rho_s = \frac{2m_0}{\sqrt{s_{t\bar{t}+1\text{-jet}}}} \tag{3.11}$$

where m_0 is a constant of the order of the top-quark mass, fixed to 170 GeV in [40, 41, 149], and $s_{t\bar{t}+1\text{-jet}}$ is the invariant mass of the $t\bar{t}+1$-jet system. Different values of m_t changes the shape of $\mathcal{R}$ as it is shown in Fig. 3.11.

The sensitivity of the observable of Eq. (3.10) to the top-quark mass can be calculated as:

$$\mathcal{S}(\rho_s) = \sum_{\Delta=\pm\delta} \frac{|\mathcal{R}(m_0+\Delta m, \rho_s) - \mathcal{R}(m_0, \rho_s)|}{\Delta m \cdot \mathcal{R}(m_0, \rho_s)} \sim \frac{\Delta\mathcal{R}}{\mathcal{R}} \frac{1}{\Delta m}, \tag{3.12}$$

where Δm is the range of the mass change. The sensitivity is almost independent of the choice of Δm, since the dependency of the observable on m_t^{pole} is almost

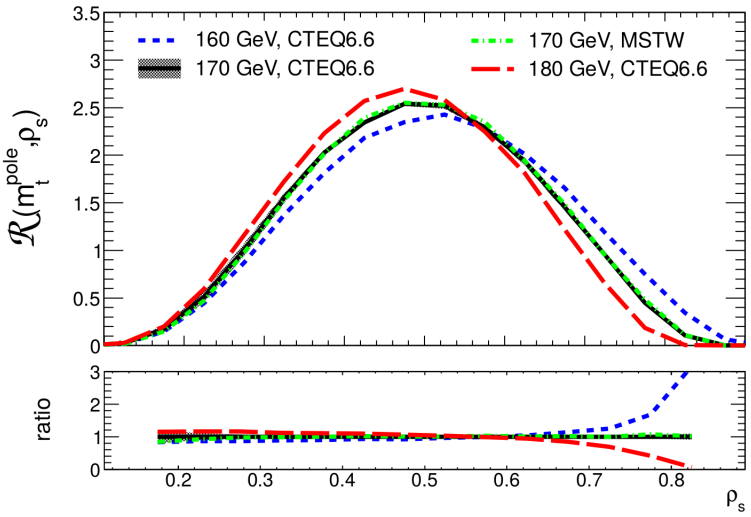

Figure 3.11: The normalized differential cross section $\mathcal{R}(m_t^{\text{pole}}, \rho_s)$ at parton level. The x-axis represents ρ_s. Plot is taken from Ref. [40], where the observable was calculated at a 7 TeV centre of mass energy. Several curves are shown for different values of the top mass.

linear., from Eq. (3.9). The green curve in Fig. 3.12 corresponds to the pole mass sensitivity for Δm with values of 5 and 10 GeV. The labels on the rightmost y-axis of Fig. 3.12 correspond to the product of the top-quark pole mass and the sensitivity of Eq. (3.12), that relates the fractional change in the observable with that in the top-quark pole mass: $\frac{\Delta\mathcal{R}}{\mathcal{R}} \sim (m_t^{\text{pole}} \times \mathcal{S}) \cdot \frac{\Delta m_t^{\text{pole}}}{m_t^{\text{pole}}}$. For small values of the invariant mass of the $t\bar{t}+1$-jet system, or $\rho_s > 0.7$, the sensitivity grows strongly. It reaches ~ 20 for values of ρ_s around 0.8, meaning that a 1% variation in the top mass results in a 20% $\mathcal{R}$ variation, roughly four times higher than for the inclusive $t\bar{t}$ cross section.

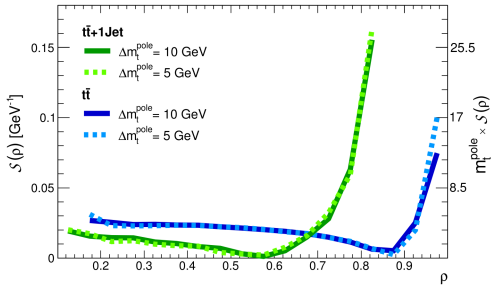

Figure 3.12: The sensitivity of $\mathcal{R}(m_t^{\text{pole}}, \rho_s)$ to the top-quark mass. The sensitivity for a similar observable for the $t\bar{t}$ topology is also shown, where the invariant mass of the $t\bar{t}+1$-jet system is replaced by the invariant mass of the $t\bar{t}$ system. Plot from Ref. [40].

The observable defined in Eq. (3.10) has lots of good properties, in particular:

- $\mathcal{R}$ has a good sensitivity to the top-quark pole mass, in particular compared to other top-quark pole mass measurements based on $t\bar{t}$ cross section.
- The $t\bar{t}$+1-jet event topology represents approximately 30% of all $t\bar{t}$ events. Thus a large sample is available, making the observable experimentally accessible and with reduced statistical uncertainties.
- $\mathcal{R}$ has been calculated to NLO precision in QCD [150, 151], unambiguously fixing the re-normalization scheme. Also, a minimum p_{T} is required for the extrajet, which makes the observable IR safe. A fit of the theory to data thus yields an interpretation in a rigorously defined mass scheme, divergences free.
- The theoretical calculations of the observable are well under control. NLO theoretical corrections are small and errors due to missing higher orders are estimated to be small, as explained in Ref.[40, 150, 151].
- Being the cross section normalized, systematic uncertainties which typically affect the inclusive cross section measurements are strongly reduced. In particular PDF and α_s uncertainties almost cancel in the normalized cross section, as it is shown in Fig. 3.13

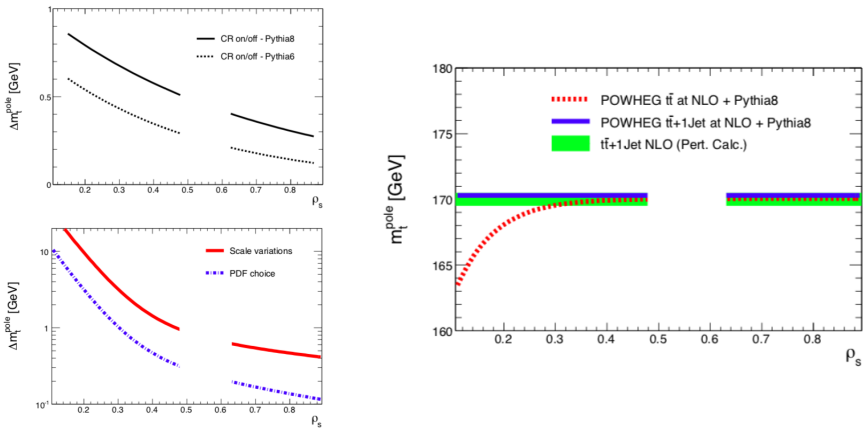

Figure 3.13: On the left, the impact of various theoretical uncertainties affecting top-quark mass extraction from the $\mathcal{R}$ observable, as estimated in Ref. [40]. The region where $0.5 < \rho_{\mathrm{s}} < 0.625$ has been excluded from the plots since it has almost no sensitivity to m_t.

In the fixed-order NLO calculation top-quarks are considered on-shell and the additional jet is reconstructed using the anti-k_t algorithm with radius parameter $R = 0.4$. In order for the observable to be IR safe, Refs. [40] required the extrajet to have a $p_{\mathrm{T}}^{\mathrm{extrajet}} > 50$ GeV and $|\eta^{\mathrm{extrajet}}| < 2.5$.

The calculation of $t\bar{t}$+1-jet topologies at NLO in QCD has been implemented in the POWHEG matrix element generator, opening the possibility to match the NLO prediction to a Monte Carlo model of the parton shower [152], to re-sum contributions (leading logs, LL) which are not taken into account in the fixed-order calculation. In order to have a well defined observable, the shower is

stopped before top-quarks decay, since top-quarks are defined on-shell to build the observable $\mathcal{R}$. This level is referred to as NLO+PS, or *parton level*. The additional jet is then reconstructed in the same way as before including all radiation which could be emitted by the tops and the initial state partons. The difference between the top-quark pole mass extracted with the fixed-order NLO alone and the merged NLO+PS calculations is found to be small [40].

The $\mathcal{R}$ observable calculated in the pole-mass scheme has been used to extract m_t^{pole} from semileptonic events collected by the ATLAS experiment at 7 TeV and resulted in the most precise measurement of m_t^{pole} at that time [41]:

$$m_t^{\text{pole}}({}^{t\bar{t}\text{+1-jet}}_{\text{ATLAS@7TeV}}) = 173.71 \pm 1.50\ (\text{stat}) \pm 1.43\ (\text{syst})^{+0.95}_{-0.49}\ (\text{theo})\ \text{GeV} \quad (3.13)$$

with a total error of $\sim$ 2.2 GeV, mainly due to the limited statistics of the dataset used, by the uncertainties on the modelling of the $t\bar{t}$ MC and by the uncertainty on the determination of the jets energy. A recent calculation of $\mathcal{R}$ in the $\overline{\text{MS}}$ scheme also allowed to extract $m_t(m_t)$ from the same observable measured by ATLAS [99].

Various strategies to reduce the total error to $\sim$ 1 GeV, taking advantage of the increased integrated luminosity of the ATLAS 8 TeV dataset, were proposed in [41]. The results of these studies are presented in Chapter 6.

3.3.3 Prospects on top-quark mass measurements

Top-quark mass measurements which use data produced by the LHC are reaching the GeV precision, as reported in Figs. 3.9 and 3.10, and recently a new run of the LHC with very high luminosity, the High-Luminosisty LHC (HL-LHC), has been approved. Hence, more precise measurements of m_t are foreseen. Stud-

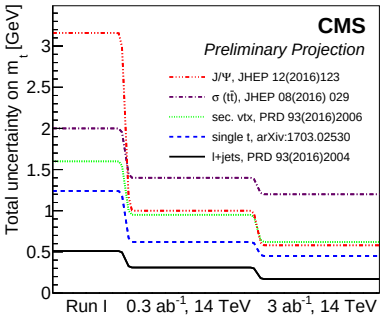

Figure 3.14: Prospect for top-quark mass measurements at the LHC, for various methods cited in Section 3.3.1. Figure from Ref. [153].

ies have been performed [153] which show that single m_t^{MC} measurements can reach the $\sim$ 0.5 GeV experimental uncertainty with the full Run 2 dataset, which could be even more improved to $\sim$ 0.2 GeV with the future 3000 fb^{-1} of the HL-LHC Run, as it is shown in Fig. 3.14. It is clear that with such a high experimental precision, the theoretical interpretation of m_t^{MC} becomes really relevant. Inclusive top-quark cross section measurements on the other hand are

not expected to give a m_t^{pole} value with an uncertainty below $\sim$ 1 GeV (theoretical error included), as it is shown in Fig. 3.14 (violet curve). Differential cross sections and combinations of single measurements can instead reduce the global error on m_t below the GeVthreshold, hopefully shredding some light on the $\mathcal{O}$(1GeV) ambiguity between m_t^{pole} and the m_t^{MC}.

Future e^+e^- colliders [154–156] also could help to reduce the uncertainties on m_t. For example, the position of the top-quark pair production threshold in lepton colliders depends on m_t, as it is shown in Fig. 3.15 (left). Thanks to available precise calculations of the $t\bar{t}$ cross section at the threshold [157, 158], a theoretical uncertainty of $\sim$ 0.05 GeV on m_t can be achieved, as it is shown in Fig. 3.15 (right). From an experimental point of view instead, it has been argued that a systematic uncertainty of $\sim$ 0.05 GeV can be achieved for such observable [159].

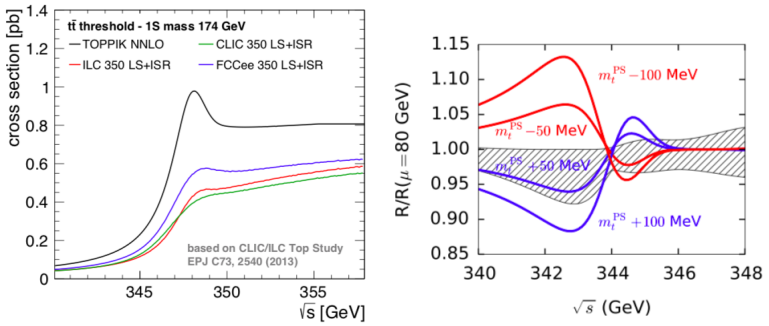

Figure 3.15: In the leftmost plot, the cross section at the threshold is compared for different possible future e^+e^- colliders taking into account experimental effects, and compared to the theoretical prediction (black curve). In the rightmost plot, the relative change in shape due to a shift of the top quark mass is shown for mass variations up to 100MeV and can be compared to the theoretical uncertainties affecting the threshold cross section (shaded area). Figures from Ref. [159]

Also jet and photon radiation rates can be used in the context of a electron-positron collider to extract m_t, similarly to what is done in Section 3.3.2 for pp collisions. Such measurements are expected to have a precision of few hundred MeV, according to recently published studies [160].

Summarising, in the near future measurements of m_t with precisions below 1 GeV are foreseen. They will have a strong impact on the the sensitivity of SM consistency tests and BSM searches, as it has been explained in Section 3.2, and will allow to have a better understanding on the stability of the Higgs field and its effects on the evolution of the Universe.

Chapter 4

The ATLAS experiment

The Large Hadron Collider (LHC) is a top-quark factory: by the end of 2018 it will have pruduced around $1.5 \cdot 10^8$ top-quarks. This fact makes the LHC the best available machine to perform precise studies of the top-quark properties. Top produce top-quarks, the LHC collides protons which have been accelerated in various steps up to energies of 13 TeVby the CERN accelerators. In Section 4.1 the various steps of the acceleration process are presented, together with the facilities which make it possible, as mainly referenced in [161–165]. The LHC is the last step of the accelerating process and it is introduced in more detail in Section 4.1.1, together with the experiments which are connected to it.

The amount of top-quarks which has been produced by the LHC is enormous, but not all top-quark events can be measured directly by the experiments. Hence, experimetns have to look at particular regions of the phase space, where the signal topology is enhanced. To do so, a good knowledge of the experimental setup used to collect the data is needed. As already anticipated, in this thesis data collected by the ATLAS (A Toroidal Large ApparatuS) detector has been used. ATLAS is one of the most important experiments in the world, counting more than 3000 people in its collaboration, and the largest in size at CERN. Clearly a very detailed explanation of the working of such a system could cover hundreds of pages, as it was the case for the construction reports [] ,and it is out of the scope of this thesis. The most important parts of the ATLAS detectors are presented shortly in Section 4.2. A particular focus will be given to the inner tracker in Section 4.2.1, which summarises the knowledge acquired during the shifts in the ATLAS control room in the years of the doctorate studies. Another work done for the ATLAS collaboration in which I have been involved actively is the in-situ calibration of large radius jets, which is quickly summarised in Section 4.3 and resulted in various public documents [166–169].

4.1 The protons journey to the LHC

The LHC is situated in between France and Switzerland, in the area near Geneva. It mainly collides proton beams at very high energies: in 2011 pp collisions were produced at a centre of mass energy of the proton pair system of 7 TeV, then in 2012 energy was raised to 8 TeV and, since 2015, LHC is operating at 13 TeV. Accelerating protons at such high energy is complicated and

cannot be done by one machine only, hence a number of intermediate particle accelerators is needed to increase step by step the protons speed, before the collisions can actually happen. The map of the accelerator facilities at CERN is shown in Fig. 4.1.

Protons are extracted at the very beginning from a bottle of hydrogen gas, thanks to an electric field which get rid of the hydrogen electrons. The extracted protons are then passed to a linear accelerator, Linac 2 [162], which is made of a series of cylindrical conductors, alternatively charged positively or negatively by radio frequency cavities. When passing through the conductors, a proton is pushed ahead by the conductor behind it, while the conductor after it pulls it toward itself. At the end of the accelerating process in Linac 2, protons are accelerated up to 50 MeV, while the beam of protons stays collimated thanks to the presence of small quadrupole magnetic field. A similar linear accelerator exists, Linac3 [170], which uses the same physics to increase ions speed. After

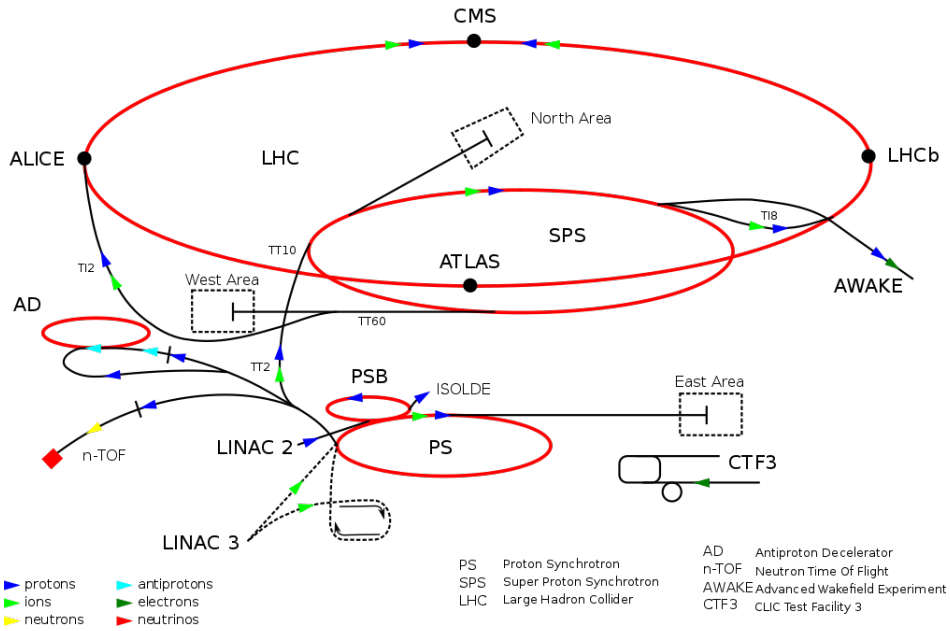

Figure 4.1: Map of the accelerators at CERN. Also some of the CERN experiments are included. Coloured arrows indicate the type of particles circulating inside the colliders.

this first stage, the proton beam enters the proton synchrotron booster (PSB), which accelerate the protons through its four rings up to 1.4 GeV. At this stage, accelerators are still of relatively small dimensions, being the radius of the PSB rings 25 meters long. A small fraction of the PSB protons is collided against fixed targets, yielding a large variety of atomic fragments which are studied by the ISOLDE [171] experiment, while most of the protons enter the Proton Synchrotron (PS), a synchrotron ring of more than 600 meters circumference. The PS is at the heart of the CERN facilities, since it also accelerates beams of other heavy particles such as lead atoms. In the PS, protons reach energies of 25 GeV, and a fraction of them is already used by different CERN experiments.

For instance, the DIRAC [172] experiment use the decay of bounded states of pions, formed along the beam, to test QCD behaviour at low energy; CLOUD [173] instead use the protons as a source of artificial cosmic rays, to study the processes happening in the atmosphere, but in a controlled environment. Part of the PS beam is also fired against blocks of metal and lead, producing neutrons, which are used to understand nuclear data via neutron time-of-flight by the n-TOF experiment [174], and anti-protons, which are collimated and decelerated in an anti-proton beam by the Antiproton Decelerator [175] and then used in anti-matter experiments [176–180].

Nevertheless, the largest fraction of the protons of the PS are passed to the Super Proton Synchrotron (SPS), which is the second largest accelerator at CERN, its tunnel being 7 kilometres long, and accelerates protons up to approximately 450 GeV. A part of the SPS beam is used to study the decay of mesons called kaons [181], which gives insights into how top-quark decays, or to study the products of the collisions of protons with fixed targets [182, 183]. Another part of the SPS protons is also directed towards the AWAKE accelerator [184] which is studying a new technique (electro-magnetic weak modes) to accelerate particles, which in the future could make feasible the construction of smaller particle accelerators.

The largest part of the beam accelerated by SPS though, and of the initial protons from the hydrogen bottle in general, enters the LHC, which is the main accelerator at CERN and is explained in more details in the next Section 4.1.1.

4.1.1 The LHC and its experiments [185]

The LHC is the largest collider ever built. The tunnel which contains it is 27 km long and has been dig between 50 and 150 meters underground.

The proton beams are kept on circular motion by 1232 dipole magnetic fields, with 392 quadrupole magnets keeping the beams collimated, while higher order multipole magnets are used to correct for other smaller effects. The dipole

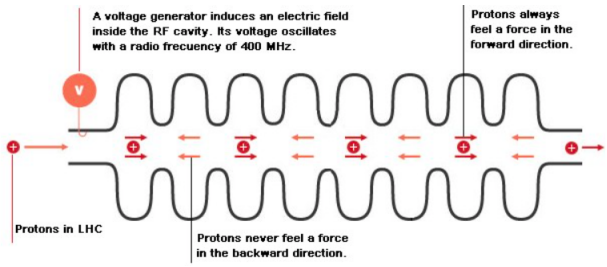

Figure 4.2: Schematic view of the accelerating system of the LHC. Figure from [185].

magnetic fields are produced by radio-frequency (RF) cavities, schematically presented in Fig. 4.2. To accelerate a protons of mass 1 GeV at relativistic energies of few TeV, a magnetic field of $\sim$ 7 Tesla intensity is needed. To produce it, super-magnetic conductors are used at cryogenic temperatures. In total, 96 tonnes of super-fluid helium-4 are used to cool down at 1.9 K the 10.000 magnets of the LHC. The RF cavities generate a longitudinal oscillating voltage so that the particle sees an accelerating voltage at the gap, and the voltage

then cancels out as the particle goes around the rest of the machine. One hence must be sure that the protons always see an accelerating voltage at the gap, which is achieved using a RF frequency f_{RF} integer multiple of the revolution frequency f_{rev} with which protons circulate in the accelerator ring. All the protons in the accelerator oscillate longitudinally around the ones which are synchronised with the RF frequency (synchronous protons), hence the protons are not spread in uniform beams when being accelerated, but are grouped in bunches around the synchronous particle. In the last operative period of the LHC, up to 2808 bunches with around $115 \cdot 10^9$ protons per bunch are collided. In average it means an interaction every 25 ns[1], or a bunch crossing frequency of $f^{\mathrm{bunch}} = 40 \cdot 10^6$ Hz.

The beam lines only cross in four points along the ring, where quadrupole magnets are used to squeeze the beams down to the section of a human hair, around $\sim 6 \cdot 10^{-6} m$, to increase the probability of the collisions between protons of two bunches. One parameter useful to describe the intensity of the collisions is the luminosity $\mathcal{L}$, which is defined as the number of interactions between two beams per cross section per time. Supposing the two proton beams inside the

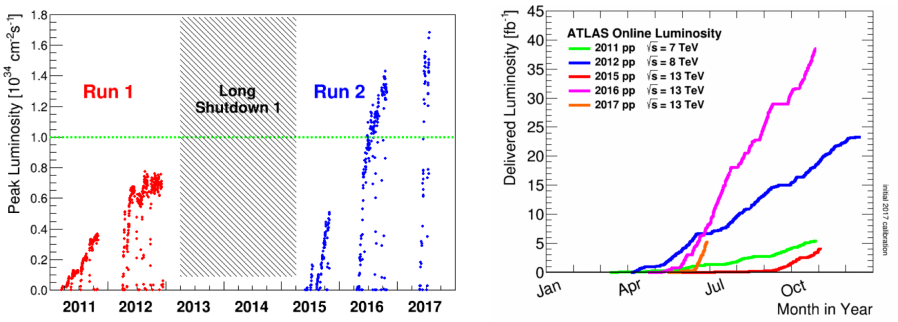

Figure 4.3: Instantaneous luminosity (left) and integrated luminosity delivered by the LHC year by year. It can be clearly seen how the nominal luminosity (green line in left plot) has been exceeded during Run2.

LHC have Gaussian bidimensional cross section, with widths σ_x and σ_y in the transversal plane, the luminosity can be calculated as

$$\mathcal{L} = \frac{1}{4\pi} \frac{N_1 N_2}{\sigma_x \sigma_y} f^{\mathrm{bunch}} \tag{4.1}$$

being $N_{1/2}$ the number of protons contained in each of the N_b bunches crossing and f^{bunch} is the frequency of the bunch collisions. The LHC is designed to work at a nominal maximum luminosity of $L \sim 10^{34} cm^{-2} s^{-1}$, but it surpassed the design limit in 2017, providing luminosities up to $2.1 \cdot 10^{34} cm^{-2} s^{-1}$, as it can be seen in Fig. 4.3. A quantity directly related to the instantaneous luminosity can be defined, which measure the total number of interaction per cross section happened. It is usually called integrated luminosity, L^{int}, and it is defined as

$$L^{\mathrm{int}} = \int \mathcal{L} \tag{4.2}$$

[1]Protons are accelerated by the PS and SPS before entering the LHC. In reality, the 25 ns bunch spacing is due to the PS cavities, but we thought it was best to describe briefly RF cavities in this section.

Luminosity plots of the LHC are shown in Fig. 4.3 for different years of the LHC campaign.

The luminosity has to be maximised in order to perform precise measurements and study very rare processes or very particular regions of the phase space. In fact, the total number N_X of event produced from a certain process $pp \to X$ which has a cross-section $\sigma_{pp\to X}$ is given by

$$N_X = \epsilon \cdot \sigma_{pp\to X} \cdot L^{\text{int}} \tag{4.3}$$

where$\epsilon < 1$ is a factor taking into account detector effects and phase space efficiency. Hence, the higher the luminosity the largest is the data sample of $pp \to X$ events which can be analysed.

At very high luminosities though, various problems arise. Firstly, the beam radiation become high, increasing the probability of damaging the part of the detectors which are veru close to the interaction points. Secondly, the average number of simultaneous pp interactions happening at every bunch collision ($\langle\mu\rangle$) also increase with the luminosity, as can be seen in Fig. 4.4. Simultaneous interactions provoke in the detectors the so-called *pile-up* effect: particles from different pp collision hitat the same time exactly the same part of the detector, being measured as a single event with higher energy. Both effects can be mitigated in experiments, both with hardware and software methods, as it is shortly explained in Section 4.2.

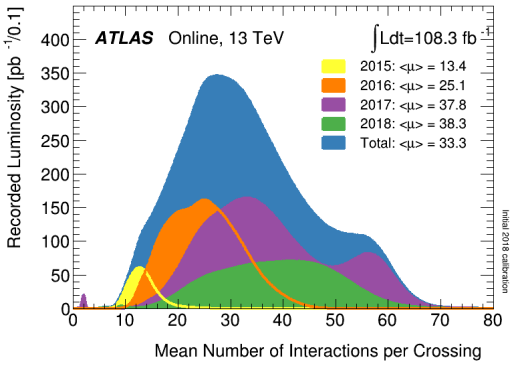

Figure 4.4: Number of interactions per bunch crossing in pp collisions at the LHC during Run 2. Comparing this Figure with Fig. 4.3, it can be seen how to high instantaneous lumionisty is associated an increase of $\langle\mu\rangle$.

Four big caverns have been dig in the LHC tunnel around each interaction point, in order to place seven detectors to measure the products of the pp collisions. Four of such experiments have really large size, as it is shown in Fig. 4.5, where they can be compared to the size of human bodies. They are:

- CMS (Compact Muon Solenoid)[186] it has been designed to perform precise SM and Higgs measurements, as well as BSM searches. It has a cylindrical shape and is formed by a inner tracker, an electromagnetic calorimeter (ECAL), a hadronic calorimeter (HCAL) and a muon detector, for a total length of 20 m and a radius of 15 m. The world's largest magnet

surround the inner detector and the calorimeters, producing a 4 T magnetic field which bends the trajectories of the charged particles. With a total weight of 14000 tonnes, it is the heaviest experiment at CERN.

The inner tracker is made of $\sim 10^7$ silicon strips and $\sim 6.6 \cdot 10^7$ silicon pixels, which allows to reconstruct with high accuracy the momenta of the tracks left by the charged particles. The ECAL is made of crystals of $PbWO_4$ and its job is to absorb all the photons and electrons and to measure the energy they leave in the crystals. The HCAL is built of layers of absorbing material, such as brass and lead, alternated to plastic scintillators, and it plays the same role as the ECAL, but on hadrons instead. The muon spectrometer is composed by drift tubes in the most central region, by cathode strip chambers in the region closest to the beam pipe, and by resistive plate chambers in the between.

The strong 4 T magnetic field is produced by a single solenoid magnet, which is so big to impose limits on CMS construction. For instance, the calorimeter system had to be place inside the magnetic field volume, negatively affecting its performances. On the other end the large magnetic field allows to measure charged particles momenta with high accuracy even when they have very high energy. A summary of the resolution of the CMS detector is reported in Table 4.1.

- ATLAS (A Toroidal Large Apparatus)[187] is also a general purpose experiment and share with CMS its construction design, being made of four main sub-detectors. A detailed description of the subs-systems is reported in Section 4.2, while in the following only the main differences with respect to CMS are reported, which are a consequence on the decision on how to minimize the error on particles momenta reconstruction.

  The error with which the momentum is measured at a distance l from the interaction point is given by the equation of motion of a charged particle with momentum p in a magnetic field of intensity B:

  $$\frac{\sigma(p)}{p} \propto p\frac{\Delta x}{Bl^2} \tag{4.4}$$

  being Δx the spatial resolution with which a particle is detected. Since Δx depends on the available technology chosen to build detector components, it is almost the same for the two experiments. Hence, to minimise $\sigma(p)$ one can either maximize the magnetic field, as CMS did, or measuring particles at large distance l, as its has been chosen by the ATLAS collaboration. Both approaches have advantages and disadvantages, making the two experiments complementary in their physics research.

  Elements and technologies used to build the ATLAS and CMS sub-detectors were optimised according to the very initial decision taken. While CMS only uses silicon in its tracking system, ATLAS inner tracker is composed by silicon strips and pixels only in the very inner part, using less performant gaseous detectors elsewhere. The ATLAS toroidal magnets are smaller than the (only) CMS solenoid, and it was then possible to collocate them between the inner tracker and the calorimeters, allowing a better calorimeter resolution. Also, ATLAS magnets can be used as a separate

spectrometer for the muons, while CMS can perform independent measurements for muon only using the magnetic field in the return yoke of the solenoid, with lower performance. A summary of the global differences of the main sub-detectors resolutions between ATLAS and CMS is shown in Table 4.1.

Sub-detector		ATLAS resolution	CMS resolution
Inner Tracker	$\frac{\sigma(p_T)}{p_T}$	$\sim 5 \cdot 10^{-5} p_T \oplus 0.01$	$\sim 1.5 \cdot 10^{-5} p_T \oplus 0.005$
ECAL	$\frac{\sigma(E)}{E}$	$\sim \frac{0.1}{\sqrt{E}}$	$\sim \frac{0.2-0.5}{\sqrt{E}}$
HCAL	$\frac{\sigma(E)}{E}$	$\sim \frac{0.5}{\sqrt{E}} \oplus 0.03$	$\sim \frac{1}{\sqrt{E}} \oplus 0.05$
Muon detectors	$\frac{\sigma(p_T)}{p_T}$	~ 0.07 (for 1 TeVmuons)	~ 0.10 (for 1 TeVmuons)

Table 4.1: Summary table of the resolution of the CMS and ATLAS detectors. Values are approximate and refers to the Run 1 of the LHC. It can beseen how the design of the two experiments influence their performances: CMS has better resolution in the inner tracker, while ATLAS performs better in the hadrons and muon energy reconstruction.

- ALICE (A Large Ion Collider Experiment)[188] has been mainly designed to study strongly interacting matter at very high energies and pressures. In this conditions a new phase of the matter forms, which is called quark-gluon plasma (QGP). This phenomena has been shown to exist when the LHC collides ions, recreating conditions which are believed to be similar to those just after the bing bang, when temperature and pressure were so high that quarks and gluons were free of moving.

  The ALICE collaboration produced QGP at the record temperature of 5 trillion grades [189] and found that it behaves approximately as a perfect liquid [190]. It also found, between other interesting results, that p-Pb collisions at the LHC, which take place for few weeks a year, have a completely unexpected double-ridge structure with so far unknown origin [191].

  The design of the ALICE detector is significantly different from the ATLAS and CMS ones, even if the three are comparable in size. ALICE is composed by 19 sub-detectors and has the widest coverage to the forward region of the four LHC experiments. The high number of sub-detectors is necessary to distinguish between the different charged hadrons that are produced in the Pb-Pb collisions, since the method used by the ATLAS and CMS experiments is not suitable in these conditions.

- LHCb (Large Hadron Collider beauty)[192] has been built to study the physics of the b-quark, which can help in explaining the matter-antimatter asymmetry of the universe, by measuring the charge-parity (CP) violation parameters in the interactions of heavy hadrons containing a b-quark (b-hadrons). The design of LHCb reflects the fact that pairs of b-hadrons are mostly produced by pp collisions in the same cone along the beam axis. Hence LHCb has been designed as a single arm forward spectrometer, long 25m and with a 10 m diameter, covering a polar angle in the forward

region of 300 mrad in the horizontal plane and 250 in the vertical one. A 1500 tonnes dipole magnet breaks the symmetry between horizontal and vertical planes.

Recently LHCb found evidence of a deviation from SM expectations in the ratio of probabilities of a particular $b-$hadron [193], which violates lepton universality with a significance of ~ 2.3 standard deviations[2].

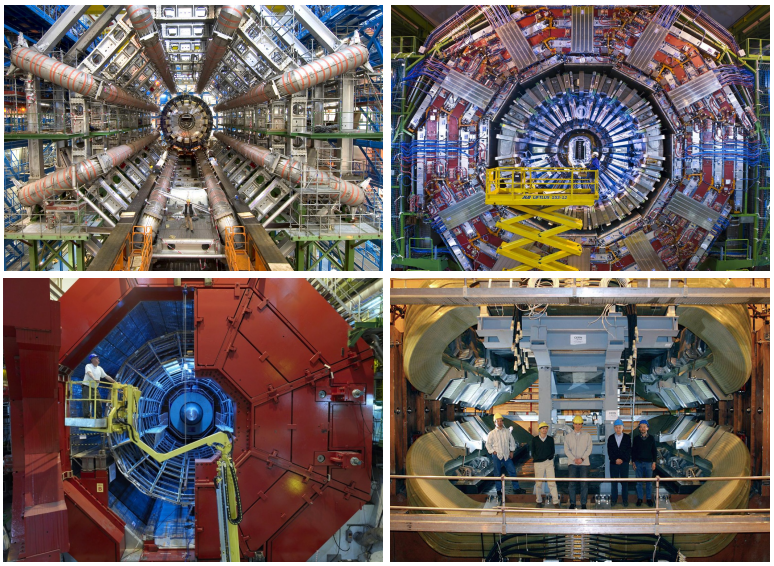

Figure 4.5: Images of ATLAS (top left), CMS (top right), ALICE (bottom left), LHCb (bottom right) experiments. Their dimensions can be compared to the size of people in each image separately.

The other three smaller detectors share a cavern with one of the previously cited experiments.

- LHCf (Large Hardon Collider forward) [194] consists on two detectors placed at 140m from the ATLAS interaction point. It studies the neutral pions produced in the regions close to the beam axis (the so-called forward regions) and it is the smallest of the seven LHC experiments.
- Monopole and Exotics Detector At The Lhc (MoEDAL) [195] has been designed to find magnetic monopoles and (pseudo-) stable massive particles. Compared to other experiments in the world searching for monopoles, it has the highest sensitivity among them. It was the latest LHC experiment to be approved and is mounted inside the LHCb cavern.
- TOTal Elastic and diffractive cross section Measurement (TOTEM)[196] is mounted in the CMS cavern. A the name suggests, it aims to separate different processes contributing to the total cross sections of pp collisions. In fact, not all the collisions happens at very high transferred energy, and

[2]The lower limit to declare a discovery has been set to 5 standard deviations, which means that the probability of having observed statistical fluctuations is $\sim 10^-7$. A 2.3 significance, means that the probability of having observed a fluctuation is $\sim 1/50$.

elastic and single diffractive processes contribute to the pp cross section inelastic,. For instance, at 7 TeV centre of mass energy, the total pp cross section is approximately $\sigma_{pp}^{\text{tot}} \sim 110 \cdot 10^{-3}$ barn and can be divided into $\sigma_{pp}^{\text{inelastic}} \sim 60 \cdot 10^{-3}$ barn, $\sigma_{pp}^{\text{diffractive}} \sim 12 \cdot 10^{-3}$ barn and $\sigma_{pp}^{\text{elastic}} \sim 40 \cdot 10^{-3}$ barn.

In this thesis, data collected by the ATLAS detector during the year 2012 has been used. Hence, a detailed description of the experimental setup and of its components is given in Section 4.2.

4.2 The ATLAS detector and its components

The ATLAS experiment has been built around the collision point denominated P1, near the CERN buildings at the Meyrin site in Switzerland. Its construction was completed in 2008 and took almost a decade. It is the biggest detector at CERN, measuring 46 m in length and 25 m in diameter.

A system of coordinates can be defined to describe the ATLAS detector with origin of the axis coinciding with the P1 interaction point. The $x-$axis can then be defined to point towards the centre of the LHC ring, the y-axis to point up-wards and the $z-$axis to coincide with the tangent to the beam axis, with positive direction given by the right-hand rule. Polar coordinates (r, θ, ϕ), with $r = \sqrt{x^2 + y^2}$, are better to describe the cylindrical symmetry of the detector. The azimuthal angle ϕ is defined such that $\phi = 0$ coincides with the $x-$axis, while a null value of the polar angle θ coincides with the positive direction of the $z-$axis. In collider experiments it is often useful to define the pseudorapidity, η, associated to the polar angle:

$$\eta = -\ln\left[\tan\left(\frac{\theta}{2}\right)\right] \tag{4.5}$$

such that $\eta = 0$ is perpendicular to the beam axis, while $|\eta| = \infty$ coincides with the beam $(z-)$ axis.

The whole ATLAS detector covers a 4π polar angle and it consists of four main sub-systems with cylindrical symmetry around the interaction point: the inner tracker, two calorimeter systems and the muon spectrometer. All the sub-systems are made of a barrel part which has a cylindrical shape and two parts closing each side of the cylinder, called end-caps. A schematic representation of the ATLAS detector and its components is given in Fig. 4.6. Each of the main sub-detectors have different components, which are described in the next Sections 4.2.1 to 4.2.3.

4.2.1 The inner tracker [197]

The closest detector to the LHC beams is the inner tracker. It originally consisted of three sub-systems, to which an additional one was joined in 2014 as an upgrade for LHC Run 2:

- The pixel detector (PIX) consists of 80 millions semiconductor silicon pixel elements, which cover an area of 1.4 m^2 in the $|\eta| < 2.5$ region.

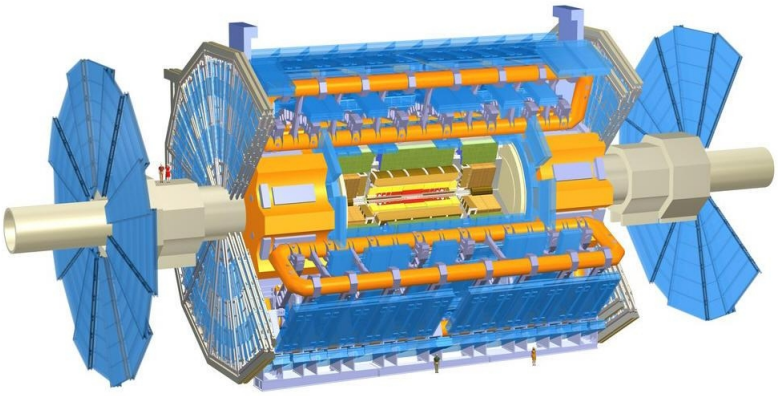

Figure 4.6: Section of the ATLAS experiment, showing its main parts. The inner detector is painted in red, the calorimeter systems are show in light brown (ECAL) and green (HCAL), while the muon detectors are blue. Magnetic field is generated by a magnetic solenoid (yellow) around the inner detector and by toroidal magnets (orange).

The working principle of a semiconductor detector is the following: a charged particle passing through a silicon semiconductor ionize the medium creating lots of electron-hole pairs which are attracted to the sides of the semiconductor which are polarised by an electric field. Hence negative (positive) charges are attracted to the positive (negative) pole and create a differential of potential which is measured by a read-out device and interpreted as the passage of a very energetic charged particle in the detector. Every pixel has an associated read-out channel. Three layers (B-layer, Layer-1 and Layer-2) of pixels are placed in the barrel at distances of 50.5 mm, 88.5 mm and 122.5 mm from the beam pipe, with 67 millions pixels in total. The 13 millions pixels left are installed in three disks in each end-cap.

- The semiconductor tracker (SCT) is a microstrip tracker placed outside the PIX, at a distance to the beam axis going from 30 cm to 51.4 cm, which also use silicon technology. It covers a total area of 60 m^2 distributed over 18 end-cap disks ($1.4 < |\eta| < 2.5$ region) and 4 barrel layers (for $|\eta| < 1.4$ region), with 6 millions read-out channels in total. It allows to measure the position of charged particles at a 17 μm precision, roughly one fourth of the section of a human hair.

- The transition radiation tracker (TRT) is a gas detector made of $350 \cdot 10^3$ straw tubes. Straw tubes are cylinders with an external layer of insulating material, filled with gas and with a anode wire along their axis. Each tube is filled with a gas mixture of $Xe/CO_2/O_2$ and has a gold plated tungsten anode wire, while the external layer is made of kapton, which provides electrical insulation at low thermal gradients. Charged particles passing through a straw tube ionize the gas, and negative charged are attracted by the anode wire which then takes the charges to the read-out system.

The TRT system covers the $|\eta| < 2$ region at a distance between 0.55 m and 1.08, to the beam.

- The Insertable B-Layer (IBL) was added to the ATLAS detector on the 7th May 2014, as part of the detector upgrade in preparation to the Run 2 data taking, and is the closest part of the detector to the beam, at only 33.5mm from the beam. With the luminosity in the LHC Run 2 expected to be very high, significant radiation damage to the PIX layers could have occurred, causing a loss in tracking efficiency, especially in tagging the decay of the $b-$quarks. To minimise such risk an insertable layer was added instead of replacing the existing B-layer in the PIX. To integrate the IBL in the inner tracker though, the diameter of the beam pipe was shrunk and a 2mm gap between the PIX B-layer and the pipe structure was created where the IBL was inserted.

The whole inner detector is immersed in a 2 T magnetic field, parallel to the beam axis, which bend the trajectories of charged particles, depending on each particle momentum. In this way the charges of the particles are measured, as well as their transverse momentum. Additionally the longitudinal (z_0) and transverse (d_0) impact parameters[3] of each charged particle are computed. The

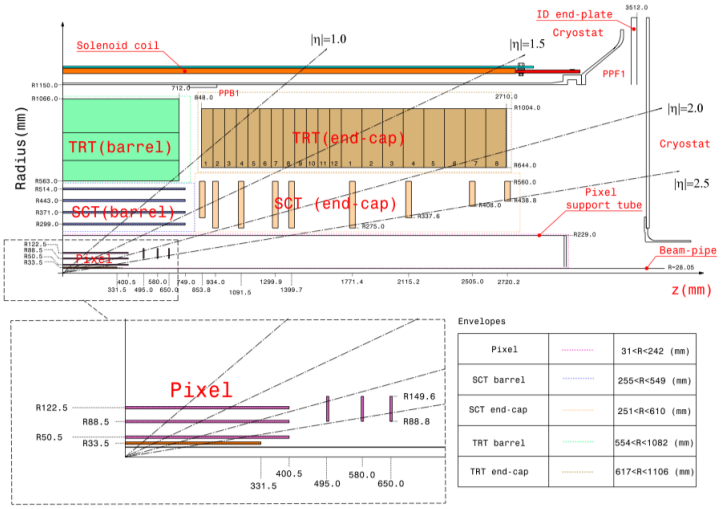

Figure 4.7: The $r - z$ cross section view of the layout of the ATLAS Inner Detector for Run 2. The top panel shows the whole Inner Detector, whereas the bottom panel shows a magnified view of the PIX detector region, including the IBL. Figure taken from [197].

precisions with which such parameters are measured by the ATLAS inner tracker are reported in table Table 4.2. A schematic representation of the whole inner tracker is shown in Fig. 4.7 instead.

[3] Impact parameters are the distances with respect to the primary collision.

Tracking parameter	Inner tracker resolution	(unit)
ϕ_0	$\sigma(\phi_0) \sim 0.075 \oplus \frac{18}{p_T\sqrt{\sin\theta}}$	mrad
θ	$\sigma(1/\tan\theta) \sim 0.7 \cdot 10^{-3} \oplus \frac{2 \cdot 10^{-4}}{p_T\sqrt{\sin^3\theta}}$	
p_T	$\sigma(1/p_T) \sim 0.36 p_T \oplus \frac{13}{\sqrt{\sin\theta}}$	TeV^{-1}
d_0	$\sigma(\phi_0) \sim 11 \oplus \frac{73}{p_T\sqrt{\sin\theta}}$	μm
z_0	$\sigma(z_0) \sim 87 \oplus \frac{115}{p_T\sqrt{\sin^3\theta}}$	μm

Table 4.2: Performances of the ATLAS inner detector on measureing the azimuthal angle (ϕ_0), the polar angle (θ_0), the transverse momentum (p_T) and the impact parameters d_0 and z_0.

4.2.2 The calorimeters system [198, 199]

Calorimeters are made of layers of materials absorbing particles energy (absorbers) interleaved with layers of ionizing/scintillator materials. When a particle interacts with the absorber material, it produces a multitude of other particles (shower) with lower energy, which are then measured in the subsequent scintillating layer by a sampling system. In calorimeter, such a process is repeated until the energies of the particles in the shower are not enough to allow them passing through a block of absorbing material. In the electromagnetic (EM) calorimeters, showers are initiated either by photons or electrons and the shower is produced by either bremsstrahlung or e^+e^- pairs creation, allowing only electrons and photons as components of the shower. In hadronic calorimeters the shower is started by a hadron instead and it is mediated mainly by strong force. Hadronic showers always have an EM part too, and the final state particles can be of different types.

The typical parameter which describe calorimeter showers is the interaction length x_0, which is the typical length of absorbing material which reduces the energy of particles in the shower by a factor e^{-1}. A particle producing a shower which pass through absorbers for a length equivalent to $l = nx_0$ before being not measured by a scintillator, is reconstructed as a particle with initial energy $E^{\text{init}} = \exp(nx_0)$.

For EM showers typically $x_0 \propto A/Z^2$, being respectively A and Z the mass and atomic numbers the absorber atoms. The great majority of an EM shower product use to be completely contained in a length of $L \sim 20x_0 \sim 1\ m$, independently of the material the absorber is made of. The ECAL colorimeter in ATLAS uses lead ($A_{\text{Pb}} = 82$) as absorbing material, liquid Argon (LAr) at a working temperature of 88 K as a scintillator, and electrodes with an accordion shape for sampling. Three sampling levels exist, with a solid angle granularity of $\Delta\eta \times \Delta\phi$ respectively of 0.003×0.1, 0.025×0.025 and 0.05×0.025. The EM calorimeter is placed just outside the magnet solenoid which envelopes the inner tracker, at a distance $115\ cm < d < 228\ cm$ from the beam axis, and it has a barrel part covering the $|\eta| < 1.475$ region and a end-cap one to cover $1.475\,|\eta| < 3.2$ phase space.

For hadronic showers $x_0 \propto A^{1/3}$, hence hadrons with enough initial energy are not stopped by the lead absorbers of the EM calorimeter, pass through all of them and reach the ATLAS hadronic calorimeter. The HCAL calorimeter is

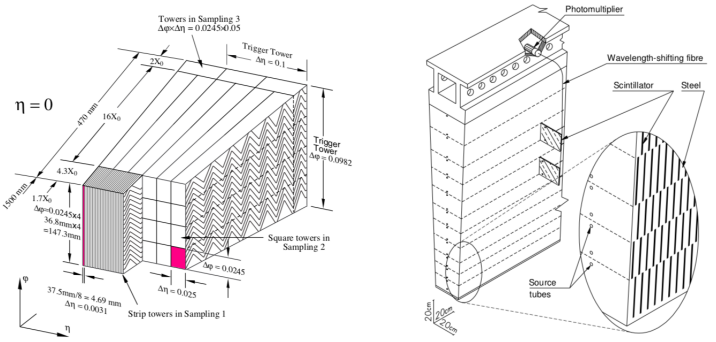

Figure 4.8: Modules of the ATLAS calorimeter system using the liquid argon technology (LAr, on the left) and the plastic scintillating one (TileCale, on the right). The accordion structure of the ECAL barrel calorimeter, which ensures azimuthal simmetry and a complete coverage of the whole $\eta - \phi$ space, can be noticed in the figure on the left. Figures from Refs. [198, 199].

built around the ECAL, at a distance to the beam axis between 228 cm and 382.5 cm . In the most central region (covering $|\eta| < 1.7$) it is formed by 14 mm layers of iron ($A_{\text{Fe}} = 26$) alternated to $3mm$ of plastic scintillator plates, called tiles. This part of the ATLAS calorimeter is usually called TileCal, because of the sampling technology it uses, and has 0.1×0.1 granularity . In the end-caps instead the $|\eta|$ coverage goes from 1.5 to 3.2 and copper ($A_{\text{Fe}} = 23$) has been chosen as the absorber material, while the sampling material is liquid argon, with a $\Delta\eta \times \Delta\phi$ resolution of 0.2×0.2.

An additional region is covered by the forward calorimeter, FCal, made of copper/tungsten and LAr, which measures hadrons emitted small polar angle, covering the $3.2 < |\eta| < 4.9$ region, with a 0.1×0.1 granularity. The FCal is important for instance in vector boson fusion processes, where two jets are mostly produced in the forward regions.

The performances of the ATLAS calorimeters are reported in Table 4.3, while a schematic figure of two ECAL and HCAL modules installed in the barrel is presented in Fig. 4.8.

Calorimeter	Absorber-Sampling material	$\frac{\sigma(E)}{E}$
ECAL	Pb-LAr	$\frac{10\%}{\sqrt{E}} \oplus 0.7\%$
HCAL barrel	Fe-Tile	$\frac{53\%}{\sqrt{E}} \oplus 6\%$
HCAL end-caps	Cu-Tile	$\frac{50\%}{\sqrt{E}} \oplus 3\%$
HCAL forward	Cu/W-Tile	$\frac{100\%}{\sqrt{E}} \oplus 10\%$

Table 4.3: Typical resolution of the calorimeters used in ATLAS detector.

ATLAS calorimeters fully absorb most of the particles, the only muons and neutrinos passing through the ECAL and HCAL absorbing layers. Neutrinos are not absorbed because they have a really small cross section with every material. Muons in the electromagnetic calorimeter do very little bremsstrahlung, since

their mass is ~ 40 times the electron mass and the bremsstrahlung effect goes as m^{-4}, and hence not stopped by the ECAL. They neither are stopped by the HCAL, since leptons do not interact via strong force, making it necessary a dedicated detector to measure them.

4.2.3 The muon spectrometer [200, 201]

The muon spectrometer is the largest of the ATLAS sub-detectors, starting from a distance to the beam of $\sim 4.25\ m$ and extending up to $\sim 11\ m$. With such muon detecting arms, the muon momenta can be measured with very high precision, as already anticipated already in Section 4.1.1. The muon spectrometer working principle is similar to the one of the inner tracker. A magnetic field is provided by three systems of toroidal magnets (one in the barrel region formed by 8 coils and two in the end-caps with 8 coils each) and has an intensity of 4 T on the magnets surface. The spectrometer is composed by four smaller sub-systems, which position is shown in Fig. 4.9. Two of them serve as trigger systems, while the others measure muons momenta:

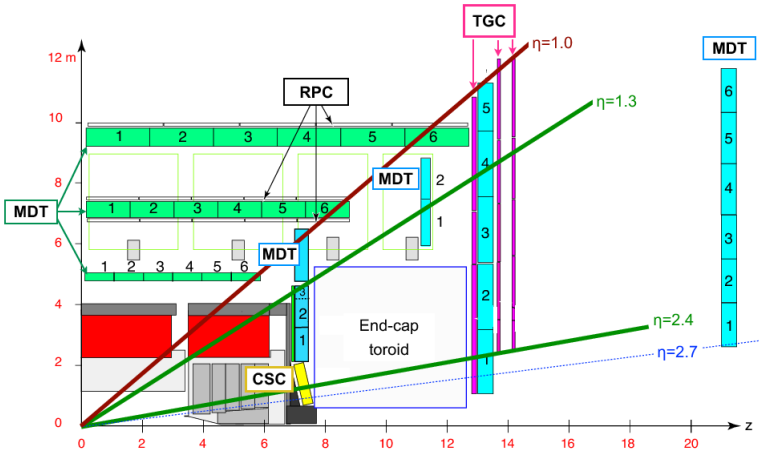

Figure 4.9: The $r-z$ cross section view of the layout of the ATLAS Muon Spectrometer for Run 2. The four sub-systems of the muon spectrometer are shown: MDTs (green in barrel and blue in the end-cap), TGCs (violet lines), RPCs (grey lines, near the barrel MDTs) and CSCs (yellow). Also, the dimensions of the spectrometer can be compared to other parts of the ATLAS detector, such as the hadronic calorimeter (red). Figure taken from [201].

- Thin Gap Chambers (TGC) are used for triggering in the end-cap region, covering the region $1 < |\eta| < 2.7$ and in total there are three layers of TGCs, for a total number of 192 chambers, covering an area of 2900 m^2.

- Resistive Plate Chambers (RPC) are also used for triggering, but in the region up to $|\eta| < 1$. Also RPCs are organised in three layers, for a total of 596 chambers covering 3650 m^2

- Monitored Drift Tubes (MDT) give precision measurement for muons with $|\eta| < 2.7$. They cover a 5500 m^2 area and in total there are 1194 MDTs, distributed in three layers or levels. Small-diameter MDT (sMDT), which have one order of magnitude higher rate capability and can be installed in detector regions where MDT chambers do not fit, have been installed in ATLAS in 2014 as an upgrade of the muon system for the LHC Run 2.

- Cathode Strip Chambers (CSC) also measures muons momenta precisely, but they cover the forward region $2.4 < |\eta| < 2.7$. Since the phase space region the CSC cover is small (27 m^2), only 32 chambers are needed.

The muon spectrometer was designed to have a momentum resolution of $\frac{\sigma(p_T)}{p_T} < 10^{-4} p_T/\text{GeV}$ for muons with $p_T > 300$ GeV, allowing a good resolution in reconstruction of mass of heavy resonances decaying into two or four muons (i.e. $H \to \mu^+\mu^-$, or $H \to ZZ \to \mu^+\mu^-\mu^+\mu^-$). The trigger selectivity was designed to be around $p_T > 10 - 20$ GeV for muons from such high-mass states, nevertheless muons with $p_T \sim 5$ GeV, which are useful for $b-$physics and CP violation studies, can also be measured.

4.2.4 The trigger system and data storage [202, 203]

When the LHC collides proton bunches at 40 MHz, around 10^7 Terabytes of data are produced every second by the ATLAS detector. To reduce the flow of data to manageable levels, events which are categorised as potentially interesting are selected by the ATLAS trigger system.

The trigger system is a computing system which, during Run1, was structured into three levels of increased complexity:

- The Level-1 trigger (L1) decides if an event is interesting based on a subset of information coming from the calorimeters and the muon spectrometer. It is hardware based, with a rejection rate of $\sim 2.5/10^{-3}$ and a characteristic time response smaller than $2 \cdot 10^{-6}$ s. Hence, on average only 100,000 of the 40 million events produced per second pass the L1 filter. The information of the selected events is collected into buffers and passed to the second level of decision.

- The Level-2 trigger (L2) is software based and analyses in detail specific regions of the event which were already pre-selected by the L1 trigger, using a larger number of the event variables. It takes milliseconds to decide if the event should be discarded and typically only ~ 1000 events per second are then not rejected and passed to the last filtering step.

- The Event Filter (EF) is also software based and performs a detailed analysis of the full event data in few seconds. Around ~ 200 events per second pass all of the three triggers and are saved permanently to be used later for offline analyses.

For Run 2 the trigger system had to be renewed because of the increase in energy of the pp collisions, which increased trigger rates by a factor $2 - 2.5$. The L1 trigger was largely improved to mitigate pile-up effects and suppress the fake-muon rate[4], while also increasing the triggera rate limit from 70 to 100

[4] the rate with which non-muon particles where actually identified as muons by the ATLAS detector.

kHz. The L2 and EF levels were merged into a single High Level Trigger (HLT) which allowed a better resource sharing and simplified both the hardware and software configurations. The differences in the ATLAS trigger system between Run1 and Run 2 of the LHC are summarised in Fig. 4.10.

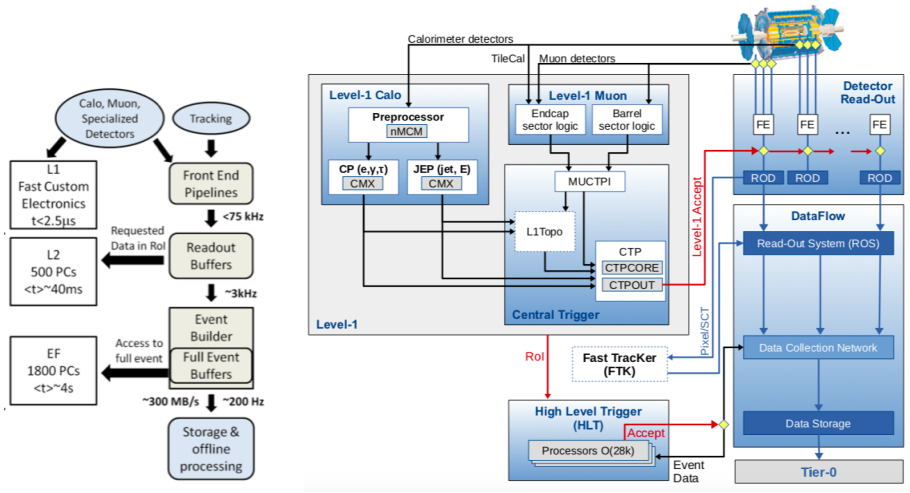

Figure 4.10: The trigger systems used during Run 1 (left, figure from [202]) and the one which is being used for Run 2 (right, figure from [203])

The permanently saved events are in the end only about the 0.0005% of the total, which still is an enormous quantity of data to be stored or analysed in one computing site only. For this reason a network of computing centres was created, the Worldwide LHC Computing Grid (WLCG), to share the resources of various site all around the world. The WLCG is structured into four levels, called Tiers, which are computer centres providing specific services. Tier0 is where all the data from every LHC experiment pass through, it is located in the CERN Data Centre and backed up in another centre in Budapest, and information is saved there in a very raw format, which cannot be used easily by analysers. Tier1 are responsible for storing a proportional share of raw and reconstructed data, as well as performing large-scale reprocessing and storing the corresponding output. There are 13 Tier1 centres all around the world. They also re-distribute data between the 155 Tier2 centres, which typically are universities and research centres with adequate computing power. Finally, individual scientists and students can access the reprocessed information at local computing resources, Tier3, which can also be individual computers, where data are available in a usable format. Event information as it is measured in the detector is reconstructed in physics objects before it can be used in analyses. How ATLAS define such objects is explained in the next Section 4.2.5. A detailed definition of the physical objects used in the top-quark mass extraction of Chapter 6, is contained in Chapter 5.

4.2.5 Physics objects reconstruction

The starting point of any ATLAS physics analysis is the reconstruction and identification of objects representing the particles which interacted with the

detectors. The only objects which are measured by ATLAS are, as already mentioned, electrons, photons, hadrons and muons and a number of physics objects can be defined:

- Electrons [204]

  Electrons are reconstructed from a shower in the ECAL, matched to a track reconstructed in the inner detector. The major electron misidentification backgrounds are photons decaying into e^+e^- pairs, as well as energy deposit in the ECAL left by charged hadrons. Such backgrounds can be reduced by requiring a particular shape of the electromagnetic shower, by matching calorimeter energies to track momenta and by asking a minimum number of hits in the B-Layer and TRT. Three reconstruction working points (loose, medium and tight) have been defined, with increasingly stringent cuts. The efficiency with which electrons with $p_{\mathrm{T}} > 25$ GeV are reconstructed ranges from 80% to 95%.

- Photons [205]

  Photons also are defined from energy deposits in the ECAL. If they have no associated track in the inner detector, they are called *unconverted*, while *converted* photons are reconstructed as e^+e^- pairs by associating two charged track in the ID compatible with the same origin and ECAL energy deposit. The identification efficiency increases from 60-70% for $E_{\mathrm{T}} = 20$ GeV to 87-95% (90-99%) for $E_{\mathrm{T}} > 100$ GeV for unconverted (converted) photons. The main background of the photon physic object is due to hadronic jets contamination, which is reduced by requiring the jet to be isolated from other particles of the event and particular jets shape properties.

- Muons [206]

  Muons leave tracks both in the inner detector and muon spectrometer and are measured independently by the two systems. Also, muons could leave a small energy deposit in the calorimeter, which could be misidentified as the decay of pions and kaons. The two muon tracks are checked to be compatible and then four momenta are reconstructed via a global track fit. Four muon identification selection are provided (medium, loose, tight and high-p_{T}), with reconstruction efficiencies above 95%.

- Hadronic jets [207, 208]

  The outgoing quarks and gluons from the hard-scattering collision are reconstructed as collimated jets of radius $R = \sqrt{\Delta\eta^2 + \Delta\phi^2} = 0.4$ (small-R jets). Jets are built in ATLAS from topological calorimeter clusters using FastJet [209] with the anti-k_t algorithm [75]. Jets originating from a b-quark can be identified exploiting the long lifetime, high mass, and the decay multiplicity of b-hadrons as well as the b-quark fragmentation function. The b-tagging in ATLAS has been strongly improved for the LHC Run 2, thanks to the insertion of the IBL, which improved the b-tagging efficiency by $\sim 10\%$ at fixed rejection rate. Also jets with larger radius (large-R jets, typically with $R \sim 1$) are used to reconstruct hadronically decaying particles with high mass, when they have high p_{T}. More details on this kind of jets are given in Section 4.3.

- Missing energy

  Neutrinos do not leave any track in the detector and hence produce an imbalance in the vector sum of p_{T} of all objects in the final state, called missing transverse energy ,$E_{\mathrm{T}}^{\mathrm{miss}}$. $E_{\mathrm{T}}^{\mathrm{miss}}$ is mainly affected by the residual soft energy (typically from pile-up) which is not clustered into jets and is therefore lost after jet reconstruction. A Soft Term Vertex Fraction algorithm has been developed which almost cancel such effect. The missing energy cannot be measured along the beam axis, where no detector can be placed, making it necessary to add additional information to determine neutrinos four momenta.

All the physics objects, after being reconstructed, are calibrated to take into account for possible detector effects distorting the four momenta of the interacting particles. In the following Section 4.3, studies of the detector response to jets with large radius are reported, as a summary of the qualification work done for the ATLAS collaboration. Section 4.3 is a summary of three publications [166–168] which employ data (in-situ techniques) collected during 2015 and 2016 to describe how the jet mass and energy is reconstructed and distorted by the ATLAS detector.

4.3 In-situ study of the ATLAS detector response to large radius jets energy and mass

Jets with large radius (large-R jets) are ideal to describe massive particles produced at high transverse momentum. When a massive unstable particle decaying hadronically is produced with a significant Lorentz boost in fact, the stream of its decay products can be very collimated along the direction of the intial particle. In fact, supposing the decay products are emitted isotropically in the particle rest frame, they are not in the laboratory rest frame where the unstable particle was moving with $\beta = v/c$ before decaying. After a Lorentz boost of β along an axis x, the angle θ_i which a decay product i form with the boost axis is transformed as:

$$\cos\theta_i{}' = \frac{\cos\theta_i + \beta}{1 + \beta\cos\theta_i} \tag{4.6}$$

hence for a very boosted particle with $\beta \to 1$, one has $\cos\theta_i' \to 1$, which means that the decay products are collimated around the boost axis. In particular the decay products are observed in the laboratory frame within a distance approximately of $R \sim 2\theta_i{}' \sim 2\frac{m}{p}$. Hence hadronic W bosons with $p_{\mathrm{T}} \gtrsim 200$ GeV and hadronically decaying top-quarks with $p_{\mathrm{T}} \gtrsim 300$ GeV are typically contained in a jet of radius $R \approx 1$.

Many ATLAS searches needs to distinguish between large-R jets coming from a heavy resonance from jets built from other background sources. To do so, jets properties, such as jet p_{T} and mass can be used to enhance signal over background and the sensitivity of the analysis can heavily depend on the precision with which such variables are known. in ATLAS jets are built from energy deposits in the detector and are then calibrated to the level of stable particle using MC simulations [207]. The simulated detector response and resolution is then checked and corrected using data-driven methods, the so-called *in-situ*

calibrations. The steps which are needed to obtain a fully calibrated large-R jet in ATLAS are summarised in Fig. 4.11.

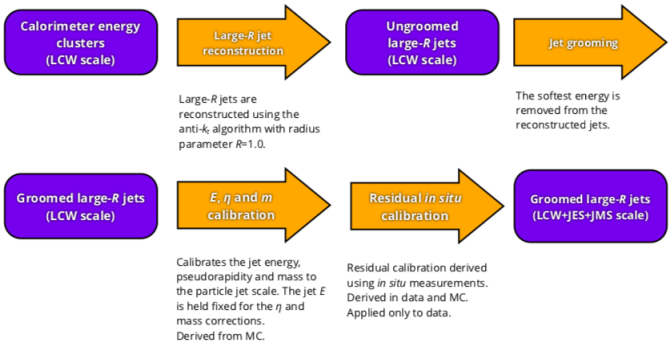

Figure 4.11: The typical reconstruction and calibration sequence applied to obtain the standard large-R jet collection used in many ATLAS analyses. The in-situ calibration is the very last step of the procedure. Figure taken from [169].

Four variables can be defined to parametrise the differences between data and MC in the detector response to the jet p_{T} and m, which are the Jet Energy Scale and Resolution (JER and JER, parametrising p_{T} response) and Jet Mass Scale and Resolution (JMS and JMR, parametrising the mass response), defined as:

$$\begin{aligned} JES &= \frac{\langle p_{\mathrm{T}}^{\mathrm{data}} \rangle}{\langle p_{\mathrm{T}}^{\mathrm{MC}} \rangle} \qquad JER = \frac{\sigma(p_{\mathrm{T}}^{\mathrm{data}})}{\sigma(p_{\mathrm{T}}^{\mathrm{MC}})} \\ JMS &= \frac{\langle m^{\mathrm{data}} \rangle}{\langle m^{\mathrm{MC}} \rangle} \qquad JMR = \frac{\sigma(m^{\mathrm{data}})}{\sigma(m^{\mathrm{MC}})} \end{aligned} \tag{4.7}$$

where $\langle x \rangle$ and $\sigma(x)$ stand for mean value and resolution of the distribution x. In the following, how such variables are calculated with one particluar method is explined.

4.3.1 The Forward Folding method

One possible way to compute realtive JES, JER, JMS and JMR quantites is to use the Forward Folding (FF) method [210]. Typically, to compute response functions a functional form has to be assumed for the reponse, which must either be well motivated physically ot introduce an additional error covering a the particular choice of reposnse shape. For FF, it is not necessary to assume any response function instead.

Take a jet variable x of a jet reconstructed with transverse momentum ${p_{\mathrm{T}}}^{\mathrm{reco}}$ and define $f(x_{\mathrm{true}}, {p_{\mathrm{T}}}^{\mathrm{reco}})$ the detector response to the variable x, as a function of its particle-level value (x_{true}) and ${p_{\mathrm{T}}}^{\mathrm{reco}}$. The FF writes the detector-level reconstructed distribution of the variable x as a function of two independent parameters r and s:

$$x_{\mathrm{reco}} = x_{\mathrm{true}} \left[s f(x_{\mathrm{true}}, {p_{\mathrm{T}}}^{\mathrm{reco}}) + (f(x_{\mathrm{true}}, {p_{\mathrm{T}}}^{\mathrm{reco}}) - \langle f(x_{\mathrm{true}}, {p_{\mathrm{T}}}^{\mathrm{reco}}) \rangle)\,(r - s) \right] \tag{4.8}$$

The parameters r and s are, by construction, shifts in the standard deviation and in the average of the response function:

$$\begin{aligned} s &= \frac{\langle x_{\text{reco}}/x_{\text{true}} \rangle}{\langle f(x_{\text{true}}, {p_{\text{T}}}^{\text{reco}}) \rangle} \\ r &= \frac{\sigma\left(x_{\text{reco}}/x_{\text{true}}\right)}{\sigma\left(f(x_{\text{true}}, {p_{\text{T}}}^{\text{reco}})\right)} \end{aligned} \tag{4.9}$$

and by definition for a detector-level MC distribution one has $r = s = 1$. For data instead, r and s value is chosen to minimise the differences between x_{reco} in data and MC, thorugh a χ^2 minimisation. Recalling Eq. (4.7), when choosing x to be the mass (p_{T}) of the jet in data, r and s can be interpreted as the relative JMS (JES) and JMR (JER) of data respect to MC.

The FF method can be applied to extract the detector response from a variety of distributions and in Section 4.3.2 a selection of jet collections and mass definitions, which have been used in the FF context, is reported. One technical requirement of the FF is that the input distributions should have a peak, to get an accurate estimation of the r and s parameters from the χ^2 minimisation; in fact the narrower the peak, the higher the precision wuth which the parameters are extracted. For mass distributions of heavy resonances, this requirement is almost automatically fulfilled. For the estimation of JES and JER, it is convenient to use as input distributions balances of the large-R jet momentum with momentum of other better measured objects, such as leptons or small jets, as it is done in Ref. [166] and in other standard methods which also evaluate energy response.

4.3.2 Jets and jet mass definitions in ATLAS

In ATLAS standard large-R jets are built from topological calorimeter clusters using FastJet with the anti-k_t algorithm [75] with radius $R = 1$. Such jets are then cleaned from soft radiation via the so called trimming [211] procedure: jets constituents are re-clustered into sub-jets using the k_t algorithm with parameters $R_{\text{sub}} = 0.2$ and all the resulting sub-jets with p_{T} smaller than 5% the p_{T} of the original jet are removed from the constituents list. Such jets are called AntKt10Trimmed5Rsub20 jets.

For AntKt10Trimmed5Rsub20 jets, the usual mass definition is calorimeter based:

$$m^{\text{calo}} = \sqrt{\left(\sum_{i \in \text{constituents}} E_i\right)^2 - \left(\sum_{i \in \text{constituents}} \vec{p_i}\right)^2} \tag{4.10}$$

which is not very performant at high jet p_{T}, because of the limitations in granularity of the calorimeters. For hight p_{T} jets hence, one can extend Eq. (4.10), to take advantage of the information contained in the tracks associated to the jet, defining the track-assisted mass:

$$m^{\text{TA}} = \frac{p_{\text{T}}^{calo}}{{p_{\text{T}}}^{\text{tracks}}} \times m^{\text{tracks}} \tag{4.11}$$

being ${p_{\text{T}}}^{\text{tracks}}$ and m^{tracks} the transverse momentum and mass of the four-vector built as a sum of all the tracks associated to the jet.

Another possible large-R jet definition uses a re-cluster procedure has also been used in the FF context within the ATLAS collaboration [167]. The re-clustered jets (RC jets) are obtained from fully calibrated anti-k_t jets with radius $R = 0.4$, which are used as input constituents to the anti-k_t jet algorithm with $R = 1$. Forward Folding was used in Ref. [167] to extract the relative detector response of

$$m^{\mathrm{RC}} = \frac{\text{mass of large-}R\text{ jet obtained}}{\text{from re-clustering small-}R\text{ jets}} \tag{4.12}$$

The RC approach has the advantage of propagating the calibration obtained from the small-R jet , typically more precise and faster to obtain, to the large-R ones. In Ref. [167] it has been shown that the calibration propagation was performing well enough to not need to add an additional uncertainty due to misinterpretations of reclustering very close small jets ("close-by" effects). The FF confirmed that the relative mass response of the re-clustered and AntKt10Trimmed5Rsub20 jets is compatible.

4.3.3 In-situ calibration of large-R jets in the W boson and top-quark topology

The FF method has been used to extract the in-situ response of jets of large radius containing the hadronic decay products of boosted W bosons and top-quarks. To obtain a sample enriched of heavy mass boosted particles, the event selection cuts which have been applied to select semileptonic $t\bar{t}$ events is:

- a single muon, with ${p_{\mathrm{T}}}^{\mathrm{lep}} > 25$ GeV and $|\eta| < 2.5$
- at least one small-R ($R = 0.4$) jet with ${p_{\mathrm{T}}}^{\mathrm{lep}} > 25$ GeV and $|\eta| < 2.5$
- $E_{\mathrm{T}}^{\mathrm{miss}} > 20$ GeV and $E_{\mathrm{T}}^{\mathrm{miss}} + m_T^W > 60$ GeV [5] mimicking a neutrino
- at least one $b-$tagged small-R jet
- a small-R jet, j, located at $\Delta R < 1.5$ of the muon
- one large-R jet with $p_{\mathrm{T}} > 200$ GeV and $|\eta| < 2$, distant $\Delta R > 2$ from j

where only the $\mu+$ jets final state was chosen to avoid multi-jet background contamination. To enhance the W (top-quark) mass peak, the b-tagged jetwas required to lie outside (inside) of the large-R jet cone.

Various distributions can be constructed with the events passing the aforementioned selection and used to extract the relative detector response via the FF method. m^{calo} and m^{TA} distributions are used to extract relative JMS and JMR, while balances of the p_{T} of the large-R jet with p_{T} of the selected lepton (${p_{\mathrm{T}}}^{\mathrm{lep}}$) , p_{T} of the lepton and b-jet system (${p_{\mathrm{T}}}^{\mathrm{lep\ +\ b\text{-}jet}}$) and p_{T} of the system defined by the lepton, close b-jet and reconstructed neutrino (leptonic top system, ${p_{\mathrm{T}}}^{\mathrm{top\ lep}}$) can be used to measure the large-R jet JES and JER. The result of applying the FF method on these kind of distributions, built from selected events collected during 2015 by ATLAS, is shown in Fig. 4.12.

The method was then applied to extract the in-situ relative JMS and JMR of re-clustered jets [167] and it was then extended to compute the m^{calo} and

[5] m_T^W is the transverse mass of the leptonically decaying W boson. It is defined as ${m_T^W}^2 = 2{p_{\mathrm{T}}^{\mathrm{lep}}}E_{\mathrm{T}}^{\mathrm{miss}}\,(1 - cos\Delta\phi)$, being ϕ the angle between the lepton and direction of the $E_{\mathrm{T}}^{\mathrm{miss}}$.

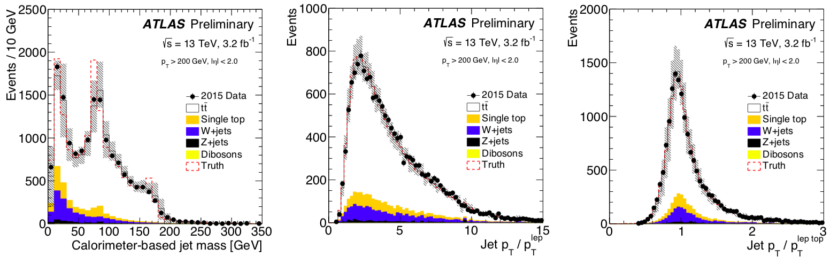

Quantity		Value	Stat. Uncert	Modeling	Jets	Total Syst.
m^{calo}	$s^{\text{MC}}_{\text{data}}$	0.984	0.6 %	1.7 %	1.6 %	**2.3 %**
m^{calo}	$r^{\text{MC}}_{\text{data}}$	1.047	6.6 %	18.1 %	7.0 %	**19.4 %**
m^{TA}	$s^{\text{MC}}_{\text{data}}$	0.981	1.1 %	2.4 %	4.8 %	**5.3 %**
m^{TA}	$r^{\text{MC}}_{\text{data}}$	1.036	6.1 %	14.6 %	5.0 %	**15.5 %**
$p_{\text{T,jet}}/p_{\text{T}}^{\text{lep}}$	$s^{\text{MC}}_{\text{data}}$	1.011	0.7 %	1.3 %	0.4 %	**1.3 %**
$p_{\text{T,jet}}/p_{\text{T}}^{\text{lep}}$	$r^{\text{MC}}_{\text{data}}$	0.945	4.1 %	6.8 %	2.7 %	**7.3 %**
$p_{\text{T,jet}}/p_{\text{T}}^{\text{lep + b-jet}}$	$s^{\text{MC}}_{\text{data}}$	0.985	0.4 %	0.7 %	1.2 %	**1.4 %**
$p_{\text{T,jet}}/p_{\text{T}}^{\text{lep + b-jet}}$	$r^{\text{MC}}_{\text{data}}$	0.903	6.1 %	5.5 %	4.7 %	**7.2 %**
$p_{\text{T,jet}}/p_{\text{T}}^{\text{lep top}}$	$s^{\text{MC}}_{\text{data}}$	0.987	0.2 %	0.3 %	2.1 %	**2.1 %**
$p_{\text{T,jet}}/p_{\text{T}}^{\text{lep top}}$	$r^{\text{MC}}_{\text{data}}$	1.024	3.1 %	6.2 %	6.0 %	**8.6 %**

Figure 4.12: FF results obtained for the relative scale and resolution of the detector response to various observables. 3.2 fb^{-1} of 13 TeV data collected during 2015 have been used to produce these results. Numerical results are reported in the bottom table, for a set of jet observables. Figures and table are from Ref. [166].

m^{TA} and the $p_{\text{T}}/p_{\text{T}}^{\text{top lep}}$ response for different values of the p_{T} of the large AntKt10Trimmed5Rsub20 jets, since data collected had enough statistic to have significant estimations. The results of this last analysis are summarised by the plots in Fig. 4.13 and were included in [169].

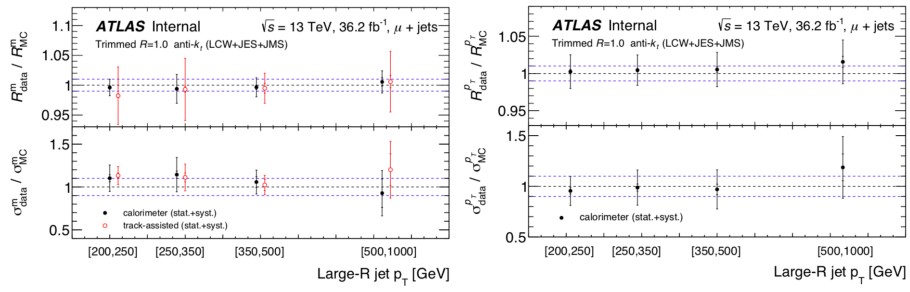

Figure 4.13: Summary of the in-situ constraints on the modelling of the large-R AntKt10Trimmed5Rsub20 jets response in $t\bar{t}$ events with μ+jets final state. Left plots show the relative JMS (top) and JMR (bottom), while on the right relative JES (top) and JER (bottom) are presented. Figure from Ref. [169].

Top-quark mass measurement using $t\bar{t} + 1\text{-jet}$ events in pp collisions at $\sqrt{s} = 8$ TeV with the ATLAS detector at the LHC

Chapter 5

Selection of the $t\bar{t}$ + 1-jet event topology and reconstruction of the $t\bar{t}$ + 1-jet system

The mass of the top-quark is a key parameter of the Standard Model of particle physics that must be determined experimentally. Its value is fundamental in consistency checks of the SM, for the evolution of the Higgs potential and for many BSM scenarios, as it has already been highlighted in Section 3.2. In this analysis the top-quark mass is extracted from the differential cross section of top-quark pair production in association with at least one energetic jet ($t\bar{t}$ + 1-jet), taking advantage of the good properties introduced in Section 3.3 of inferring the top-quark mass from a cross section measurement.

The measurement of the $t\bar{t}$ + 1-jetdifferential cross-section is performed in 8 TeV proton-proton collisions collected with the ATLAS experiment in 2012. The experimental strategy consists in identifying top events by their semileptonic channel: events are selected by requiring exactly one electron or muon candidate, at least five jets in the final state, and significant missing transverse momentum ($E_{\mathrm{T}}^{\mathrm{miss}}$) indicating the presence of an undetected neutrino. The $t\bar{t}$ + 1-jet system is then reconstructed asking additional requirements on the selected objects.

The details on the data sample and Monte Carlo simulations used to simulate the signal and background events are given in Section 5.1 The event selection instead is explained in Section 5.2, while Section 5.3 contains the criteria of $t\bar{t}$ + 1-jet events reconstruction.

5.1 Data and Monte Carlo simulations

Data from pp collision at a center of mass energy of 8 TeV collected by the ATLAS detector are analysed. The data sample includes all 2012 data taking periods with stable beam conditions, where all relevant subdetector systems were operational. The data set corresponds to a total integrated luminosity of $\mathcal{L}^{\mathrm{int}} = 20.3\ \mathrm{fb}^{-1}$, with an uncertainty of $\pm 1.9\%$ [212].

For the simulation, Monte Carlo samples are used that belong to the MC12 production campaign [213]. The following releases have been used for the different stages of the simulation [214]:

- AtlasProductions 17.2.0.2.1 and 17.2.0.4.1 for the event generation.
- AtlasProduction 17.2.6.2 for the simulation of the detector response with GEANT [215]. The GEANT simulation has been used with conditions OFLCOND-MC12-SIM-00
- AtlasProduction 17.2.1.4 for the digitization and reconstruction, with conditions OFLCOND-MC12-SDR-06
- ATLAS geometry used is ATLAS-GEO-20-00-01

A variety of MC event generators are used to model the signal and Standard Model background processes. Details on the production tags can be found in [216] (ptag used p1575, p1770 where p1575 not available).

The nominal $t\bar{t}$ sample used to correct the data is generated at NLO with the POWHEG [46, 217, 218] hvq package [219]. The top-quark mass is set to m_t =172.5 GeV. The CT10 [220] parton distribution functions (PDF) are used. The h_{damp} parameter, which determines the strength of the NLO emission in POWHEG, is set to $h_{\text{damp}} = m_t^{\text{MC}}$. Showering is added, using the PYTHIA [221] program with the Perugia2011C tune [222]. This is the sample which is used by default in data unfolding and analysis optimisation. A k-factor is applied to take into account the most precise $t\bar{t}$ cross section prediction (NNLO+NNLL computed with top++2.0 [115, 223–232]): $\sigma_{t\bar{t}} = 253^{+13}_{-15}$ pb at a center-of-mass energy of 8 TeV.

Additional $t\bar{t}$ samples with different choices of the value of the MC top-quark mass, and otherwise the same settings as the nominal sample, are used to validate the analysis.

Uncertainties coming from PDFs and α_s choices are calculated following the PDF4LHC prescriptions [233], using different sets of PDFs (MSTW200868%CL NLO [230, 231, 234], CT10NLO and NNPDF2.3 [232]) which use different values of the strong coupling constant at the scale of the mass of the Z boson.

Uncertainties related to the modelling of the initial and final state radiation parameters are evaluated by varying values of renormalisation and factorisation scales, the value of the h_{damp} factor and shower tunes. Two samples, that represent the envelope of the possible deviations from the nominal settings, are generated. The first has settings which produce less radiation, and it is obtained with $\mu_{\text{ren}} = \mu_{\text{fac}} = 2\mu_{\text{fac}}^{\text{nom}}$, $h_{\text{damp}} = 172.5$ GeV, radLo tune. In the second more radiation is generated by using $\mu_{\text{ren}} = \mu_{\text{fac}} = \frac{1}{2}\mu_{\text{fac}}^{\text{nom}}$, $h_{\text{damp}} = 345$ GeV, radHi tune.

To estimate the uncertainty of the shower and hadronisation modelling the POWHEG simulation is matched to the HERWIG [47, 235] event generator with the ATLAS AUET2 tune and JIMMY [236] code for multiple parton interactions. Differences in the calulation of the hard process are evaluated using the MADGRAPH5_aMC@NLO [45] matrix element generator with CT10 NLO PDF, which is then matched to HERWIG with the same tunes as the previous one.

Two further $t\bar{t}$ samples, identical to the nominal except for shower tunings, are generated. They are used to estimate uncertainties in the modelling of color reconnection and the underlying event.

When available, $t\bar{t}$ POWHEG simulations have been chosen to have $h_{\mathrm{damp}} = m_t^{\mathrm{MC}}$. When only $t\bar{t}$ POWHEG simulations with $h_{\mathrm{damp}} = \infty$ were available, they were reweighted to $h_{\mathrm{damp}} = m_t^{\mathrm{MC}}$, following the strategy presented in [237].

Electroweak single top-quark production is simulated with POWHEG matched with PYTHIA v6.4. The tune used for the parton shower and hadronisation is Preguia2011C, for all the electroweak production modes: s-channel, t-channel and Wt-channel. When studying systematics in the modelling of the background, further samples are considered.

Vector bosons plus jets production is simulated using ALPGEN [92] generator with CTEQ6L1 PDF. The parton shower is handled by HERWIG together with JIMMY. Samples corresponding to the production of a W-boson in association heavy-flavor quarks (b and c type quarks) are generated separately, at leading order and with a correct treatment of the mass of heavy quarks. Double counting due to heavy quarks produced in the parton shower is avoided using the Heavy Flavour Overlap Removal (HFOR) tool [238].

Diboson events are generated with HERWIG with the CTEQ6L1 PDF.

All the MC simulations described above follow the standard prescription of the ATLAS top physics group. Details on the generator input files, together with links to the samples and further information, can be found in Ref.[213].

The multijet background is estimated using a data-driven method described in [239].

5.2 Object definitions and basic event selection

For this analysis the event selection requires exactly one electron or muon, at least two b-tagged jets, at least three jets from light quarks or gluons, and the presence of significant missing transverse energy due to a neutrino escaping detection.

Basic object reconstruction and object definitions used in this analysis are shared with most top physics analysis in ATLAS, following prescriptions from [240]. The TopCoreRelease-14-00-28, together with the AnalysisTop-1.13.00 package, is used for object definition and their calibrations.

Electron candidates [241] are reconstructed from clusters of energy deposits in the electromagnetic calorimeter, matched with a reconstructed inner detector track. The calorimeter cluster is required to have $p_T > 25$ GeV, $|\eta|$ ¡ 2.47. Clusters in the transition between barrel and end-cap and $1.37 < |\eta| < 1.52$ are excluded. Non-prompt electrons (from heavy-flavour decay) are rejected by two 90% efficient cuts, on the sum of transverse energy deposited in a cone with $\Delta R < 0.2$ around the calorimeter cells associated to the electron, and on the sum of track p_T in a cone of radius $\Delta R < 0.3$. The longitudinal impact parameter z_0 of the electron track with respect to the selected event primary vertex (PV) is required to be smaller than 2 mm.

Muon candidate reconstruction [242] is based on track segments in the muon spectrometer combined with inner detector tracks. The combined track must satisfy $p_T > 25$ GeV and $|\eta| < 2.5$. Muon candidates have to be separated from any jet by $\Delta R > 0.4$ and the sum of the transverse momenta of tracks within a cone of $\Delta R < 10\ \mathrm{GeV}/p_{\mathrm{T}}^{\mu}$ around the muon candidate is required to be less than 5% of the muon transverse momentum. The longitudinal impact parameter z_0 with respect to the PV is required to be smaller than 2 mm.

Jet reconstruction starts from topological clusters [243] of energy deposits in the calorimeters. A local calibration scheme [244] corrects for non-compensation, dead material and out-of-cluster leakage. Jets are reconstructed on these topological clusters using the anti-k_t algorithm [75, 245] with a radius parameter of $R = 0.4$. Jets are calibrated to the level of stable particle jets using Monte Carlo simulation and the response is verified in situ [246]. Jet reconstruction is implemented in the FastJet package [209].

Jets are accepted if $p_T > 25$ GeV and $|\eta| < 2.5$ after the calibration. To reduce the contribution from pile-up, jets with $p_T < 50$ GeV and $|\eta| < 2.4$ must have a jet-vertex-fraction (fraction of tracks associated to the jet pointing to the primary vertex) greater than 0.5. The closest jet within $\Delta R < 0.2$ of selected electrons is discarded to avoid double-counting of the electron deposit as a jet.

Jets with B-hadrons are tagged with the MV1 algorithm, based on multivariate techniques exploiting impact parameter and secondary vertex information [247]. The working point corresponds to a tagging efficiency of 70%, a light jet rejection factor of 130 and a charm rejection factor of 5. The simulated b-tagging efficiency is corrected to match the efficiency measured in data.

The missing transverse momentum (and its magnitude $E_{\mathrm{T}}^{\mathrm{miss}}$) is reconstructed from the vector sum of the transverse momenta of the reconstructed calibrated physics objects and the transverse momentum deposited in the calorimeter cells not associated with these objects.

The basic event selection follows what has been done in other analysis of $t\bar{t}$ events with a lepton+jets final state [248, 249]. It requires:

- a single lepton trigger, with thresholds at 18 GeV (22 GeV) for muons (electrons)
- matching of the selected lepton and trigger object (within $\Delta R < 0.15$)
- no identified noise burst in the liquid argon calorimeter
- the presence of at least one primary vertex with at least five good associated tracks
- exactly one good lepton with $p_T > 25$ GeV
- at least five jets passing high quality cuts
- exactly two b-tagged jets, using the MV1 algorithm at 70% working point.
- a significant amount of transverse missing energy ($E_{\mathrm{T}}^{\mathrm{miss}} > 30$ GeV)
- a W-boson transverse mass (m_T^W)[1]greater than 30 GeV.

The selection differs from the usual $t\bar{t}$ analysis in two aspects. Firstly, five jets are required instead of four. The minimum number of jets needed to reconstruct the $t\bar{t}$ system is four, thus for $t\bar{t}+1$-jet one more is needed. Secondly, $E_{\mathrm{T}}^{\mathrm{miss}}$ and m_T^W cuts are the same for the e and μ channels, in order to have more uniform e+jets and μ+jets selections.

The event yields after this basic selection are compared to the SM expectations in Table 5.1. The uncertainties on the MC yields include experimental

[1] $m_T^W = \sqrt{2p_{T,l} \cdot p_{T,\nu}[1 - \cos(\phi_l - \phi_\nu)]}$, where l is the selected lepton and ν is the neutrino (whose p_T is identified with the missing transverse momentum).

sources such as the jet energy scale (JES), b-tagging efficiency, MC modelling uncertainties, as well as the uncertainties in the cross sections of the SM processes. A detailed description of all the systematics uncertainties is presented in Section 6.4.

$\int \mathcal{L} = 20.3\text{fb}^{-1}$ Data	e+jets channel 22971	μ+jets channel 28525
$t\bar{t}$	19624	25114
Singletop	826	1036
W+jets	490	735
Z+jets	122	70
Diboson	8	6
QCD	142	29
Total MC	21212	26990
MC/Data	0.92	0.95

Table 5.1: Event yields after the basic selection explained in the text.

The distributions of several important kinematic variables are compared to the MC expectation in Figure 5.1. Good agreement is found between data and expectations for all variables.

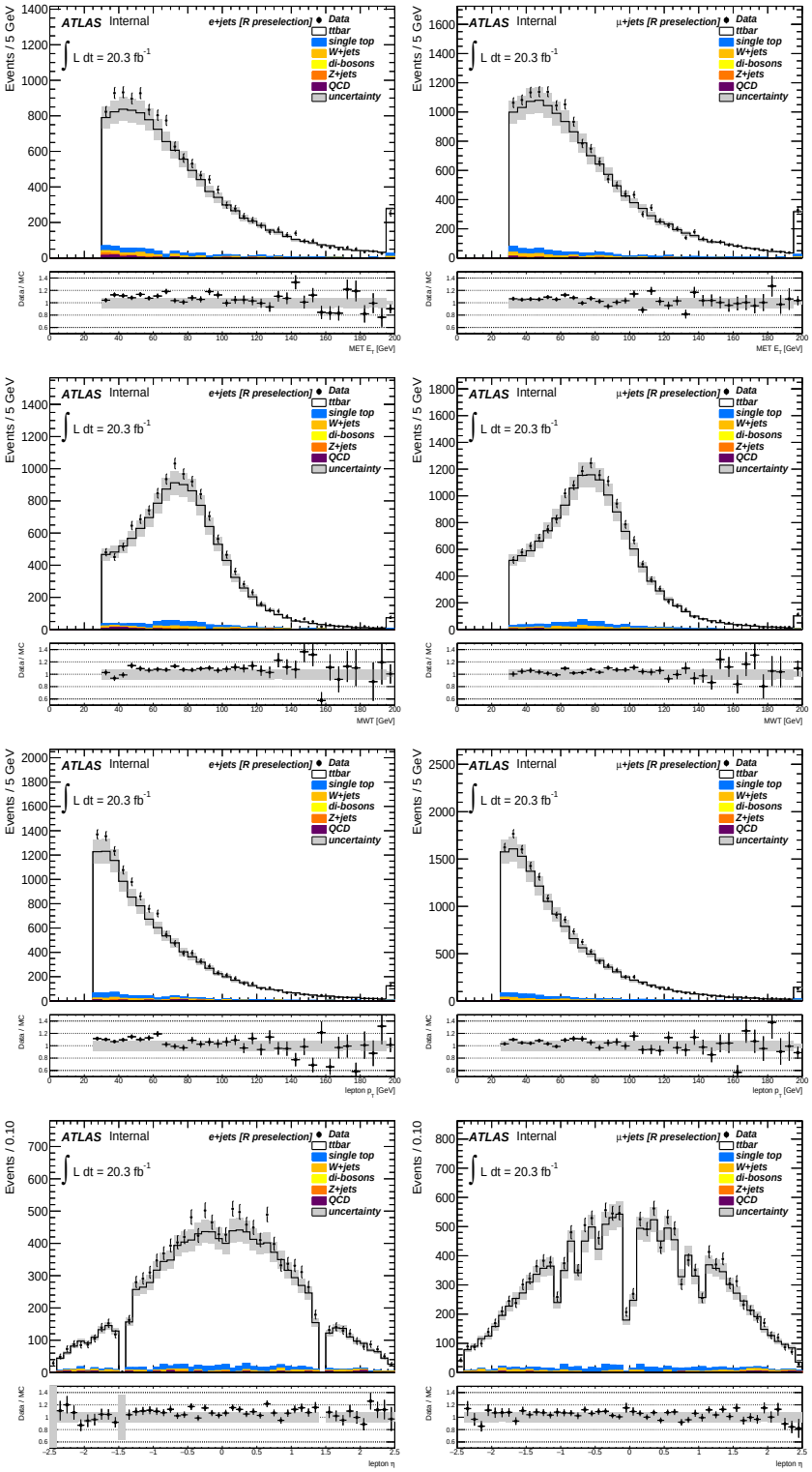

Figure 5.1: Comparison of the observed distributions and the ATLAS MC expectation for several kinematic variables used in the signal selection: the magnitude of the missing transverse momentum $E_{\mathrm{T}}^{\mathrm{miss}}$, the transverse mass of the W-boson m_T^W and the transverse momentum and pseudo-rapidity (η) of the charged lepton. The uncertainty band estimates the error of the MC normalisation [250] as $8.5\%\sigma_{t\bar{t}} + 7.8\%\sigma_{\mathrm{single}-t} + 32.8\%\sigma_{\mathrm{V+jets}} + 52.8\%\sigma_{\mathrm{QCD}} + 500\%\sigma_{\mathrm{VV}}$.

5.3 $t\bar{t}$ + 1-jet system reconstruction and final selection

The ρ_{s} observable is reconstructed for events that pass the basic selection. In order to reconstruct the $t\bar{t}$ + 1-jet system, a number of objects are needed. Candidates are reconstructed for the W-bosons, one decaying hadronically and one leptonically. The b-tagged jets are combined with the W-boson candidates to reconstruct the top-quark four-momentum.

Leptonic W-boson candidates are reconstructed by combining the selected charged lepton and reconstructed neutrino. The component along the beam axis of the neutrino momentum is reconstructed using a constraint on the mass of the leptonic W-boson, requiring:

$$\left(M_W^{\text{leptonic}}\right)^2 = m_l^2 + 2\left(E_l E_\nu - \vec{p}_l \cdot \vec{p}_\nu\right) = \left(M_W^{\text{PDG}}\right)^2 \tag{5.1}$$

where l indicates the charged lepton, $p_a = (E_a, \vec{p}_a)$ is the four-momentum of particle a, and M_W^{PDG} is the value of the W-boson mass reported by the particle data group (PDG) [251]. Equation 5.1 is a second order equation for the componenet of the neutrino along the beam axis. Depending on the value of the radicand in the determinant of Equation 5.1, up to two solutions can exist for $p_{\nu z}$. If the radiacand is positive, two leptonic W boson candidates are obtained with this procedure. If the radicand is negative instead, the magnitude of $E_{\mathrm{T}}^{\text{miss}}$ is adjusted to get a null radicand. In this case only one leptonic W boson is reconstructed.

Hadronic boson candidates are obtained from two selected jets, which are not b-tagged. After the basic selection at least three of such jets exist. It is therefore important to study all the possible pairings and choose the one which best describes a W boson. For each pair (i, j), its invariant mass m_{ij} and its angular distance $\Delta R_{ij} = \sqrt{\Delta\phi(i,j)^2 + \Delta\eta(i,j)^2}$ are defined. To reduce the combinatorial background, to minimize the effects of jet energy corrections on light jets and to improve the mapping of reconstructed hadronic W-boson candidates to truth level W-bosons, pairs that satisfy the following criteria are selected:

- $0.9 < \alpha < 1.25$, with $\alpha = \frac{M_W^{\text{PDG}}}{m_{ij}}$
- $\Delta k_t^{ij} = \min(p_t^i, p_t^j) \cdot \Delta R_{ij} < 90$ GeV.

Among all the possible combinations of W-boson candidates and b-tagged jets, the one that minimizes the following criteria are selected:

$$\beta' = \frac{M_{t_{\text{lept}}} - M_{t_{\text{had}}}}{M_{t_{\text{lept}}} + M_{t_{\text{had}}}} \tag{5.2}$$

This selects the combination where the two reconstructed top-quark candidates have the smallest difference between their kinematical masses.

The impact of these selection cuts do not introduce any bias on the measured top-quark mass as discussed in Appendix A.

As soon as all objects used in the reconstruction of the $t\bar{t}$ system are chosen, the four-momenta of the light jets identified with the decay of the hadronic

W-boson are corrected by the factor α defined above (this ensures the hadronic W-boson candidate has the proper PDG mass).

The additional jet (extra jet) which is needed to reconstruct the $t\bar{t}+1$-jet system is selected from all jets which have not been used to reconstruct the top-quark candidates (i.e. two light jets and two b-taggged jets are discarded). Among the remaining jets, the leading p_T jet is chosen. The event is accepted if the additional jet satisfies the conditions:

- $p_T^{\text{extrajet}} > 50$ GeV
- $\left|\eta^{\text{extrajet}}\right| < 2.5$

An additional cut is applied to improve the purity and data over background ratio, which is:

$$\frac{M_{t_{\text{lept}}}}{M_{t_{\text{had}}}} > 0.9 \tag{5.3}$$

The choice of the p_T cut on the extra jet is studied in detail in Refs. [252, 253] and in Appendix B of this note. The larger the p_T^{extrajet} cut, the less sensitive $t\bar{t}+1$-jet theoretical calculations are to higher order corrections. On the other hand, a high p_T cut reduces the number of reconstructed events which increases the statistical uncertainty on the measurement. In Ref. [252] a p_T cut of 50 GeV has been determined as a reasonable compromis of the two competing effects. We assum that the difference of the center-of-mass energy between the analysis of Ref. [252] and the one presented here does not change the conclusion. In addition Appendix B shows no indication of any bias due to the selection of the p_T^{extrajet} cut. Similar results are presented in Refs. [253, 254].

The efficiency of the above described procedure, defined as the ratio between the final number of selected events and the number of events which passed the basic selection, is $\sim 28\%$. In Table 5.2 the event yield after the final selection cuts is presented. The distributions of the transverse momentum and pseudo-rapidity of the top-quark candidates and the additional jet are presented in Figure 5.2. Additional control plots are available in Appendix C.

$\int \mathcal{L} = 20.3$ fb^{-1} Data	e+jets channel 6379 ± 80	μ+jets channel 7824 ± 88
$t\bar{t}$	5529 ± 470	7079 ± 602
Singletop	191 ± 15	226 ± 18
W+jets	100 ± 33	121 ± 37
Z+jets	24 ± 8	13 ± 4
Diboson	1± 0	0± 0
QCD	21 ± 11	0 ± 0
Total MC	5866 ± 537	7439 ± 661
MC/Data	0.92	0.95

Table 5.2: Event yields after final selection.

Finally, the invariant mass of the $t\bar{t}+1$-jet system, $s_{t\bar{t}+1\text{-jet}}$ is obtained by summing the four vectors of the five selected jets, the charged lepton and the reconstructed momentum of the neutrino. Such an inclusive quantity does not have a strong dependence on ambiguities in combinatorics, in particular it does not depend on the choice of matching b-jets with W bosons candidates.

The distribution of $t\bar{t}$ + 1-jet events as a function of $\rho_s = \frac{340\ \text{GeV}}{\sqrt{s_{t\bar{t}+1\text{-jet}}}}$ is presented in Figure 5.3.

To obtain the final $\mathcal{R}$ distribution the predicted background contributions are subtracted. The remaining distribution is normalized to the number of background subtracted events. The binning choice is motivated in Appendix D. Finally, the value of normalized cross section in each bin is divided by the bin width. The distribution obtained is shown is Figure 5.4 together with the prediction of the nominal ATLAS $t\bar{t}$ MC sample as defined in Section 5.1.

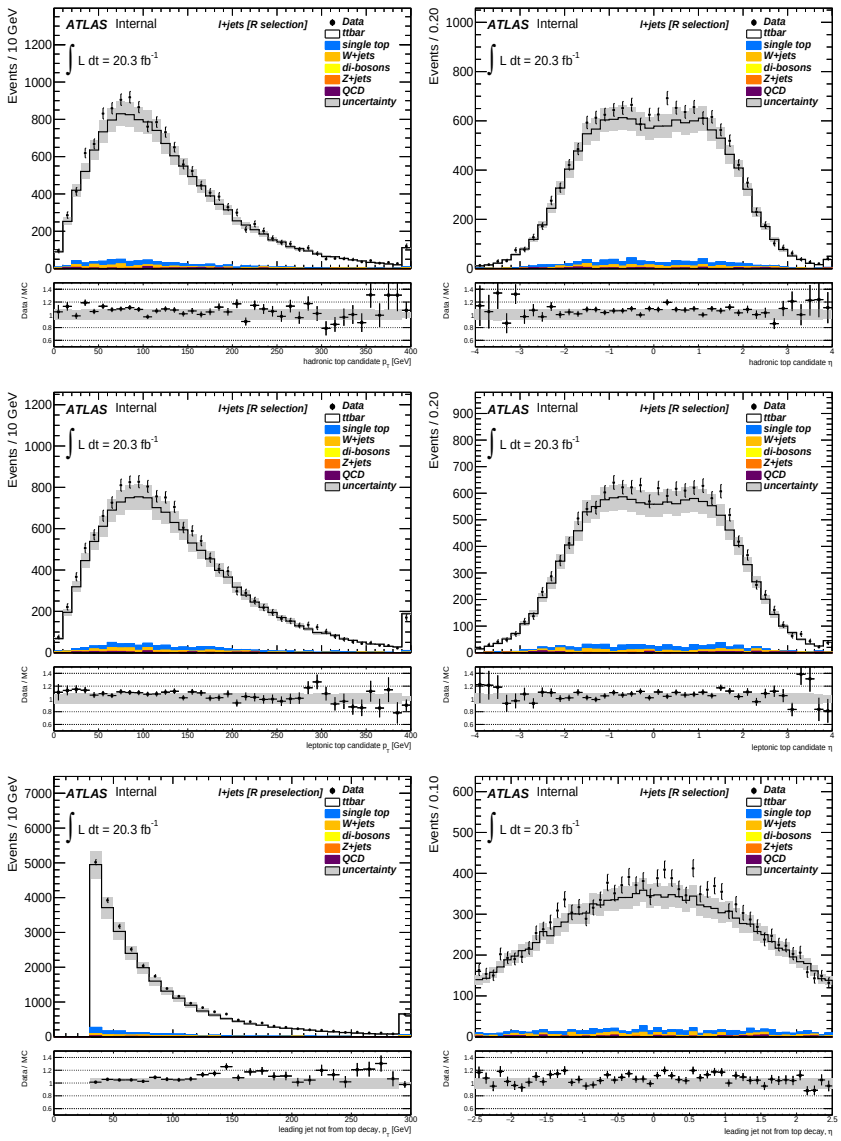

Figure 5.2: Control plots for the p_T and η of the reconstructed leptonic and hadronic tops, together with the jet which is identified as the extrajet of the detector level $t\bar{t}+1$-jet system. The uncertainty band represents an estimation of the error of the MC normalisation, as defined in Figure 5.1

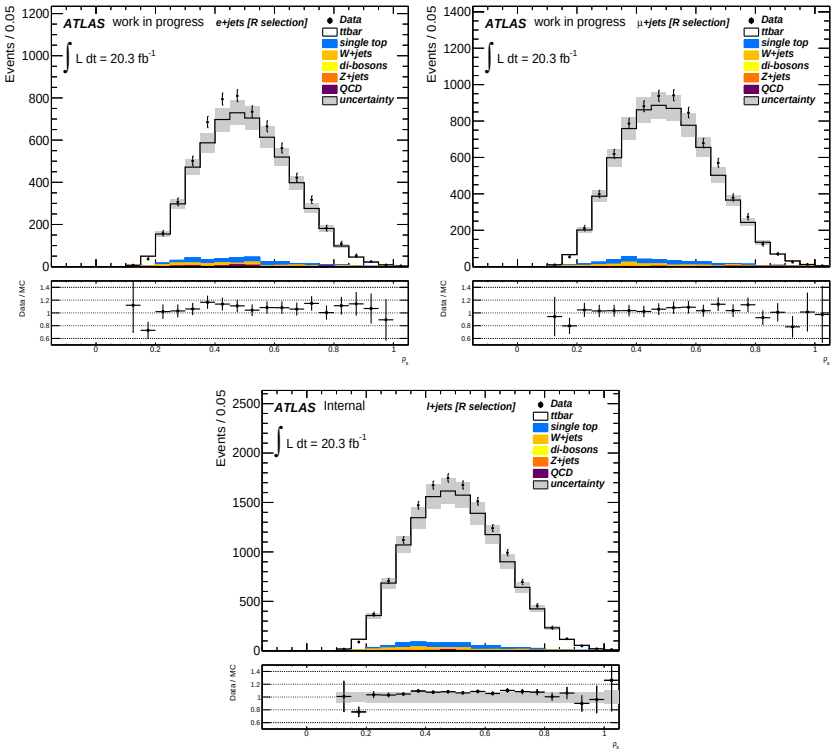

Figure 5.3: Distributions of the ρ_s variable in the $t\bar{t}$ + 1-jet system after the final selection. Data are compared to the SM expectation. Events in different channels are shown separately in the uppermost plots, and their combination is shown in the lowermost plot. The uncertainty band represents an estimation of the error of the MC normalisation, as defined in Figure 5.1.

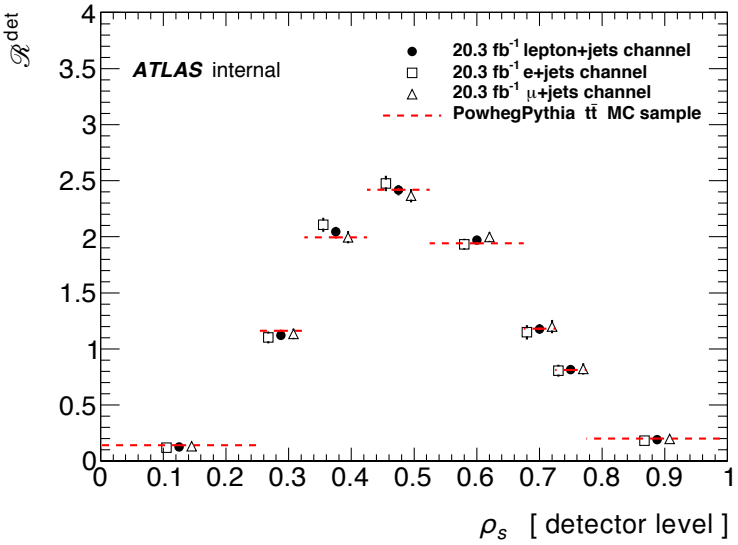

Figure 5.4: The differential normalized ρ_s distribution in the selected $t\bar{t}$ + 1-jet events after background subtraction. The data points are shown for the electron+jets and muon+jets channels separately and for the combination of both channels. The result is compared to the nominal ATLAS $t\bar{t}$ MC sample (red dashed line).

Chapter 6

Top-quark mass extraction at parton level

In this Section the $\mathcal{R}$ distribution as observed in data is corrected to parton level and compared to the theoretical predictions of Refs. [40, 99] which are computed at NLO QCD theoretical accuracy. These calculations are performed on the basis of the pole mass scheme [40] and the $\overline{\text{MS}}$ scheme [99] allowing to extract both the top-quark pole mass (Section 6.6) and the top-quark running mass (Section 6.7). Comparing both results and their compatibility represents an interesting test. The comparisonn allows to assess the impact of uncalculated higher orders. Furthermore, it is conceivable that one scheme shows a better perturbative convergence that another scheme. In the present case, the relation between m_t^{pole} and $m_t(m_t)$ does not involve large logarithms so that no major difference is expected. The first applications of this method [99, 252], using 4.6 fb^{-1} of 7 TeV pp collisions, resulted in an uncertainty of 2.3 GeV (1.3%) on the top-quark pole mass and of 2.4 GeVfor the running mass.

The chapter is structured as follows. The definition of the level at which the measurement is performed and the main strategy of the mass extraction is presented in Section 6.1. The approach developed in Refs. [40, 99] and introduced in Section 3.3.2 is followed. Selected and reconstructed events are corrected to the level of sable top-quarks via an unfolding procedure which is explained in Section 6.2. The evaluation of the uncertainties on the unfolding procedure and on the mass extraction is estimated in Section 6.4 and the fiability of such estimation is cross-checked in Section 6.5. The top-quark mass is extracted both in the pole mass scheme (Section 6.6) and in the $\overline{\text{MS}}$ scheme (Section 6.7). The two results are found to be compatible with each others, as it explained in Section 6.8.

6.1 $t\bar{t}+1$-jet system definition at different reconstruction levels

The observable $\mathcal{R}$ which is used to extract the top-quark mass can be computed and compared to data at parton, particle and detector levels. The required theory input to construct the observable is however different at each of these

levels. At parton level our present ansatz considers the top quarks as a stable particles having well defined four momenta. At particle level the four momenta of the top quarks are reconstructed by identifying and clustering the information from the decay products of the top quarks, the gluon radiation and later hadronization. At detector level the experimental signals and effects due to the particles transversing the ATLAS detector need to be considered in addition. It is thus reasonable to get different $\mathcal{R}$ distributions at each of these levels which should however be coherently connected using correction factors depending on the same parameters, and in particular the same top-quark mass. These correction factors need to be computed using the nominal ATLAS Monte Carlo.

At parton level the observed $\mathcal{R}$ distribution is corrected (unfolded) and directly compared to the prediction of Ref. [40]. On the contrary, at detector level the theoretical prediction is corrected (folded) and compared to the observed $\mathcal{R}$ distribution after detector effects. The particle level represents an intermediate stage in which the data are corrected (unfolded) for detector effects and compared to the corrected (folded) theoretical distribution at this level. The description of the different $\mathcal{R}$ distribution using the same value of the top-quark mass at each of these levels represents a highly non-trivial test of the coherence of the method as each level involves different identification and reconstruction techniques with different fit procedures.

The previous analysis at 7 TeV [252] only considered the parton level. In the present work results are obtained for the three levels. At parton and detector levels the coherence and compatibility of the method is examined. At particle level only the $\mathcal{R}$ distribution is presented.

In the following the detailed definition of the $t\bar{t}$ + 1-jet system at the different reconstruction levels is summarised[1]:

- *parton level:* top quarks are considered on-shell before decaying but QCD radiation (including initial and final state radiation) is enabled. The parton shower evolution is included at this level while keeping the top-quarks on-shell,
- *particle level:* this is the level in which the stable particles[2] are considered before their interaction with the detector. The $t\bar{t}$ + 1-jet system is reconstructed using decay products of the top-quarks. At this level the four momenta of neutrinos are known exactly. More details are available in [255],
- *detector level:* the $t\bar{t}$ + 1-jet system is reconstructed from objects as identified in the detector following the strategy developed in Sections 5.2 and 5.3.

Unfortunately, the parton level, as described above, is not directly accessible in the ATLAS nominal $t\bar{t}$ MC sample (Powheg+Pythia) as the information to build the four momenta of the top-quarks is not kept in the n-tuples. More detail on the missing information is available in Ref. [253]. Therefore, another intermediate level is introduced which is available in the nominal MC sample and is relatively close to the parton level:

[1] It is always required that the extra jet fulfills the conditions of $p_{\mathrm{T}}^{\mathrm{extrajet}} > 50$ GeV and $|\eta^{\mathrm{extrajet}}| < 2.5$)

[2] a particle is considered stable if its lifetime is greater than ∼3 ns.

- 1^{st} *emission level* or $t\bar{t}+g$*:* the observable is defined using top-quarks as in the parton level but the additional jet is identified with the first emission of the hard process MC generator[3].

To correct the data to the parton level, the standard nominal ATLAS $t\bar{t}$ MC sample and a $t\bar{t}$ MC sample produced with the same ATLAS settings are used. In this last sample the information as required to build the correct four momenta of the top-quarks is saved. The complete procedure to unfold the data is then performed in two steps:

1. correct the data from detector level to the first emission ($t\bar{t}+g$) level using the nominal ATLAS MC sample

2. apply a correction to obtain the distribution from first emission level to the parton level. This step is needed to compare with the theoretical calculation ($t\bar{t}+g \rightarrow t\bar{t}+1$-jet). This last correction is obtained with the privately produced MC sample, in which the parton level information is saved. The private sample was validated using ATLAS samples and the validation plots can be found in Appendix E.

In [252] it has been proven that unfolding data to parton level directly is equivalent to do it via the first emission level.

6.2 Data correction to parton level

In order to get the $\mathcal{R}$ distribution at parton level, as defined in Section 6.1, the data needs to be unfolded. By this process, the observed $t\bar{t}+1$-jet distribution is corrected for detector, hadronisation, gluon radiation and top-quark decay effects. This correction is calculated using simulated events from the nominal ATLAS $t\bar{t}$ MC that pass the same event selection criteria as applied to data. The full correction is applied in steps first by constructing a migration matrix $\mathcal{M}$ and later, by bin-to-bin factors. The first factor, f, takes into account the correction for acceptance and the difference between the first emission ($t\bar{t}+g$) and $t\bar{t}+1$-jet at parton level. The second factor, $f^{\text{Ph.Sp.}}$, accounts for the available phase-space to produce events which pass the selection criteria depending on the top mass.

The migration matrix $\mathcal{M}$ gives the probability that an event generated with a certain value of ρ_{s} at first emission is reconstructed with the same or other value of ρ_{s} at detector level. The acceptance factors consider the fact that there could be events which are selected at detector level but did not come from events which pass the first emission level selection cuts, and vice-versa. The last phase-space correction takes into account the probability of producing events passing the selection cuts depending on the top mass. This last factor is very small and only affects the bins close to the threshold region. It can be easily factorized as a function of $\mathcal{R}$ and ρ_{s} as will be explained below.

The unfolding method is thus defined as a three-step procedure. The first step uses the inverse of the migration matrix from first emission to detector

[3]When matching POWHEG to PYTHIA, the hardest emission is taken care of by POWHEG. The parton shower is then started at the kinematical limit, and emissions harder than the first one are vetoed. A detailed discussion is available in [256].

level to convolute the data. The inversion of $\mathcal{M}$ is regularized with an iterative algorithm based on the procedure that is called Bayesian unfolding [257]. A detailed study of the choice of the unfolding method and its regularization parameter is presented in Appendix F.

The second step factorizes the acceptance and the difference between first emission ($t\bar{t}+g$) and $t\bar{t}+1$-jet using a bin-by-bin correction. Finally an additional factor accounts for the phase-space correction.

To explain the whole procedure in detail let's start by defining $\mathcal{R}^{t\bar{t}+g}_{\text{preACC.}}$ as the observable built at detector level with events which pass the complete selection, corrected to the first emission level. Notice that $\mathcal{R}^{t\bar{t}+g}_{\text{preACC.}}$ is still affected by the detector level cuts, even if it is corrected to parton level. It is then possible to define $\mathcal{R}^{t\bar{t}+\text{1-jet}}$ as the parton level observable built from parton level events which pass the cuts at that level ($p_{\text{T}}^{\text{extrajet}} > 50$ GeV, $|\eta^{\text{extrajet}}| < 2.5$). Their ratio $f(\rho_{\text{s}}) := \frac{\mathcal{R}^{t\bar{t}+\text{1-jet}}}{\mathcal{R}^{t\bar{t}+g}_{\text{preACC.}}}(\rho_{\text{s}})$ can be computed from MC simulation. The correction factor f gives the magnitude of the $t\bar{t}+1$-jet specific cuts which are applied, as well as the small correction accounting for the transformation from first emission to parton level The factor extracted from the nominal $t\bar{t}$ MC sample is presented in Figure 6.1.

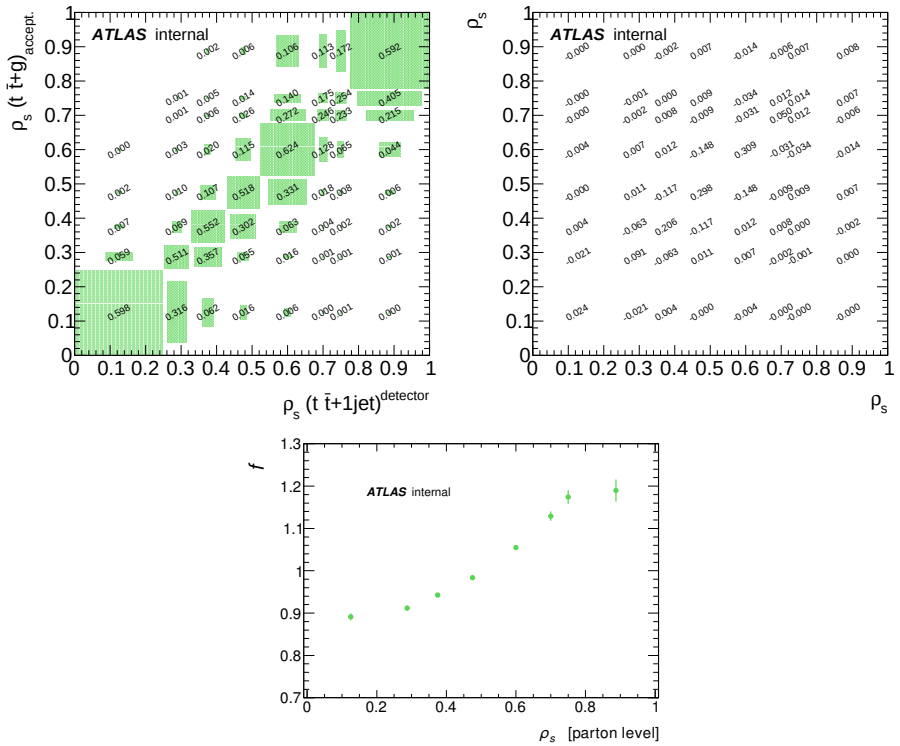

Figure 6.1: Efficiency matrix of the unfolding (top left) and associated covariance matrix (top right) normalised to number of entries. Also the bin-by-bin acceptance correction $\frac{\mathcal{R}^{t\bar{t}+\text{1-jet}}}{\mathcal{R}^{t\bar{t}+g}_{\text{preACC.}}}(\rho_{\text{s}}) := f(\rho_{\text{s}})$ is shown (bottom).

The $\mathcal{R}$ distribution is divided in 8 bins as the result of detailed study between

two binning choices, 6 bins versus 8 bins as reported in Appendix D. This binning is shown in Figure 5.4 and its most relevant features are:

- Sensitivity: the binning choice isolates the region where the distribution is most sensitive to the mass ($\rho_s \gtrsim 0.7$).
- Efficiency: migrations are limited. The value of the efficiency matrix[4] in the most sensitive bin (i.e. $\rho_s^{1^{st}\ \text{emission}} \in [0.8, 1]$ and $\rho_s^{\text{detector}} \in [0.8, 1]$) is well above 50% (Figure 6.1).
- Statistics: all bins are sufficiently populated minimizing statistical fluctuations.

Results in Appendix D confirm that compatible values are extracted for top-quark mass by either using 6 or 8 bins without introducing any bias. The statistical accuracy is however improved significantly by using 8 bins. Further studies employing a finer binning did not produce stable results due to the decrease in the number of events populating the bins close to the top threshold.

The f correction factor was computed for a variety of different $t\bar{t}$ MC simulations. As mentioned above, it encodes the extrapolation outside the phase space defined by the detector level cuts.

In addition, near the threshold the $\mathcal{R}$ end-point changes as a function of the top-quark mass due to the required available phase-space needed to produce a gluon-jet with$p_T^{\text{extrajet}} > 50$ GeV, $|\eta^{\text{extrajet}}| < 2.5$. Eventually for a large enough mass value of the top quark the $t\bar{t}+1$-jet events can be produced outside the closest bin to the threshold. As the bin size is fixed the impact of this correction is relevant as the bins close to the threshold get smaller. Hence these effects, even if are small, need to be quantified and considered in the analysis. This is possible by using a large range of top-quark masses and Figure 6.2 illustrates the impact of this correction for top-quark masses between 165 and 180 GeV. As it can be seen in Figure 6.2, the aforementioned effect is almost un-existing for 6 bins. Hence a comparison between the results obtained for 6 and 8 bins can be taken as an estimate for any bias due to this correction.

The dependence of the available phase-space can be parametrised continuously as a function of $\mathcal{R}^{t\bar{t}+g}_{\text{preACC.}}$.as indicated in Appendix G. One can then factorise the pure dependence on the modelling of the phase space from the acceptance cuts, by defining a factor $f^{\text{Ph.Sp.}}$ such that takes a value depending on $\mathcal{R}^{t\bar{t}+g}_{\text{preACC.}}$.

The correction procedure can be summarised as:

$$\mathcal{R}^{t\bar{t}+1\text{-jet}}_{\text{data}}(\rho_s) = \left[\mathcal{M}^{-1} \otimes \mathcal{R}^{\text{det}}_{\text{data}}(\rho_s)\right] \cdot f(\rho_s) \cdot f^{\text{Ph.Sp.}}\left(\rho_s, \mathcal{R}^{t\bar{t}+g}_{\text{preACC.}}\right) \tag{6.1}$$

where the two correction factors f and $f^{\text{Ph.Sp.}}$ distinguish between two distinct effects: the acceptance correction (f, as presented in Figure 6.1) and the phase space correction ($f^{\text{Ph.Sp.}}$, presented for each bin in Figure 23 at Appendix G).

The interval of $\mathcal{R}^{t\bar{t}+g}_{\text{preACC.}}$ for which the $f^{\text{Ph.Sp.}}$ factor has been evaluated covers an equivalent mass range of 15 GeV. Where the correction is most important (in the region $0.775 < \rho_s < 1$) the effect is to modify the observable by $\sim \frac{1\%}{\text{GeV}}$.

[4]The efficiency matrix is defined as the fraction of events of a bin at 1^{st} emission level which are reconstructed in another bin at the detector level.

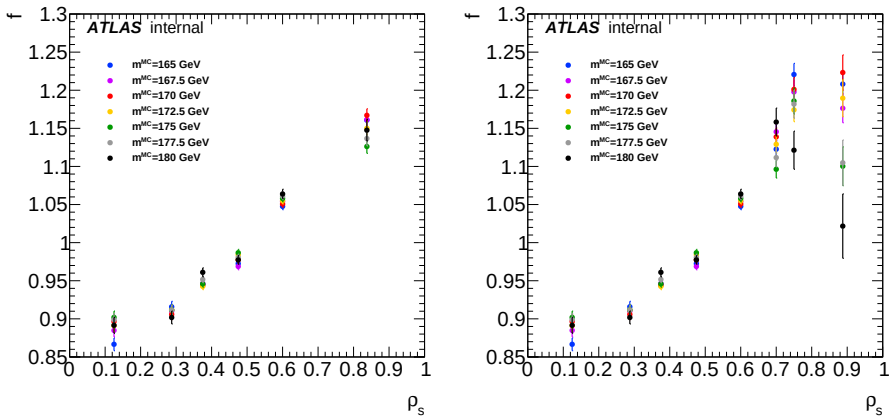

Figure 6.2: The dependence of f correction factor for different choices of the MC used in the definition of the unfolding procedure. On the left the factor is defined using only 6 bins, as it was done in Ref. [252], and shows no dependence, since last bin has not enough resolution to reveal the effect. On the right, the factor is presented for the finer binning used in this analysis. The dependence in the region $\rho_{\mathrm{s}} \sim 1$ can be seen.

The overall impact of this correction is small anyway, as it is expected a value from data of $\mathcal{R}^{t\bar{t}+g}_{\mathrm{preACC.}}$, near to the one obtained from the nominal $t\bar{t}$ MC sample (i.e. the nominal MC is suppposed to best describe data.). In Appendix G additional cross-checks and considerations on the $f^{\mathrm{Ph.Sp.}}$ factor are presented. No bias is observed by introducing this correction and a procedure to estimate its systematic uncertainty is also derived.

The output of the unfolding process is a distribution at parton level corrected for modelling and detector effects, which can be compared to the NLO QCD theoretical prediction. The result at the parton level is presented in Figure 6.3. A covariance matrix is provided that takes into account the correlations between bins. The covariance matrix normalized to the number of entries is shown in Figure 6.1.

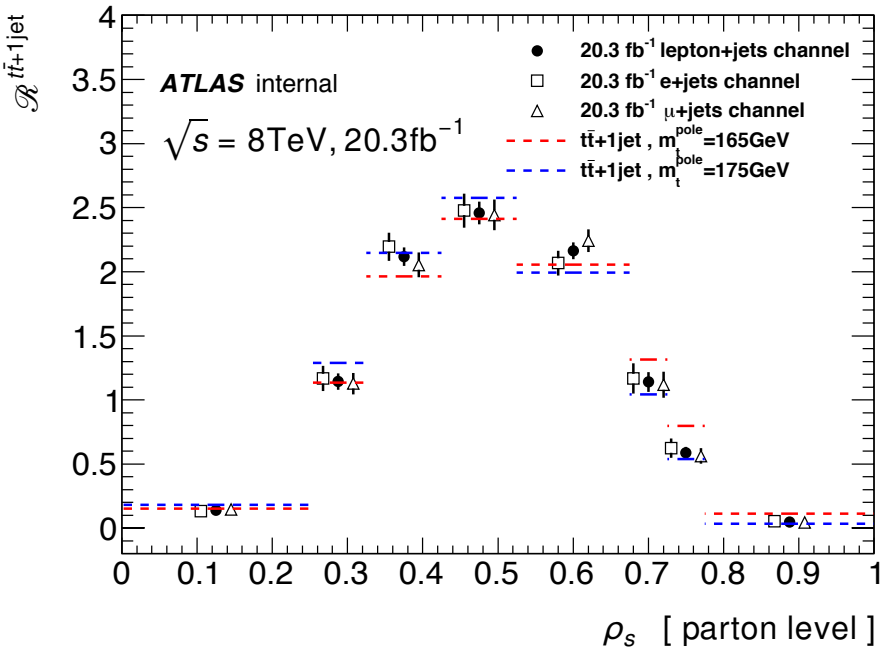

Figure 6.3: Corrected, parton level $\mathcal{R}$ distribution for the e+jets, μ+jets and l+jets channels in 8 TeV pp collision data. The result is compared to a $t\bar{t}$ + 1-jet @NLO+PS calculation for pole mass values of 165 GeV(red line) and 175 GeV(blue line)

6.3 Pole mass measurement: fit to $t\bar{t}$ + 1-jet @NLO+PS prediction

To extract the value of the top-quark pole mass from the unfolded distribution, a fit to $\mathcal{R}_{\text{data}}^{t\bar{t}\text{+1-jet}}$ with the $t\bar{t}$ + 1-jet @NLO+PS calculation is performed. The fit uses the least squares method, where the best value of m_t^{pole} is chosen to be the one which minimizes:

$$\chi^2 = \sum_{i,j} \left[\mathcal{R}_{\text{data}}^{t\bar{t}\text{+1-jet}} - \mathcal{R}_{\text{theo@NLO+PS}}^{t\bar{t}\text{+1-jet}}(m_t^{\text{pole}})\right]_i \left[V^{-1}\right]_{ij} \left[\mathcal{R}_{\text{data}}^{t\bar{t}\text{+1-jet}} - \mathcal{R}_{\text{theo@NLO+PS}}^{t\bar{t}\text{+1-jet}}(m_t^{\text{pole}})\right]_j , \tag{6.2}$$

where indices i and j refer to the bin number, and V is the covariance matrix normalized to the number of events which passes the detector level event selection. The statistical uncertainty on the measurement is taken as the mass shift which changes the χ^2 by one with respect to the minimal value. Since the observable $\mathcal{R}$ is normalised, bins are not independent of each other. Thus one bin has to be excluded in the sum of Equation 6.2. The nominal choice has been to exclude the first bin ($0 < \rho_s < 0.25$), as it was done in [252]. The resulting χ^2 distribution is shown in Figure 6.4. The effect of dropping a different bin with similar sensitivity is evaluated in Appendix H and has a negligible contribution on the extracted value. Differences in the extracted m_t^{pole} values are compatible with 0 within their statistical uncertainty, while values of χ^2_{min} vary in range between 0.5 and 2.

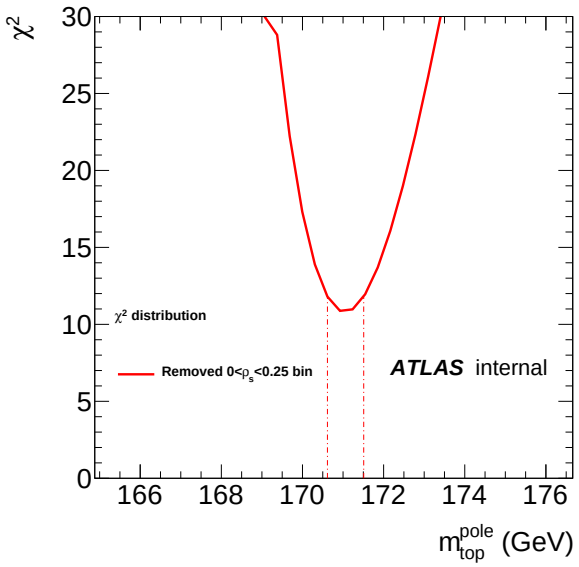

Figure 6.4: χ^2 distribution from Equation 6.2. Vertical dashed lines shows the $\Delta\chi^2 = \pm 1$ variation.

No analytical prediction is available for $\mathcal{R}_{\text{theo@NLO+PS}}^{t\bar{t}\text{+1-jet}}(m_t^{\text{pole}})$, thus the parametric dependence on the top-quark pole mass is approximated using a second order polynomial. Nine different theoretical predictions for values of $\frac{m_t^{\text{pole}}}{\text{GeV}} =$

$\mathcal{R}^{t\bar{t}+1\text{-jet}}_{\text{theo@NLO+PS}}$				
mass [GeV]	$0 < \rho_s < 0.25$	$0.25 < \rho_s < 0.325$	$0.325 < \rho_s < 0.425$	$0.425 < \rho_s < 0.525$
160	0.1388 ± 0.0027	1.073 ± 0.011	1.816 ± 0.014	2.342 ± 0.018
165	0.1522 ± 0.0017	1.134 ± 0.012	1.963 ± 0.015	2.413 ± 0.017
167.5	0.1637 ± 0.0020	1.188 ± 0.010	1.991 ± 0.013	2.428 ± 0.015
170	0.1686 ± 0.0017	1.211 ± 0.011	2.052 ± 0.012	2.466 ± 0.015
172.5	0.1718 ± 0.0015	1.256 ± 0.010	2.078 ± 0.013	2.511 ± 0.014
173.75	0.1763 ± 0.0019	1.255 ± 0.010	2.119 ± 0.012	2.572 ± 0.015
175	0.1804 ± 0.0016	1.290 ± 0.010	2.146 ± 0.015	2.576 ± 0.015
177.5	0.1851 ± 0.0024	1.336 ± 0.010	2.224 ± 0.014	2.597 ± 0.016
180	0.1922 ± 0.0022	1.378 ± 0.010	2.254 ± 0.013	2.639 ± 0.015
mass [GeV]	$0.525 < \rho_s < 0.675$	$0.675 < \rho_s < 0.725$	$0.725 < \rho_s < 0.775$	$0.775 < \rho_s < 1$
160	2.102 ± 0.015	1.399 ± 0.022	0.939 ± 0.015	0.1634 ± 0.0038
165	2.056 ± 0.012	1.317 ± 0.022	0.796 ± 0.019	0.1124 ± 0.0037
167.5	2.060 ± 0.010	1.271 ± 0.018	0.740 ± 0.013	0.0826 ± 0.0023
170	2.050 ± 0.011	1.183 ± 0.021	0.675 ± 0.014	0.0657 ± 0.0018
172.5	2.049 ± 0.011	1.092 ± 0.014	0.633 ± 0.014	0.0459 ± 0.0014
173.75	2.012 ± 0.013	1.059 ± 0.016	0.565 ± 0.010	0.0424 ± 0.0020
175	1.995 ± 0.012	1.042 ± 0.014	0.540 ± 0.014	0.0343 ± 0.0015
177.5	1.968 ± 0.012	0.976 ± 0.016	0.449 ± 0.011	0.0218 ± 0.0010
180	1.941 ± 0.011	0.931 ± 0.018	0.375 ± 0.010	0.0134 ± 0.0007

Table 6.1: The observable $\mathcal{R}$ predicted by a $t\bar{t}$ + 1-jet @NLO+PS calculation for different m_t values. The requirements on the additional jet are $p_T > 50$ GeV and $|\eta| \leq 2.5$. The uncertainties represent the statistical accuracy of the calculation.

$\{160, 165, 167.5, 170, 172.5, 173.75, 175, 177.5, 180\}$ are computed. For each bin j the theoretical dependence on m_t^{pole} is parametrized as:

$$\left[\mathcal{R}^{t\bar{t}+1\text{-jet}}_{\text{theo@NLO+PS}}(m_t^{\text{pole}})\right]_j = a_j + b_j\left(m_t^{\text{pole}} - 170\text{ GeV}\right) + c_j\left(m_t^{\text{pole}} - 170\text{ GeV}\right)^2, \tag{6.3}$$

where coefficients a_j, b_j, c_j are extracted using the four mass points which have the nearest values to $\left[\mathcal{R}^{t\bar{t}+1\text{-jet}}_{\text{data}}\right]_j$. Theoretical calculations of the observable for each bin are reported in Table 6.1, while the second order polynomial curves of Equation 6.3 for each bin are shown in Figure 6.6. Different parametrizations give compatible results. More details can be found in Section 6.4.4.

Finally, an important result to be noticed is that with such fit and unfolding procedure, the correction of the data to parton level is independent of the assumed top-quark mass which is used in the MC (m_t^{MC}). This fact is reflected in Figure 6.5 within a 15 GeV mass range. The plot shows the difference between the extracted and the input quark masses when the MC simulated data are and the reference fit curves are produced using the MC prediction at parton level. The result confirms the findings already reported in Refs. [252] and strongly supports the method to extract the top-quark mass from a direct comparison between the theoretical prediction and the corrected distribution without any further assumption.

The observable, as obtained from data corrected for detector and hadronisation effects, is presented in Figure 6.3. The top-quark pole mass is extracted from fitting the $\mathcal{R}$ distribution at NLO+PS level, as explained in this section. The value obtained is:

$$m_t^{\text{pole}} = 171.05 \pm 0.43(\text{stat})\text{ GeV} \tag{6.4}$$

where only the statistical uncertainty is considered. The value of the mass was

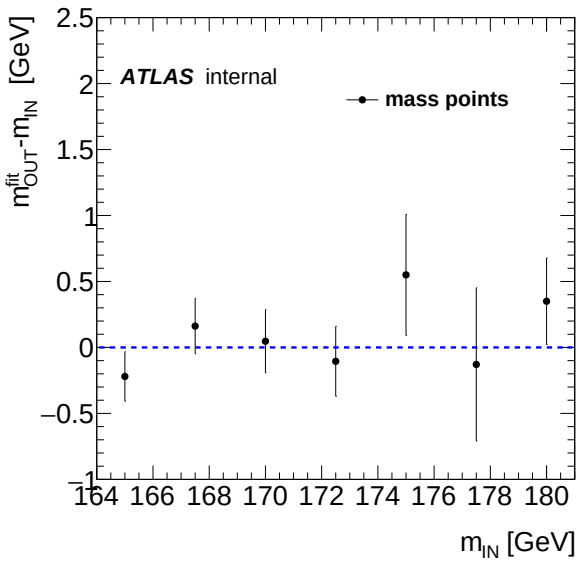

Figure 6.5: Difference between the extracted top-quark mass value and its input value when using the unfolding procedure described in Section 6.2. No dependence is observed in the range of top-quark masses between 165 GeVand 180 GeV. Error bars indicate the statistical precision of the MC sample used for each test.

also measured separately for the e+jets and μ+jets channels, resulting in:

$$\begin{aligned} m_t^{\text{pole}}\ (e\text{+jets}) &= 171.14 \pm 0.51(\text{stat})\ \text{GeV} \\ m_t^{\text{pole}}\ (\mu\text{+jets}) &= 170.97 \pm 0.66(\text{stat})\ \text{GeV} \end{aligned} \tag{6.5}$$

All values are compatible with each other.

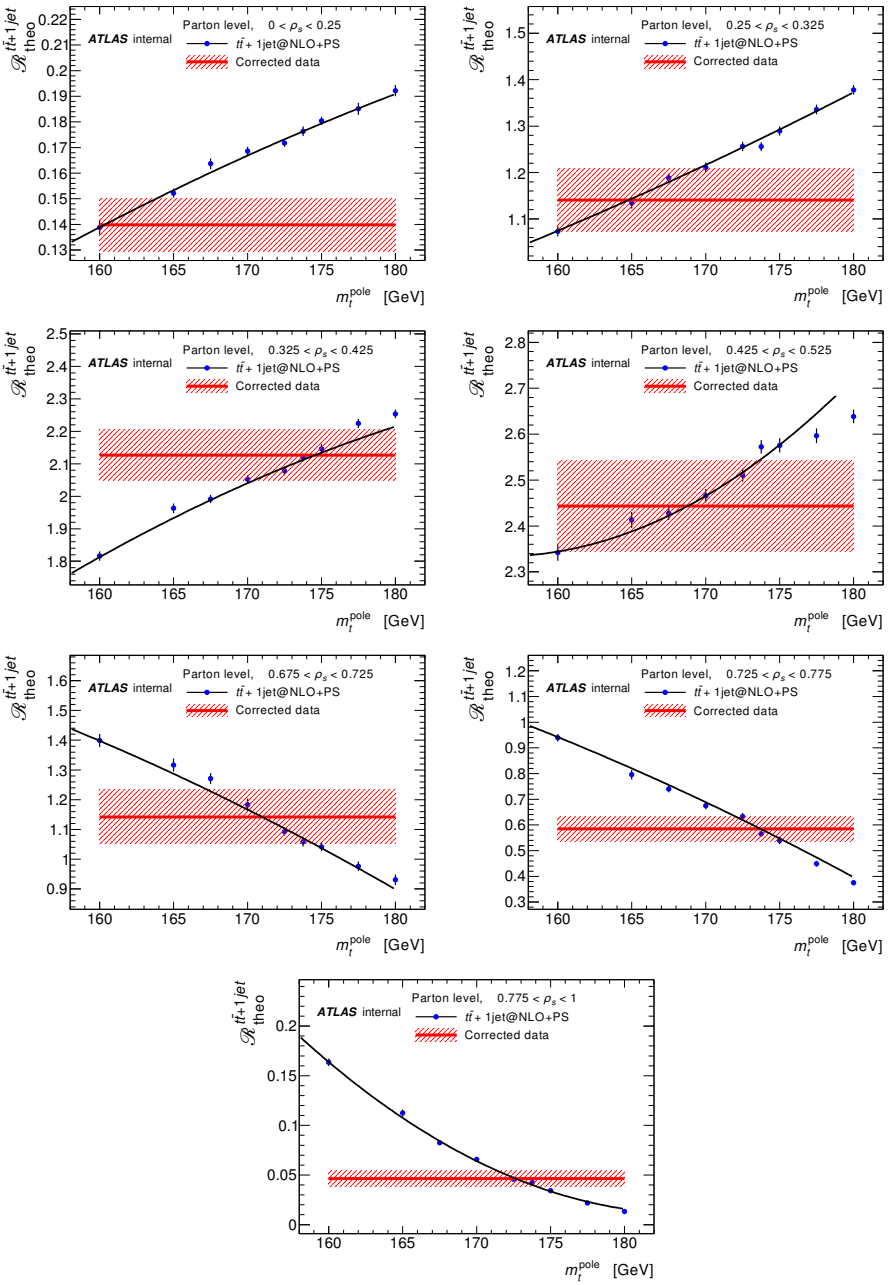

Figure 6.6: Parametrization of the mass dependence of the observable $\mathcal{R}$ with a second order polynomial. Each plot corresponds to one bin of the $\mathcal{R}$ distribution. The bins with $0.525 < \rho_s < 0.675$ are not shown since their sensitivity is very low.

6.4 Pole mass measurement: systematic uncertainties

In this section the uncertainties that affect the measurement of the top-quark pole mass are studied. Statistical uncertainties on the corrected data have been calculated by repeating the unfolding procedure on pseudo-experiments, as already discussed in 6.2.

The uncertainty due to the limited size of the MC sample used in the definition of the unfolding procedure has also been evaluated, by repeating the unfolding procedure varying the unfolding matrix within its errors. A set of 5000 pseudo-matrices were used and the distribution of the results of the unfolding had a gaussian distribution. The width of such gaussian was referred to as error due to the statistic of the MC sample used in the unfolding. It has been taken into account as a systematic uncertainty. The impact on the top-quark mass due to the limited size of the MC sample has been estimated as $\Delta(\text{MC-stat}) = 0.16$ GeV.

The uncertainty sources which remain can be split in four categories: signal modeling uncertainties, detector modeling uncertainties, theoretical uncertainties and method uncertainties. In the next sections it is explained how these uncertainties are evaluated, while in 6.6 their values are reported all together.

For each systematic error, its statistical uncertainty is also reported when possible, as obtained from the mass extraction from alternative MC samples. When multiple components are considered for a systematic source (i.e. jet energy scale), the statistical errors are added in quadrature without taking into account correlations.

In general the evaluation of the systematic errors proceeds as follows. The nominal procedure to extract the top quark mass is applied to the different MC samples which correspond to different predictions for $\mathcal{R}$ depending on the specific effects under study. The difference between the values obtained for the top-quark mass when applying the unfolding procedure to these simulated event samples is quantified and following the ATLAS prescriptions the systematic uncertainty is determined.

6.4.1 Theoretical uncertainties

Theoretical uncertainties mainly come from two sources:

- missing higher orders in the perturbative calculations.
- imperfect knowledge of the proton PDFs and the QCD coupling α_s.

The uncertainty related to uncalculated higher order corrections is evaluated with the conventional procedure of varying factorisation (μ_f) and renormalisation (μ_r) scales around the value chosen. For the $t\bar{t}$ + 1-jet @NLO+PS calculation, the nominal choice has been $\mu_f = \mu_r = m_t^{\text{pole}}$, while the variations taken into account are $\mu_f = \mu_r = 2m_t^{\text{pole}}$ and $\mu_f = \mu_r = \frac{1}{2}m_t^{\text{pole}}$. An example of how the theoretical prediction for $\mathcal{R}$ change with the scale is shown in Figure6.7. The usual procedure is then to fit corrected data with the different theoretical predictions, and take the difference of the result as error. The results one would

obtain with this method are (including only data statistical error):

$$\begin{aligned} &m_t^{\text{pole}}[t\bar{t}+\text{1-jet template}, \mu_r = \mu_f = \mu_0] = 171.05 \pm 0.43 \text{ (stat.) GeV} \\ &m_t^{\text{pole}}[t\bar{t}+\text{1-jet template}, \mu_r = \mu_f = \frac{1}{2}\mu_0] = 171.81 \pm 0.40 \text{ (stat.) GeV} \\ &m_t^{\text{pole}}[t\bar{t}+\text{1-jet template}, \mu_r = \mu_f = 2\mu_0] = 170.82 \pm 0.48 \text{ (stat.) GeV} \end{aligned} \quad (6.6)$$

Using this procedure though, various errors are taken into account simultaneously and it is not easy to isolate scale choice effects. For instance, when using a different set of mass points, it is needed to re-parametrise (i.e obtain parametrisation coefficients) the theoretical dependence on the top-quark pole mass and above mentioned values can vary up to 0.15 GeV. Thus using this method, uncertainties on the parametrisation are entangled with uncertainties due to the scale choice.

In order to reduce such effects, distributions generated with different scales choice have been fit with the nominal theoretical prediction. Three values are then extracted for the mass of each scale variation, $m_t^{\text{pole}}(\mu = \mu_0)$, $m_t^{\text{pole}}(\mu = 2\mu_0)$ and $m_t^{\text{pole}}(\mu = \frac{1}{2}\mu_0)$, where μ_0 is the nominal choice of the factorisation an renormalisation scales. The following quantities are taken as errors:

$$\begin{aligned} \Delta^+(\mu) &= -\min\left(\left[m_t^{\text{pole}}(\mu = 2\mu_0) - m_t^{\text{pole}}(\mu = \mu_0)\right], \left[m_t^{\text{pole}}(\mu = \frac{1}{2}\mu_0) - m_t^{\text{pole}}(\mu = \mu_0)\right]\right) \\ \Delta^-(\mu) &= -\max\left(\left[m_t^{\text{pole}}(\mu = 2\mu_0) - m_t^{\text{pole}}(\mu = \mu_0)\right], \left[m_t^{\text{pole}}(\mu = \frac{1}{2}\mu_0) - m_t^{\text{pole}}(\mu = \mu_0)\right]\right) \end{aligned} \quad (6.7)$$

where the minus sign takes into account that a positive (negative) shift in this error evaluation method, correspond to a negative (positive) shift when corrected data are fit with different theoretical predictions. The final scale error amounts to:

$$\Delta(\mu) = \begin{matrix} +\ 0.62 \\ -\ 0.24 \end{matrix} \text{ GeV} \quad (6.8)$$

To evaluate PDFs and α_s errors on the theoretical prediction, $\mathcal{R}^{t\bar{t}+\text{1-jet}}_{\text{theo@NLO+PS}}$ have been generated with three different set of PDFs and α_s values:

- CT10nlo PDF with $\alpha_s(M_Z) = 0.118$, the nominal choice.
- MSTW2008nlo90cl PDF with $\alpha_s(M_Z) = 0.120$
- NNPDF23 PDF with $\alpha_s(M_Z) = 0.119$

and extracting a mass value for each of them using the nominal theoretical prediction. The shape of these distributions is shown in Figure 6.8. Half of the maximum difference between nominal and the variations is taken as the error of the PDFs and α_s choice:

$$\Delta(\text{PDF}+\alpha_s) = \frac{1}{2}\max\left(\left|m_t^{\text{pole}}(\text{CT10}) - m_t^{\text{pole}}(\text{NNPDF})\right|, \left|m_t^{\text{pole}}(\text{CT10}) - m_t^{\text{pole}}(\text{MSTW})\right|\right) \quad (6.9)$$

which amounts to 0.22 GeV.

The total theoretical uncertainty is the quadratic sum of the scale and PDF$\oplus\alpha_s$ and it amounts to $\Delta(\text{theo}) = \begin{matrix} +0.66 \\ -0.32 \end{matrix}$ GeV .

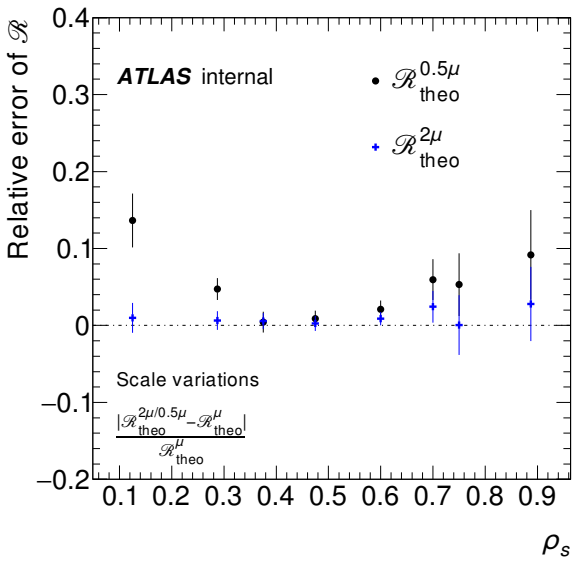

Figure 6.7: Absolute difference between $\mathcal{R}^{t\bar{t}+\text{1-jet}}_{\text{theo@NLO+PS}}$ generated for different choices of the factorisation and renormalisation scales. Samples have been generated with $m_t^{\text{pole}} = 172.5$ GeV.

6.4.2 Detector modelling

In this section, uncertainties on the top-quark pole mass due to reconstruction efficiency and physics objects (lepton, $E_{\text{T}}^{\text{miss}}$ and jets) reconstruction are studied. These kind of systematic variations are implemented in TopRootCore (TopRootCoreRelease-14-00-28), and a set of different $\mathcal{R}^{\text{det}}$ is obtained. Those distributions are then unfolded following the nominal procedure and from the unfolded distributions various top-quark pole mass values are extracted. If detector modelling variations are obtained by changing a parameter with a higher value ("up" variation) and a lower one ("down" variation), the error on the top-quark pole mass is taken as half of the difference between the "up" and "down" results:

$$\Delta(\text{var}^{\text{up}}_{\text{down}}) = \frac{1}{2}\left|m_t^{\text{pole}}(\text{var}^{\text{up}}) - m_t^{\text{pole}}(\text{var}^{\text{down}})\right| \tag{6.10}$$

If instead the detector variation is obtained by changing a parameter in one direction only (alternative, "alt", variation), the quantity

$$\Delta(\text{var}^{\text{alt}}) = \left|m_t^{\text{pole}}(\text{var}^{\text{alt}}) - m_t^{\text{pole}}(\text{var}^{\text{nominam}})\right| \tag{6.11}$$

is used to quantify the uncertainty.

Jet energy and b-jet energy scales: Uncertainties on jet energy determination are taken into account by scaling their energy scale up and down within its uncertainty for a number of uncorrelated components [258–260]. The breakdown of the full JES uncertainty into the different nuisance parameters is presented in Table 6.2. A separate uncertainty is assigned to b-quark jets scale (BJES), which is uncorrelated with the JES. The effect of JES uncertain-

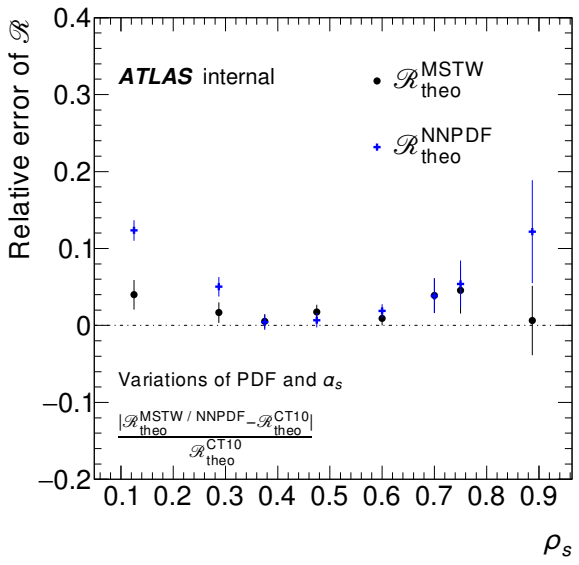

Figure 6.8: Relative difference between $\mathcal{R}^{t\bar{t}\text{+1-jet}}_{\text{theo@NLO+PS}}$ generated for different choices of the the PDFs and $\alpha_s(M_Z)$ value. Samples have been generated with $m_t^{\text{pole}} = 172.5$ GeV.

ties on the unfolded distributions is shown in Figure6.9, where all the different uncertainty components have been added in quadrature.

In [252] JES uncertainty was one of the most important systematics. In this analysis its impact has been strongly reduced: from one side the increased statistics allowed to use a finer binning which increased the sensitivity of $\mathcal{R}$ to the top-quark pole mass; from another side the better knowledge of the detector reduced the error on the jet energy scale by itself.

The error due to JES, including b-jet contribution, is 0.38 GeV.

Jet reconstruction efficiency (JEFF), jet energy resolution (JER) and jet vertex fraction (JVF): Uncertainty on m_t^{pole} due to the jet energy resolution is taken into account by smearing the energy of the jets with a Gaussian with width in agreement with the JER error, for a number of uncorrelated components. Jet reconstruction efficiency is evaluated by discarding a fraction of jets from the events randomly. Variations on the choice of the jet vertx fraction cut is also considered These procedures are performed before event selection, thus they mainly affect the number of events selected, but their impact on the shape of $\mathcal{R}^{\text{det}}$ is small, since it is a normalised quantity. The breakdown of JER uncertainty in its components is shown in Table 6.3, while the impact of JEFF is reported in Table 6.6.

The contribution of the jet reconstruction efficiency error is really small, while the one from JER amounts to 0.18 GeV.

***b*-tagging efficiency:** To estimate the uncertainty coming from b-tagging efficiency and c-jet and light-jet mistag rates, every parameter of the eigenvector method [247, 261, 262] is varied by $\pm 1\sigma$ with respect to its nominal value. Impact of these variations on the top-quark pole mass is presented in Table 6.4.

Parameter name	Δm_t^{pole} [GeV]	stat. error on syst unc. [GeV]
EtaIntercalibrationModel	0.125	0.053
EtaIntercalibrationTotalStat	0.064	0.053
flavor_comp	0.013	0.053
flavor_response	0.027	0.053
JesEffectiveDet1	0.117	0.053
JesEffectiveDet2	0.092	0.053
JesEffectiveDet3	0.003	0.053
JesEffectiveMix1	0.085	0.053
JesEffectiveMix2	0.018	0.053
JesEffectiveMix3	0.018	0.053
JesEffectiveMix4	0.005	0.053
JesEffectiveModel1	0.132	0.053
JesEffectiveModel2	0.004	0.053
JesEffectiveModel3	0.053	0.053
JesEffectiveModel4	0.007	0.053
JesEffectiveStat1	0.103	0.053
JesEffectiveStat2	0.091	0.053
JesEffectiveStat3	0.066	0.053
JesEffectiveStat4	0.029	0.053
jvf	0.037	0.053
Pileup_OffsetMu	0.040	0.053
Pileup_OffsetNPV	0.069	0.053
Pileup_Pt	0.026	0.053
Pileup_Rho	0.073	0.053
PunchThrough	0.002	0.053
SinglePart	0.000	0.053
ALL JES (no bJES)	0.329	-
bJES	0.162	0.053

Table 6.2: Breakdown of the JES systematic uncertainty in its uncorrelated components.

The total uncertainty from b-tagging contribute 0.07 GeV to the total error.

Leptons identification and energy resolution, modelling of $E_{\mathrm{T}}^{\mathrm{miss}}$: Correction factors are applied to take into account efficiency of lepton identification and leptons energy/momentum scale [263, 264]. Uncertainties on such correction factors are propagated to m_t^{pole}. Modelling of $E_{\mathrm{T}}^{\mathrm{miss}}$ [265, 266] is affected by uncertainties on jet and lepton scales, cell out terms and pile-up modelling. The final impact of all lepton and $E_{\mathrm{T}}^{\mathrm{miss}}$ systematic uncertainties on the precision of the top-quark pole mass is limited, as can be seen in Table 6.6. It amounts to 0.05 GeV for the MET modelling and to 0.02 GeV for lepton modelling.

6.4.3 Signal modelling

Several elements enter in the modelling of signal and background events. In particular, uncertainties on $t\bar{t}$ MC are studied, which comes from: choice of hard process MC generators, showering and hadronisation model, PDF choice, modelling of initial and final state radiation, colour reconnection effects, modelling of underlying event. Various $t\bar{t}$ MC samples have been generated in ATLAS, with variations of input parameters which cover uncertainties coming from these effects. To evaluate the impact of these changes on m_t^{pole}, alternative input spectra are unfolded and fit with the nominal procedure, resulting in different values of m_t^{pole}. These last values are then properly compared to extract uncertainty

Parameter name	Δm_t^{pole} [GeV]	stat. error on syst unc. [GeV]
jer_diff	0.000	0.075
jer_noise_forward	-0.006	0.074
jer_np0	0.101	0.052
jer_np1	0.086	0.052
jer_np2	0.033	0.052
jer_np3	0.011	0.052
jer_np4	0.067	0.052
jer_np5	0.045	0.052
jer_np6	0.016	0.052
jer_np7	0.028	0.053
jer_np8	0.018	0.053
ALL JER	0.163	0.189

Table 6.3: Breakdown of the JER systematic uncertainty in its uncorrelated components.

Parameter name	Δm_t^{pole} [GeV]	stat. error on syst unc. [GeV]
btag0	0.003	0.053
btag1	0.032	0.053
btag2	0.005	0.053
btag3	0.026	0.053
btag4	0.042	0.053
btag5	0.012	0.053
btag6	0.001	0.053
btag7	0.000	0.053
btag8	0.001	0.053
btag_highpt_e	0.002	0.053
ALL BTAG	0.0674	0.161

Table 6.4: Breakdown of the b-tagging systematic uncertainty in its components.

from a particular effect, which is reported in Table 6.6.

For the modelling of background (i.e. non $t\bar{t}$ MCs), normalisation variations have been taken into account. Data are then subtracted of the different background variations and corrected to parton level with the nominal procedure. Difference in extracted mass from the nominal value are taken as systematic errors.

Hard process generator: Uncertainty in the choice of the calculation of the matrix element is computed by comparing two different NLO hard process generators, matched with the same parton shower, hadronisation model and tuning. These samples are POWHEG+HERWIG and aMC@NLO +HERWIG . The full difference between the extracted mass is taken as systematic uncertainty, namely:

$$\Delta(\text{hardMC}) = \left| m_t^{\text{pole}}(\text{POWHEG + HERWIG}) - m_t^{\text{pole}}(\text{aMC@NLO + HERWIG}) \right| \tag{6.12}$$

Impact of hard process modelling variation on the unfolded $\mathcal{R}$ distributions is presented in Figure6.10. Its contribution to the total error is 0.24 GeV.

Showering and hadronisation: Hadronisation and parton shower modelling effects are estimated by comparing the same $t\bar{t}$ MC hard generator (POWHEG),

matched to two different programs: Pythia and Herwig. The full difference

$$\Delta(\text{Hadronisation}) = \left| m_t^{\text{pole}}(\text{Powheg + Herwig}) - m_t^{\text{pole}}(\text{Powheg + Pythia}) \right| \tag{6.13}$$

of the two extracted top-quark pole mass is taken as the showering and hadronisation uncertainty. Comparison between the unfolded distributions is shown in 6.11. This error has been found to be one of the main systematic errors, contributing with 0.41 GeV.

Initial and final state radiation: Initial and final state radiation (ISR and FSR) is affected mainly by three variables in $t\bar{t}$ events generated with Powheg and consequently showered by Pythia:

- factorisation and normalisation scales, which set the energy at which parton shower program starts. They are changed by a factor 2 around the nominal value $\mu_0 = 172.5$ GeV.

- the damping parameter *hdamp*, which control the strength of the first radiative emission in Powheg. This parameter is also changed by a factor of 2 around the nominal value $hdamp_0 = 172.5$ GeV. The impact of *hdamp* is very small in the measurement of the top-quark mass using this method. The whole variation between the extreme limits of $hdamp_0 = 172.5$ and $hdamp_0 = \infty$ gives a change on the measured value of the top-quark mass of $\Delta(m_t^{\text{pole}}) = 0.23 \pm 0.07$ GeV. See Appendix I for a more detailed discussion.

- shower scale, which is the scale at which radiation is emitted in Pythia. The strong coupling constant in the radiation from a parton with transverse momentum p_t has nominal value $\alpha_s(p_t)$, and its variations are $\alpha_s(2p_t)$ and $\alpha_s(\frac{1}{2}p_t)$. They are called $radHi$ and $radLo$ variations.

Simultaneous change of these variables are taken into account and two samples build the envelope of all scale variations. They have respectively $[2 \cdot \mu_0, hdamp_0, radLo]$ and $\left[\frac{1}{2} \cdot \mu_0, 2 \cdot hdamp_0, radHi\right]$, their difference with respect to a sample with all nominal values is shown in Figure 6.12. Half of the maximum of the absolute difference in the extracted m_t^{pole} between the variation samples and the nominal one istaken as systematic uncertainty:

$$\Delta(\text{IFSR}) = \frac{1}{2}\max\left(\left| m_t^{\text{pole}}(\text{moreRad}) - m_t^{\text{pole}}(\text{nominal}) \right|, \left| m_t^{\text{pole}}(\text{lessRad}) - m_t^{\text{pole}}(\text{nominal}) \right|\right) \tag{6.14}$$

The ISR and FSR modelling error amounts to 0.22 GeV.

Colour reconnection and underlying event: When hadronisation happens, colour-less hadrons are built from coloured quark particles. How the sum over coloured particles is handled in a hadronisation program can affect how events are reconstructed at particle and detector level. The impact of such an effect is taken into account by comparing two MC samples with different tunes (PerugiaTune2012 and PerugiaTune2012loCR [222]), which handle the strength of the colour reconnections. The same procedure is used to extract the uncertainty from underlying event modelling, where PerugiaTune2012 is compared with PerugiaTune2012mpiHi.

In both cases the full difference in the extracted m_t^{pole} is taken as systematic uncertainty

$$\Delta(\text{CR / UE}) = \left| m_t^{\text{pole}}(\text{Perugia2012}) - m_t^{\text{pole}}(\text{Perugia2012(loCr/mpiHi)}) \right| \tag{6.15}$$

Differences on the unfolded distributions are shown in Figure 6.13. Colour reconnection systematic contributes with 0.42 GeV, while underlying event with 0.31 GeV. It has to be noticed though that the statistical error associated to these values is of ~ 0.2 GeV, due to limited MC statistics. For all the other systematic errors, the associated statistical uncertainty is ~ 0.1 GeV instead.

Proton PDF: Uncertainties on m_t^{pole} coming from proton PDFs are evaluated following the PDF4LHC recommendations [233]. Three PDF sets have been considered: CT10, MSTW2008nlo68cl and NNPDF23. For each of them error sets are given, which build an envelope containing the variations of the PDF due to uncertainties in their parametrisation. To propagate such uncertainties to m_t^{pole}, the nominal POWHEG + PYTHIA $t\bar{t}$ MC sample has been reweighted for all the nominal and error sets. Reweighted distributions are then unfolded and fit with the nominal procedure, and three envelopes are constructed for the top-quark pole mass values, as it is shown in 6.14. The envelopes are constructed following the method with which PDF are constructed (asymmetric Hessian for CT10 and MSTW2008, standard deviation for NNPDF23).

Half of the maximum difference between the envelopes is taken as proton PDF uncertainty on m_t^{pole}, which amounts to 0.18 GeV.

Background modelling: Non $t\bar{t}$ MC samples can also affect the measurement of m_t^{pole}, since expected background is subtracted from data at detector level. Nevertheless, selection of $t\bar{t}+1$-jet topologies is quite pure and uncertainties due to background variations are small.

The theory uncertainty on inclusive V+jets cross section is 4%, on top of this one has to add in quadrature a 24% uncertainty per additional jet. Since five jets are asked in the event selection at detector level, the total normalisation uncertainty to be propagated is 54%.

Single top plus jets background normalisation and its dependence on the MC top-quark mass have also been studied, by varying single-top cross section within its uncertainties and using single-top samples generated with different values of m_t^{MC}.

To study the effect of possible backgrounds not taken into account, m_t^{pole} extracted from data without any background subtraction has been compared with the nominal value, yielding a difference of 0.10 GeV.

6.4.4 Method uncertainties

Additional uncertainties coming from the unfolding algorithm and the parametrisation of the dependence of the theoretical prediction on m_t^{pole} are studied in this section.

Parametrisation of theoretical prediction: Theoretical prediction for $\mathcal{R}^{t\bar{t}+1\text{-jet}}_{\text{theo@NLO+PS}}$ as a continuous function of m_t^{pole} is used in the fit. It is interpolated from $t\bar{t}+1$-jet @NLO+PS MC samples generated for nine different values of m_t^{pole}. These samples have been fit with different choices of parametrisation of the dependence on m_t^{pole}. If the parametrisation would be perfect, extracted

m_t^{pole} would match the value of the mass used as input in the generation of the samples. In practice, non perfect parametrisation results in differences between the input mass and the extracted one, as it shown in Figure 6.15. An envelope is built from a fit to the $y = 0$ curve. It covers all possible misparametrisation-parametrisation effects and has a maximum width of 0.20 GeV. Such uncertainty is added to the total systematic error.

Unfolding matrix regularisation: The unfolding algorithm relies on the choice of a parameter, which works as a regulator in the inversion of the migration matrix. Such a regulator is needed in order to invert a matrix which is not enough populated due to lack of statistic in the MC sample. In the case of the Bayesian unfolding, the parameter is the number of iterations of the method. To evaluate the impact of this choice on the extracted value of the top-quark pole mass, data has been corrected with different values of the regulator. Differences amount to up to ~ 0.20 GeV for changes of ± 5 in the number of iterations. Statistical error on m_t^{pole} also change, up to ~ 0.10 GeV, for the same interval of iterations number, but it is half smaller than the systematic error on the value itself. Hence, an ambiguity of $\lesssim 0.20$ GeV come from the choice of the regularisation parameter of the unfolding. More details are reported in Appendix F. This effect has a statistical origin, since it comes from the limited statistic of the MC sample used in the unfolding process. To avoid double counting of the MC statistical error (which evaluation is explained at the beginning of Section 6.4), it is not added to the total error.

Stability of the acceptance factor on the m_t chosen in the unfolding Monte Carlo: The phase space correction factor $f^{\text{Ph.Sp.}}$ introduced in Section 6.2 introduce an additional systematic error on the measurement. As it is explained in Appendix G, when choosing a less finer binning near $\rho_s \sim 1$ the phase space correction is negligible. Hence half of the maximum difference between results obtained with and without the phase space correction is taken as systematic error. Such an error corresponds to ~ 0.15 GeV. This choice is also justified by the fact that extracted m_t^{pole} differs at maximum by a couple of GeVfrom the value of the top-quark mass chosen as input of the nominal $t\bar{t}$ MC. Since the correction modifies the corrected observable at most a $\sim \frac{1\%}{\text{GeV}}$ in the most sensitive bin, such effects translate on a 0.3 GeV effect on the resulting mass. Half of such quantity can also be taken as an error on the correction, which is again 0.15 GeV.

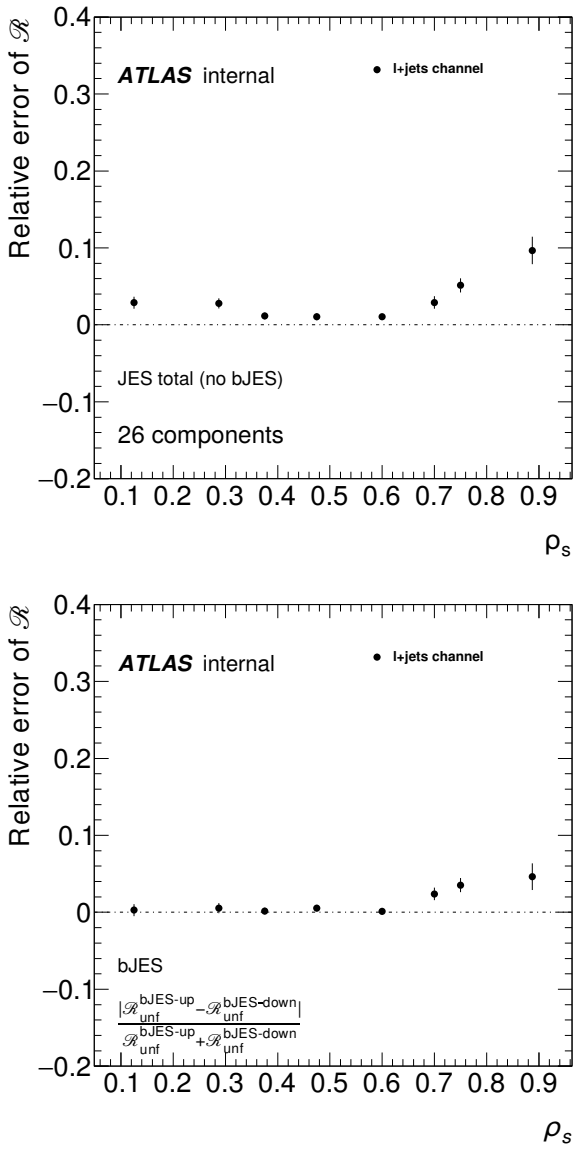

Figure 6.9: Relative difference in the unfolded distributions for JES (26 components added in quadrature) and b-JES systematics.

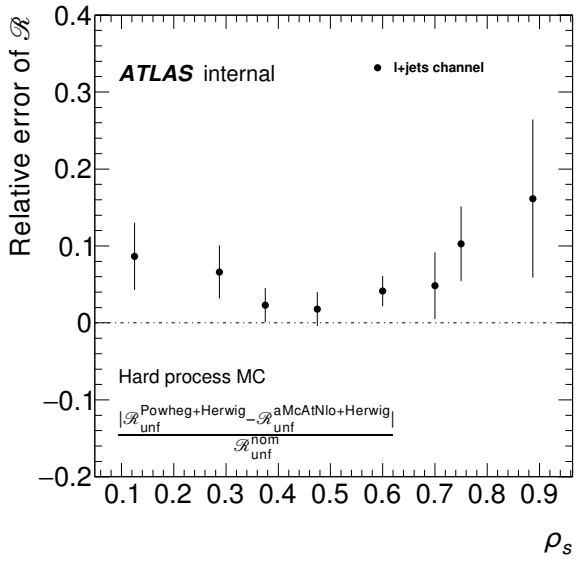

Figure 6.10: Relative difference in the unfolded distributions of POWHEG + HERWIG and aMC@NLO +HERWIG $t\bar{t}$ MC samples.

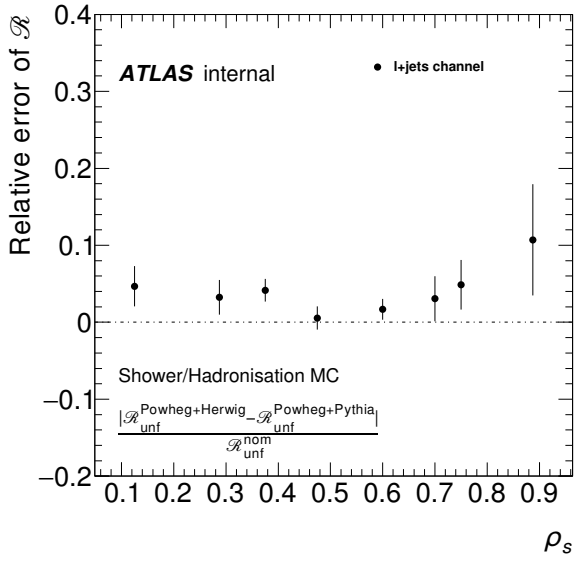

Figure 6.11: Relative difference in the unfolded distributions of POWHEG + HERWIG and POWHEG + PYTHIA $t\bar{t}$ MC samples.

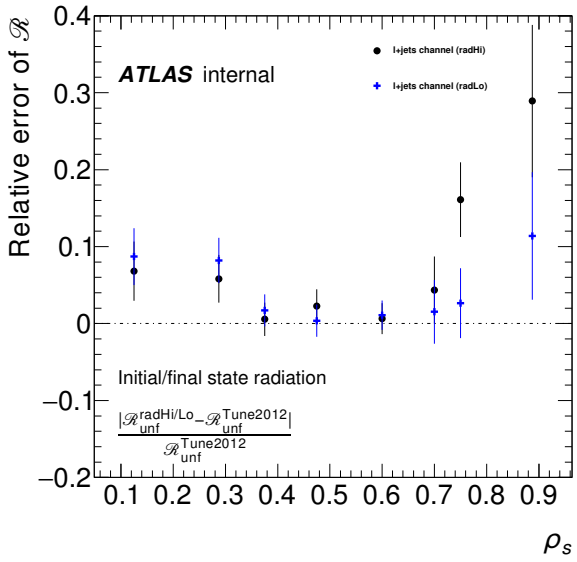

Figure 6.12: Relative difference in the unfolded distributions of POWHEG + HERWIG and POWHEG + PYTHIA $t\bar{t}$ MC samples.

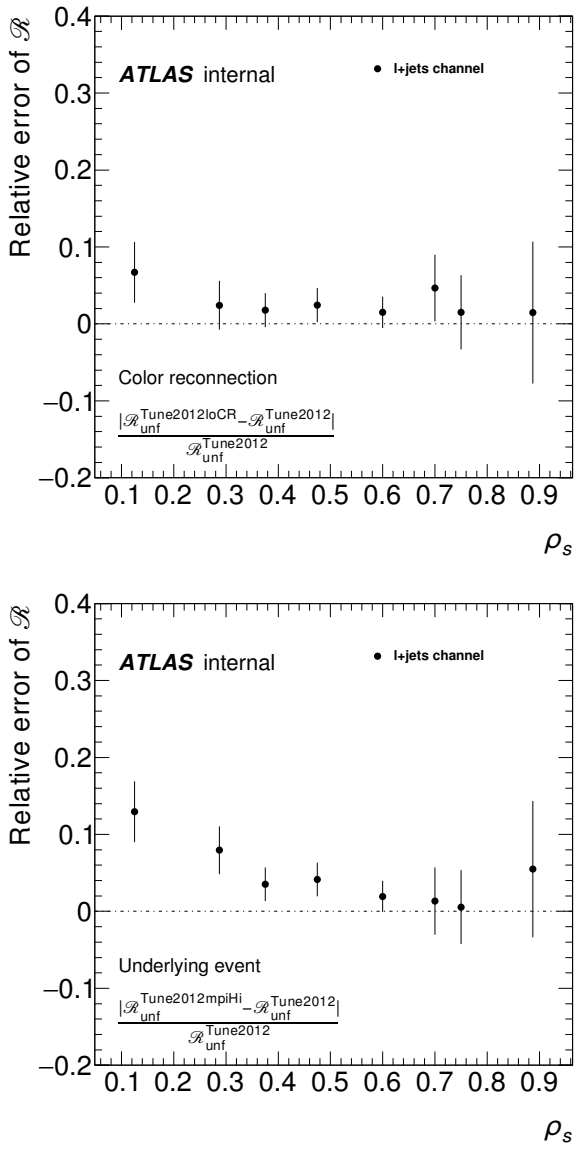

Figure 6.13: Relative difference in the unfolded distributions of POWHEG + PYTHIA $t\bar{t}$ MC samples with Perugia2012loCr and Perugia2012mpiHi tunes, compared to Perugia2012 tune.

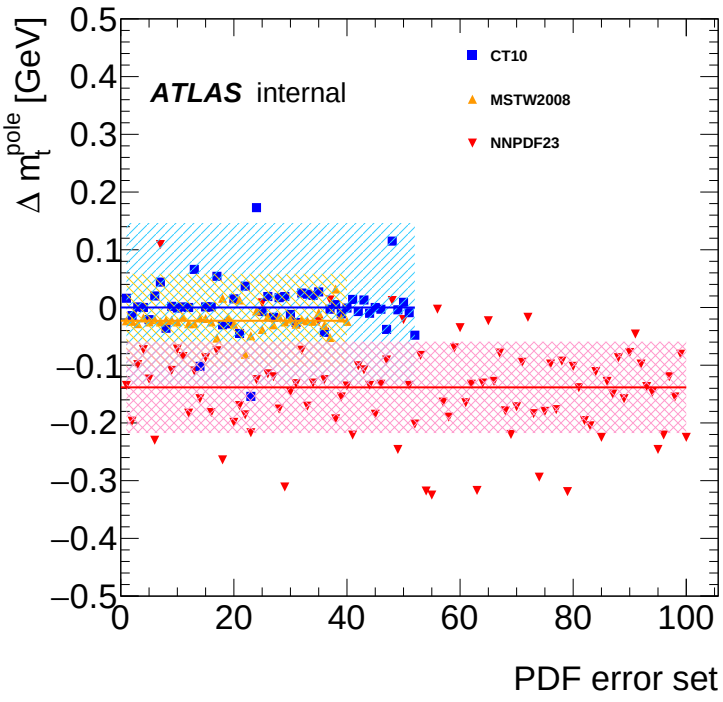

Figure 6.14: Changes in m_t^{pole} due to different choice of PDF set. The CT10 (blue), MSTW2008 (yellow) and NNPDF23 (red) PDF nominal and error sets are shown. Points represent shifts of m_t^{pole} respect to the nominal value for one particular PDF set. Filled areas represent the three envelopes.

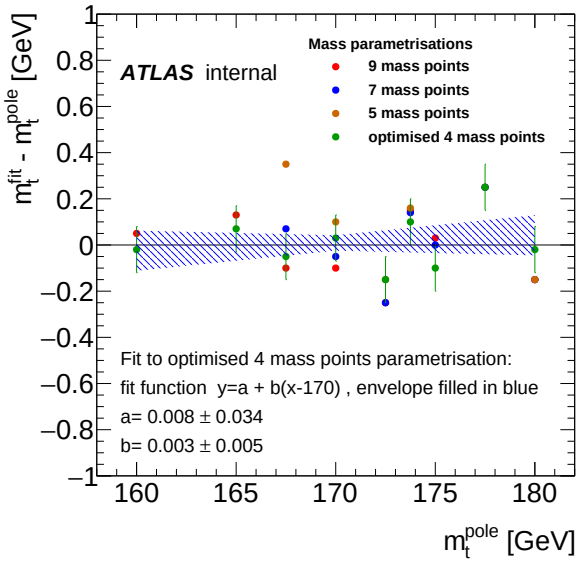

Figure 6.15: Differences between the value of the top-quark used as input of the MC $t\bar{t}$ + 1-jet @NLO+PS calculations and the extracted value ones. Each mass point generated (mass values between 160 GeVand 180 GeV) has been fit. A first order polynomial has been used to extract the different continuos parametrisations. Red dots correspond to a continuos parametrisation extracted from a linear fit to 9 mass points, blue points to a linear fit using 7 mass points and brown dots to a linear fit using 5 mass points. The green dots represents the nominal choice of using the four mass point which have $\mathcal{R}$ values the closest to the data $\mathcal{R}$ value.

6.5 An alternative evaluation of systematic effects

In the previous Section 6.4 the systematic errors of the analysis are calculated. The strategy developed so far has been to use the nominal procedure to extract the top quark mass from the different MC samples as it is done for data. These simulated events correspond to different predictions for $\mathcal{R}$ depending on the specific effects under study. The difference between the values obtained for the top-quark mass when applying the unfolding procedure to these simulated event samples is quantified and following the ATLAS prescriptions the systematic uncertainty is determined. Another approach however can also be considered in which the different MC samples are used to re-calculate the unfolding matrices. The data are then corrected with the new unfolding matrices giving different values of the measured top-quark mass which are then used to evaluate the corresponding systematic uncertainties in a similar way as the nominal method.

In this section the second approach mentioned is employed and compared to the nominal approach. Only two examples have been chosen for this study to illustrate possible differences between both methods: *the jet energy reconstruction (detector effects)* and *the hadronisation model (signal modelling)*. The results of this comparison are shown in Table 6.5. The statistical precision on the calculation of the associated errors is also indicated. Both methods give compatible results within their statistical accuracy though the nominal approach shows a slightly better precision.

Systematic	$\lvert\Delta m_t^{\text{pole}}\rvert \pm$ (stat.unc) (GeV) nominal method	$\lvert\Delta m_t^{\text{pole}}\rvert \pm$ (stat.unc) (GeV) alternative method
JesEffectiveModel1	0.13 ($\pm$ 0.07)	0.08 ($\pm$ 0.15)
JesEffectiveMix1	0.09 ($\pm$ 0.07)	0.07 ($\pm$ 0.15)
JesEffectiveStat1	0.10 ($\pm$ 0.07	0.09 ($\pm$ 0.15)
JesEffectiveDet1	0.12 ($\pm$ 0.07)	0.15 ($\pm$ 0.15)
PYTHIA 6 vs HERWIG	0.41 ($\pm$ 0.13)	0.52 ($\pm$ 0.20)

Table 6.5: Main jet modelling systematics evaluated with the method explained in Section 6.4 compared to the alternative method described in Section 6.5. Statistical errors are indicated in parenthesis.

Adding the errors of Table 6.5 (excluding double-counting of statistical errors from correlated samples) in quadrature one gets:

$$\begin{aligned} \Delta m_t^{\text{pole}}| \text{ (nom. method)} &= 0.46\pm \sim 0.14(\text{ MC stat. }) \text{ GeV} \\ \Delta m_t^{\text{pole}}| \text{ (alt. method)} &= 0.58\pm \sim 0.25(\text{ MC stat. }) \text{ GeV} \end{aligned} \tag{6.16}$$

which confirms that the two methods give compatible results but the alternative method seems to be more sensitive to statistical fluctuations for the same sample of simulated MC events.

6.6 Pole mass measurement: Result

The observable, as obtained from data corrected for detector and hadronisation effects, is presented in Figure 6.3. The top-quark pole mass is extracted from

a fit to a theoretical prediction of the $\mathcal{R}$ distribution at NLO+PS level, as explained in Section 6.3. Uncertainties on the measurement are described in detail in Section 6.4 and are summarized in Table 6.6.

The result obtained for the top-quark pole mass is:

$$m_t^{\text{pole}} = 171.05 \pm 0.43(\text{stat}) \pm 0.92(\text{syst}) \; {}^{+0.66}_{-0.32} \; (\text{theo}) \;\; \text{GeV} \qquad (6.17)$$

The first uncertainty is statistical, due to the limited size of the collected sample. Systematic uncertainties in modelling the detector response for signal and background processes are included in the second uncertainty, which also includes the statistical uncertainty due the finite size of the Monte Carlo sample used in the unfolding procedure. The third uncertainty includes the impact of missing higher orders in the NLO calculation, evaluated by varying the factorization and renormalization scales by a factor 2 and $\frac{1}{2}$ around the central value. It also includes the uncertainty of the PDFs and in the value of the strong coupling constant.

A summary of the individual systematic errors affecting the measurement is reported in Table 6.6.

Description	Value [GeV]	stat. unc on syst [GeV]
m_t^{pole}	**171.05**	
Statistical uncertainty	**0.43**	
MC statistics	0.16	0.05
Signal MC generator	0.24	0.14
Shower and hadronization	0.41	0.11
Proton PDF	0.18	-
ISR/FSR	0.22	0.11
Color reconnection	0.42	0.22
Underlying event	0.31	0.2
b-tagging eff and mistag	0.067	0.16 (12comp)
jet reco efficiency	0.003	0.075
JES (with b-JES)	0.38	0.27 (26comp)
JER	0.18	0.19 (11comp)
MET	0.052	0.074
lepton	0.017	0.18
background	0.039	0
Unfolding modelling	0.15	–
Total exp. systematics	**0.92**	0.43
Scale variations	$(+0.62, -0.24)$	0.13
Theory PDF$\oplus\alpha_s$	0.22	0.054
Total theory systematics	**(+ 0.66, - 0.32)**	-
Total uncertainty	**(+ 1.21, -1.07)**	-

Table 6.6: Summary table of the uncertainties on the measurement of m_t^{pole}.

6.6.1 Crosschecks summary

As referred in previous sections several tests were performed in order to check the stability of the values obtained for the top-quark mass value. They are summarized following:

- *selection criteria:* the specific cuts to define the $t\bar{t}$ + 1-jet system and the required minimum p_T^{extrajet} of the extra jet which are considered in Appendix A and Appendix B, respectively,

- *binning choice:* the binning choice of the observable $\mathcal{R}$ which is studied in Appendix D,
- *fit procedure:* the unfolding method, its regularization parameter, the pull-test distributions, stress tests of the unfolding, and the bin removal as presented in Appendices F, H and J.
- *alternative evaluation of systematic uncertainties:* a different approach to calculate the systematic uncertainties as discussed in Section 6.5.

The results of all the above studies indicate that:

1. the method applied in this analysis is free from biasses,
2. the measured value of the top-quark mass is stable within present accuracy,
3. the correction of the data to parton level is independent of the top-quark mass value used in the MC event generator.

6.7 Top-quark running mass measurement

Recently, the $\mathcal{R}$ observable for $t\bar{t}+1$-jet production was computed in the modified minimal subtraction ($\overline{\text{MS}}$) scheme [99]. This calculation is used to extract the running mass $m_t(m_t)$ from the same corrected parton level data.

The theoretical prediction for the $\mathcal{R}$ observable, as a function of the top-quark running mass is presented in Figure 6.16. Nine mass points were generated, corresponding to:

- $\frac{m_t(m_t)}{\text{GeV}} = \{\ 152.5;\ 155;\ 157.5;\ 160;\ 165;\ 167.5;\ 170;\ 172.5;\ 175\ \}$.

The top-quark running mass is extracted following the procedure described in Section 6.3. Systematic uncertainties, evaluated exactly in the same way as in Section 6.4, are presented in Table 6.7.

A value of $m_t(m_t)$ of:

$$m_t(m_t)(8\text{ bins}) = 162.89\ \pm 0.45\ (\text{stat.})\ \pm 0.98\ (\text{syst.})\ ^{+2.08}_{-1.23}\ (\text{theo})\ \text{GeV} \quad (6.18)$$

is found with a total error of $^{+2.34}_{-1.63}$ GeV

The main error comes from the theoretical uncertainty which is larger than the corresponding one for m_t^{pole}. The theoretical uncertainty of the $\overline{\text{MS}}$ scheme gets worse when approaching the threshold production of the $t\bar{t}+1$-jet system which on the other hand is the region with the higher sensitivity to the top-quark mass. This effect has also been observed and discussed in Ref. [99]. This behavior is inverted when higher energetic bins of $\mathcal{R}$ are considered but then either statistics or/and mass sensitive get smaller.

To validate such result, the measurement of $m_t(m_t)$ is also performed using 6 bins as in Refs. [99] and [252]. With a coarser binning near the threshold region, theoretical uncertainties are reduced as the weight of events close to the threshold region is smaller. Unfortunately when doing so the sensitivity of $\mathcal{R}$ to $m_t(m_t)$ is also reduced. In fact, while theoretical uncertainties get halved, the experimental ones almost double. This is reported in Table 6.7 and should be expected from previous arguments.

Description	Value [GeV]	Description	Value [GeV]
$m_t(m_t)$	**163.13**	$m_t(m_t)$	**162.89**
Statistical	**0.82**	**Statistical**	**0.45**
MC statistics	0.21	MC statistics	0.21
Signal MC generator	0.41	Signal MC generator	0.37
Shower/hadronization	0.55	Shower/hadronization	0.55
Proton PDF	0.61	Proton PDF	0.23
ISR/FSR	0.62	ISR/FSR	0.18
Color reconnection	0.31	Color reconnection	0.41
Underlying event	0.14	Underlying event	0.22
b-tagging eff/mistag	0.19	b-tagging eff/mistag	0.09
jet reco efficiency	0.02	jet reco efficiency	0.003
JES (with b-JES)	0.71	JES (with b-JES)	0.37
JER	0.11	JER	0.17
MET	0.04	MET	0.056
lepton	0.12	lepton	0.027
background	0.14	background	0.041
Phase space modelling	0.05	Phase space modelling	0.14
Total experimental	**1.41**	**Total experimental**	**0.98**
Scale uncertainty	$(+1.6, -0.8)$	Scale uncertainty	$(+2.05, -1.18)$
Theory PDF	0.25	Theory PDF	0.35
Total theoretical	**(+1.62,-0.84)**	**Total theoretical**	**(+2.08,-1.23)**
Total uncertainty	**(+ 2.29,-1.83)**	**Total uncertainty**	**(+2.34,-1.63)**

Table 6.7: Value of $m_t(m_t)$ and of its uncertainties. Fit performed for 6 (left) and 8 (right) bins, using the NLO theoretical prediction from [99].

For 6 bins the value obtained is:

$$m_t(m_t)(6 \text{ bins}) = 163.13 \ \pm 0.82 \text{ (stat.)} \ \pm 1.41 \text{ (syst.)} \ ^{+1.62}_{-0.84} \text{ (theo) GeV} \quad (6.19)$$

resulting in a total error of $^{+2.29}_{-1.83}$ GeV. More details on the binning choice are given in Appendix D

The $m_t(m_t)$ measurement for the 6 bins and 8 bins choices are well compatible between each other and they have a similar total error. The result using 8 bins is chosen as it better expresses the main observations found: similar statistical and experimental precision for both mass-scheme definitions but different theoretical behavior close to threshold.

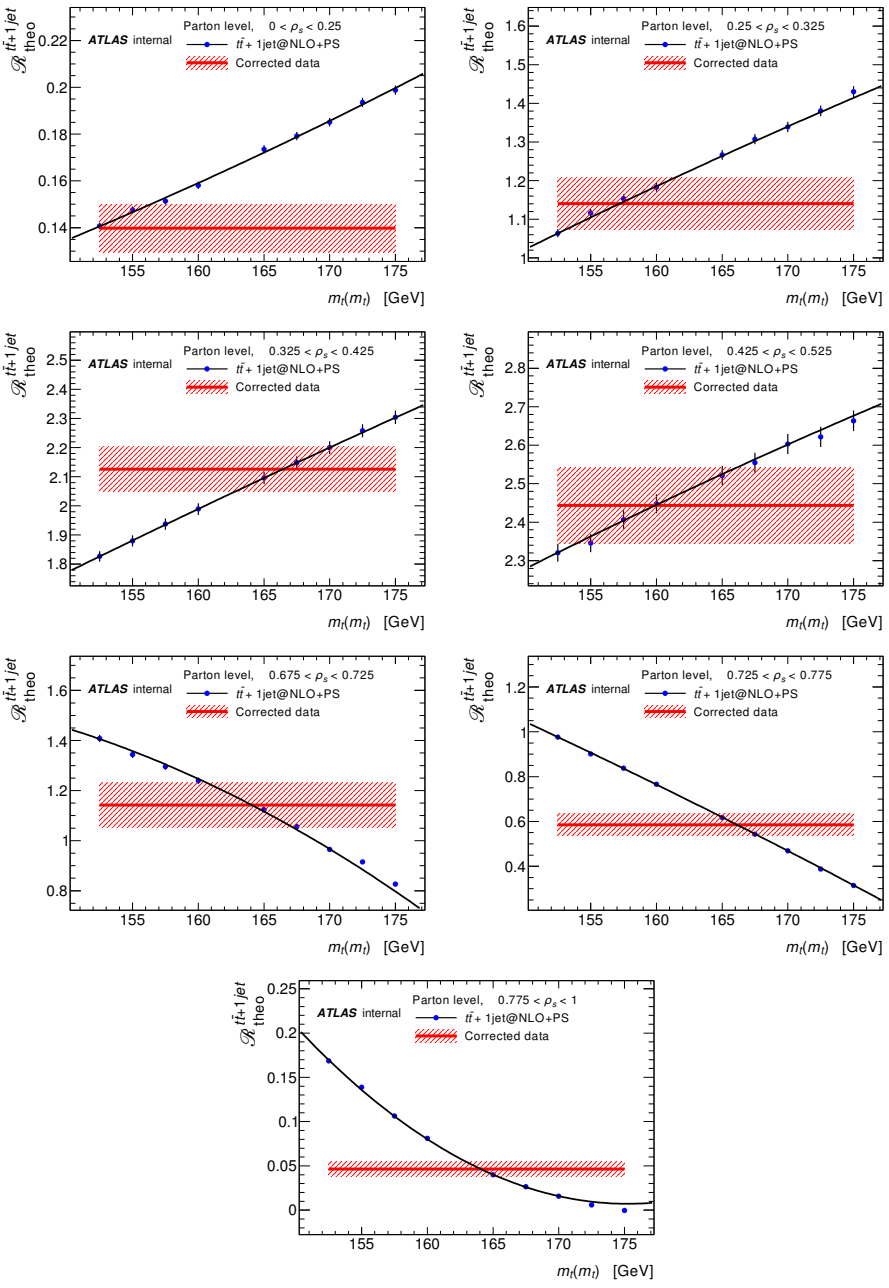

Figure 6.16: Parametrization of the mass dependence of the observable, using a second order polynomial, for different bins, as a function of $m_t(m_t)$. Bins with $0.525 < \rho_s < 0.675$ are not shown since their sensitivity is very low.

6.8 Compatibility between the pole and running mass schemes

The values measured using the pole ($m_t(m_t)$) and the running ($m_t(m_t)$) mass schemes can be compared given the known relation between the top-quark mass parameter in the two renormalization schemes. This relation is known up to four loop [267]. At NLO in QCD[5] as it has been used in [99], such relation reads:

$$m_t^{\text{pole}} = m_t(m_t)\left(1 + \frac{4}{3}\frac{\alpha_s(\mu)}{\pi}\right) + \mathcal{O}(\alpha_s^2) \tag{6.20}$$

which for $\alpha_s(165\ \text{GeV}) \sim 0.116$, the value of $m_t(m_t) = 162.89$ GeV gets $m_t^{\text{pole}} \sim 170.91$ GeV to be compared with that obtained in Eq. 6.17. The translation procedure is sketched in Figure 6.17.

Both measured mass values are thus found to be compatible with each other when using the conversion equation at NLO

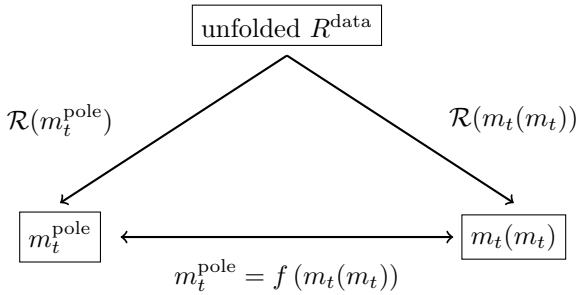

Figure 6.17: Scheme explaining how to extract m_t^{pole} and $m_t(m_t)$ from an unfolded distribution and how to convert m_t from one renormalisation scheme into another.

[5]The conversion between the pole and running mass is made at NLO for coherence with the calculation of $\mathcal{R}$ which is also made at NLO.

Chapter 7

Top-quark pole mass measurement at detector and particle levels

In this chapter the measurement is repeated at detector and at particle level. The detector level analysis is aiming to show the robustness and consistency of the parton level top-quark mass measurement by comparing both results. At particle level, data are only corrected by detector effects and the results are presented in terms of the $\mathcal{R}$ observable. The top-quark pole mass is not extracted at particle level, since there is conceptually no difference to the detector level measurement, but it is technically much more involved as it requires folding and unfolding processes. On the other hand at this level producing the experimental $\mathcal{R}$ can be useful to compare with future theoretical predictions which could reproduce the observable defined at this level.

The procedure to fit the top-quark mass at detector level and the corresponding result obtained are introduced in Section 7.1. The unfolding procedure to particle level and the detector-corrected $\mathcal{R}$ are presented in Section 7.2.

In this section the analysis is repeated at detector and at particle level. The detector level analysis is aiming to show the robustness and consistency of the parton level measurement by comparing both results. At particle level, data are only corrected by detector effects and the results are presented in terms of the $\mathcal{R}$ observable. The top-quark pole mass is not extracted at particle level, since there is conceptually no difference to the detector level measurement, but it is technically much more involved as it requires folding and unfolding processes. On the other hand at this level producing the experimental $\mathcal{R}$ can be useful to compare with future theoretical predictions which could reproduce the observable defined at this level.

7.1 Detector level

In order to check that whole analysis is consistent the nominal value and the statistical uncertainty of the m_t^{pole} mass measurement is evaluated at both parton and detector level. In this way a closure test is performed giving consistency

to the measurement by checking that an equivalent result is obtained either by folding the theoretical predictions or by unfolding the data. In fact at detector level data can be compared directly to fixed order calculations, when properly folded to account for top-quark decay, parton shower, hadronization and detector effects.

This can be done by performing the inverse procedure of the unfolding procedure described in Section 6.2, which is described below.

The first step of the folding procedure is to correct parton level predictions for the fraction of parton level events that fail to pass the selection at detector level. Following the scheme of Section 6.2 the predicted NLO+PS distribtuion is also corrected to the 1^{st} emission level. Such corrections are include in a bin-by-bin factor, called $f_1^{\text{FOLD-DET}}$.

As a second step, the $\mathcal{R}$ distribution is folded to the detector level including the shower, hadronization and detector effects by multiplying by a matrix $\mathcal{M}^{\text{FOLD-DET}}$ constructed with $t\bar{t}$ events that pass both parton level and detector level cuts.

Finally one has to take into account the acceptance at detector level. This last correction is again implemented in a bin-by-bin correction ($f_2^{\text{FOLD-DET}}$).

It has to be noticed that the so defined correction factors are related to the bin-by-bin factors defined in Section 6.2, but they are not exactly the same. The difference comes from the fact the starting point is different. While in the unfolding procedure one starts from reconstructed events which pass detector level selection, in the folding one has to start from parton level events which pass their parton level selection.

In one equation, the folding procedure can be written as:

$$\mathcal{R}^{t\bar{t}\text{+1-jet}}_{\text{theo@detector}} = \left[\mathcal{M}^{\text{FOLD-DET}} \otimes \left(f_1^{\text{FOLD-DET}} \cdot \mathcal{R}^{t\bar{t}\text{+1-jet}}_{\text{theo@NLO+PS}}\right)\right] \cdot f_2^{\text{FOLD-DET}} \tag{7.1}$$

The migration matrix, together with the acceptance factors, is presented in Figure 7.1. Both factors and migration matrix are constructed with the nominal $t\bar{t}$ MC sample. The folding performed on the theoretical prediction is simply the inverse of the nominal unfolding procedure used to extract the value of m_t^{pole} at parton level. In the following, to make the discussion clearer, the folding matrix M^{fold} is defined as:

$$M_{ij}^{\text{fold}} = f_2^{\text{FOLD-DET}}{}_i \cdot \mathcal{M}^{\text{FOLD-DET}}{}_{ij} \cdot f_1^{\text{FOLD-DET}}{}_j \tag{7.2}$$

representing the migration matrix with acceptance factors included, where the bin indices i, j have been explicitly written out.

Once the theoretical prediction is folded, the top-quark mass is extracted by minimizing the χ^2 function:

$$\chi^2 = \sum_{i \in \text{bins}} \frac{\left(\left[\mathcal{R}^{\text{det}}\right]_i - \left[\mathcal{R}^{t\bar{t}\text{+1-jet}}_{\text{theo@detector}}(m_t^{\text{pole}})\right]_i\right)^2}{\text{Var}\left(\left[\mathcal{R}^{t\bar{t}\text{+1-jet}}_{\text{theo@detector}}\right]_i\right)}, \tag{7.3}$$

where $\mathcal{R}^{\text{det}}$ is the observable at detector level and $\text{Var}\left(\left[\mathcal{R}^{t\bar{t}\text{+1-jet}}_{\text{theo@detector}}\right]_i\right)$ the variance of the theoretical prediction in bin i. No covariance matrix is needed in this fit since no correction for detector effects nor hadronization ones is applied to

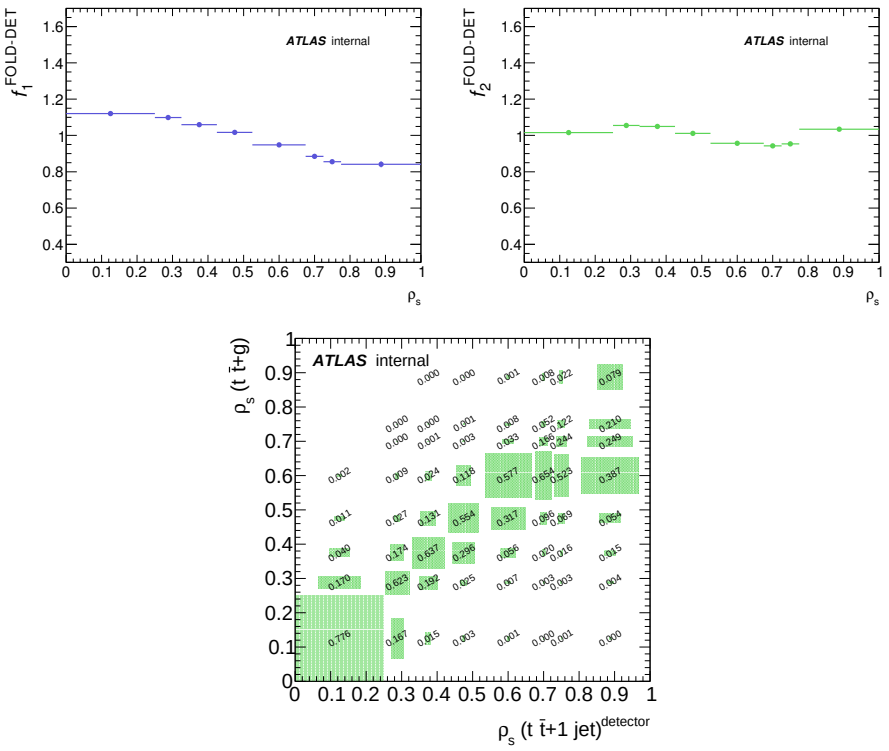

Figure 7.1: Acceptance factors and migration matrix used in folding the theoretical prediction to detector level. The matrix is normalised by column, each bin value represents the fraction of events of the parton level distribution which contribute to the detector level bin.

data. As usual, the statistical uncertainty on the measurement is then obtained by varying $\Delta\chi^2 = \pm 1$ around its minimum value.

The most important issue is the evaluation of $\text{Var}\left(\left[\mathcal{R}^{t\bar{t}+1\text{-jet}}_{\text{theo@detector}}\right]_i\right)$. In the present work two different hypotheses have been studied.

The first possibility considered has been to assume that in each bin i, the theoretical prediction $\left[\mathcal{R}^{t\bar{t}+1\text{-jet}}_{\text{theo@detector}}\right]_i$ follows a Poissonian distribution and each bin is independent of each other. This means that no correlations are assumed between the bins with no assumptions on the underlying model used to populate them. This model includes the theoretical and experimental/detector inputs. In this case one obtains:

$$\text{Var}\left(\left[\mathcal{R}^{t\bar{t}+1\text{-jet}}_{\text{theo@detector}}\right]_i\right) = \left[\mathcal{R}^{t\bar{t}+1\text{-jet}}_{\text{theo@detector}}\right]_i \tag{7.4}$$

This assumption is rather naive and ignores the fact that the detector level expectations are obtained from folding of parton level ones and further detector effects.

The second possible hypothesis is to notice that from the result of Eq. 7.1, the expected values of $\mathcal{R}^{t\bar{t}+1\text{-jet}}_{\text{theo@detector}}$ in each bin are correlated between them, the correlation given by the folding matrix which transforms the $\mathcal{R}$ observable

from parton level to detector level. This second method is already expected to agree with the unfolding method which in fact considers the knowledge of all these effects. In this case, the result for the variance of the detector level expectation becomes:

$$\mathrm{Var}\left(\left[\mathcal{R}^{t\bar{t}\text{+1-jet}}_{\text{theo@detector}}\right]_i\right) = \sum_j M^{\text{fold}}_{ij}\left[M^{\text{fold}}_{ij} + M^{\text{fold}}_{ik_0}\right]\mathrm{Var}\left(\left[\mathcal{R}^{t\bar{t}\text{+1-jet}}_{\text{theo@NLO+PS}}\right]_j\right) \tag{7.5}$$

This expression also takes into account that, since parton level distributions are normalised, one bin (k_0) can be written in terms of the others. The detailed calculation is available in Appendix K, where it is also shown that the result is independent on the choice of k_0. In Appendix K the full discussion and comparison of both methods is presented.

When neglecting bin correlations, in Eq.7.4 and therefore no knowledge of the theory or experimental effects is used in the fit, the result obtained is:

$$m_t^{\text{pole}}(\text{detector level}) = 170.91 \pm 0.71(\text{stat.}) \quad \text{GeV} \tag{7.6}$$

When the bin mixing information is instead contained in the definition of 7.5 the fit gives:

$$m_t^{\text{pole}}(\text{detector level}) = 170.84 \pm 0.48(\text{stat.}) \quad \text{GeV} \tag{7.7}$$

By comparing the values and associated errors of Eqs. 7.6 and 7.7 one finds that:

- both mass values are compatible,
- the errors are different being the one obtained without considering correlation significantly larger,
- the mass value and its error obtained considering bin correlations are compatible with the result obtained at parton level of Eq. 6.17:

As an additional cross-check, the central value of the top-quark mass is extracted using ATLAS $t\bar{t}$ MC samples. It also gives a compatible result.

Next step is to infer which of the two methods gives the correct estimation of the error. For that a set of pseudo distributions was produced starting from a well defined top-quark mass and later the two methods were exercised to recover the original value. In addition the pulls of the distributions were also evaluated. A Gaussian distribution of mass values was generated with a central value $m_0 = 171$ GeV and $\sigma = 1$ GeV. For each mass value the corresponding distributions were folded to detector level, and then the top mass was extracted using each of the two methods each with its variance definition 7.4 and 7.5.

In this exercise the correct method is expect to give fitted masses values, m_i, which have a gaussian shape, centered in $< m_i >= m_0$ and with a standard deviation $\sigma(m_i) = 1$ GeV. If errors are correctly evaluated, the distributions of the errors δ_i on the fitted mass values should have average value $< \delta_i > \sim$ 1 GeV. This facts can also be studied together in a pull distribution, defined as $P_i = (m_i - m_0)/\delta_i$. The fit definition giving the correct error estimate would then be the one which has a pull distribtuion with $< P_i >= 0$ and $\sigma < P_i >= 1$.

The outcome of this study using both methods is shown in Figure 7.3. Both fit methods give the correct shape of the fitted mass distributions and the average mass values agree. However when including bin correlations the expected error distribution is obtained while when ignoring them the errors are overestimated by a factor ~ 2. This result is confirmed by the pull distribution for the variances. More details can be found in Appendix K.

Summarising, at parton and detector level compatible results are obtained when the same amount of knowledge is used. It has to be noticed, in addition, that since the top-quark mass is not an observable its measurement always needs an underlying theory model even when ignoring detector effects.

A further test can also be performed at detector level which is to extract the value of top quark pole mass for each individual bin of ρ_s. This is a non-trivial check of the consistency of the theoretical model and its description of the data for different values of the invariant mass of the $t\bar{t}+1$-jet system. The result of a bin-by-bin fit is shown in Figure 7.4. It should be noticed that the two bins corresponding to high invariant masses show a small difference between the data and the prediction. Such difference is not significant given the errors on the measurement, but it can be interesting to check if it gets confirmed in future analyses.

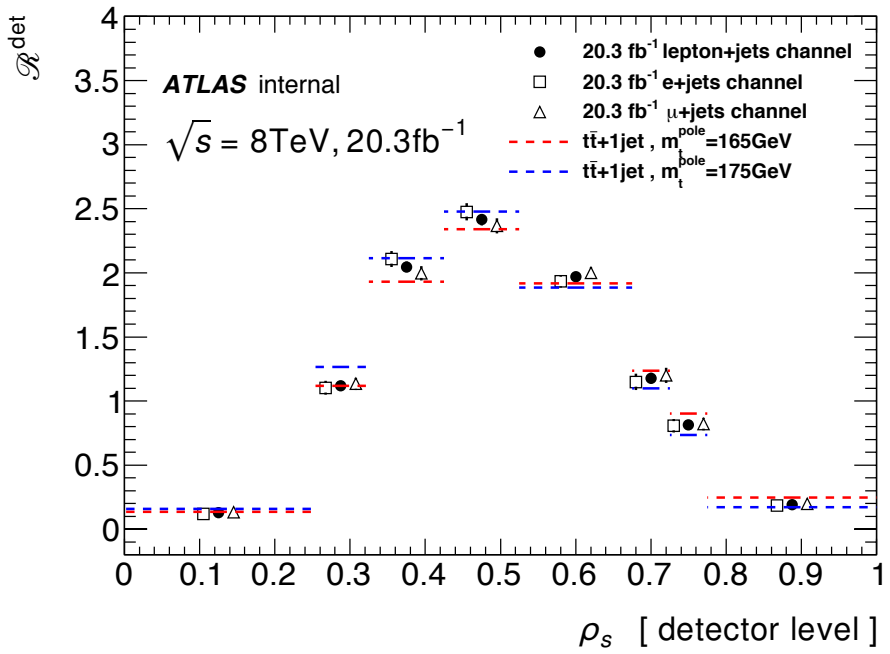

Figure 7.2: The differential normalized ρ_s distribution in the selected $t\bar{t}$ + 1-jet events at detector level after background subtraction. The data points are shown for the electron+jets and muon+jets channels separately and for the combination of both channels. The result is compared to the $t\bar{t}$ + 1-jet theoretical prediction at NLO ($m_t^{\text{pole}} = 165$ GeV in red, $m_t^{\text{pole}} = 175$ GeV in blue) folded to the detector level. The folding procedure is explained in Section 7.1.

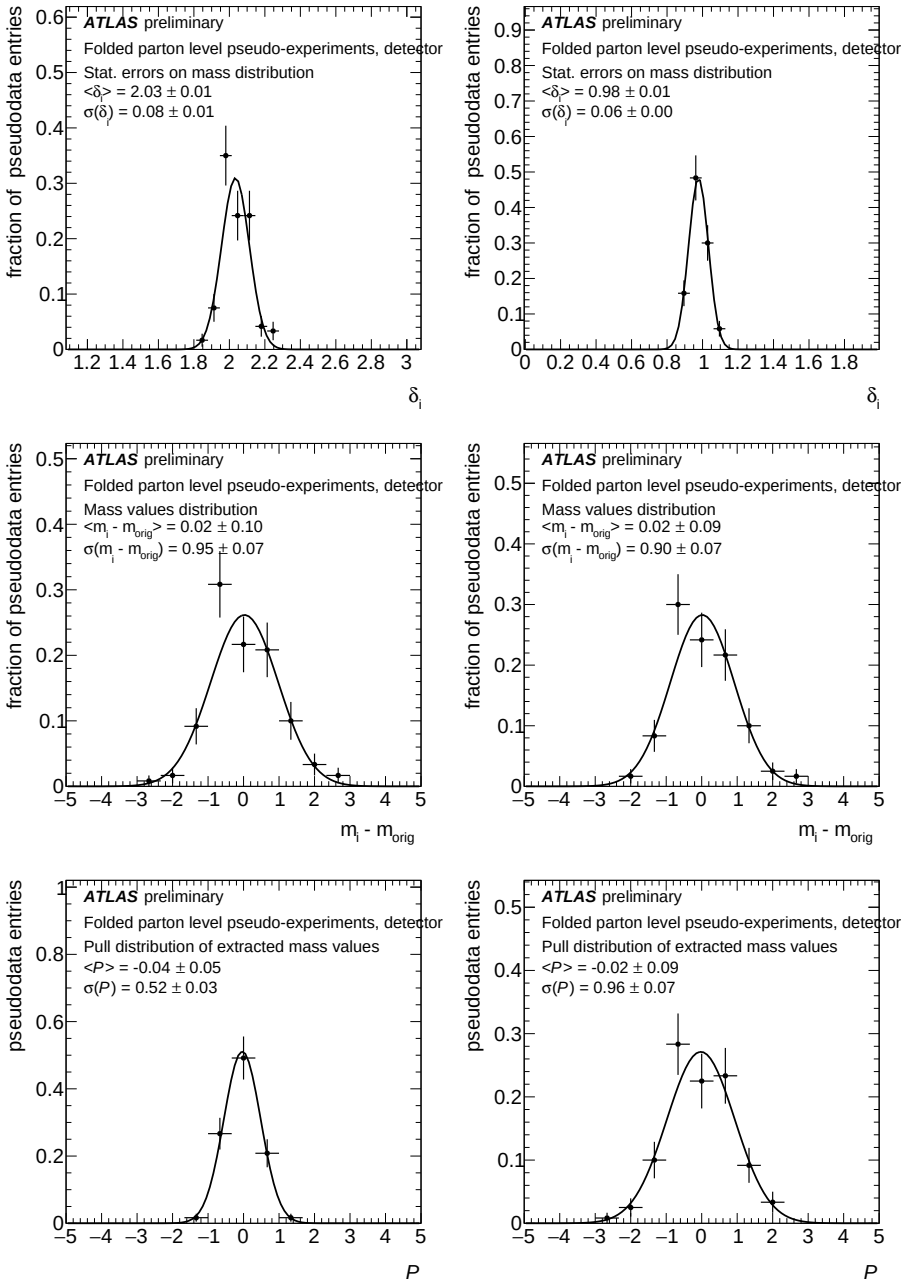

Figure 7.3: Distribution of fitted masses, their errors and pull distributions for detector level fit ignoring bin correlations (left) and including bin correlations (right)

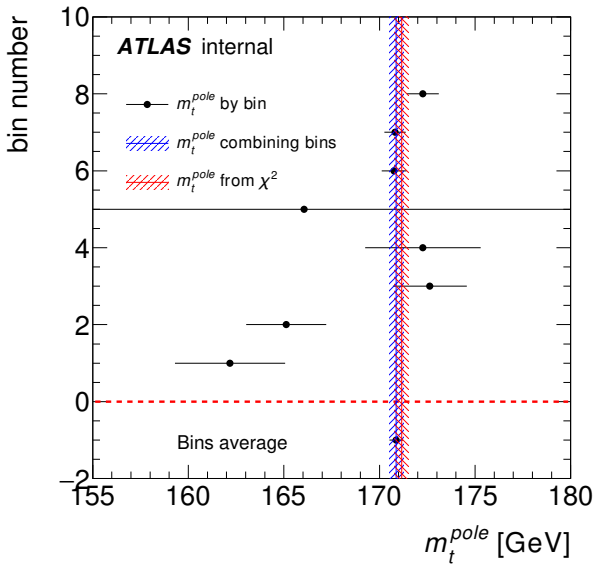

Figure 7.4: The top-quark pole mass value extracted from each bin of the observable at detector level. Only statistical error is taken into account in this plot. Extracting $m_t^{\rm pole}$ from χ^2 minimisation considering bin correlations one gets $m_t^{\rm pole} = 171.16 \pm 0.39$ (stat.) GeV, while a naive bin-by-bin combination gives $m_t^{\rm pole} = 170.85 \pm 0.45$ (stat.) GeV

7.2 Particle level

It is possible to measure the $\mathcal{R}$ observable also at particle level. This level is built from stable particles, with a mean lifetime longer than 0.3×10^{-10} seconds, before they interact with the detector. Only particles within ATLAS pseudorapidity range are considered. Ref. [255] gives more details on how photons, electrons, muons, missing energy, jets and b-jets are constructed at particle level. The $t\bar{t}+1$-jet system is reconstructed from particle level objects with the same algorithm used for the system recontruction at detector level, with the same cuts described in Section 5.3. The neutrino is treated as detectable particle and does not have to be reconstructed. In this way the theory dependence of the unfolding procedure is minimised.

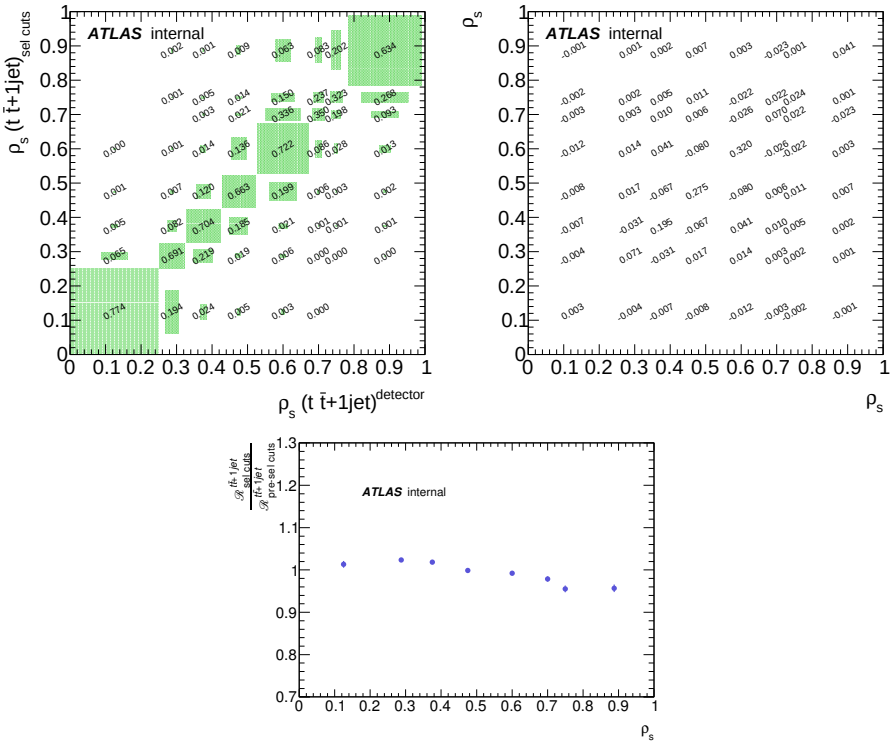

Figure 7.5: Acceptance factor (bottom) and efficiency migration matrix (top-left) used in unfolding data to particle level. Also the covariance matrix used in the fit at particle level is shown (top-right).

It is out of the scope of this note to extract the mass at particle level, since there is no conceptual difference with respect to the detector level fit, but technical difficulties arise since data has to be unfolded and theoretical predictions has to be folded at the same time.

It is anyway important to report the observable corrected for detector effects, $\mathcal{R}^{\text{particle}}$, since this measurement has the smallest theory assumption. It can thus be compared directly to new calculations.

In the particle level analysis, data are corrected to a fiducial volume, which

is defined with similar cuts to the one applied at detector level, but on particle level objects.

It should be noticed that the observable defined at particle level is different from the one defined at parton level. Even if the formal definition is the same, the definition of the top-quarks changes drastically. While at parton level top-quarks are considered as free and stable particles, at particle level top-quarks do not exist, and they are reconstructed after decay and radiation. Top-quark candidates reconstructed from their decay products are often referred as *pseudo-tops*. The reconstruction algorithm can not be perfect, hence

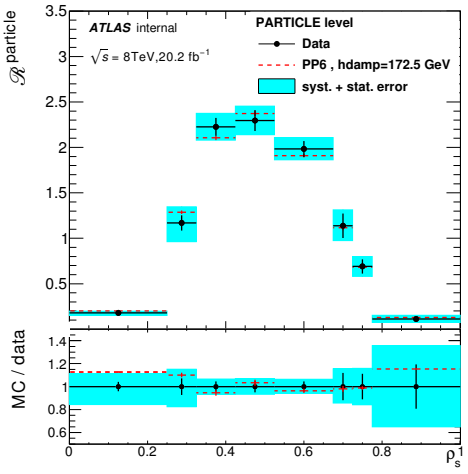

Figure 7.6: Unfolded distribution at particle level. Data are represented by black dots, while the nominal $t\bar{t}$ MC sample is shown in red. The statistical uncertainties on data are represented with a balck line, while the cyan band shows the total error.

bin	$\mathcal{R}^{particle}$	stat.	syst.
$0.000 < \rho_s < 0.250$	0.179	± 0.007	$^{+0.019}_{-0.027}$
$0.250 < \rho_s < 0.325$	1.169	± 0.085	$^{+0.156}_{-0.188}$
$0.325 < \rho_s < 0.425$	2.226	± 0.099	$^{+0.110}_{-0.107}$
$0.425 < \rho_s < 0.525$	2.296	± 0.115	$^{+0.111}_{-0.106}$
$0.525 < \rho_s < 0.675$	1.982	± 0.087	$^{+0.091}_{-0.081}$
$0.675 < \rho_s < 0.725$	1.138	± 0.135	$^{+0.112}_{-0.090}$
$0.725 < \rho_s < 0.775$	0.690	± 0.077	$^{+0.078}_{-0.078}$
$0.775 < \rho_s < 1.000$	0.113	± 0.022	$^{+0.034}_{-0.033}$

Table 7.1: Value of the unfolded observable in each of the bins, together with its statistical and systematic errors. Systematic errors have been evaluated bin-by-bin following the procedure defined in Section 6.4

the four-momentum of a pseudo-top is different from its associated parton level top-quark. In fact, as the definition of the observable changes, a fit of the particle level distribution with a template obtained from parton level predictions, could and in fact gives a different value of m_t^{pole}. It is important then to correctly compare unfolded data with theoretical predictions at the same level. If different levels are connected in a coherent way, the extracted value of m_t^{pole} should be independent of the level at which the measurement is performed. This topic is discussed with more detail in next Section 8.1.

Unfolding to particle level follows the same approach employed in the parton level unfolding but only including detector effects. First, $\mathcal{R}$ at detector level is unfolded using the Bayesian algorithm. Second, a bin-by-bin acceptance factor is applied. It corrects for events which pass particle level selection cuts, but are not selected at detector level.

The acceptance factor and the efficiency migration matrix used in the particle level unfolding are presented in Figure 7.5. The quality of the unfolding procedure has been tested by using pseudoexperiments, as it has been done for

the parton level unfolding of Section 6.2. Pull distributions are presented in Appendix F.2, showing no bias in the unfolding procedure.

Figure 7.6 and Table 7.1 show the $\mathcal{R}$ distribution together with their associated statistical and systematic uncertainties.

Chapter 8

Discussions of the results

In this chapter the results obtained at parton, particle and detector level are discussed. Firstly, in Section 8.1, differences in the shape of $\mathcal{R}$ and its properties are analyzed at differenet levels. Secondly, a detail study on the particle level mass measurement, evaluating the impact of missing higher orders in the calcualtion of top-quark decays and the impact of off-shell effects, is reported in Sections 8.2 and 8.3.

8.1 Discussion of the results obtained at parton, particle and detector levels

The observable $\mathcal{R}$ at particle and parton levels is constructed using different information. At parton level the top is reconstructed as a stable particle whereas at particle level the top quark is reconstructed by identifying and clustering the information from the decayed particles, gluon irradiation and later hadronization. At detector level the experimental effects in the reconstruction of the observable $\mathcal{R}$ need to be considered in addition.

The absolute difference between the parton and particle level can be estimated in terms of a mass shift of the extracted values for the top-quark pole mass using both predictions. For this purpose the value of m_t^{pole} can be extracted from a fit to the observable $\mathcal{R}$ at particle level using the parton level template with and without the folding/unfolding correction. An example of these distributions can be seen in Figure 8.1. The difference observed is stable in the range of top-quark masses considered, around 165-175 GeV, and has a value of:

$$\Delta m_t^{\text{pole}} \text{ (particle vs parton)} \sim 3.5 \text{ GeV}. \tag{8.1}$$

In other words, the whole top decay, gluon radiation and hadronization modelling modifies the extracted top-quark mass by a factor of ∼2%. The uncertainties affecting this difference arise from the limited accuracy of the QCD perturbative calculation, the parton shower model and the hadronization modelling. Taking the values from Table 6.6 gives:

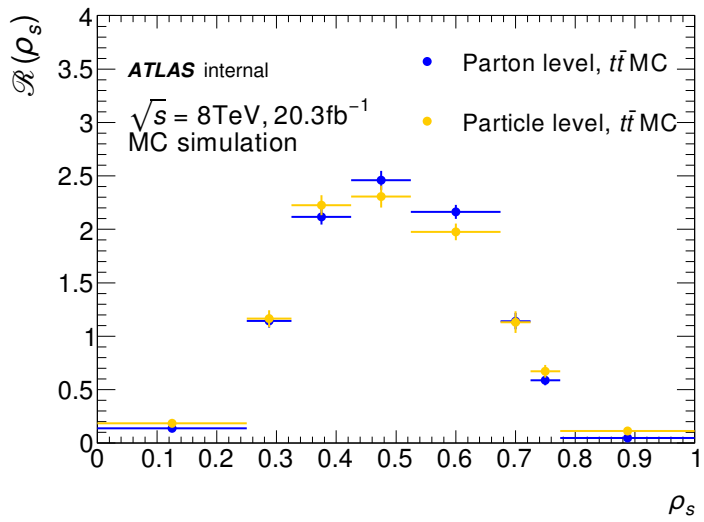

Figure 8.1: The observable $\mathcal{R}$ reconstructed at particle level (yellow) and parton level (blue) for a $t\bar{t}$ MC sample with a top-quark mass of 172.5 GeV. The particle level distribution extends to higher ρ_s values than the parton level.

$$\Delta m_t^{\text{pole}} \text{ (particle vs parton)} \sim 3.5 \pm 0.71 \text{ (syst-hadronization modelling) } {}^{+0.66}_{-0.32} \text{ (theo) GeV.} \quad (8.2)$$

Obviously this difference is accounted for by the folding/unfolding procedure giving equal results of m_t^{pole} within 0.1-0.2 GeV at both levels.

8.2 Discussion of the off-shell versus on-shell effects

The determination of the top-quark mass presented here is based on the method proposed in Ref.[40] where stable on-shell top quarks are considered. A correction is applied to transform the results obtained within fixed order perturbative QCD at parton level to the observed distribution at detector level. This correction includes effects due to the top-quark decay, additional gluon radiation from top-quark decay products as well as hadronisation and experimental detector effects. It is well known that additional gluon radiation from top-quark decay products can lead to sizeable effects [268]. As a consequence the aforementioned corrections lead to sizeable shifts of the extracted top-quark mass of about 2% (see Eq. 8.2). This observation is in perfect agreement with Ref.[122] where similar effects have been observed when comparing results for the $\mathcal{R}$ distribution at the level of stable top-quarks with results obtained for the true final states including off-shell and interference effects.

In Refs. [269, 270] it has been shown that interference effects are suppressed for sufficiently inclusive quantities. Note that finite width effects can be approximately included through an appropriate modification of the phase space

integration taking into account the kinematic effects owing to the relaxed on-shell condition. Including off-shell effects as described before the interference effects are estimated in Refs. [269, 270] to be formally of the order $\frac{\Gamma_t}{m_t}$, where Γ_t denotes the width of the top-quark. Corrections of the order $\frac{\Gamma_t}{m_t}$ are produced by non-resonant backgrounds while corrections due to the additional emission of gluons are further suppressed by additional powers of the coupling constant. The results of Refs. [269, 270] give thus a first indication that interference effects are negligible. However, given the aimed precision in top-quark mass measurements further studies are certainly welcome.

In Ref. [122] the impact of finite width and interference effects on top-quark mass measurements has been studied in detail. For two specific observables (m_{lb} and m_{T2} for details we refer to Ref. [122]) the extracted masses using different theoretical descriptions are compared. As pseudo-data, events generated using the 'full' calculation including finite width as well as interference effects, have been used. Comparing with theoretical predictions based on the narrow width approximation, including NLO corrections in the production and decay, mass shifts of (0.83 ± 0.07) GeV for m_{lb} and (0.6 ± 0.06) GeV for m_{T2} were observed. In both cases the uncertainty associated with the scale variation is of similar size and thus cover the uncertainty due to a different theoretical modeling. Obviously m_{lb} and m_{T2} are rather sensitive to off-shell effects since both observables depend on the kinematics of the top-quark decay products. As a consequence we expect smaller effects in the top-quark mass extracted from the $\mathcal{R}$ distribution since it is less sensitive to off-shell effects.

In Ref. [271] a study similar to the one presented in Ref. [122] has been presented. Ref. [271] shows also results for the $\mathcal{R}$ observable. However, the results presented in Ref. [271] are not conclusive. First of all the full calculation, including off-shell and interference effects, and the theoretical prediction based on the narrow width approximation are evaluated for a different scale setting. It is well known (see for example Ref. [40] or Ref. [252] and also the results presented in Ref. [271]) that scale variation leads to sizeable effects on the extracted top-quark mass. In Ref. [271] it is shown for example that the results for the two different scale settings disagree at the level of 3–4 sigma (see table 5 of Ref. [271]). Furthermore, in difference to Ref. [122] the uncertainty of the observed mass shifts using different theoretical predictions is not estimated in Ref. [271]. It is thus unclear whether the reported shifts are significant or not.

8.3 Evaluation of off-shell effects on $\mathcal{R}$ at 13 TeV

In this section the impact of off-shell effects on the top-quark mass extraction from the $\mathcal{R}$ observable are evaluated. In fact, four different theoretical approaches can be used to produce predictions for $\mathcal{R}$ at particle level:

- Full calculation (Full):

  defined as $pp \longrightarrow W^+W^-b\bar{b}j$ at NLO in QCD, including off-shell effects and non-resonant top-quark contributions. This is the most complete approach at $\mathcal{O}(\alpha_s^4\alpha^4)$.

- Narrow width approximation (NWA):

defined as $pp \rightarrow ttj \longrightarrow W^+W^-b\bar{b}j$ at NLO in QCD. Top-quarks are considered on-shell and NLO effects on the top-quark decay are included. Non-resonant top-quark and off-shell effects are not taken into account instead.

- Narrow width approximation, with NLO effects in production only (NWAprod):

  defined as $pp \xrightarrow{\text{NLO QCD}} ttj \xrightarrow{\text{LO}} W^+W^-b\bar{b}j$. Next-to-Leading-Order effects in this calculation are only taken into account in top-quark production, while top-quark decays are treated at LO only.

- Powheg+Pythia8 (PP8):

  defined as $pp \xrightarrow{\text{POWHEG}} ttj \xrightarrow{\text{PYTHIA8}} W^+W^-b\bar{b}j$, this calculation matches a NLO QCD matrix element Monte Carlo generator (POWHEG) to a program performing event-by-event showering and hadronization (PYTHIA8). In this approach, top-quarks are produced in association with a parton at NLO and subsequently the shower program performs top-quark decay at LO, but including leading logarithms at all !QCD orders. Also, the shower program is tuned to data.

Table 8.1 summarizes the characteristics of the previously defined theoretical approaches.

NAME	Initial State	Calculation			Final State
NWAprod	pp	$\xrightarrow{\text{NLO}}$	$t\bar{t}j$	$\xrightarrow{\text{LO}}$	$e\mu b\bar{b}\nu_e\nu_\mu j$
NWA	pp	$\xrightarrow{\text{NLO}}$	$t\bar{t}j$	$\xrightarrow{\text{NLO}}$	$e\mu b\bar{b}\nu_e\nu_\mu j$
Full	pp		$\xrightarrow{\text{NLO}}$		$e\mu b\bar{b}\nu_e\nu_\mu j$
PP8	pp	$\xrightarrow{\text{POWHEG}}$	$t\bar{t}j$	$\xrightarrow{\text{PYTHIA}}$	$e\mu b\bar{b}\nu_e\nu_\mu j$

Table 8.1: Table summarising the different theoretical approaches which has been used in this section. The only calculations which include off-shell effects have both W bosons decay leptonically as $WW \rightarrow e\mu\nu_e\nu_\mu$ [122]. Hence the final state for the process is $e\mu b\bar{b}\nu_e\nu_\mu j$.

In order to evaluate the effects of the different theoretical approaches on the $\mathcal{R}$ observable, a common level have to be defined where the comparison make sense. Since for calculations including off-shell effects it does not make sense to talk about *parton level*, the only meaningful comparison can happen at particle level, in a common fiducial phase space. Begin the calculation of the $pp \rightarrow WWbbj$ process using purely perturbative approaches technically difficult, results for the Full, NWA, NWAprod approaches have been taken from Ref.[122]. Hence the same fiducial volume is used for the comparison, which is defined in the following.

8.3.1 Generation of the Monte Carlo predictions and fiducial phase space

The only calculation of $pp \to W^+W^-\bar{b}bj$ which includes off-shell effects has been computed only recently [122], at an energy of the pp collisions of 13 TeV. Because of the technical difficulties of the calculation, these results are only available for the $e\mu\nu_e\nu_\mu b\bar{b}j$ final state. Various free parameters, such as the particle masses, the PDFs and the Fermi constant G_μ, had to be set to perform the calculation. In the following the POWHEG+PYTHIA8 simulation was produced with the same parameters of the other approaches [122]:

$$\begin{array}{cc} m_W = 80.40 \text{ GeV} & \Gamma_W = 2.10 \text{ GeV} \\ m_Z = 91.19 \text{ GeV} & \Gamma_Z = 2.51 \text{ GeV} \\ \Gamma_t^{\text{on-shell}} = 1.37 \text{ GeV} & \text{CT14nlo PDF} \\ G_\mu = 1.6637 \cdot 10^{-5} \text{ GeV}^{-2} & \alpha_s(m_Z) = 0.118 \end{array}$$

whereG_μ is the Fermi constant and the electroweak coupling and the weak mixing angle are computed in the G_μ scheme:

$$\begin{aligned} \sin^2\theta_W &= 1 - \frac{m_W^2}{m_Z^2} \\ \alpha &= \frac{\sqrt{2}}{\pi} G_\mu m_W^2 \sin^2\theta_W \end{aligned} \tag{8.3}$$

All the calculations were produced with input top-quark mass value of $m_t = 173.2$ GeV and with renormalisation and factorisation scale $\mu_R = \mu_F = m_t$.

The fiducial phase space at particle level, where the off-shell calculations were produced, is made of jets, leptons and neutrinos. Jets are defined from final state partons with pseudo-rapidity $|\eta| < 5$, using the anti-k_t algorithm with R=0.5 parameter using the energy recombination scheme (jet momentum is the sum of four-vectors of selected partons). While fin the case of fixed order calculations (Full, NWA, NWAprod) only two b-quarks, one jet and eventually the NLO real radiation exist, in the Monte Carlo approach a high multiplicity final state is generated by the shower program. Thus, in the POWHEG+PYTHIA8 case, all partons before the hadronization[1] are considered as final state partons, to avoid being dependent on the modelling of the hadronization process. Jets are $b-$tagged if jet and b-quark momenta have an angular distance $\Delta R < 0.5$, i.e. the initial b-quark iles inside the jet cone. All jets are required to have $p_{\text{T}}(j) > 40$ GeV, $|\eta_j| < 2.5$ and being separated one from each other ($\Delta R_{jj} > 0.5$).

In Ref. [122] exactly one muon and one positron are required. For the POWHEG+PYTHIA8 approach, also anti-muons and electrons are considered, since it does not affect the shape of $\mathcal{R}$ but helps in increasing the statistic of the simulation. Leptons are recombined with photons in jets of R=0.1 with the anti-k_t jet algorithm. Exactly two leptons leptons are required, with $p_{\text{T}}(l) > 40$ GeV and $|\eta_l| < 2.5$, being angularly separated to jets, $\Delta R_{lj} > 0.4$, and between themselves $\Delta R_{ll} > 0.4$. Neutrinos are treated as detectable particles, and their four momenta is considered to be known. Nevertheless, a cut on the transverse momentum of the neutrinos sum (p^{miss}) is applied, as it is often done in experiments. In particular it is required that ${p_T}^{\text{miss}} > 40$ GeV.

[1] Partons before hadronization are identified in PYTHIA8 by the particle status 71.

8.3.2 Results

The $\mathcal{R}$ observable is defined at particle level as the differential normalised cross-section as a function of

$$\rho_s = \frac{340 \text{ GeV}}{\sqrt{(p(j_{b1}) + p(j_{b2}) + p(l^-) + p(l^+) + p(\nu_1) + p(\nu_2) + p(j))^2}} \tag{8.4}$$

where j_b is a b-tagged jets, l a leptons, ν a neutrino and j the light jet with the hardest p_{T}.

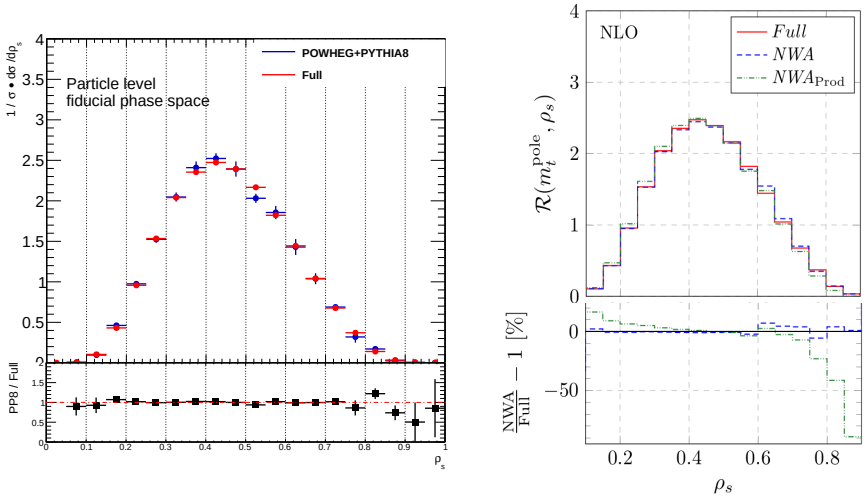

Figure 8.2: Comparison between the $\mathcal{R}$ observables computed with different approaches at particle level. The right-most plots are taken from Ref. [122].

The shape of $\mathcal{R}$ for the different theoretical approaches considered are shown in Fig. 8.2. The POWHEG+PYTHIA8, NWA and Full approaches agrees within 10% across the whole ρ_s range. Where the observable is most sensitive to the top-quark mass ($\rho_s > 0.6$) the different approaches show less similarity. Nevertheless differences between the POWHEG+PYTHIA8 and Full approaches are not significant and could possible be due to statistical fluctuations in the less populated bins, $\rho_s > 0.8$, where the Monte Carlo sample generated are statistically very limited.

One could ask what would be the top-quark mass value when different theoretical predictions are used to extract m_t from data. To answer such question, the top-quark mass is extracted from each of the $\mathcal{R}$ distributions of Fig. 8.2. Knowing that all the distributions were generated with the same input value of the top-quark mass ($m_t = 173.2$ GeV), shifts in the extracted top-quark mass will give the differences one would get when inferring m_t from data using one prediction or another.

To extract the top-quark mass, a parton level template is produced with various mass points. A continuous parametrisation is obtained by fitting the mass points with a second order polynomial, as already done in Chapter 6. The

template is then folded to the fiducial volume at particle level. The folding is implemented via a bin-by-bin correction obtained from a POWHEG+PYTHIA8 simulation, where the information of both parton and particle level was available. The parton level template, as well as the correction factors, are shown on Appendix M.

Top-quark mass values are extracted as the values which minimize the function:

$$\chi^2 = \sum_{i \in \text{bins}} \frac{\left[\mathcal{R}_i^O - \mathcal{R}_i(m_t)\right]^2}{\sigma^2\left[\mathcal{R}_i(m_t)\right]} \tag{8.5}$$

where $\mathcal{R}^O$ is the distribution to be fit and $\mathcal{R}(m_t)$ is the particle level template. Four different possible binning choices were studied: 6 bins as used in Ref. [41], 8 bins as used in Chapter 6, 10 bins and 20 bins. The results of the top-quark mass extraction are reported in Fig. 8.3. No dependence on the binning choice is found. Parameters belonging to the MC simulation only, such as *hdamp*, tuning choice, modelling of multi-particle interactions, have been varied to cross-check the stability of the folding procedure. Three alternative bin-by-bin correction factors were used for the folding and no large deviations have been found with respect to the nominal case, as it is reported in Appendix M. For different sets of parameters used in the fitting procedure, extracted values are stable within ~ 0.5 GeV.

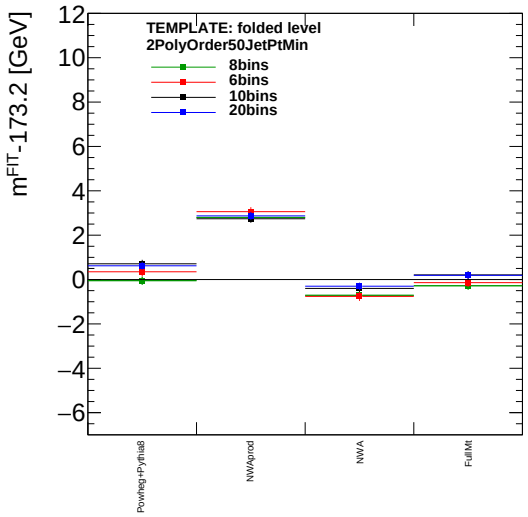

Figure 8.3: Differences in the top-quark mass extraction due to different theoretical approaches chosen.

The mass values inferred for the POWHEG+PYTHIA8, NWA and Full theoretical approaches were found to be compatible within $\lesssim 1$ GeV. Hence, all top-quark mass extractions which use one of the above approaches should give compatible result within $\lesssim 1$ GeV. When completely ignoring top-quark NLO decay effects instead, the top-quark mass extracted is found to be shifted by ~ 3 GeV from its input value.

The results reported in Fig. 8.3 suggest that off-shell effects on top-quark mass extraction from $\mathcal{R}$ at particle level are small, and well within the errors

on the top-quark mass reported in Chapter 6. Larger deviations could occur if NLO effects in top-quark decay are ignored. In the Monte Carlo approach where a matrix element generator is configured to a parton shower program, the top-quark decays are treated at Leading-Order also, but the contribution of leading large logarithms is taken into account at all orders. This recovers a good description of the process and allows to obtain results which are within $\lesssim 1$ GeV to other more refined calculations (NWA and Full).

Chapter 9

Conclusions

The top-quark plays a key role in the SM and in many of its extensions. It is hence important to measure accurately its properties, looking for small deviations from SM expectations and reducing the parameters space of BSM theories. One particular parameter, the top-quark mass, has been studied in detail in this thesis, also taking advantage of the data collected by the ATLAS experiments at a collision energy of 8 TeV.

Various top-quark mass measurements have reached an experimental uncertainty smaller than 1 GeV. With such a precision, a number of theoretical aspects become relevant, such as the definition of the measured mass. The so-called *standard* methods relies on the definition of top-quark mass as it is defined in MC generators, m_t^{MC}. In such picture, the top-quark is considered as an unstable particle, which mass distribution follows a Breit-Weigner distribution centred in m_t^{MC}. Such a parameter though, cannot be interpreted directly as the top-quark mass as defined in the SM Lagrangian, and a theoretical uncertainty on its interpretation of hundresd of MeV should be taken into account. Top-quark inclusive and differential cross sections depend on the top-quark mass also. Since prediction for such observables are available at fixed QCD order, without the need of using Monte Carlo simulations, the top-quark mass can be extracted from their measurements, in a theoretically more rigorous way.

In order to have a good resolution on the extracted top-quark mass, the chosen observables should be as much as possible sensitive to it. Also, they should be well defined theoretically (free of divergences, computed at least at NLO in a defined renormalisation scheme) and the theoretical uncertainties associated to their calculations should be well under control. Then of course, the calculated observables must be experimentally accessible, in order to compare to the real data measured.

The differential cross section

$$\mathcal{R}(\rho_{\mathrm{s}}) = \frac{1}{\sigma_{t\bar{t}+\text{1-jet}}} \cdot \frac{\mathrm{d}\sigma_{t\bar{t}+\text{1-jet}}}{\mathrm{d}\rho_{\mathrm{s}}}, \tag{9.1}$$

presented in Section 3.3.2, largely satisfies such requirements and it is therefore ideal to measure the top-quark mass. It shows a strong sensitivity to m_t in the threshold region, where the invariant mass of the system formed by a top-quark, an antitop-quark and a jet is close to roughly two times the top-quark mass

($\rho_s > 0.7$). Compared to measurements of inclusive cross-sections in fact, the threshold region of $\mathcal{R}$ has a ~ 5 times higher sensitivity to m_t. The calculation of $\mathcal{R}$ suffers of small uncertainties, since NLO QCD corrections are small, while errors from QCD coupling constant and PDF uncertainties cancel at first order, being $\mathcal{R}$ a normalised quantity. To get rid of possible IR divergences which could spoil convergence of the perturbative QCD series, the extra-jet is required to have a minimum transverse momentum and a maximum pseudo-rapidity, which avoids the soft and collinear regimes. The renormalisation schemes in which calculations of $\mathcal{R}$ are available are the pole-mass scheme and the modified minimal subtraction scheme, which allow the measurement of the top-quark pole mass, m_t^{pole}, and running mass at its scale, $m_t(m_t)$. At the LHC, an enormous amount of top-quark pairs has been produced, and a good part of them has been produced in association with a high momentum extra-jet, which allows to have a good experimental precision on a measurement of $\mathcal{R}$.

In this thesis, a measurement of the differential cross section of top-quark pair production in association with an energetic jet in 8 TeV proton-proton collisions is presented. The pp collision data, corresponding to an integrated luminosity of 20.3 fb^{-1}, were collected by the ATLAS experiment in 2012. The analysis procedure selected final state objects in such a way that the background contamination was small and had a minimal impact on the final result, as it happened for the same analysis carried out using data at from 7 TeVcollisions. The distribution of the inverse of the invariant mass of the $t\bar{t}$+1-jet system $\rho_s = \frac{2m_0}{\sqrt{s_{t\bar{t}+1\text{-jet}}}}$ observed in the lepton+jets final state is normalized and corrected to parton and particle level.

The unfolding to parton level corrected the measured $\mathcal{R}$ for detector, hadronization and top-quark decays effects and it is found to be independent on the top-quark mass value, as it is shown in Fig. 6.5. Top quark mass was then extracted from the measured and corrected $\mathcal{R}$ comparing its values in bins of ρ_s to the theoretical expectations as a function of the renormalised top-quark mass, through a χ^2 minimisation. The MC simulations in this case are used only to correct data, while top-quark pole mass extraction is performed using fixed order NLO QCD calculations. Data correction procedure has been proven to be independent of the binning of the observable (Appendix D), on the value of m_t used in the MC to define the unfolding procedure (Appendix G) as well as on the cut on the extra-jet transverse momentum (Appendix B).

A number of experimental uncertainties affected the $\mathcal{R}$ measurement. Firstly, a statistical uncertainty was associated to the limited sample of data selected and was estimated by looking at which mass values were varying the χ^2 by one unity around its minimum value. Systematic uncertainties due to the definition of final state objects were found to have a minor impact on the result, the only significant one coming from the determination of the scale of the jets energy. The largest source of experimental uncertainty was coming from the choice of the MC used in the modelling of $t\bar{t}$ production. Theoretical uncertainties due to missing order in the perturbative calculation of $\mathcal{R}$ were evaluated by varying the renormalisation and factorisation scales by a factor 2, while the impact of the choices of α_s and PDF was estimated by using three sets of PDF using different values of the strong coupling constant.

Measurements and definitions of the observable at parton, particle and detector level have been discussed in Section 8.1, where the $\mathcal{R}$ observable was

also unfolded to particle level in a fiducial volume defined by kinematical cuts. At such level top-quarks already decayed, but algorithms exist to reconstruct *pseudo-tops* from the top-quarks decay products. The $\mathcal{R}$ presented at particle level is corrected only for detector effects and theoretical assumptions on it are minimised if the *pseudo-tops* algorithms are. Such distribution can be compared directly to fixed order calculations defined in the same fiducial volume, which is theoretically well defined. The effects of potential off-shell contributions to the definition of the observable are discussed in Section 8.2. While in most of the literature such effects have been reported to be small a recent article [122] claims that off-shell effects could play a more relevant role instead. Section 8.3 covers a detailed discussion on this topic and concludes that off-shell effects are small, and well within the errors accounted.

To conclude, the measured values of the pole mass and the unning mass at it scale, extracted from parton level $\mathcal{R}$ calculated in the pole scheme and in the $\overline{\text{MS}}$ scheme respectively, are:

$$\begin{aligned} m_t^{\text{pole}} &= 171.05 \pm 0.43\ (\text{stat.}) \pm 0.92\ (\text{syst.})\ ^{+0.66}_{-0.32}\ (\text{theo})\ \text{GeV}. \\ m_t(m_t) &= 162.89\ \pm 0.45\ (\text{stat.})\ \pm 0.98\ (\text{syst.})\ ^{+2.08}_{-1.23}\ (\text{theo})\ \text{GeV} \end{aligned} \tag{9.2}$$

which are compatible estimates of the same bare parameter of the SM Lagrangian, given the known relation which connects the two renormalised masses at four loops in QCD. Differences in the two renormalization schemes have been discussed in Section 6.7, where it is shown that the results of the measurements of m_t^{pole} and $m_t(m_t)$ are compatible estimates of the same bare parameter of the SM Lagrangian, within their uncertainties and given the QCD relation [267] between the top-quark mass in the pole and $\overline{\text{MS}}$ schemes. The highest theoretical uncertainty on $m_t(m_t)$ is due to the $\overline{\text{MS}}$ scheme having a poor description of thresholds regions, where $\mathcal{R}$ has the highest sensitivity to the top-quark mass.

The pole mass result is compatible within the errors with the pole mass result obtained with the same method at 7 TeV and with other pole mass determinations [41, 138, 148, 149, 272–275], as it is shown in Figure 9.1. The statistical uncertainty is much reduced compared to the 7 TeV result of Ref. [252] and is now sub-dominant to the experimental systematic uncertainties.

For a well defined top-quark mass, a fiable estimate can be made on the magnitude of the missing next orders in the perturbative calculation and on the uncertainties in the parton density functions. The obtained result confirms that a precision higher than 1% starts to being achieved in measurements of a quark mass in a well defined theoretical framework. The measurement presented in this analysis is the most precise measurement of the top-quark pole mass up to date, with a total error of $^{+1.21}_{-1.06}$ GeV.

Future measurements of the top-quark mass at the LHC will take advantage of an increased luminosity, which allos to reduce the statistical uncertainty. To obtain a much better measurement of the top-quark mass from jet rates at the LHC though, a better modelling of the MC is needed, in order to reduce the dominant uncertainties on this measurement, as well as a more refined theoretical calculation of the $\mathcal{R}$ observable. Such improvements would allow to reduce the total error on the top-quark mass below 1 GeV. Jet (and photon) rates can also be used to extract top-quark mass from an observable similar to $\mathcal{R}$ in lepton colliders. The advantage in this case come from the energy of the collision being fixed by the particle accelerator, and studies have been carried out showing that

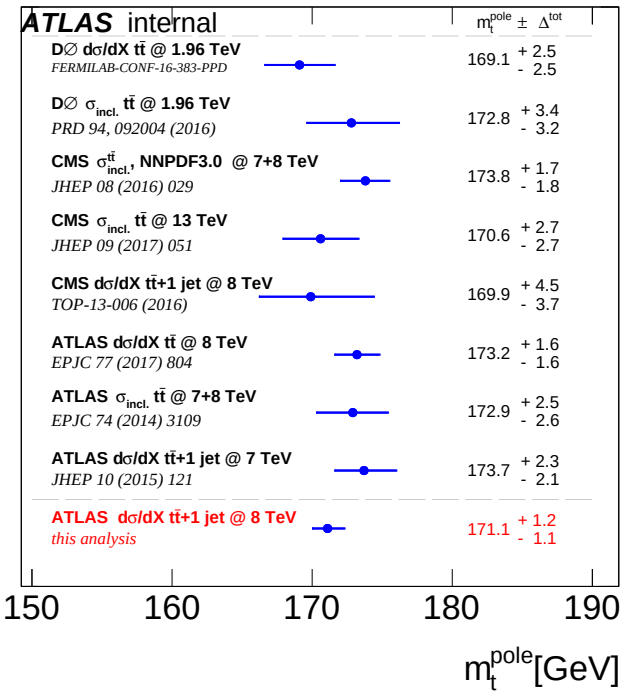

Figure 9.1: Summary plot of the top-quark pole mass measurements at the Tevatron and LHC [41, 138, 148, 149, 272–275].

uncertainties on m_t below 1 GeVare possible in e^+e^- collisions, as reported in Section 3.3.3.

With measurements of well defined top-quark masses reaching precision below 1 GeV, interesting scenarios open up. A deeper knowledge of how the elementary particles interact between each others will become accessible and answers to questions on the future of the SM and of our universe will might be given.

Resumen en Español

El Modelo Estándar ("Standard Model", SM, en inglés) es el modelo teórico que a día de hoy mejor describe el universo en el que vivimos: una teoría cuántica de campos relativista que es capaz de reproducir la mayoría de las medidas llevadas a cabo por distintos experimentos en física de partículas. El SM se desarrolló a partir de la primera mitad del 1900 para describir unas cuantas evidencias de física experimental. Sus predicciones se comprobaron en posteriores experimentos de colisionadores de partículas, con un éxito sin precedentes, como se introduce en el Capítulo 1 de esta tesis.

En física de partículas, los experimentos suelen medir secciones eficaces y probabilidades de decaimientos de partículas inestables. Dichos observables pueden ser calculados por el SM, con herramientas cada vez más sofisticadas y para condiciones tan complicadas técnicamente como las del Gran Colisionador de Hadrones ("Large Hadron Collider", LHC, en inglés). Una introducción sobre estos temas se expone en el Capítulo 2.

El SM establece la existencia de diecisiete partículas elementales: doce fermiones (seis leptones y seis quarks) que forman la materia, cuatro bosones que median las interacciones entre ellas, y el bosón de Higgs que confiere masa a las partículas pesadas. Todas estas partículas se han medido en varios experimentos, siendo la última, el bosón de Higgs, descubierta en 2012. El quark top se descubrió en 1995 y el Capítulo 3 está totalmente dedicado a describir las propiedades y la fenomenología de esta partícula en el LHC.

Con una masa alrededor de 170 GeV, el quark top es la partícula más pesada del SM, la que le confiere la característica única de desintegrarse antes de que el proceso de hadronización tenga lugar. Esto hace que el quark top sea el único quark que se pueda estudiar en condiciones de partícula casi libre. Además, el quark top juega un papel especial en la teoría de las interacciones electrodébiles: el quark top introduce enormes correcciones en los cálculos teóricos, siendo su gran masa debida a un acoplamiento muy fuerte con el bosón de Higgs. Suponiendo la validez del SM hasta escalas de energía muy altas, la estabilidad del vacío electrodébil y del universo en el que vivimos también depende fuertemente del valor de la masa del quark top. Por estas razones la medida precisa de las propiedades del quark top, y en concreto de su masa, es fundamental.

Las medidas de la masa del quark top que tienen menor incertidumbre experimental, realizadas por los experimentos del LHC, alcanzan precisiones experimentales menores de 1 GeV. Estos métodos, llamados medidas directas o de masa cinemática, miden la masa del quark top a través de las propiedades de sus productos de desintegración. Las últimas combinaciones de estas medidas tienen un error experimental total de 0.5 GeV. Con medidas tan precisas, hay as-

pectos teóricos que empiezan a ser relevantes. En el caso de la masa cinemática, no existe una relación conocida entre las masas medidas en los experimentos y la masa definida en la teoría. Se ha estimado que la incertidumbre debida a la interpretación de las masas medidas puede ser del orden de varias centenas de MeV El error total de las medidas directas, entonces, tendría que incluir dicha incertidumbre del mismo orden de magnitud de los errores evaluados en los experimentos.

Otra posibilidad para medir la masa del quark top es a través de su dependencia en secciones eficaces. En el caso las secciones eficaces sean calculadas a órdenes mayores que el primero, es necesario definir un esquema de renormalización, que relaciona parámetros extraídos desde la sección eficaz medida a aquellos usados en el SM. Comparando datos con cálculos puramente perturbativos es posible medir una masa del quark top bien definida teóricamente, incluyendo una estimación completa de sus incertidumbres teóricas. Sin embrago, las secciones eficaces inclusivas son poco sensibles la masa del quark top, motivo por el cual este tipo de medidas suelen tener errores mayores que los métodos directos. En los últimos años, se han desarrollado cálculos de secciones eficaces diferenciales y nuevos métodos que permiten estudiar regiones del espacio fásico que tienen una fuerte dependencia con la masa.

En esta tesis se ha medido la masa del quark top a partir de la sección eficaz de eventos tt+1 jet , diferencial respecto a la masa invariante del sistema tt+1jet, usando datos producidos en el LHC. El observable elegido, llamado R en la tesis, varias propriedades que permiten una medida de la masa de alta precisión. Primero, tiene una alta dependencia con el valor de la masa del quark top, en la región de baja masa invariante del sistema tt+1jet. Segundo, se puede medir con alta precisión en los experimentos, siendo la topología de eventos considerada un buen subconjunto de todos los quarks top producidos por el LHC. Estos hechos permiten tener una buena resolución experimental. Además, el observable se ha calculado con cálculos perturbativos a órdenes mayores que el primero ("Next-to-Leading-Order", NLO, en inglés), que permiten extraer una masa bien definida. Las correcciones perturbativas son pequeñas y controladas, y permiten que errores debidos a la no inclusión de todos los términos del cálculo perturbativo sean pequeños .

Esta tesis usa datos provenientes de colisiones de los protones de 8 TeV y recogidos por el experimento ATLAS. ATLAS es unos de los experimentos más importantes en física de partículas y está compuesto por muchos detectores que trabajan de forma coordinada para medir las partículas producidas por el LHC, como se describe en detalle en el Capítulo 4. Para seleccionar eventos de topología tt+1jet, se estudió el canal semileptónico del sistema top-antitop, donde se producen un lepton (electrón o muón), al menos cinco jets (de los cuales dos provienen de quarks de tipo b) y una gran cantidad de energía transversa no detectada asociada a la presencia de un neutrino. Se utiliza un sistema de cortes para seleccionar la señal y reconstruir el sistema tt+1jet a nivel detector. Una vez sustraídos los fondos esperados, es posible definir el observable R a nivel de detector, como se explica en Capítulo 5.

Para poder extraer la masa del quark top es necesario comparar la distribución medida con los cálculos perturbativos, en un espacio fásico común, llamado volumen fiduciario. Los volúmenes fiduciarios se pueden definir a nivel de partones, donde los quarks top no han decaído aún, y a nivel de partículas, formado por partículas casi estables que típicamente interaccionan con los de-

tectores de ATLAS. Otra posible opción es añadir a la predicción teórica los efectos del detector y hacer la comparación a nivel de detector.

El Capítulo 6 de esta tesis describe la metodología para extraer la masa del quark top desde el observable definido a nivel partónico. La determinación de la masa se obtiene tras corregir la distribución de nivel detector por los efectos de detector, hadronización y de decaimiento del quark top. El método de corrección elegido se basa en la inversión y regularización de una matriz de respuesta obtenida desde simulaciones Monte Carlo. Este método ha resultado ser independiente de la masa utilizada en las muestras Monte Carlo.

Las incertidumbres sistemáticas que afectan la medida, experimentales y teóricas, se han estudiado en detalle. Las teóricas son las asociadas a los órdenes perturbativos y a la elección de la PDF del protón en el cálculo teórico. Las incertidumbres experimentales tienen origen en el modelado de la señal, del detector y de la señal de fondo. Las incertidumbres experimentales dominantes han resultado ser las del modelado de la radiación inicial y final, del modelado de la hadronización, y las debidas a la calibración de la energía de los jets.

En el Capítulo 7, la masa polo se ha extraído a nivel detector, añadiendo efectos de detector a la predicción teórica de nivel partónico. El resultado de la medida a nivel detector es compatible con el obtenido a nivel partónico, cuando la misma información es utilizada en el ajuste. Además en el mismo capítulo, el observable se ha presentado a nivel de partícula, para que pueda ser utilizada en la comparación con otros futuros cálculos definidos al mismo nivel. La extracción de la masa no se llevó a cabo al nivel de partículas debido a dificultades técnicas. Sin embargo, el nivel de partículas no tiene diferencias conceptuales con el nivel de detector, dado que en ambos niveles el quark top solo se puede definir desde sus productos de desintegración. Por lo tanto las conclusiones obtenidas para el nivel detector son validas para el nivel de partículas.

Una discusión sobre los resultados obtenidos en distintos niveles se recoge en el Capítulo 8. Una evaluación de los efectos sobre la medida de quark top en condiciones off-shell se ha llevado a cabo, concluyendo que dichos efectos son pequeños y contenidos en los errores evaluados.

El valor obtenido para la masa polo del quark top y sus incertidumbres son:

$$m_t^{\text{pole}} = 171.06 \pm 0.43 \text{ (stat.)} \pm 0.92 \text{ (syst.)}^{+0.66}_{-0.32} \text{ (theo.) GeV}$$

en acuerdo con los valores anteriormente obtenidos para la masa polo.

Recientes cálculos del observable R a nivel partón, en el esquema de renormalización de sustracción mínima modificada , permiten también extraer desde los mismo datos corregidos a nivel partónico, la masa "running" a su escala:

$$m_t(m_t) = 162.89 \pm 0.45 \text{ (stat.)} \pm 0.98 \text{ (syst.)}^{+2.08}_{-1.23} \text{ (theo.) GeV}$$

Los resultados de la masa polo y masa "running" resultan ser compatibles, teniendo en cuenta la relación entre los dos esquemas de renormalización. El error teórico evaluado para la masa "running" es mayor que el de la masa polo porque los correspondientes esquemas de renormalización describen de manera más o menos precisa el observable en la región donde la sensibilidad a la masa del quark top es mayor.

Todos los resultados y los aspectos estudiados están resumidos en el Capítulo 9, con el que concluye la tesis. Con una incertidumbre total de $\sigma(m_t^{\text{pole}}) = ^{+1.2}_{-1.1}$, el resultado de esta tesis representa la mejor medida de la masa polo del quark top hasta el momento.

Appendices

A Energy re-scaling of light jets from the hadronic W boson candidate

The top-quark candidates are reconstructed at detector level from stable particles, following the algorithm described In Section 5.3. The event selection was optimised in the context of the 7 TeV analysis [253], and it was favoured with respect to ohter event selections, as described in its Appendix D. In one of the steps of the selection, the hadronic W boson candidates are reconstructed from a pair of light jets. The pair of jets reconstructing the hadronic W should pass the criteria:

- $0.9 < \alpha < 1.25$, with $\alpha = \frac{M_W^{\rm PDG}}{m_{ij}}$
- $\Delta k_t^{ij} = \min(p_t^i, p_t^j) \cdot \Delta R_{ij} < 90$ GeV.

and, in order to recover the exact value of the W boson PDG mass, their four momentum is after the selection re-scaled by α.

In this Appendix, the impact of such correction on the $\mathcal{R}$ observable and on the migration matrix is evaluated.

The observables $\mathcal{R}$ and migration matrices obtained with and without the α correction are compared in Figure 2, Figure 3 and Figure 4. The additional correction increases slightly the diagonal of the migration matrix and helps in the background reduction while its effects on the reconstructed $\mathcal{R}$ are extremely small as shown in Figure 2. In fact measured value of the extracted top-quark mass in this analysis including, or not including, the α correction changes by less than 0.20 GeV which is well contained within the accuracy of the method taking into account statistical fluctuations and uncertainties inherent to the fit procedure. See Table 6.6 and the corresponding values of the uncertainties labelled as the *statistical* and *unfolding modelling* .

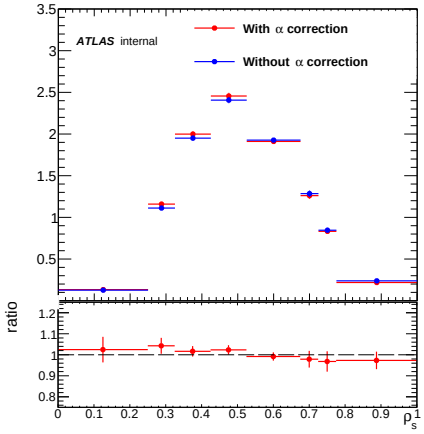

Figure 2: $\mathcal{R}$ at detector level computed with and without the α correction on the light jets from hadronic W boson four momenta.

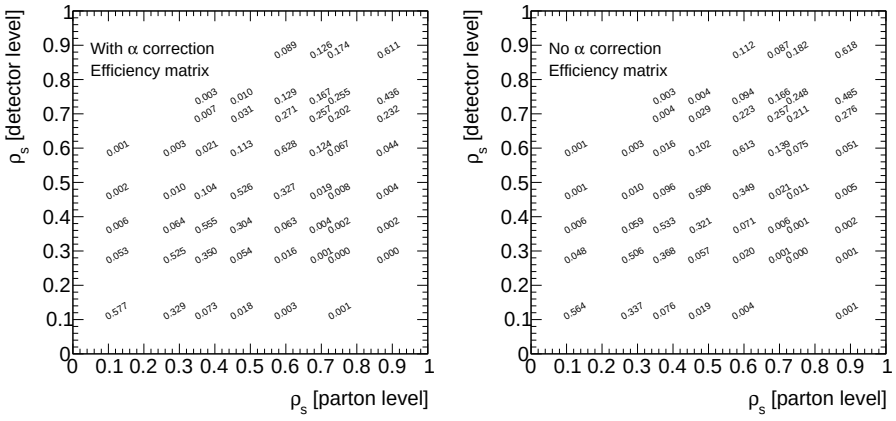

Figure 3: Efficiency of migration matrices with and without the α correction on the light jets from hadronic W boson four momenta. Errors on the bin values are of the order of sub-percent, but are not reported to make the matrices more readable.

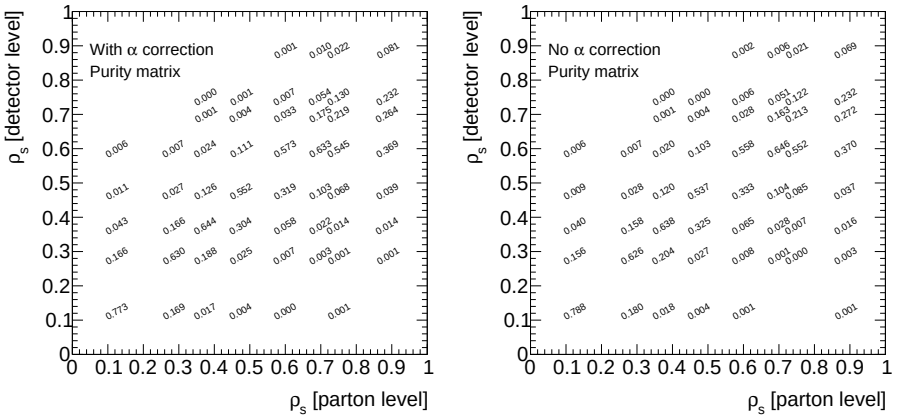

Figure 4: Purity of migration matrices with and without the α correction on the light jets from hadronic W boson four momenta. Errors on the bin values are of the order of sub-percent, but are not reported to make the matrices more readable.

B Change of $p_T^{\mathbf{extrajet}}$

One of the cross-checks which have been performed was studying the impact of the choice of the extra-jet transverse momentum (p_T^{extrajet}) at detector level, on the extracted value of m_t^{pole}.

Different cuts have been chosen for the extra-jet at detector level, while keeping the same nominal cut for the extra-jet at detector level. The expected effects were:

- No change (within statistical errors) of the nominal value of m_t^{pole}
- Increase of statistical uncertainty on the measurement, because of smaller number of events.

As it is shown in Figure5, these conditions are satisifed for p_T^{extrajet} cuts of 40, 50, 60 and 70 GeV.

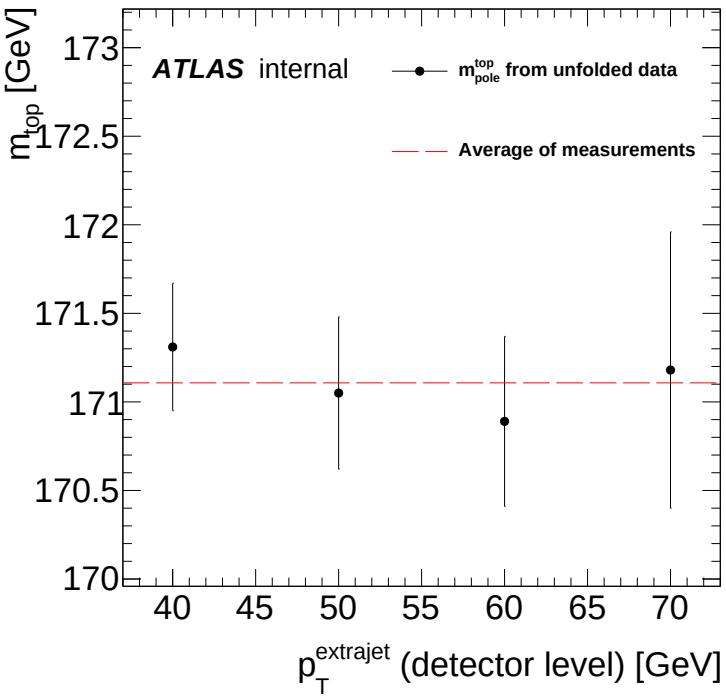

Figure 5: Extracted m_t^{pole} for different choices of the detector level extrajet transverse momentum cut. All values are compatible within their statistical error. Statistical error increases while asking a stronger cut, as expected. Also the average of the four values is shown (red line).

C Additional control plots

In this appendix more control plots are shown. In particular, in some analyses differences in the transeverse momentum spectrum of the $t\bar{t}$ system were observed when comparing data and MC. The control plots for such a distribution is shown in Figure 6, both after pre-selection cuts and $t\bar{t}+1$-jet specific cuts.

Other distributions are then showed, Figures from 7 to 16 , which are used in the reconstruction of the $t\bar{t}+1$-jet system reported in Section 5.3.

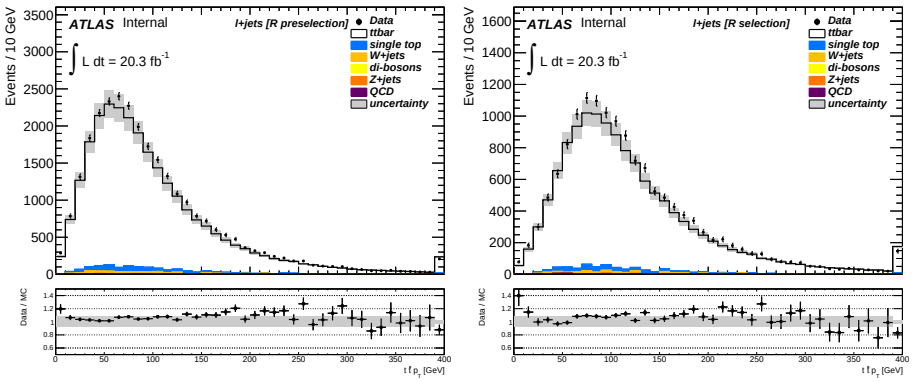

Figure 6: The transverse momentum of the reconstructed $t\bar{t}$ system. The distribution is built from events which pass pre-selection cuts only (left) or events which pass the final $t\bar{t}+1$-jet selection (right).

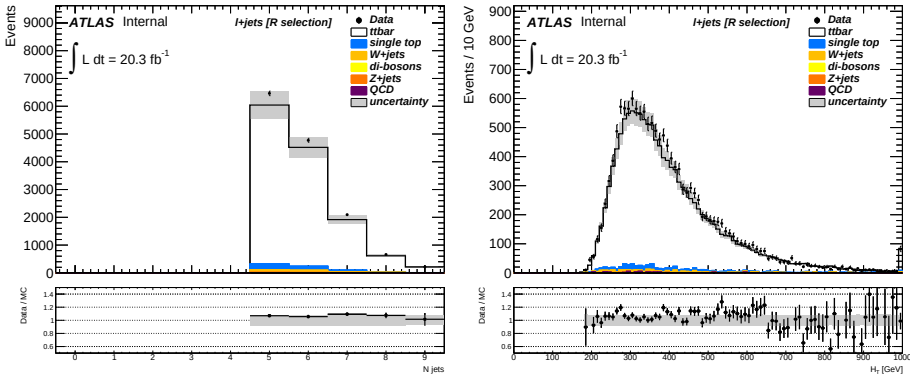

Figure 7: The number of jets and the scalar sum of the transverse momenta of the objects reconstructiing the $t\bar{t}+1$-jet system (H_T). Distribtuions built from events passing the final $t\bar{t}+1$-jet selection.

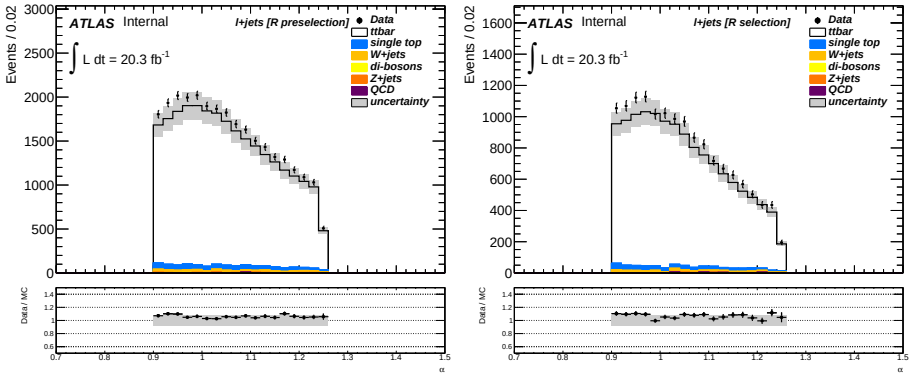

Figure 8: The α variable for which the four momentum of the hadronic W canididate is corrected, as explained in Section 5.3. The distribution is built from events which pass pre-selection cuts only (left) or events which pass the final $t\bar{t}+1$-jet selection (right).

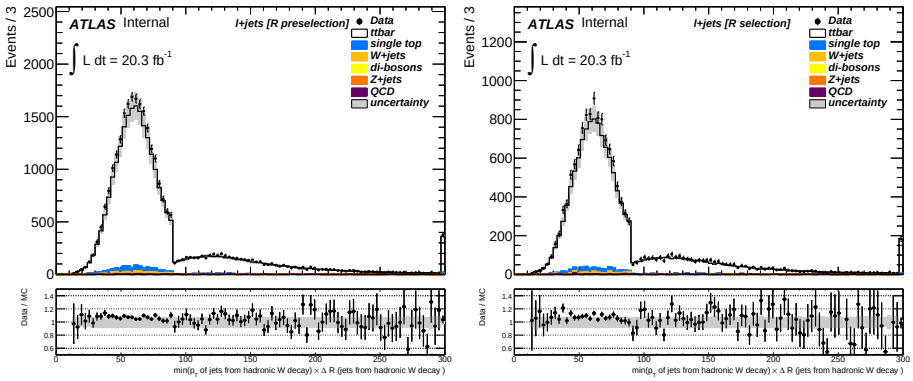

Figure 9: The Δk variable which is used to select jets coming from hadronic W candidates. The distribution is built from events which pass pre-selection cuts only (left) or events which pass the final $t\bar{t}+1$-jet selection (right).

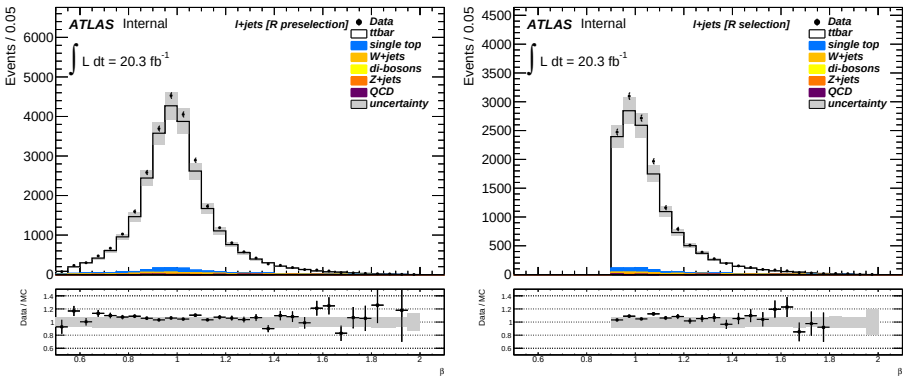

Figure 10: The $\beta = \frac{m_{\text{lep. top}}}{m_{\text{had. top}}}$ variable. The distribution is built from events which pass pre-selection cuts only (left) or events which pass the final $t\bar{t}$ + 1-jet selection (right).

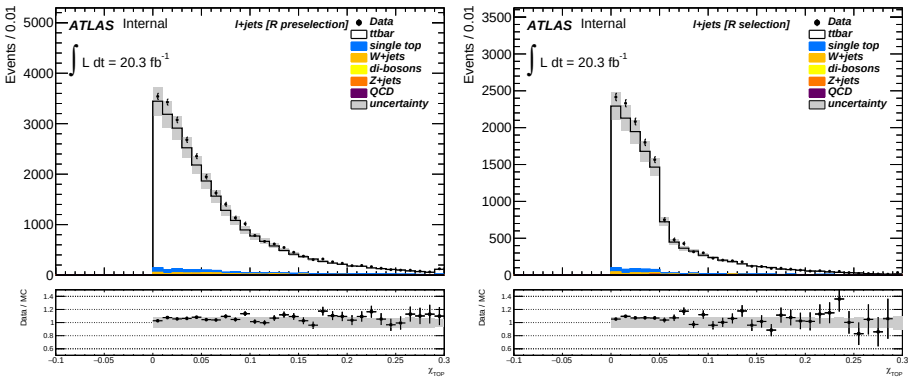

Figure 11: The $\chi_{\text{TOP}} = \frac{|m_{\text{lep. top}} - m_{\text{had. top}}|}{m_{\text{lep. top}} + m_{\text{had. top}}}$ which is minimized in the $t\bar{t}$ + 1-jetsystem reconstruction. The distribution is built from events which pass pre-selection cuts only (left) or events which pass the final $t\bar{t}$ + 1-jet selection (right).

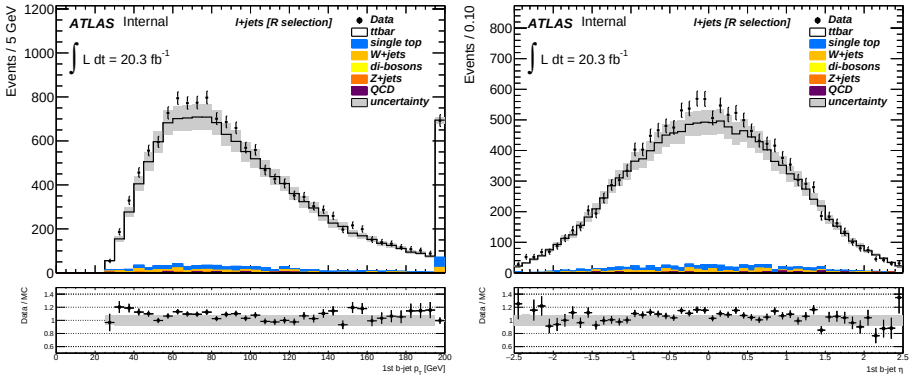

Figure 12: The p_t and η distribution of the leading selected b-jet, built from events passing the final $t\bar{t}$ + 1-jet selection.

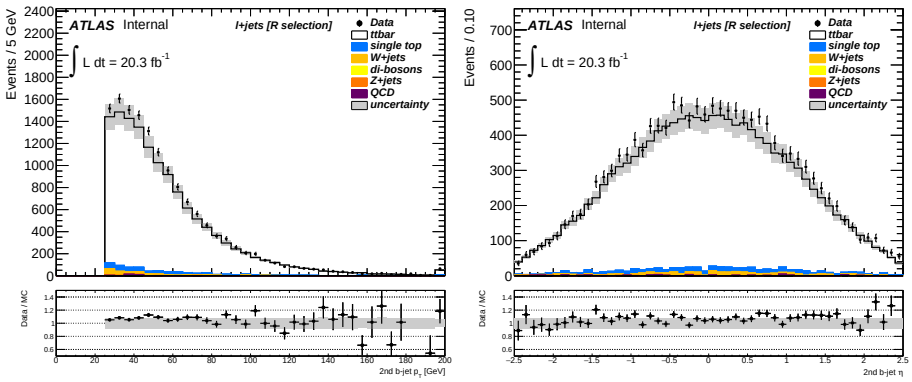

Figure 13: The p_t and η distribution of the sub-leading selected b-jet, built from events passing the final $t\bar{t}$ + 1-jet selection.

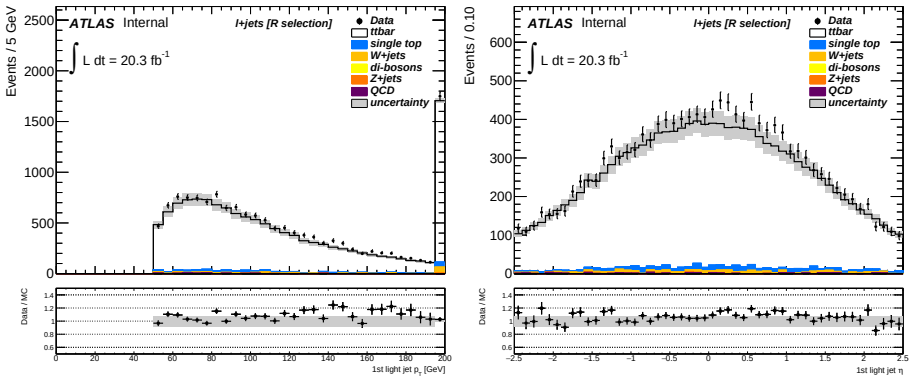

Figure 14: The p_t and η distribution of the leading selected light jet, built from events passing the final $t\bar{t}$ + 1-jet selection.

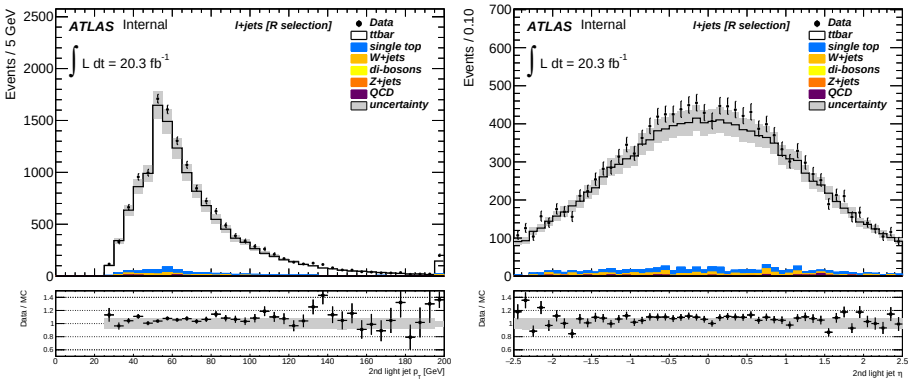

Figure 15: The p_t and η distribution of the sub-leading selected light jet, built from events passing the final $t\bar{t}$ + 1-jet selection.

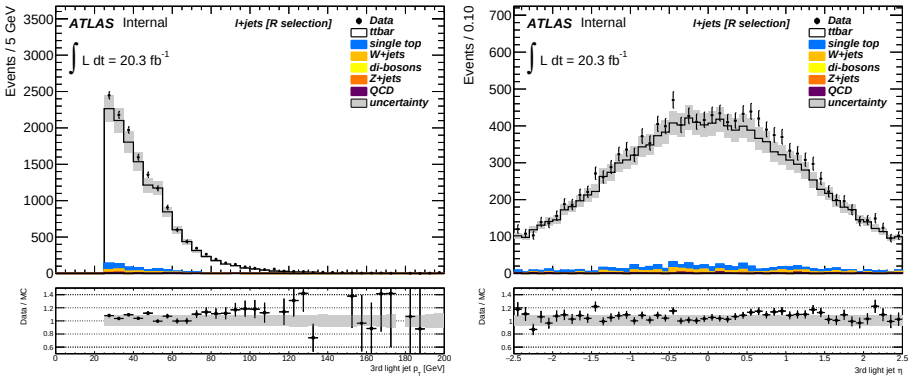

Figure 16: The p_t and η distribution of the sub-sub-leading selected light jet, built from events passing the final $t\bar{t}$ + 1-jet selection.

D Binning choice

After event selection and system reconstruction, it has been chosen to re-bin $\mathcal{R}$ with 8 variable-size bins. Different choices of the binning have been studied and are presented in this section. In particular we present studies performed for the binning used in [252] (6 variable-size bins). Bins definition are reported in Table 1.

binning	bins for $\rho_s < 0.675$				
6 bins	[0, 0.25]	[0.25, 0.325]	[0.325, 0.425]	[0.425, 0.525]	[0.525, 0.675]
8 bins	[0, 0.25]	[0.25, 0.325]	[0.325, 0.425]	[0.425, 0.525]	[0.525, 0.675]
	bins for $\rho_s > 0.675$				
6 bins	[0.675, 1]				
8 bins	[0.675, 0.725]		[0.725, 0.775]		[0.775, 1]

Table 1: Definition of the different binning choices studied.

In [252], bin choice was optimised to

- isolate regions where distribution is more sensitive on the mass and minimising migrations in this bin.
- isolate regions where the sensitivity is very low (in particular in $0.525 < \rho_s < 0.675$).
- maximise the number of events in the diagonal of the migration matrix.

That is why bins with $\rho_s < 0.675$ have not been modified. From $\rho_s > 0.675$ sensitivity on m_t^{pole} increases, which makes it worth to divide this ρ_s interval in more than one bin. The price to pay when dividing the $\rho_s \in [0.675, 1]$ interval in smaller bins is the loss of diagonality of the efficiency of the migration matrix. While increasing the number of bins, the migrations between them also increase. Efficiencies of the migration matrix for different choices of the binning are reported in Figure17

Data has been corrected to parton level with different choices of binning, with the nominal Bayesian unfolding procedure. Top-quark pole mass and its statistical uncertainty are then extracted minimising a χ^2 function and taking its ± 1 variations. The results obtained are:

$$\begin{aligned} m_t^{\text{pole}}(8 \text{ bins}) &= 171.05 + 0.43(\text{stat.}) \text{ GeV} \\ m_t^{\text{pole}}(6 \text{ bins}) &= 170.76 + 0.96(\text{stat.}) \text{ GeV} \end{aligned} \tag{3}$$

where method error includes ~ 0.2 GeV from uncertainties on parametrisation of $\mathcal{R}^{t\bar{t}+\text{1-jet}}_{\text{theo@NLO+PS}}(m_t^{\text{pole}})$, and ~ 0.20 GeV from errors in the choice of the unfolding regulator. Results are compatible within their errors.

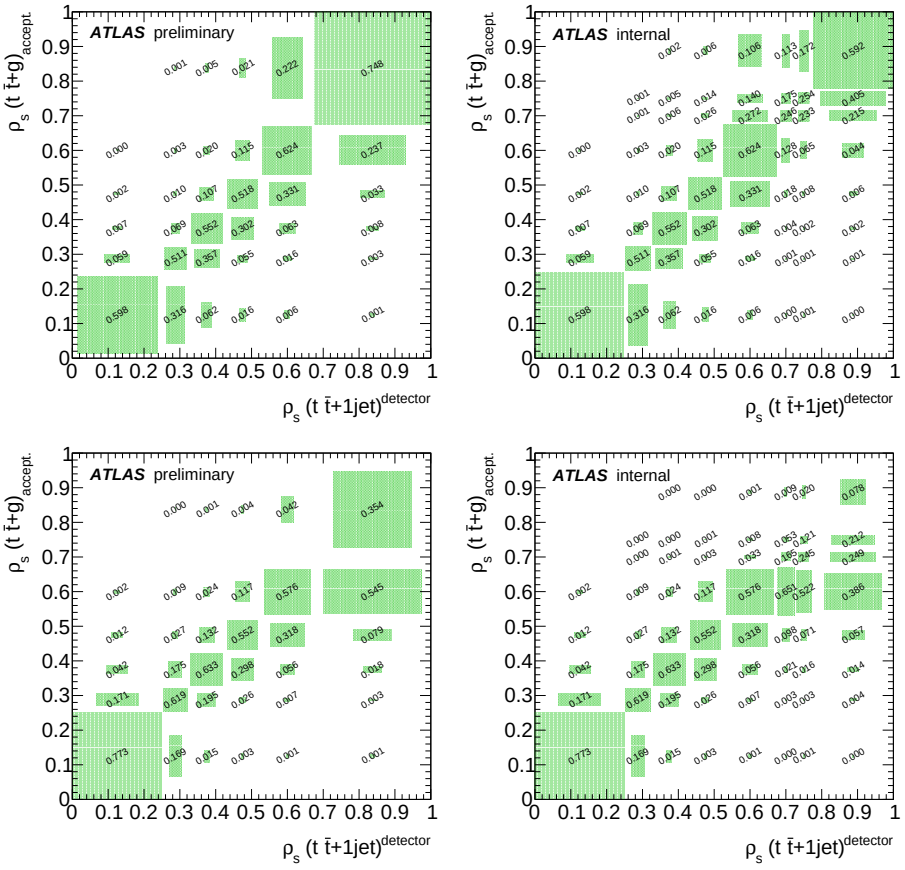

Figure 17: Efficiencies (top) and purities (bottom) of the migration matrix when choosing 6 bins (left) and 8 bins (right).

E Validation of private samples

As discussed in Section 6.1 a bin-by-bin correction to obtain the distribution from 1$^{\text{st}}$ emission level to the parton level is needed to compare with the theoretical calculation ($t\bar{t} + g \rightarrow t\bar{t} + 1$-jet). This last correction is obtained with the privately produced MC sample, in which the parton level information is saved. The private sample was validated using ATLAS samples and the validation plots are shown in Figure 18.

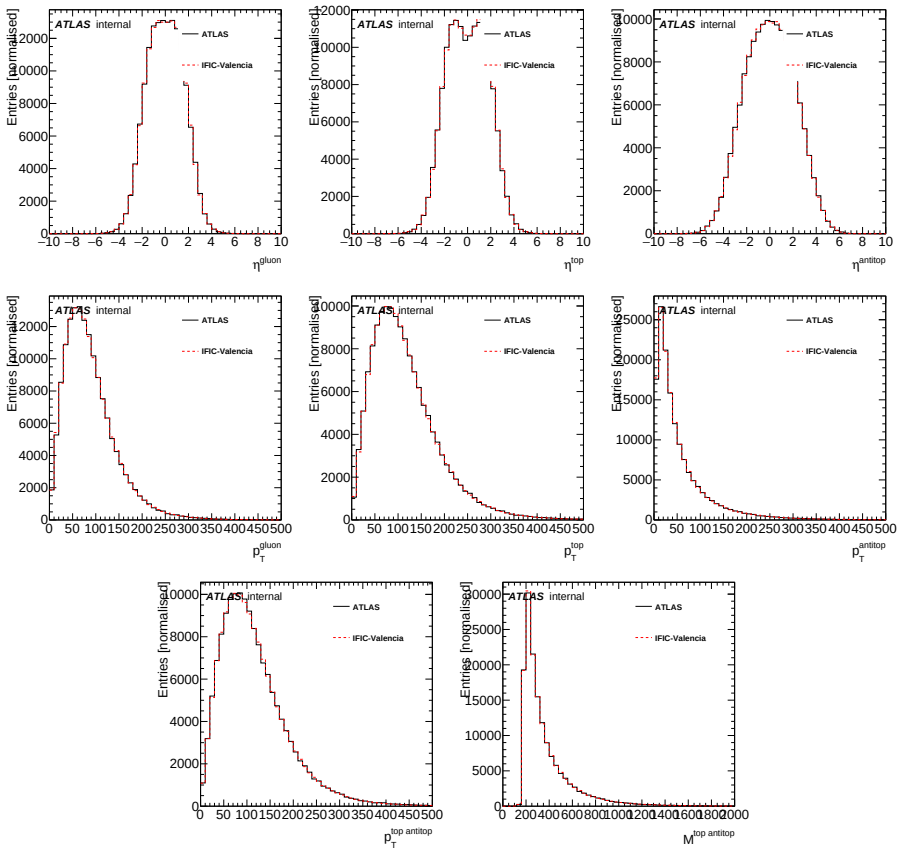

Figure 18: Validation plots for privately produced POWHEG $t\bar{t}$ MC samples. The validated samples are used as input to access the MC parton level information of the $t\bar{t} + 1$-jet system. The number of privately generated parton level events amount to 10^6.

F Unfolding algorithm

To correct data for detector (and hadronisation in our case) effect is a complex topic. Different algorithms exist which do it, eveyone with its positive and negative aspects. In [252] the SVD method [276] has been used to unfold data to parton level, while in this analysis the Bayesian one has been chosen. In this section this choice is motivated and the two methods are compared.

The unfolding problem can be formulated in the following way. Call $\mathcal{R}^{t\bar{t}+g}$ the truth distribution and $\mathcal{R}^{\mathrm{det}}$ the distribution measured after hadronisation and detector effects. The information on how the observable changes from truth to reco level is contained in a migration matrix $\mathcal{M}$.

For MC, both $\mathcal{R}^{t\bar{t}+g}$ and $\mathcal{R}^{\mathrm{det}}$ distributions are known, thus one can define $\mathcal{M}$, by:

$$\mathcal{R}^{t\bar{t}+g\,\mathrm{MC}} \times \mathcal{M} = \mathcal{R}^{\mathrm{det}\,\mathrm{MC}} \tag{4}$$

For data, the only distribution known is the one measured at detector level, $\mathcal{R}^{\mathrm{det}\,\mathrm{data}}$ and its correspondent truth distribution is obtained by inverting above equation:

$$\mathcal{R}^{t\bar{t}+g\,\mathrm{data}} = \mathcal{R}^{\mathrm{det}\,\mathrm{data}} \times \mathcal{M}^{-1} \tag{5}$$

This last step relies on the inversion of a matrix. To avoid large statistical fluctuations due to bins with few or zero events, matrix inversion has to be regularised. In the two unfolding methods studied in this section, the regularisation is handled by one parameter only for each method.

Of course one can test the closure of the method by checking that:

$$\mathcal{R}^{t\bar{t}+g\,\mathrm{truth}} \sim \mathcal{R}^{\mathrm{det}\,\mathrm{MC}} \times \mathcal{M}^{-1} \tag{6}$$

as it is shown in Figure 19.

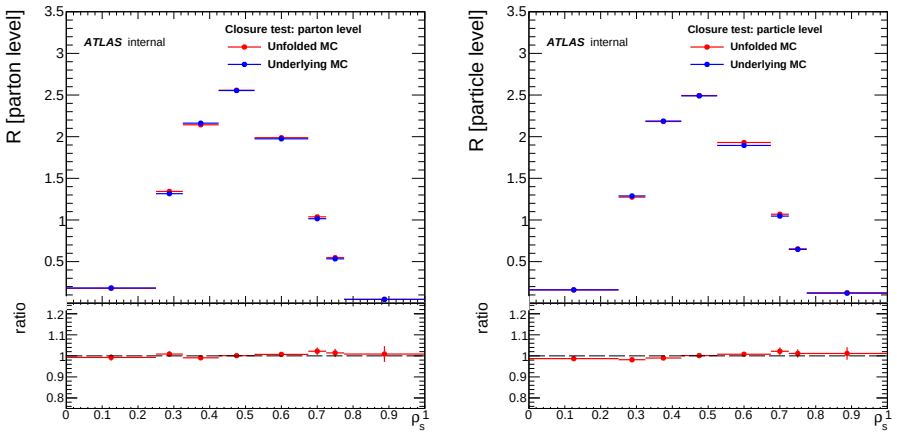

Figure 19: Closure test of the unfolding procedure to parton level (left) and particle level (right). The unfolded nominal $t\bar{t}$ MC sample is compatible with the truth distribution.

The SVD method relies on the choice of a parameter, called k_{reg}, which determines how strongly the unfolded distribution is regularised. Too low values of k_{reg} bias the unfolded distribution towards the reference MC distribution, while higher values bias give more weight to the spectrum to be unfolded. If the distribution has been binned in n bins, k_{reg} can take values between 1 to n. A $k_{\text{reg}} = 1$ gives exactly the underlying MC truth distribution. This algorthm performs better for distributions with a high number of bins, which is not our case. For few bins, few values of k_{reg} can be tested, and sometimes convergence of the procedure is not reached.

The Bayesian unfolding is an iterative method in which the strength of the unfolding is handled by the number of iterations performed (n_{iter}). Too small values of n_{iter} bias the distribution towards MC, while too high iterations gives too big uncertainty on the measurement and the unfolded distribution start to fluctuate within its error.

For both methods, no precise prescription exists for the choice of the unfolding parameter. Thus the observable is unfolded using the two methods and k_{reg} and n_{iter} are chosen in such a way that the extracted values of m_t^{pole} and their statistical errors are compatible. Plots comparing the extracted values and their statistical errors are reported in Figure 20, for the 6 bins and 8 bins binning choices. For 10 bins, the SVD method did not converge, so no plot is reported.

The unfolding method chosen for this analysis is the Bayesian one, since variations of its regularator parameter give more stable results for m_t^{pole} and its statistical error. The number of iterations chosen to obtain the nominal result is 20. Variations of $\Delta n_{\text{iter}} = \pm 5$ around the nominal value have been taken to estimate the uncertainty on the choice of the regularisation parameter. Their impact on m_t^{pole} is ~ 0.20 GeV.

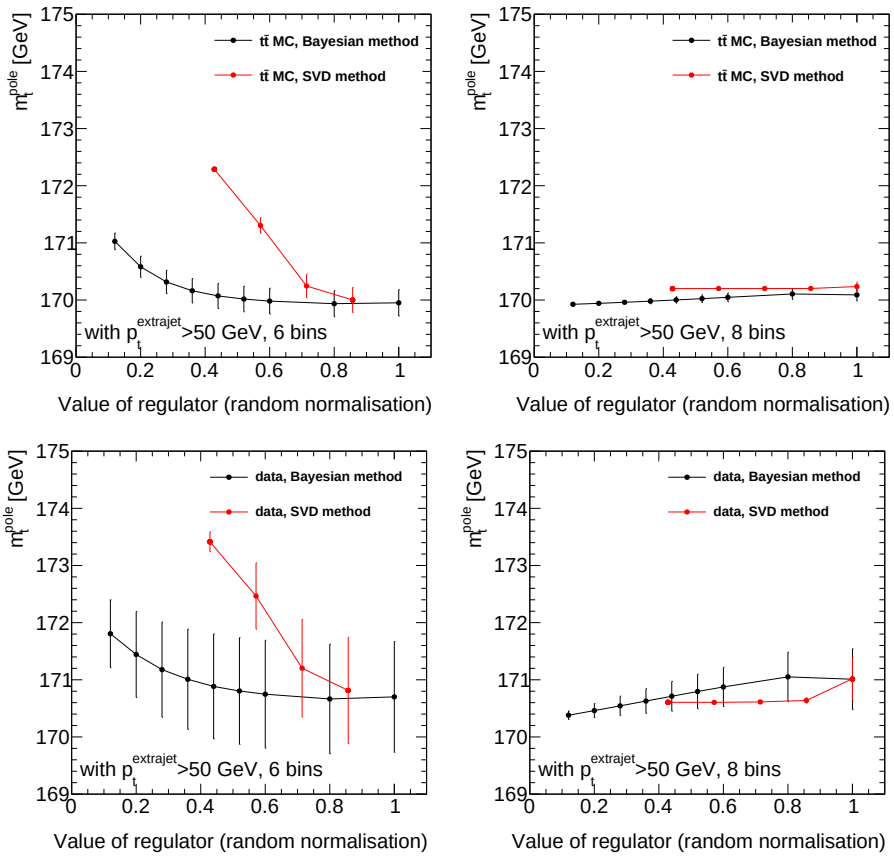

Figure 20: Dependence of the extracted pole mass on the unfolding algorithm. Results for the SVD (red) and Bayesian (black) methods are shown, for different values of the regularisation parameter. Plots for nominal $t\bar{t}$ MC (top), used in the definition of the unfolding procedure, and data (bottom) are reported. Values of the regularisation parameters increase along the x-axis. Higher values approach values of 1 on the x-axis. k_{reg} values between 3 and 7 are shown, $k_{\mathrm{reg}} = 7$ is forbidden for a 6bins binning choice. Values of n_{iter} are shown up to $n_{\mathrm{iter}} = 25$.

F.1 Pull distributions - parton level

To validate the unfolding procedure, pseudo data samples have been generated by varying the bin content of the observable at detector error indipendently, according to a Poisson distribution with mean values the nominal bin values. Pull distributions defined as $P_i = \frac{N_i^{\text{pseudo}} - N_i^{\text{nominal}}}{\sigma_i^{\text{pseudo}}}$ have been produced for each bin of the unfolded observable. Distributions were found to be compatible with gaussian distributions centered in zero and width compatible with the unity, as it is shown in Figure 21. This test confirms that the analysis procedure is unbiased and correctly estimates the statistical uncertainties.

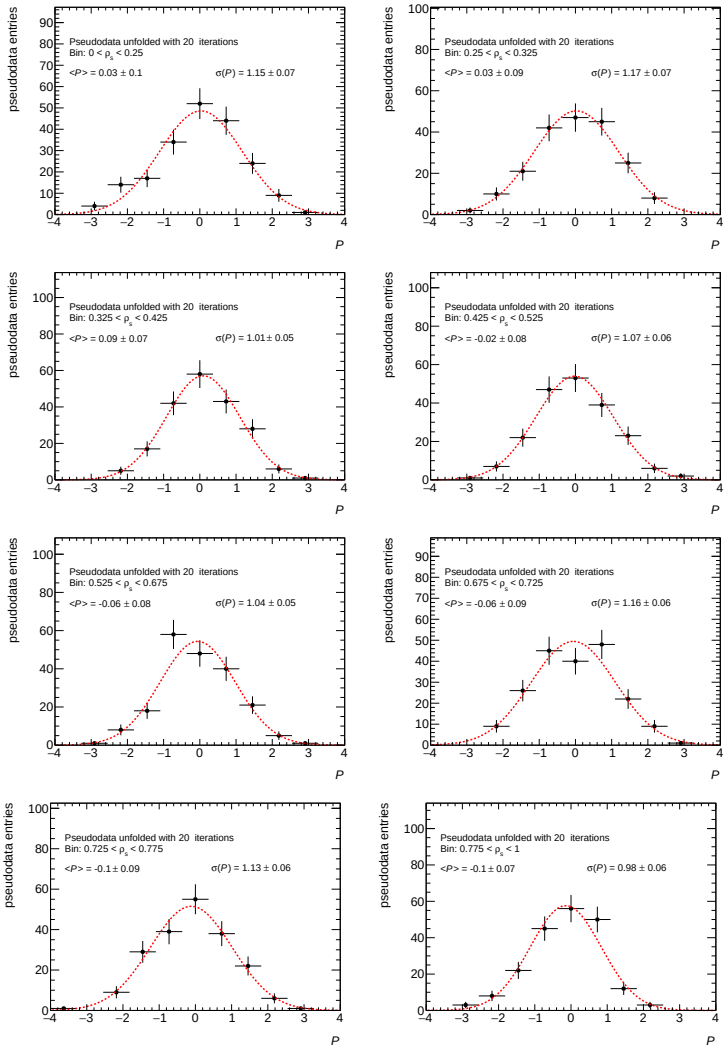

Figure 21: Pull distributions for each bin of the observable corrected to parton level. The distributions were found to be centered in zero with width compatible with the unity.

F.2 Pull distributions - particle level

The same valdation discussed in has been applied to the unfolding to particle level. Also in this case, the test confirms that the correction procedure is unbiased and correctly estimates the statistical uncertainties.

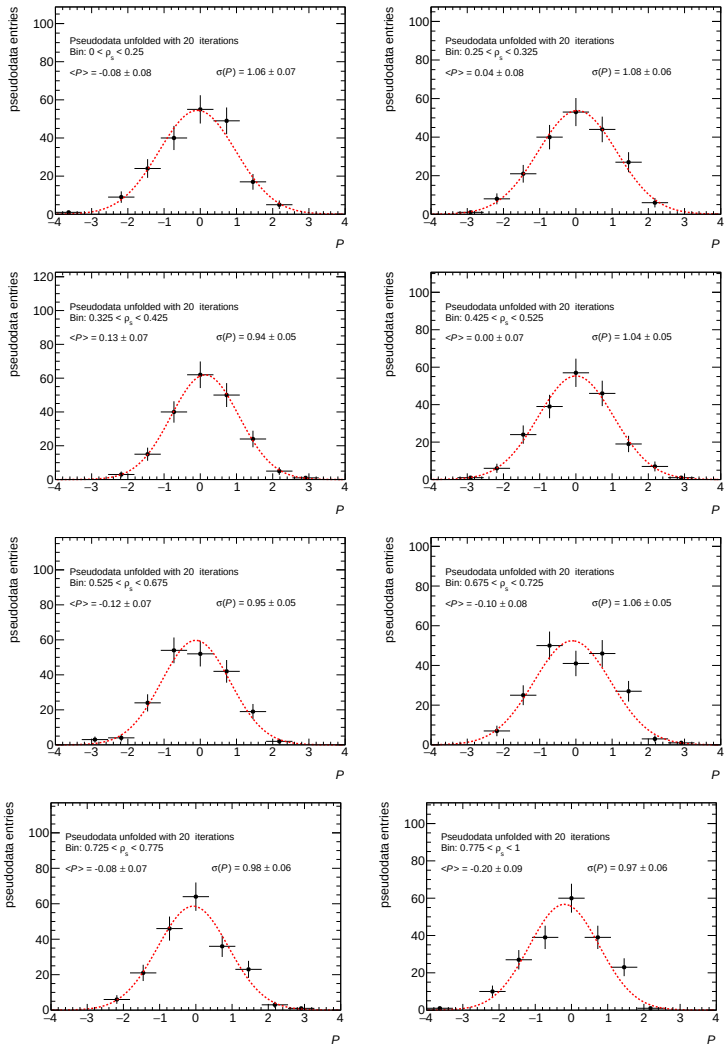

Figure 22: Pull distributions for each bin of the observable corrected to particle level. The distributions were found to be centered in zero with width compatible with the unity.

G Consideration on $f^{\text{Ph.Sp.}}$ correction factors

In this appendix details are given on the phase space correction factor $f^{\text{Ph.Sp.}}$, which is used in bin-by-bin correction of data in Section 6.2.

As already shown in Figure 23, the effect of introducing such a correction is of the order of $\frac{1\%}{\text{GeV}}$, in a range of masses considered going from 165 to 180 GeV. Such a correction can be translated into a correction of $\sim \frac{0.15\ \text{GeV}}{\text{GeV}}$, starting from the mass value of the nominal MC used in the unfolding procedure.

To cross-check that the correction procedure actually works correctly, it is possible to extract masses from $t\bar{t}$ MC with an input m^{IN} in the range [165 GeV , 180 GeV]. As it can be seen from Figure 6.5, the correct value of the mass is extracted from the $t\bar{t}$ MCs. Hence, data correction procedure is independent of the input top-quark mass value.

Another aspect to study is the dependence of the correction with the binning of the observable. If choosing the same binning used in the 7 TeV analysis [252], the correction factors are shown in Figure 24. The correction is negligible, taking into account the precision with which m_t is extracted.

This is due to the fact that the extrapolation to fulll phase space is less sensitive to events in a small corner of phase space, when a less fine grained binning is chosen.

Since the analysis with a 6-bins observable does not suffer from this correction, it is possible to estimate the error on such a correction by comparing the top-quark mass values of the 6 bin analysis with the result obtained using the 8-bins observable. Comparison of the results is presented in Table 2. As a systematic uncertainty on the correction, half of the maximum difference between both values. It amounts to 0.15 GeV.

# bins	m_t^{pole} with $f^{\text{Ph.Sp.}}$ correction [GeV]	m_t^{pole} without $f^{\text{Ph.Sp.}}$ correction [GeV]
6 bins	170,76	170,67
8 bins	171,05	170,79

Table 2: m_t^{pole} extracted values for a 6-bins and a 8-bins observable, with and without applying the phase space correction factor.

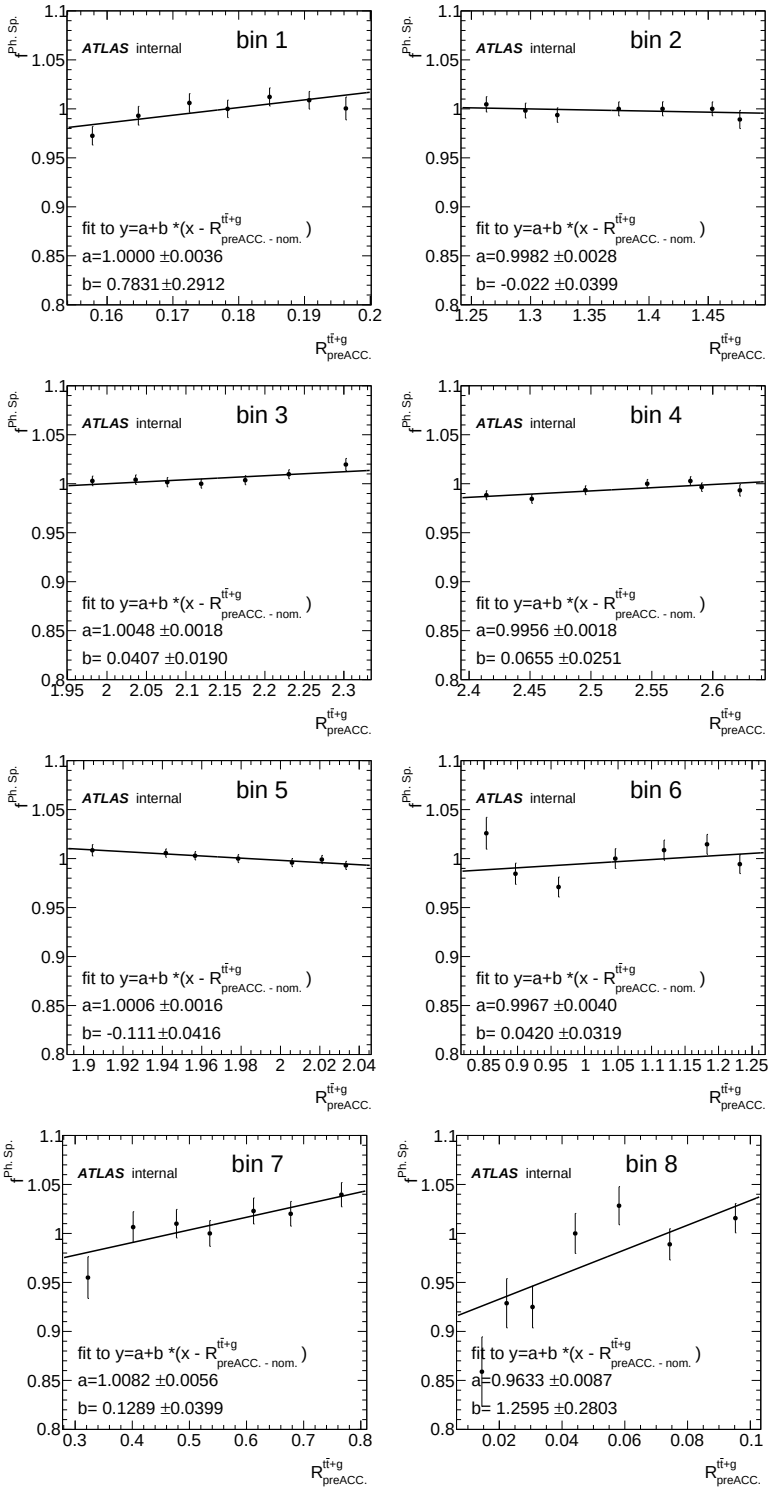

Figure 23: The correction factor $f^{\mathrm{Ph.Sp.}}\left(\rho_{\mathrm{s}}, \mathcal{R}^{t\bar{t}+g}_{\mathrm{preACC.}}\right)$, for each of the 8 bins used in the analysis. Each plot correspond to a bin of Figure 6.2. Each point i in the plot of bin j reported above correspond to the quantity $f^{\mathrm{Ph.Sp.}}{}_{i}^{[\text{bin-}j]} = \frac{f(\mathcal{R}^{t\bar{t}+g}_{\mathrm{preACC.}}{}^{[\text{bin-}j]}(m_i))}{f^{\mathrm{nominal}}}$. The $f(\mathcal{R}^{t\bar{t}+g}_{\mathrm{preACC.}}{}^{[\text{bin-}j]}(m_i))$ factors are reported in Figure 6.2 and f^{nominal} in 6.1. The parametrisation has been functionally continued by a first order polynomial.

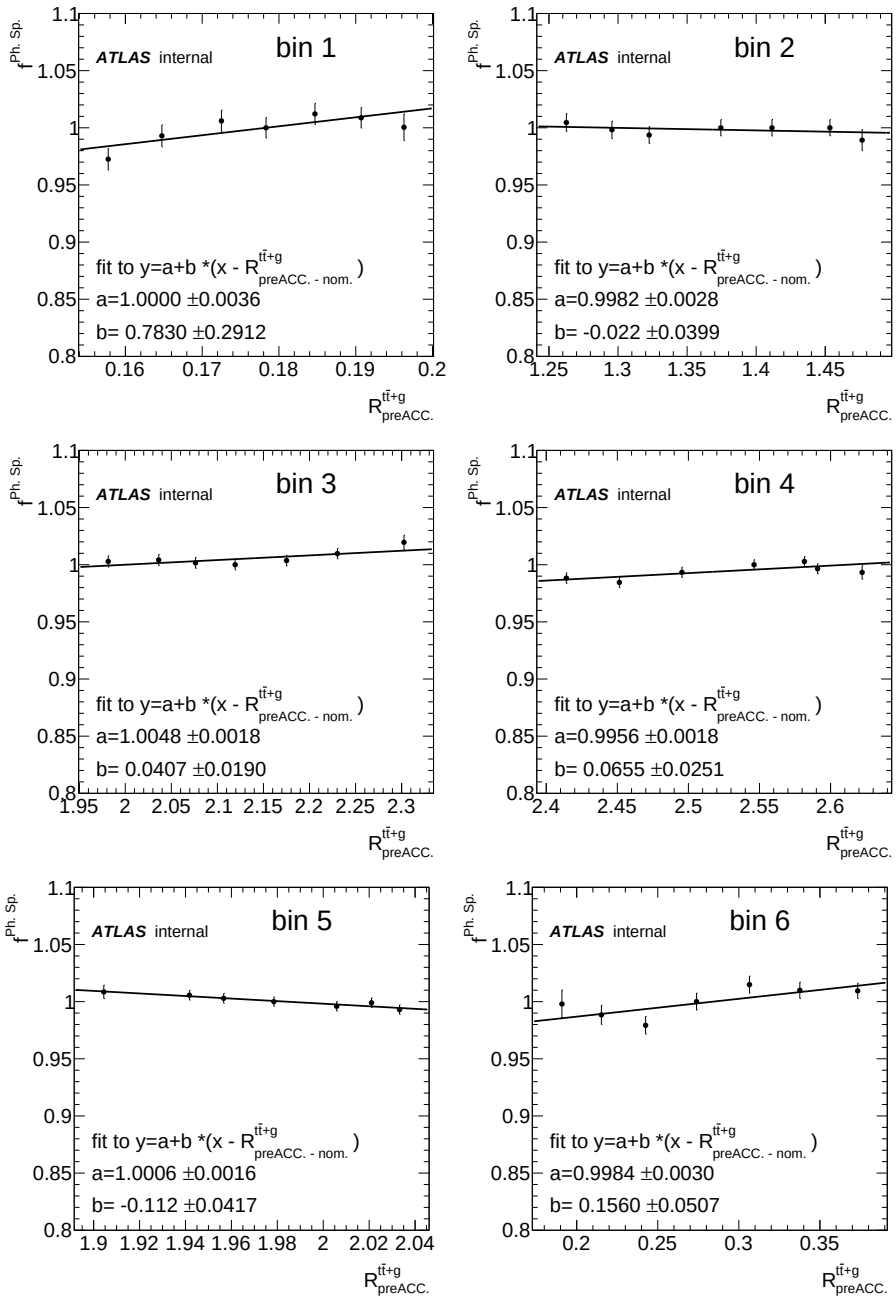

Figure 24: Same as Figure 23, but showing the effect of the correction on a 6 bins observable. Correction is negligible.

H Bins removal from χ^2

Since the observable used in the extraction of m_t^{pole} is normalised, not all its bins are independent between each other. To take this fact into account one bin is removed from the sum over all bins which is performed in the calulation of the χ^2. The nominal choice has been to remove the first bin, with $\rho_s \in (0, 0.25)$, since it improved the value of the χ^2 at the minimum. Other choices could have been performed in principle, but as it is shown in Table 3, the differences are minimal.

Removed bin	m_t^{pole} [GeV]	Δm_t^{pole} (stat) [GeV]
$0 < \rho_s < 0.25$	171.05	0.43
$0.25 < \rho_s < 0.325$	170.94	0.42
$0.325 < \rho_s < 0.425$	170.80	0.41
$0.425 < \rho_s < 0.525$	170.89	0.41
$0.525 < \rho_s < 0.675$	170.85	0.41

Table 3: Value of extracted pole mass at parton level, for different choices of removed bin.

As it is seen from the bin-by-bin fit at detector level, in Figure7.4, the high value of χ^2 is due to bins at low ρ_s.

I Discussion on the *hdamp* parameter

The *hdamp* parameter determines the strength of the NLO correction in POWHEG. For $t\bar{t}$ + 1-jet@ NLO the *hdamp* parameter controls the strength of the second-leading jet, hence it poorly affects the $t\bar{t}$ + 1-jetsystem, only through clustering effects. However the $\mathcal{R}$ observable built from $t\bar{t}$ @ NLO production is instead affected by the choice of *hdamp* since the four momentum of the leading extra-jet of the $t\bar{t}$ + 1-jet system (contrary to the $t\bar{t}$ + 1-jet@ NLO+PS case) entirely depends on it. Large effects are thus obtained in this case as reported in [277] (Table 13), where differences up to $\sim$ 3 GeV are seen for the top-quark mass. Similar effects are seen for $\mathcal{R}$.

In addition the migration matrix is fairly insensitive to this parameter. When unfolding data with alternative $t\bar{t}$ MC samples with *hdamp*= ∞, and using $t\bar{t}$ + 1-jet@ NLO+PS theoretical prediction as a template for the fit at parton level, results in a difference in the extracted top-quark mass of:

$$\Delta m_t^{\text{pole}}(\textit{hdamp } t\bar{t} \text{ unfolding}) \sim 0.20 \text{ GeV}$$

well within the statistical uncertainty.

In summary the *hdamp* parameter has a negligible impact on $\mathcal{R}$ when constructed from the $t\bar{t}$+1-jet@ NLO+PS calculation and furthermore the unfolding procedure is very little affected by the choice of *hdamp*.

J Stressing the unfolding

To validate the analysis procedure, a series of test has been performed to confirm that both statistical and systematic errors have been correctly evaluated.

To confirm that the output of the unfolding algorithm gives is correct, corrected distributions have been folded with the procedure described in Section 7.1 and then compared to their detector level respectives. No bias can be seen when comparing the distributions, as it can be seen in Figures 25, 26 and 27.

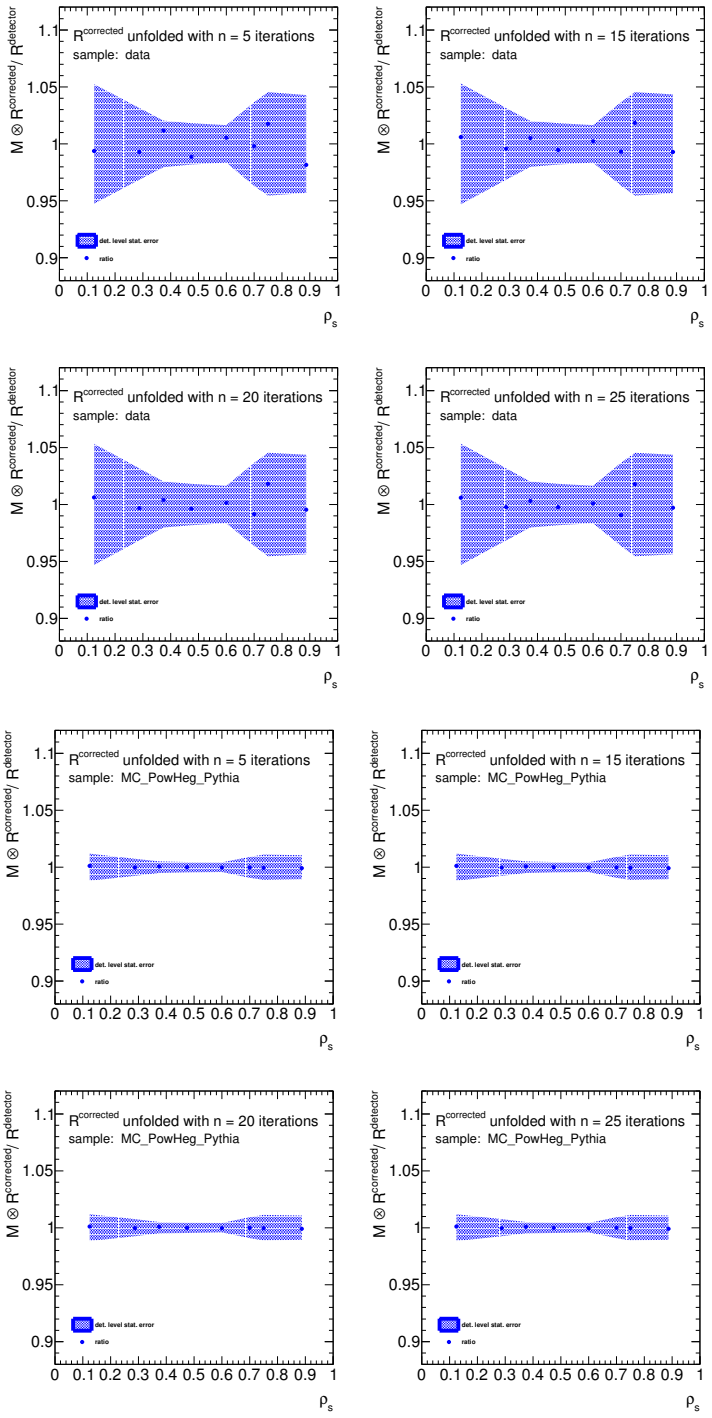

Figure 25: Ratios of detector level observable against the folded corrected distribution at parton level. Different values of the the number of iterations of the Bayesian unfolding algorithm. For all the samples unfolded with $n >= 15$ the ratio is 1, within the statistical errors of the detector level distribution. Here data and nominal $t\bar{t}$ MC samples are shown.

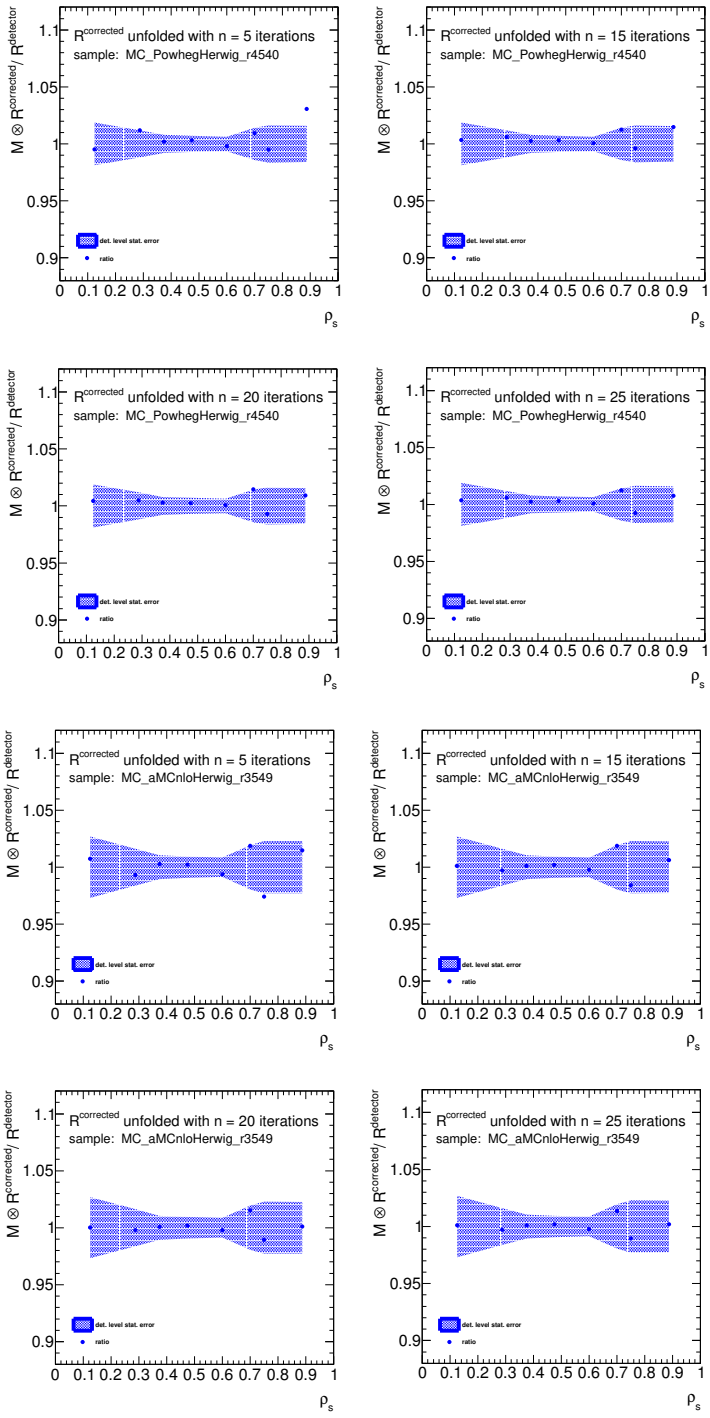

Figure 26: Ratios of detector level observable against the folded corrected distribution at parton level. Different values of the the number of iterations of the Bayesian unfolding algorithm. For all the samples unfolded with $n >= 15$ the ratio is 1, within the statistical errors of the detector level distribution. Here two alternative $t\bar{t}$ MC samples are shown.

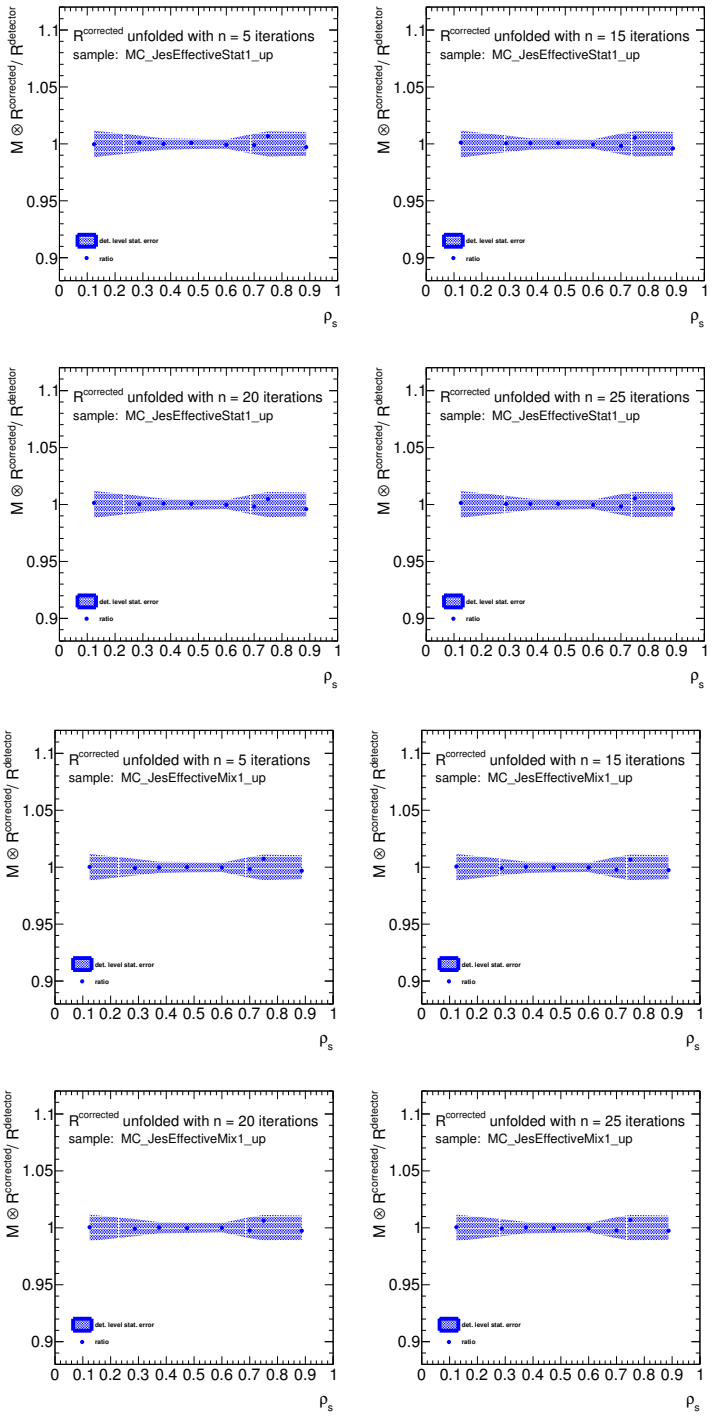

Figure 27: Ratios of detector level observable against the folded corrected distribution at parton level. Different values of the the number of iterations of the Bayesian unfolding algorithm. For all the samples unfolded with $n >= 15$ the ratio is 1, within the statistical errors of the detector level distribution. Here two detector systematic variations are shown.

K Detector level fit using migration matrix

At detector level, the top quark pole mass is extracted by fitting collected data to parton level theoretical predictions which have been folded to detector level.

In the following let us call:

- $\mathcal{R}_i^{\text{data}}$ the value of the observable built from collected data in the bin i,
- $\mathcal{R}_i^{\text{det-theo}}$ the expected value of the observable at detector level in the bin i,
- $\mathcal{R}_i^{\text{parton-theo}}$ the expected value of the observable at parton level in the bin i,
- M_{ij} the migration matrix from parton to detector level (including acceptance cuts).

To obtain detector level predictions for the observable $\mathcal{R}$, we folded parton level calculations using the migration matrix M_{ij}, obtaining:

$$\mathcal{R}_i^{\text{det-theo}} = \sum_{j \in \text{bins}} M_{ij} \cdot \mathcal{R}_j^{\text{parton-theo}} \tag{7}$$

To extract a value for the mass the χ^2 function to be minimised is defined as:

$$\chi^2 = \sum_{i \neq i_0} \frac{\left(\mathcal{R}_i^{\text{data}} - \mathcal{R}_i^{\text{det-theo}}(m_t^{\text{pole}})\right)^2}{{\sigma_i^{\text{det-theo}}}^2} \tag{8}$$

where $\sigma_i^{\text{det-theo}}$ is the expected statistical error on the bin i, and i_0 is the bin excluded in the minimisation, since we are using normalised distributions.

If one would ignore bin correlations, the correct value to chose for $\sigma_i^{\text{det-theo}}$ would be the square root of the events in bin i, which correspond to suppose for every bin a Poissonian distribution with parameter the bin content. However, this is not the case if bins at detector level are a correlation of parton level bins. Also when unfolding to parton level, the correlelation between detector level bins are used in the fit, through the covariance matrix. Hence, one has to compute the the expected variance of $\mathcal{R}_i^{\text{det-theo}}$, i.e. $\text{Var}(\mathcal{R}_i^{\text{det-theo}}) = {\sigma_i^{\text{det-theo}}}^2$.

Here the detailed calculation of $\text{Var}(\mathcal{R}_i^{\text{det-theo}})$ is presented. The equations used in the derivation are known properties of the variance:

- Variance of a linear combination of distributions f_i, with coefficients a_i:

$$\text{Var}\left(\sum_i a_i f_i\right) = \sum_i a_i^2 \text{Var}(f_i) + \sum_i \sum_{j \neq i} a_i a_j \text{COV}(f_i, f_j) \tag{9}$$

- Covariance of two independent distributions f_k and f_j:

$$\text{COV}(f_k, f_j) = 0 \tag{10}$$

- Covariance of the same distribution:

$$\text{COV}(f_j, f_j) = \text{Var}(f_j) \tag{11}$$

- Simmetry of the covariance:

$$\mathrm{COV}(f_k, f_j) = \mathrm{COV}(f_j, f_k) \tag{12}$$

Using Eq. 12, Eq. 9 can be written as:

$$\mathrm{Var}\left(\sum_i a_i f_i\right) = \sum_i a_i^2 \mathrm{Var}(f_i) + 2\sum_i \sum_{j>i} a_i a_j \mathrm{COV}(f_i, f_j) \tag{13}$$

Being the $\mathcal{R}$ distribution at parton level normalised, all their bins but one are independent from each others, i.e:

$$\mathcal{R}_{k_0}^{\text{parton-theo}} = 1 - \sum_{j \neq k_0} \mathcal{R}_j^{\text{parton-theo}} \tag{14}$$

The choice of the value of k_0 is arbitrary and has no impact on the final result. All t_j with $j \neq k_0$ are independent from each others. Hence, from Eq. 10 and Eq. 11, the following properties follow:

- if $j, k \neq k_0$ and $j \neq k$

$$\mathrm{COV}(\mathcal{R}_j^{\text{parton-theo}}, \mathcal{R}_k^{\text{parton-theo}}) = 0 \tag{15}$$

- if $j \neq k_0$

$$\begin{aligned}
\mathrm{COV}(\mathcal{R}_j^{\text{parton-theo}}, \mathcal{R}_{k_0}^{\text{parton-theo}}) &= \mathrm{COV}\left(\mathcal{R}_j^{\text{parton-theo}}, 1 - \sum_{k \neq k_0} \mathcal{R}_k^{\text{parton-theo}}\right) = \\
&= \mathrm{COV}(\mathcal{R}_j^{\text{parton-theo}}, \mathcal{R}_j^{\text{parton-theo}}) + \sum_{k \neq j, k_0} \mathrm{COV}(\mathcal{R}_j^{\text{parton-theo}}, \mathcal{R}_k^{\text{parton-theo}}) \\
&= \mathrm{COV}(\mathcal{R}_j^{\text{parton-theo}}, \mathcal{R}_j^{\text{parton-theo}}) = \\
&= \mathrm{Var}(\mathcal{R}_j^{\text{parton-theo}})
\end{aligned} \tag{16}$$

Using Eq. 13 and then Eq. 15 and Eq. 16 one gets:

$$\begin{aligned}
\mathrm{Var}(\mathcal{R}_i^{\text{det-theo}}) &= \mathrm{Var}\left(\sum_j M_{ij} \mathcal{R}_j^{\text{parton-theo}}\right) = \\
&= \sum_j M_{ij}^2 \mathrm{Var}(\mathcal{R}_j^{\text{parton-theo}}) + 2\sum_j \sum_{k>j} M_{ij} M_{ik}\ \mathrm{COV}(\mathcal{R}_j^{\text{parton-theo}}, \mathcal{R}_k^{\text{parton-theo}}) = \\
&= \sum_j M_{ij}^2 \mathrm{Var}(\mathcal{R}_j^{\text{parton-theo}}) + 2\sum_j M_{ij} M_{ik_0} \mathrm{Var}(\mathcal{R}_j^{\text{parton-theo}}) = \\
&= \sum_j M_{ij} \left[M_{ij} + 2M_{ik_0}\right] \mathrm{Var}(\mathcal{R}_j^{\text{parton-theo}})
\end{aligned}$$

which is the final formulation of the variance to be used in the χ^2 definition.

Then the last question to answer is what $\mathrm{Var}(\mathcal{R}_j^{\text{parton-theo}})$ is. In our approximation, top-quarks are produced as stable particles at parton level. Hence

we assume that in each bin, $\mathcal{R}_j^{\text{parton-theo}}$ follows a Poisson distribution with parameter value the expected bin content.

The final expression of the χ^2, including correlation between bins at detector level, becomes:

$$\chi^2 = \sum_{i \neq i_0} \frac{\left(\mathcal{R}_i^{\text{data}} - \sum_k M_{ik} \cdot \mathcal{R}_k^{\text{parton-theo}}(m_t^{\text{pole}})\right)^2}{\sum_j M_{ij}\left[M_{ij} + 2M_{ik_0}\right]\mathcal{R}_j^{\text{parton-theo}}(m_t^{\text{pole}})} \tag{17}$$

Notice that in case of no correlations between bins M_{ij} is the identity matrix, and Eq. 17 is the same as Eq. 8.

With this χ^2 definition one would get for the top quark pole mass at detector level:

$$m_t^{\text{pole}}(\text{detector level}) = 170.74 \pm 0.48(\text{stat})\ \text{GeV} \tag{18}$$

which is in good agreement with the result presented in Eq. 7.7, but has statistical error compatible to the parton level result reported in Table 6.6.

It is possible to compare different kind of fits ad check wether they give the same results. The fit at parton level corrects data via unfolding and introduce bin correlation also through the covariance matrix. Results for such fit are presented in Table 6. At the detector level, one can ignore bin correlations (Table 4) and hence overestimate the error, or include them (Table 5) and obtain a result close to the parton level one.

excluded bin	m_t^{pole}	stat error
$i_0 = 1$	170.91	0.71
$i_0 = 2$	170.77	0.71
$i_0 = 3$	170.41	0.70
$i_0 = 4$	170.50	0.69

Table 4: Extraction of the top-quark mass at parton level when ignoring bin correlations at detector level.

excluded bin (while $k_0 = 1$)	m_t^{pole}	stat error
$i_0 = 1$	171.16	0.39
$i_0 = 2$	171.19	0.40
$i_0 = 3$	171.07	0.38
$i_0 = 4$	171.09	0.38

normalisation bin (while $i_0 = 1$)	m_t^{pole}	stat error
$k_0 = 1$	171.16	0.38
$k_0 = 2$	171.14	0.38
$k_0 = 3$	171.14	0.40
$k_0 = 4$	171.21	0.41

Table 5: Extraction of the top-quark mass at detector level when taking into account bin correlations

excluded bin	m_t^{pole}	stat error
$i_0 = 1$	171.05	0.43
$i_0 = 2$	170.94	0.42
$i_0 = 3$	170.80	0.41
$i_0 = 4$	170.89	0.41

Table 6: Fit at parton level using covariance matrix, which include bin correlations

Description	Value [GeV]	stat. unc on syst [GeV]
$m_t^{\mathbf{pole}}$	**170.91**	
Statistical uncertainty	**0.71**	
MC statistics	0.25	–
Signal MC generator	1.16	0.3
Shower and hadronization	1.20	0.22
Proton PDF	0.79	–
ISR/FSR	0.98	0.23
Color reconnection	0.11	0.49
Underlying event	0.35	0.43
JES (with b-JES)	0.97	0.68 (26comp)
JER	0.12	0.47 (11comp)
others (MET, lep, b-tag, jeff, bkg)	0.48	–
Total exp. systematics	**2.39**	–
Scale variations	$(+0.76, -0.52)$	0.13
Theory PDF$\oplus\alpha_s$	0.55	0.1
Total theory systematics	**(+ 0.94, - 0.76)**	-
Total uncertainty	**(+ 2.68, -2.61)**	-

Table 7: Breakdown of the systematic error on the measurement at detector level, when ingoring correalations between bins. The total error happens to be larger than the parton level one. Statistical error on the systematic uncertainty does not take into account statistical correlations.

L Sensitivity of the observable at different levels

In 8.1 it has been shown how the sensitivity of the observable to m_t^{pole} is degraded at particle and detector levels. In this appendix this effect is explained with an example.

Firstly, simplify the folding of the observable as follows:

$$\mathcal{R}'_i = \sum_j M_{ij}\mathcal{R}_j, \tag{19}$$

where i and j are the bin numbers and M_{ij} the migration matrix. Then the sensitivity at the folded level is:

$$\begin{aligned}
\mathcal{S}'_i &= \frac{|\mathcal{R}'_i(m_0+\Delta) - \mathcal{R}'_i(m_0-\Delta)|}{2\Delta\cdot\mathcal{R}'_i(m_0)} \\
&= \frac{\left|\sum_j M_{ij}\mathcal{R}_j(m_0+\Delta) - \sum_k M_{ik}\mathcal{R}_k(m_0-\Delta)\right|}{2\Delta\cdot\mathcal{R}'_i(m_0)} \\
&= \sum_j \frac{M_{ij}\,|\mathcal{R}_j(m_0+\Delta) - \mathcal{R}_j(m_0-\Delta)|}{2\Delta\cdot\mathcal{R}'_i(m_0)}\cdot\frac{\mathcal{R}_j(m_0)}{\mathcal{R}_j(m_0)} \\
&= \sum_j M_{ij}\cdot\frac{\mathcal{R}_j(m_0)}{\mathcal{R}'_i(m_0)}\cdot\mathcal{S}_j
\end{aligned} \tag{20}$$

In the last two steps it has been multiplied and divided by $\mathcal{R}_j(m_0)$ and it has been used the definition of $\mathcal{S}_i$. In particular, it is possible to isolate the same bin number from the others, and write:

$$\mathcal{S}'_i = w_{ii}\mathcal{S}_i + \sum_{j\neq i} w_{ij}\mathcal{S}_j \qquad \text{with} \quad w_{ij} = M_{ij}\cdot\frac{\mathcal{R}_j(m_0)}{\mathcal{R}'_i(m_0)} \tag{21}$$

Notice that from Equation 19, it immediately follows that:

$$\sum_j w_{ij} = \frac{\sum_j M_{ij}\mathcal{R}_j(m_0)}{\mathcal{R}'_i(m_0)} = 1 \tag{22}$$

Consider now two particular cases, which show that the particle level is bound to be less sensitive than the parton level. In the case of a perfect reconstruction of the $t\bar{t}+1$-jet system, one would have a perfectly diagonal migration matrix and $R_i = R'_i$, obtaining thus $\mathcal{S}'_i = \mathcal{S}_i$. Hence, the more diagonal the folding matrix (i.e. the better the $t\bar{t}+1$-jet system reconstruction), the higher the sensitivity at particle level. Imagine now that at parton level, bin i has the highest sensitivity, which means that $S_j < S_i \;\forall\; j \neq i$. This is what happens for the $\mathcal{R}$ observable in the bin closest to $\rho_s \sim 1$. From Equation 21:

$$\begin{aligned}
\mathcal{S}'_i = w_{ii}\mathcal{S}_i + \sum_{j\neq i} w_{ij}\mathcal{S}_j < w_{ii}\mathcal{S}_i + \sum_{j\neq i} w_{ij}\mathcal{S}_i < \\
< \left(\sum_j w_{ij}\right)\mathcal{S}_i < \mathcal{S}_i
\end{aligned} \tag{23}$$

where it has been used $\mathcal{S}_j < \mathcal{S}_i$ (if i is the most sensitive bin) in the first step and Equation 22 in the last step. This last result confirms that at a whatever folded level, the highest possible sensitivity is smaller than the one at the level from which one started.

M Evaluation of off-shell effects at 13 TeV

In order to extract mass values from the distributions reported in Fig. 8.2, a template has been computed for the $\mathcal{R}$ at parton level using CT14nlo PDF and setting the energy of pp collisions to 13 TeV. Additional parameters have been set, as it has been explained in Section 8.3.1. Eight mass points

$$\{160, 165, 167.5, 170, 172.5, 175, 177.5, 180\}$$

have been produced, and a continuos parametrisation is obtained bin-by-bin by interpolating the mass points with a second order polynomial.

The parton level template are then folded to particle level fiducial volume, using a bin-by-bin factor, obtaining the template which is then used to extract the top-quark mass from particle level defined observables. The correction factors are shown in Fig. 28 for the case of 6 and 8 bins. The folded template for the 8 bins choice is shown in Fig. 29 instead.

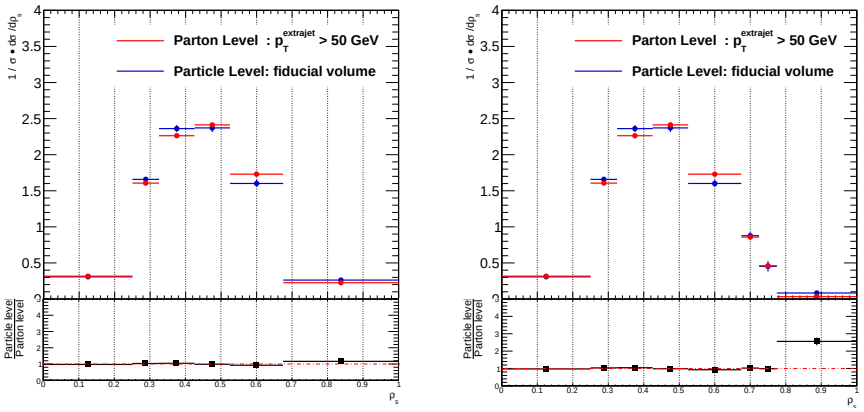

Figure 28: Comparison between the $\mathcal{R}$ observable as defined at parton level (with ${p_T}^{\text{extrajet}} > 50$ GeV) and particle level (in the fiducial volume of Section 8.3.1) for 6 bins (left) and 8 bins (right). The bin-by-bin correction factors used to correct the parton level template are obtained from the ratio of $\frac{\mathcal{R}(particle)}{\mathcal{R}(parton)}$, which is shown in the bottom part of the plots.

The result of using different folding factors, obtained from variations of parameters belonging to the Monte Carlo simulation are reported in Fig. 30. No large deviation is found.

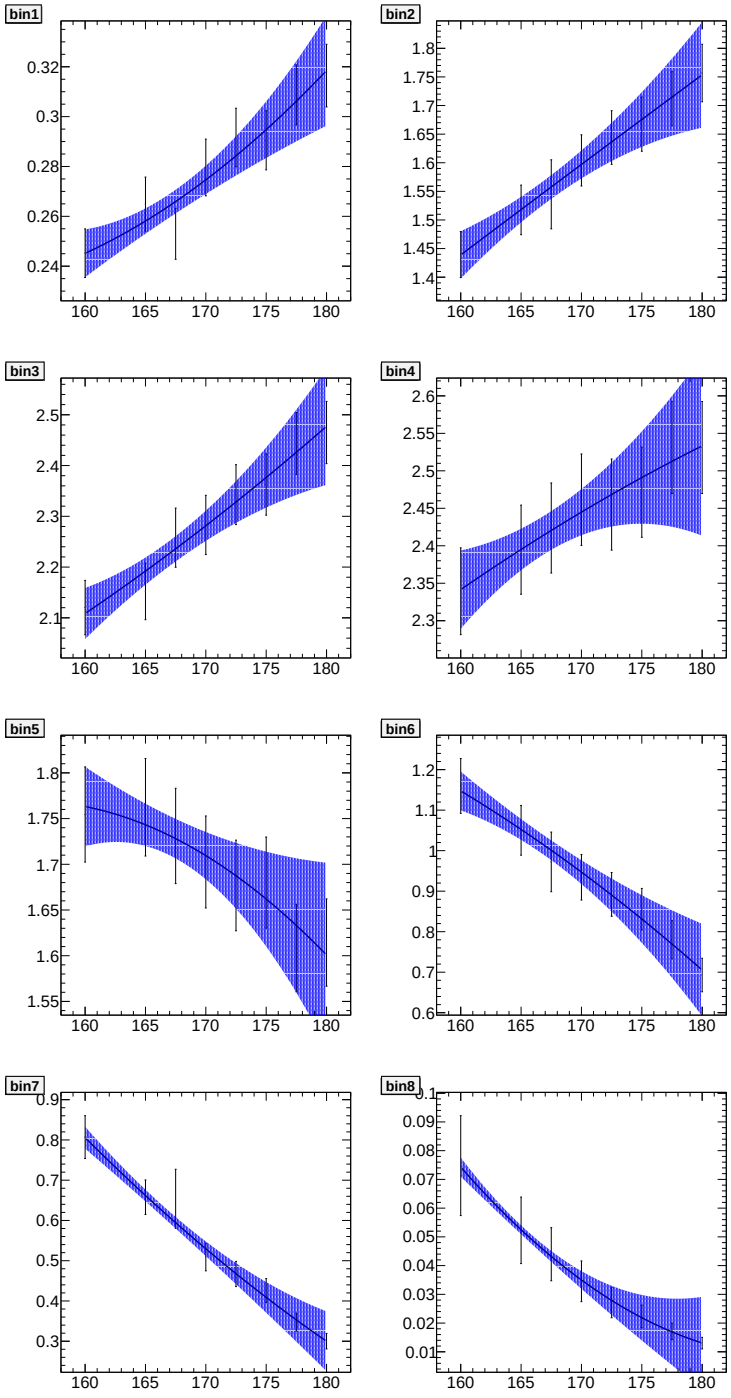

Figure 29: Dependence on m_t^{pole} of the $\mathcal{R}$ observable at parton level, for the 8 bins binnign choice. The $\mathcal{R}$ at parton level are calculated using $pp \to t\bar{t} + 1$-jet calculation at NLO QCD, with $\sqrt{s} = 13$ TeV.

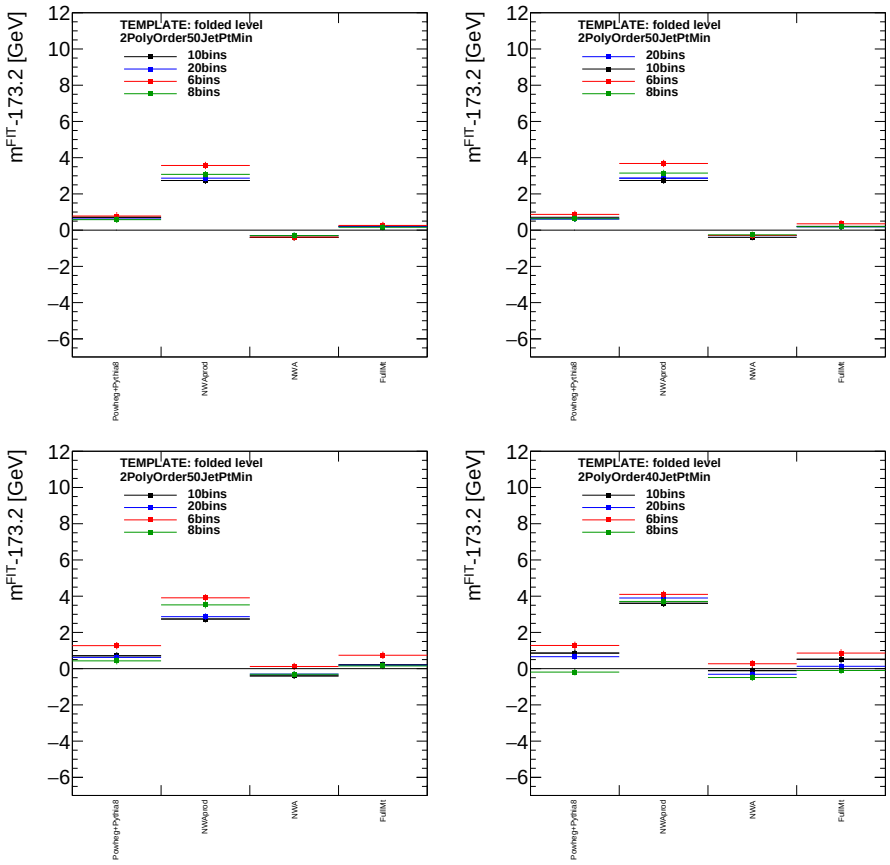

Figure 30: Results obtained when using different bin-by-bin factors in the folding procedure. The nominal folding procedure is defined with $hdamp = \infty$, $\mu_R = \mu_F = m_t$, multiple parton interaction off and the parton level defined with the extra-jet with $p_T$extrajet > 50 GeV. On the top-left the results obtained when using MC simulation with $hdamp{=}m_t$, on the top-right for $\mu_R = \mu_F = \frac{1}{2}(\sqrt{(m_t + p_{\mathrm{T}}\mathrm{top})^2} + \sqrt{(m_t + p_{\mathrm{T}}\mathrm{anti\text{-}top})^2}$, on the bottom-left for multiple parton interaction switched on, while on the bottom-right the parton level was defined with $p_T$extrajet > 40 GeV . For all the variations considered, changes on extracted masses are within ~ 0.5GeV.

Bibliography

[1] J. J. Thomson, *Cathode rays*, Phil. Mag. Ser.5 **44** (1897) 293.

[2] S. H. Neddermeyer and C. D. Anderson,
Note on the Nature of Cosmic Ray Particles, Phys. Rev. **51** (1937) 884.

[3] F. Reines and C. L. Cowan, *The neutrino*, Nature **178** (1956) 446.

[4] G. Danby et al., *Observation of High-Energy Neutrino Reactions and the Existence of Two Kinds of Neutrinos*, Phys. Rev. Lett. **9** (1962) 36.

[5] M. L. Perl et al.,
Evidence for Anomalous Lepton Production in e+ - e- Annihilation,
Phys. Rev. Lett. **35** (1975) 1489, [,193(1975)].

[6] K. Kodama et al., *Observation of tau neutrino interactions*,
Phys. Lett. **B504** (2001) 218, arXiv: hep-ex/0012035 [hep-ex].

[7] M. Gell-Mann, *A Schematic Model of Baryons and Mesons*,
Phys. Lett. **8** (1964) 214.

[8] G. Zweig, 'An SU(3) model for strong interaction symmetry and its breaking. Version 2', *DEVELOPMENTS IN THE QUARK THEORY OF HADRONS. VOL. 1. 1964 - 1978*,
ed. by D. Lichtenberg and S. P. Rosen, 1964 22, URL:
http://inspirehep.net/record/4674/files/cern-th-412.pdf.

[9] E. D. Bloom et al.,
High-Energy Inelastic e p Scattering at 6-Degrees and 10-Degrees,
Phys. Rev. Lett. **23** (1969) 930.

[10] M. Breidenbach et al.,
Observed Behavior of Highly Inelastic electron-Proton Scattering,
Phys. Rev. Lett. **23** (1969) 935.

[11] G. D. Rochester and C. C. Butler,
Evidence for the Existence of New Unstable Elementary Particles,
Nature **160** (1947) 855.

[12] S. L. Glashow, J. Iliopoulos and L. Maiani,
Weak Interactions with Lepton-Hadron Symmetry,
Phys. Rev. D **2** (7 1970) 1285,
URL: https://link.aps.org/doi/10.1103/PhysRevD.2.1285.

[13] J. .-.-E. Augustin et al.,
Discovery of a Narrow Resonance in e^+e^- Annihilation,
Phys. Rev. Lett. **33** (23 1974) 1406,
URL: https://link.aps.org/doi/10.1103/PhysRevLett.33.1406.

[14] J. J. Aubert et al., *Experimental Observation of a Heavy Particle J*, Phys. Rev. Lett. **33** (23 1974) 1404, URL: https://link.aps.org/doi/10.1103/PhysRevLett.33.1404.

[15] M. Kobayashi and T. Maskawa, *CP Violation in the Renormalizable Theory of Weak Interaction*, Prog. Theor. Phys. **49** (1973) 652.

[16] S. W. Herb et al., *Observation of a Dimuon Resonance at 9.5 GeV in 400-GeV Proton-Nucleus Collisions*, Phys. Rev. Lett. **39** (5 1977) 252, URL: https://link.aps.org/doi/10.1103/PhysRevLett.39.252.

[17] F. Abe et al., *Observation of top quark production in $\bar{p}p$ collisions*, Phys. Rev. Lett. **74** (1995) 2626, arXiv: hep-ex/9503002 [hep-ex].

[18] S. Abachi et al., *Search for high mass top quark production in $p\bar{p}$ collisions at $\sqrt{s} = 1.8$ TeV*, Phys. Rev. Lett. **74** (1995) 2422, arXiv: hep-ex/9411001 [hep-ex].

[19] A. Einstein, *Uber einen die Erzeugung und Verwandlung des Lichtes betreffenden heuristischen Gesichtspunkt*, Annalen er physik **332** (1905) 132.

[20] A. H. Compton, *A Quantum Theory of the Scattering of X-rays by Light Elements*, Phys. Rev. **21** (5 1923) 483, URL: https://link.aps.org/doi/10.1103/PhysRev.21.483.

[21] C. Berger et al., *Jet Analysis of the Υ (9.46) Decay Into Charged Hadrons*, Phys. Lett. **82B** (1979) 449.

[22] C. Berger et al., *Topology of the Υ Decay*, Z. Phys. **C8** (1981) 101.

[23] P. Bagnaia et al., *Evidence for Z0 —¿ e+ e- at the CERN anti-p p Collider*, Phys. Lett. **B129** (1983) 130, [,7.69(1983)].

[24] M. Banner et al., *Observation of Single Isolated Electrons of High Transverse Momentum in Events with Missing Transverse Energy at the CERN anti-p p Collider*, Phys. Lett. **B122** (1983) 476, [,7.45(1983)].

[25] G. Arnison et al., *Experimental Observation of Isolated Large Transverse Energy Electrons with Associated Missing Energy at s**(1/2) = 540-GeV*, Phys. Lett. **B122** (1983) 103, [,611(1983)].

[26] G. Arnison et al., *Experimental Observation of Lepton Pairs of Invariant Mass Around 95-GeV/c**2 at the CERN SPS Collider*, Phys. Lett. **B126** (1983) 398, [,7.55(1983)].

[27] T. W. B. Kibble, *Symmetry Breaking in Non-Abelian Gauge Theories*, Phys. Rev. **155** (5 1967) 1554, URL: https://link.aps.org/doi/10.1103/PhysRev.155.1554.

[28] P. W. Higgs, *Spontaneous Symmetry Breakdown without Massless Bosons*, Phys. Rev. **145** (4 1966) 1156, URL: https://link.aps.org/doi/10.1103/PhysRev.145.1156.

[29] G. S. Guralnik, C. R. Hagen and T. W. B. Kibble,
Global Conservation Laws and Massless Particles,
Phys. Rev. Lett. **13** (20 1964) 585,
URL: https://link.aps.org/doi/10.1103/PhysRevLett.13.585.

[30] P. W. Higgs, *Broken Symmetries and the Masses of Gauge Bosons*,
Phys. Rev. Lett. **13** (16 1964) 508,
URL: https://link.aps.org/doi/10.1103/PhysRevLett.13.508.

[31] P. W. Higgs, *Broken symmetries, massless particles and gauge fields*,
Phys. Lett. **12** (1964) 132.

[32] F. Englert and R. Brout,
Broken Symmetry and the Mass of Gauge Vector Mesons,
Phys. Rev. Lett. **13** (9 1964) 321,
URL: https://link.aps.org/doi/10.1103/PhysRevLett.13.321.

[33] S. Chatrchyan et al., *Observation of a new boson at a mass of 125 GeV with the CMS experiment at the LHC*, Phys. Lett. **B716** (2012) 30,
arXiv: 1207.7235 [hep-ex].

[34] G. Aad et al., *Observation of a new particle in the search for the Standard Model Higgs boson with the ATLAS detector at the LHC*,
Phys. Lett. **B716** (2012) 1, arXiv: 1207.7214 [hep-ex].

[35] D. Choudhury, R. M. Godbole, R. K. Singh and K. Wagh,
Top production at the Tevatron/LHC and nonstandard, strongly interacting spin one particles, Phys. Lett. **B657** (2007) 69,
arXiv: 0705.1499 [hep-ph].

[36] O. Antunano, J. H. Kuhn and G. Rodrigo,
Top quarks, axigluons and charge asymmetries at hadron colliders,
Phys. Rev. **D77** (2008) 014003, arXiv: 0709.1652 [hep-ph].

[37] P. Ferrario and G. Rodrigo,
Constraining heavy colored resonances from top-antitop quark events,
Phys. Rev. **D80** (2009) 051701, arXiv: 0906.5541 [hep-ph].

[38] S. Alekhin, A. Djouadi and S. Moch, *The top quark and Higgs boson masses and the stability of the electroweak vacuum*,
Phys. Lett. **B716** (2012) 214, arXiv: 1207.0980 [hep-ph].

[39] S. Heinemeyer, W. Hollik, D. Stockinger, A. M. Weber and G. Weiglein,
Precise prediction for M(W) in the MSSM, JHEP **08** (2006) 052,
arXiv: hep-ph/0604147 [hep-ph].

[40] S. Alioli et al.,
A new observable to measure the top-quark mass at hadron colliders,
Eur. Phys. J. **C73** (2013) 2438, arXiv: 1303.6415 [hep-ph].

[41] G. Aad et al.,
Determination of the top-quark pole mass using $t\bar{t}$ + 1-jet events collected with the ATLAS experiment in 7 TeV pp collisions,
JHEP **10** (2015) 121, arXiv: 1507.01769 [hep-ex].

[42] M. E. Peskin and D. V. Schroeder,
An Introduction to quantum field theory, Addison-Wesley, 1995,
ISBN: 9780201503975, 0201503972,
URL: http://www.slac.stanford.edu/~mpeskin/QFT.html.

[43] A. Pich, 'The Standard Model of Electroweak Interactions', *Proceedings, High-energy Physics. Proceedings, 18th European School (ESHEP 2010): Raseborg, Finland, June 20 - July 3, 2010*, [,1(2012)], 2012 1, arXiv: 1201.0537 [hep-ph], URL: http://inspirehep.net/record/1083304/files/arXiv:1201.0537.pdf.

[44] C. M. Becchi and G. Ridolfi, *An introduction to relativistic processes and the standard model of electroweak interactions*, 2006.

[45] J. Alwall et al., *The automated computation of tree-level and next-to-leading order differential cross sections, and their matching to parton shower simulations*, JHEP **07** (2014) 079, arXiv: 1405.0301 [hep-ph].

[46] S. Alioli, P. Nason, C. Oleari and E. Re, *A general framework for implementing NLO calculations in shower Monte Carlo programs: the POWHEG BOX*, JHEP **06** (2010) 043, arXiv: 1002.2581 [hep-ph].

[47] M. Bahr et al., *Herwig++ Physics and Manual*, Eur. Phys. J. **C58** (2008) 639, arXiv: 0803.0883 [hep-ph].

[48] T. Sjostrand et al., *An Introduction to PYTHIA 8.2*, Comput. Phys. Commun. **191** (2015) 159, arXiv: 1410.3012 [hep-ph].

[49] T. Gleisberg et al., *SHERPA 1. alpha: A Proof of concept version*, JHEP **02** (2004) 056, arXiv: hep-ph/0311263 [hep-ph].

[50] M. Boggia et al., *The HiggsTools Handbook: Concepts and observables for deciphering the Nature of the Higgs Sector*, (2017), arXiv: 1711.09875 [hep-ph].

[51] J. S. Bell, *Birmingham University thesis*, (1954).

[52] F. J. Hasert et al., *Observation of Neutrino Like Interactions Without Muon Or Electron in the Gargamelle Neutrino Experiment*, Phys. Lett. **B46** (1973) 138, [,5.15(1973)].

[53] L. D. Faddeev and V. N. Popov, *Feynman Diagrams for the Yang-Mills Field*, Phys. Lett. **B25** (1967) 29, [,325(1967)].

[54] H. Yukawa, *On the Interaction of Elementary Particles I*, Proc. Phys. Math. Soc. Jap. **17** (1935) 48.

[55] F. Englert, *Nobel Lecture: The BEH mechanism and its scalar boson*, Rev. Mod. Phys. **86** (3 2014) 843, URL: https://link.aps.org/doi/10.1103/RevModPhys.86.843.

[56] D. W. Kerst et al., *Attainment of Very High Energy by Means of Intersecting Beams of Particles*, Phys. Rev. **102** (2 1956) 590, URL: https://link.aps.org/doi/10.1103/PhysRev.102.590.

[57] J. C. Collins, D. E. Soper and G. F. Sterman, *Factorization of Hard Processes in QCD*, Adv. Ser. Direct. High Energy Phys. **5** (1989) 1, arXiv: hep-ph/0409313 [hep-ph].

[58] R. Placakyte, 'Parton Distribution Functions',
Proceedings, 31st International Conference on Physics in collisions (PIC 2011): Vancouver, Canada, August 28-September 1, 2011, 2011,
arXiv: 1111.5452 [hep-ph], URL: https://inspirehep.net/record/954990/files/arXiv:1111.5452.pdf.

[59] G. Altarelli and G. Parisi, *Asymptotic Freedom in Parton Language*,
Nucl. Phys. **B126** (1977) 298.

[60] Y. L. Dokshitzer, *Calculation of the Structure Functions for Deep Inelastic Scattering and e+ e- Annihilation by Perturbation Theory in Quantum Chromodynamics.*,
Sov. Phys. JETP **46** (1977) 641, [Zh. Eksp. Teor. Fiz.73,1216(1977)].

[61] V. N. Gribov and L. N. Lipatov,
Deep inelastic e p scattering in perturbation theory,
Sov. J. Nucl. Phys. **15** (1972) 438, [Yad. Fiz.15,781(1972)].

[62] J. Rojo, *PDF4LHC recommendations for Run II*,
PoS **DIS2016** (2016) 018, arXiv: 1606.08243 [hep-ph].

[63] R. D. Ball et al., *Parton distributions from high-precision collider data*,
Eur. Phys. J. **C77** (2017) 663, arXiv: 1706.00428 [hep-ph].

[64] J. C. Ward, *An Identity in Quantum Electrodynamics*,
Phys. Rev. **78** (1950) 182.

[65] Y. Takahashi, *On the generalized Ward identity*,
Nuovo Cim. **6** (1957) 371.

[66] A. Deur, S. J. Brodsky and G. F. de Teramond,
The QCD Running Coupling, Prog. Part. Nucl. Phys. **90** (2016) 1,
arXiv: 1604.08082 [hep-ph].

[67] G. Corcella,
Theoretical issues on the top mass reconstruction at hadron colliders,
Nuovo Cim. **C033** (2010) 81, arXiv: 1008.4498 [hep-ph].

[68] A. H. Hoang, A. Jain, I. Scimemi and I. W. Stewart,
Infrared Renormalization Group Flow for Heavy Quark Masses,
Phys. Rev. Lett. **101** (2008) 151602, arXiv: 0803.4214 [hep-ph].

[69] M. Beneke, *A Quark mass definition adequate for threshold problems*,
Phys. Lett. **B434** (1998) 115, arXiv: hep-ph/9804241 [hep-ph].

[70] K. G. Chetyrkin, *Four-loop renormalization of QCD: Full set of renormalization constants and anomalous dimensions*,
Nucl. Phys. **B710** (2005) 499, arXiv: hep-ph/0405193 [hep-ph].

[71] M. Czakon,
The Four-loop QCD beta-function and anomalous dimensions,
Nucl. Phys. **B710** (2005) 485, arXiv: hep-ph/0411261 [hep-ph].

[72] T. Kinoshita and A. Ukawa,
Mass Singularities of Feynman Amplitudes,
Lect. Notes Phys. **39** (1975) 55.

[73] T. D. Lee and M. Nauenberg,
Degenerate Systems and Mass Singularities,
Phys. Rev. **133** (1964) B1549, [,25(1964)].

[74] S. Catani, Y. L. Dokshitzer, M. Olsson, G. Turnock and B. R. Webber, *New clustering algorithm for multi - jet cross-sections in e+ e- annihilation*, Phys. Lett. **B269** (1991) 432.

[75] M. Cacciari, G. P. Salam and G. Soyez, *The Anti-k(t) jet clustering algorithm*, JHEP **04** (2008) 063, arXiv: 0802.1189 [hep-ph].

[76] S. Catani, Y. L. Dokshitzer, M. H. Seymour and B. R. Webber, *Longitudinally invariant K_t clustering algorithms for hadron hadron collisions*, Nucl. Phys. **B406** (1993) 187.

[77] S. D. Ellis and D. E. Soper, *Successive combination jet algorithm for hadron collisions*, Phys. Rev. **D48** (1993) 3160, arXiv: hep-ph/9305266 [hep-ph].

[78] Y. L. Dokshitzer, G. D. Leder, S. Moretti and B. R. Webber, *Better jet clustering algorithms*, JHEP **08** (1997) 001, arXiv: hep-ph/9707323 [hep-ph].

[79] M. Wobisch and T. Wengler, 'Hadronization corrections to jet cross-sections in deep inelastic scattering', *Monte Carlo generators for HERA physics. Proceedings, Workshop, Hamburg, Germany, 1998-1999*, 1998 270, arXiv: hep-ph/9907280 [hep-ph], URL: http://inspirehep.net/record/484872/files/arXiv:hep-ph_9907280.pdf.

[80] S. Catani, L. Trentadue, G. Turnock and B. R. Webber, *Resummation of large logarithms in e+ e- event shape distributions*, Nucl. Phys. **B407** (1993) 3.

[81] M. Bonvini and S. Marzani, *Double resummation for Higgs production*, (2018), arXiv: 1802.07758 [hep-ph].

[82] C. Anastasiou et al., *High precision determination of the gluon fusion Higgs boson cross-section at the LHC*, JHEP **05** (2016) 058, arXiv: 1602.00695 [hep-ph].

[83] F. A. Dreyer and A. Karlberg, *Vector-Boson Fusion Higgs Production at Three Loops in QCD*, Phys. Rev. Lett. **117** (2016) 072001, arXiv: 1606.00840 [hep-ph].

[84] B. Biedermann, A. Denner, S. Dittmaier, L. Hofer and B. Jager, *Next-to-leading-order electroweak corrections to the production of four charged leptons at the LHC*, JHEP **01** (2017) 033, arXiv: 1611.05338 [hep-ph].

[85] S. Dittmaier, A. Huss and G. Knippen, *Next-to-leading-order QCD and electroweak corrections to WWW production at proton-proton colliders*, JHEP **09** (2017) 034, arXiv: 1705.03722 [hep-ph].

[86] G. Simone, 'GEANT4: Simulation for the next generation of HEP experiments', *Proceedings, 8th International Conference on Computing in High-Energy and Nuclear Physics (CHEP 1995): Rio de Janeiro, Brazil, September 18-22, 1995*, 1995 147.

[87] M. Selvaggi, *DELPHES 3: A modular framework for fast-simulation of generic collider experiments*, J. Phys. Conf. Ser. **523** (2014) 012033.

[88] S. Catani and M. H. Seymour, *A General algorithm for calculating jet cross-sections in NLO QCD*, Nucl. Phys. **B485** (1997) 291, [Erratum: Nucl. Phys.B510,503(1998)], arXiv: hep-ph/9605323 [hep-ph].

[89] A. Gehrmann-De Ridder, T. Gehrmann and E. W. N. Glover, *Antenna subtraction at NNLO*, JHEP **09** (2005) 056, arXiv: hep-ph/0505111 [hep-ph].

[90] G. Ossola, C. G. Papadopoulos and R. Pittau, *CutTools: A Program implementing the OPP reduction method to compute one-loop amplitudes*, JHEP **03** (2008) 042, arXiv: 0711.3596 [hep-ph].

[91] J. Alwall et al., *A Standard format for Les Houches event files*, Comput. Phys. Commun. **176** (2007) 300, arXiv: hep-ph/0609017 [hep-ph].

[92] M. L. Mangano, M. Moretti, F. Piccinini, R. Pittau and A. D. Polosa, *ALPGEN, a generator for hard multiparton processes in hadronic collisions*, JHEP **07** (2003) 001, arXiv: hep-ph/0206293 [hep-ph].

[93] M. L. Mangano, M. Moretti and R. Pittau, *Multijet matrix elements and shower evolution in hadronic collisions: $Wb\bar{b}$ + n jets as a case study*, Nucl. Phys. **B632** (2002) 343, arXiv: hep-ph/0108069 [hep-ph].

[94] L. Lonnblad, *Correcting the color dipole cascade model with fixed order matrix elements*, JHEP **05** (2002) 046, arXiv: hep-ph/0112284 [hep-ph].

[95] T. Gleisberg et al., *Event generation with SHERPA 1.1*, JHEP **02** (2009) 007, arXiv: 0811.4622 [hep-ph].

[96] B. Andersson, G. Gustafson, G. Ingelman and T. Sjostrand, *Parton Fragmentation and String Dynamics*, Phys. Rept. **97** (1983) 31.

[97] A. Kupco, 'Cluster hadronization in HERWIG 5.9', *Monte Carlo generators for HERA physics. Proceedings, Workshop, Hamburg, Germany, 1998-1999*, 1998 292, arXiv: hep-ph/9906412 [hep-ph], URL: https://inspirehep.net/record/484684/files/arXiv:hep-ph_9906412.pdf.

[98] S. Hoche, 'Introduction to parton-shower event generators', *Proceedings, Theoretical Advanced Study Institute in Elementary Particle Physics: Journeys Through the Precision Frontier: Amplitudes for Colliders (TASI 2014): Boulder, Colorado, June 2-27, 2014*, 2015 235, arXiv: 1411.4085 [hep-ph], URL: http://inspirehep.net/record/1328513/files/arXiv:1411.4085.pdf.

[99] J. Fuster, A. Irles, D. Melini, P. Uwer and M. Vos, *Extracting the top-quark running mass using tt +1-jet events produced at the Large Hadron Collider*, (2017), arXiv: 1704.00540 [hep-ph].

[100] N. Cabibbo, *Unitary Symmetry and Leptonic Decays*, Phys. Rev. Lett. **10** (1963) 531, [,648(1963)].

[101] J. H. Christenson, J. W. Cronin, V. L. Fitch and R. Turlay, *Evidence for the 2π Decay of the K_2^0 Meson*, Phys. Rev. Lett. **13** (1964) 138.

[102] M. T. et al. (Particle Data Group), *The Review of Particle Physics*, Phys. Rev. D **98** (2018).

[103] M. Brucherseifer, F. Caola and K. Melnikov, *$\mathcal{O}(\alpha_s^2)$ corrections to fully-differential top quark decays*, JHEP **04** (2013) 059, arXiv: 1301.7133 [hep-ph].

[104] J. Gao, C. S. Li and H. X. Zhu, *Top Quark Decay at Next-to-Next-to Leading Order in QCD*, Phys. Rev. Lett. **110** (2013) 042001, arXiv: 1210.2808 [hep-ph].

[105] V. M. Abazov et al., *An Improved determination of the width of the top quark*, Phys. Rev. **D85** (2012) 091104, arXiv: 1201.4156 [hep-ex].

[106] V. Khachatryan et al., *Measurement of the ratio $\mathcal{B}(t \to Wb)/\mathcal{B}(t \to Wq)$ in pp collisions at $\sqrt{s} = 8$ TeV*, Phys. Lett. **B736** (2014) 33, arXiv: 1404.2292 [hep-ex].

[107] C. Collaboration, *Bounding the top quark width using final states with two charged leptons and two jets at $\sqrt{s} = 13$ TeV*, (2016).

[108] T. A. Aaltonen et al., *Direct Measurement of the Total Decay Width of the Top Quark*, Phys. Rev. Lett. **111** (2013) 202001, arXiv: 1308.4050 [hep-ex].

[109] T. Aaltonen et al., *Evidence for $t\bar{t}\gamma$ Production and Measurement of $\sigma_t\bar{t}\gamma/\sigma_t\bar{t}$*, Phys. Rev. **D84** (2011) 031104, arXiv: 1106.3970 [hep-ex].

[110] G. Aad et al., *Observation of top-quark pair production in association with a photon and measurement of the $t\bar{t}\gamma$ production cross section in pp collisions at $\sqrt{s} = 7$ TeV using the ATLAS detector*, Phys. Rev. **D91** (2015) 072007, arXiv: 1502.00586 [hep-ex].

[111] G. Aad et al., *Measurement of the top quark charge in pp collisions at $\sqrt{s} = 7$ TeV with the ATLAS detector*, JHEP **11** (2013) 031, arXiv: 1307.4568 [hep-ex].

[112] A. Czarnecki, J. G. Korner and J. H. Piclum, *Helicity fractions of W bosons from top quark decays at NNLO in QCD*, Phys. Rev. **D81** (2010) 111503, arXiv: 1005.2625 [hep-ph].

[113] T. Aaltonen et al., *Combination of CDF and D0 measurements of the W boson helicity in top quark decays*, Phys. Rev. **D85** (2012) 071106, arXiv: 1202.5272 [hep-ex].

[114] L. T. W. G. S. Plots, *W boson helicity summary plot, November 2017*, (2017), URL: https://twiki.cern.ch/twiki/pub/LHCPhysics/LHCTopWGSummaryPlots/helicity_summary_nov2017.pdf.

[115] M. Czakon, P. Fiedler and A. Mitov, *The total top quark pair production cross-section at hadron colliders through $O(\alpha_S^4)$*, (2013), arXiv: 1303.6254 [hep-ph].

[116] M. Guzzi, K. Lipka and S.-O. Moch,
Top-quark pair production at hadron colliders: differential cross section and phenomenological applications with DiffTop, JHEP **01** (2015) 082, arXiv: 1406.0386 [hep-ph].

[117] J. H. Kuhn, A. Scharf and P. Uwer,
Electroweak effects in top-quark pair production at hadron colliders, Eur. Phys. J. **C51** (2007) 37, arXiv: hep-ph/0610335 [hep-ph].

[118] L. T. W. G. S. Plots, *Pair production cross sections, May 2018 (inc) and November 2017 (diff)*, (2018), URL: https://twiki.cern.ch/twiki/pub/LHCPhysics/LHCTopWGSummaryPlots.

[119] L. T. W. G. S. Plots, *Pair production cross section, Nov 2017*, (2017), URL: https://twiki.cern.ch/twiki/pub/LHCPhysics/LHCTopWGSummaryPlots/singletop_allchannels_nov17.pdf.

[120] F. Cascioli, S. Kallweit, P. Maierhofer and S. Pozzorini,
A unified NLO description of top-pair and associated Wt production, Eur. Phys. J. **C74** (2014) 2783, arXiv: 1312.0546 [hep-ph].

[121] A. Denner, S. Dittmaier, S. Kallweit and S. Pozzorini,
NLO QCD corrections to WWbb production at hadron colliders, Phys. Rev. Lett. **106** (2011) 052001, arXiv: 1012.3975 [hep-ph].

[122] G. Bevilacqua, H. B. Hartanto, M. Kraus, M. Schulze and M. Worek,
Top quark mass studies with $t\bar{t}j$ at the LHC, (2017), arXiv: 1710.07515 [hep-ph].

[123] J. H. Kuhn and G. Rodrigo,
Charge asymmetry in hadroproduction of heavy quarks, Phys. Rev. Lett. **81** (1998) 49, arXiv: hep-ph/9802268 [hep-ph].

[124] W. Hollik and D. Pagani, *The electroweak contribution to the top quark forward-backward asymmetry at the Tevatron*, Phys. Rev. **D84** (2011) 093003, arXiv: 1107.2606 [hep-ph].

[125] N. Kidonakis, *Next-to-next-to-leading-order collinear and soft gluon corrections for t-channel single top quark production*, Phys. Rev. **D83** (2011) 091503, arXiv: 1103.2792 [hep-ph].

[126] N. Kidonakis, *Two-loop soft anomalous dimensions for single top quark associated production with a W- or H-*, Phys. Rev. **D82** (2010) 054018, arXiv: 1005.4451 [hep-ph].

[127] N. Kidonakis,
NNLL resummation for s-channel single top quark production, Phys. Rev. **D81** (2010) 054028, arXiv: 1001.5034 [hep-ph].

[128] M. Aaboud et al., *Observation of Higgs boson production in association with a top quark pair at the LHC with the ATLAS detector*, (2018), arXiv: 1806.00425 [hep-ex].

[129] Yu. F. Pirogov and O. V. Zenin, *Two loop renormalization group restrictions on the standard model and the fourth chiral family*, Eur. Phys. J. **C10** (1999) 629, arXiv: hep-ph/9808396 [hep-ph].

[130] S. Heinemeyer, W. Hollik and G. Weiglein, *Electroweak precision observables in the minimal supersymmetric standard model*, Phys. Rept. **425** (2006) 265, arXiv: hep-ph/0412214 [hep-ph].

[131] M. Baak et al.,
The global electroweak fit at NNLO and prospects for the LHC and ILC,
Eur. Phys. J. **C74** (2014) 3046, arXiv: 1407.3792 [hep-ph].

[132] A. R. Vieira, B. Hiller, M. D. R. Sampaio and M. C. Nemes,
Naturalness and Theoretical Constraints on the Higgs Boson Mass,
Int. J. Theor. Phys. **52** (2013) 3494, arXiv: 1207.4088 [hep-ph].

[133] G. Degrassi et al.,
Higgs mass and vacuum stability in the Standard Model a t NNLO,
JHEP **08** (2012) 098, arXiv: 1205.6497 [hep-ph].

[134] A. H. Hoang and I. W. Stewart,
Top Mass Measurements from Jets and the Tevatron Top-Quark Mass,
Nucl. Phys. Proc. Suppl. **185** (2008) 220, arXiv: 0808.0222 [hep-ph].

[135] S. Fleming, A. H. Hoang, S. Mantry and I. W. Stewart,
Jets from massive unstable particles: Top-mass determination,
Phys. Rev. **D77** (2008) 074010, arXiv: hep-ph/0703207 [hep-ph].

[136] D. Melini, *Measurements of the top quark mass using the ATLAS detector at the LHC*, PoS **DIS2017** (2018) 122.

[137] M. Aaboud et al., *Top-quark mass measurement in the all-hadronic $t\bar{t}$ decay channel at $\sqrt{s} = 8$ TeV with the ATLAS detector*,
JHEP **09** (2017) 118, arXiv: 1702.07546 [hep-ex].

[138] A. M. Sirunyan et al.,
Measurement of the $t\bar{t}$ production cross section using events with one lepton and at least one jet in pp collisions at $\sqrt{s} = 13$ TeV,
JHEP **09** (2017) 051, arXiv: 1701.06228 [hep-ex].

[139] G. Aad et al.,
Measurement of the top quark mass in the $t\bar{t} \to$ lepton+jets and $t\bar{t} \to$ dilepton channels using $\sqrt{s} = 7$ TeV ATLAS data,
Eur. Phys. J. **C75** (2015) 330, arXiv: 1503.05427 [hep-ex].

[140] A. M. Sirunyan et al., *Measurement of the top quark mass in the dileptonic $t\bar{t}$ decay channel using the mass observables $M_{b\ell}$, M_{T2}, and $M_{b\ell\nu}$ in pp collisions at $\sqrt{s} = 8$?TeV*, Phys. Rev. **D96** (2017) 032002, arXiv: 1704.06142 [hep-ex].

[141] M. Aaboud et al., *Measurement of the top quark mass in the $t\bar{t} \to$ dilepton channel from $\sqrt{s} = 8$ TeV ATLAS data*,
Phys. Lett. **B761** (2016) 350, arXiv: 1606.02179 [hep-ex].

[142] A. Collaboration, *ATLAS Top Working Group Summary Plots*, (2018),
URL: https://twiki.cern.ch/twiki/bin/view/AtlasPublic/TopPublicResults.

[143] V. Khachatryan et al., *Measurement of the top quark mass using charged particles in pp collisions at $\sqrt{s} = 8$ TeV*,
Phys. Rev. **D93** (2016) 092006, arXiv: 1603.06536 [hep-ex].

[144] V. Khachatryan et al., *Measurement of the mass of the top quark in decays with a J/ψ meson in pp collisions at 8 TeV*,
JHEP **12** (2016) 123, arXiv: 1608.03560 [hep-ex].

[145] A. M. Sirunyan et al., *Measurement of the jet mass in highly boosted* $\mathrm{t\bar{t}}$ *events from pp collisions at* $\sqrt{s} = 8$ *TeV*, Eur. Phys. J. **C77** (2017) 467, arXiv: 1703.06330 [hep-ex].

[146] ATLAS Collaboration, *Measurement of the top quark mass in topologies enhanced with single top quarks produced in the t-channel at* $\sqrt{s} = 8$ *TeV using the ATLAS experiment*, ATLAS-CONF-2014-055, 2014, URL: https://cds.cern.ch/record/1951323.

[147] A. M. Sirunyan et al., *Measurement of the top quark mass using single top quark events in proton-proton collisions at* $\sqrt{s} = 8$ *TeV*, Eur. Phys. J. **C77** (2017) 354, arXiv: 1703.02530 [hep-ex].

[148] M. Aaboud et al., *Measurement of lepton differential distributions and the top quark mass in* $t\bar{t}$ *production in pp collisions at* $\sqrt{s} = 8$ *TeV with the ATLAS detector*, Eur. Phys. J. **C77** (2017) 804, arXiv: 1709.09407 [hep-ex].

[149] 'Determination of the normalised invariant mass distribution of $\mathrm{t\bar{t}}$+jet and extraction of the top quark mass', tech. rep. CMS-PAS-TOP-13-006, CERN, 2016, URL: https://cds.cern.ch/record/2153653.

[150] S. Dittmaier, P. Uwer and S. Weinzierl, *Hadronic top-quark pair production in association with a hard jet at next-to-leading order QCD: Phenomenological studies for the Tevatron and the LHC*, Eur. Phys. J. **C59** (2009) 625, arXiv: 0810.0452 [hep-ph].

[151] S. Dittmaier, P. Uwer and S. Weinzierl, *NLO QCD corrections to t anti-t + jet production at hadron colliders*, Phys. Rev. Lett. **98** (2007) 262002, arXiv: hep-ph/0703120 [HEP-PH].

[152] S. Alioli, S.-O. Moch and P. Uwer, *Hadronic top-quark pair-production with one jet and parton showering*, JHEP **01** (2012) 137, arXiv: 1110.5251 [hep-ph].

[153] 'ECFA 2016: Prospects for selected standard model measurements with the CMS experiment at the High-Luminosity LHC', tech. rep. CMS-PAS-FTR-16-006, CERN, 2017, URL: https://cds.cern.ch/record/2262606.

[154] M. Bicer et al., *First Look at the Physics Case of TLEP*, JHEP **01** (2014) 164, arXiv: 1308.6176 [hep-ex].

[155] H. Baer et al., *The International Linear Collider Technical Design Report - Volume 2: Physics*, (2013), arXiv: 1306.6352 [hep-ph].

[156] L. Linssen, A. Miyamoto, M. Stanitzki and H. Weerts, *Physics and Detectors at CLIC: CLIC Conceptual Design Report*, (2012), arXiv: 1202.5940 [physics.ins-det].

[157] M. Beneke et al., *Next-to-Next-to-Next-to-Leading Order QCD Prediction for the Top Antitop S-Wave Pair Production Cross Section Near Threshold in* e^+e^- *Annihilation*, Phys. Rev. Lett. **115** (2015) 192001, arXiv: 1506.06864 [hep-ph].

[158] A. H. Hoang and M. Stahlhofen, *The Top-Antitop Threshold at the ILC: NNLL QCD Uncertainties*, JHEP **05** (2014) 121, arXiv: 1309.6323 [hep-ph].

[159] M. Vos et al., *Top physics at high-energy lepton colliders*, (2016), arXiv: 1604.08122 [hep-ex].

[160] H. Abramowicz et al., *Top-Quark Physics at the CLIC Electron-Positron Linear Collider*, (2018), arXiv: 1807.02441 [hep-ex].

[161] *The accelerator complex*, (2012), URL: http://cds.cern.ch/record/1997193.

[162] *Linear accelerator 2*, (2012), URL: http://cds.cern.ch/record/1997427.

[163] *The Proton Synchrotron*, (2012), URL: http://cds.cern.ch/record/1997189.

[164] *The Proton Synchrotron Booster*, (2012), URL: http://cds.cern.ch/record/1997372.

[165] *The Super Proton Synchrotron*, (2012), URL: http://cds.cern.ch/record/1997188.

[166] 'Jet mass reconstruction with the ATLAS Detector in early Run 2 data', tech. rep. ATLAS-CONF-2016-035, CERN, 2016, URL: http://cds.cern.ch/record/2200211.

[167] 'Jet reclustering and close-by effects in ATLAS run II', tech. rep. ATLAS-CONF-2017-062, CERN, 2017, URL: http://cds.cern.ch/record/2275649.

[168] 'In-situ measurements of the ATLAS large-radius jet response in 13 TeV pp collisions', tech. rep. ATLAS-CONF-2017-063, CERN, 2017, URL: http://cds.cern.ch/record/2275655.

[169] M. Aaboud et al., *In situ calibration of large-R jet energy and mass in 13 TeV proton-proton collisions with the ATLAS detector*, (2018), arXiv: 1807.09477 [hep-ex].

[170] *Linear accelerator 3*, (2012), URL: http://cds.cern.ch/record/1997426.

[171] H. K. Jarlett, *ISOLDE*, (2017), URL: http://cds.cern.ch/record/1997568.

[172] *DIRAC: Pions and the strong force*, (2012), URL: http://cds.cern.ch/record/1997205.

[173] *CLOUD: Cosmics Leaving OUtdoor Droplets*, (2012), URL: http://cds.cern.ch/record/1997206.

[174] *nTOF*, (2012), URL: http://cds.cern.ch/record/1997567.

[175] *The Antiproton Decelerator*, (2012), URL: http://cds.cern.ch/record/1997191.

[176] *ACE: Antiproton Cell Experiment*, (2012), URL: http://cds.cern.ch/record/1997209.

[177] *AEGIS: Measuring g with a beam of antihydrogen*, (2012), URL: http://cds.cern.ch/record/1997211.

[178] *ALPHA: Neutral trap to capture and analyze antihydrogen*, (2012), URL: http://cds.cern.ch/record/1997208.

[179] *ASACUSA: Making hybrid antiatoms*, (2012), URL: http://cds.cern.ch/record/1997212.

[180] *ATRAP: Peer inside atoms of antihydrogen*, (2012), URL: http://cds.cern.ch/record/1997213.

[181] *NA62: Measuring rare kaon decays*, (2012), URL: http://cds.cern.ch/record/1997204.

[182] *NA61/SHINE*, (2012), URL: http://cds.cern.ch/record/1997258.

[183] *COMPASS: Particles built from quarks and gluons*, (2012), URL: http://cds.cern.ch/record/1997210.

[184] *AWAKE: Closer to a breakthrough acceleration technology*, (2013), URL: http://cds.cern.ch/record/1997886.

[185] S. Baird, 'Accelerators for pedestrians; rev. version', tech. rep. AB-Note-2007-014. CERN-AB-Note-2007-014. PS-OP-Note-95-17-Rev-2. CERN-PS-OP-Note-95-17-Rev-2, CERN, 2007, URL: http://cds.cern.ch/record/1017689.

[186] S. Chatrchyan et al., *The CMS Experiment at the CERN LHC*, JINST **3** (2008) S08004.

[187] G. Aad et al., *The ATLAS Experiment at the CERN Large Hadron Collider*, JINST **3** (2008) S08003.

[188] K. Aamodt et al., *The ALICE experiment at the CERN LHC*, JINST **3** (2008) S08002.

[189] J. Adam et al., *Direct photon production in Pb-Pb collisions at* $\sqrt{s_{NN}} = 2.76$ *TeV*, Phys. Lett. **B754** (2016) 235, arXiv: 1509.07324 [nucl-ex].

[190] J. Adam et al., *Anisotropic flow of charged particles in Pb-Pb collisions at* $\sqrt{s_{NN}} = 5.02$ *TeV*, Phys. Rev. Lett. **116** (2016) 132302, arXiv: 1602.01119 [nucl-ex].

[191] J. Adam et al., *Forward-central two-particle correlations in p-Pb collisions at* $\sqrt{s_{NN}} = 5.02$ *TeV*, Phys. Lett. **B753** (2016) 126, arXiv: 1506.08032 [nucl-ex].

[192] A. A. Alves Jr. et al., *The LHCb Detector at the LHC*, JINST **3** (2008) S08005.

[193] R. Aaij et al., *Test of lepton universality with* $B^0 \to K^{*0} l^+ l^-$ *decays*, JHEP **08** (2017) 055, arXiv: 1705.05802 [hep-ex].

[194] O. Adriani et al., *The LHCf detector at the CERN Large Hadron Collider*, JINST **3** (2008) S08006.

[195] J. Pinfold et al., *Technical Design Report of the MoEDAL Experiment*, (2009).

[196] G. Anelli et al., *The TOTEM experiment at the CERN Large Hadron Collider*, JINST **3** (2008) S08007.

[197] 'Studies of the ATLAS Inner Detector material using $\sqrt{s}$ =13 TeV pp collision data', tech. rep. ATL-PHYS-PUB-2015-050, CERN, 2015, URL: https://cds.cern.ch/record/2109010.

[198] *ATLAS liquid argon calorimeter: Technical design report*, (1996).

[199] G. Aad et al., *Readiness of the ATLAS Tile Calorimeter for LHC collisions*, Eur. Phys. J. **C70** (2010) 1193, arXiv: 1007.5423 [physics.ins-det].

[200] *ATLAS muon spectrometer: Technical design report*, (1997).

[201] G. Aad et al., *Performance of the ATLAS muon trigger in pp collisions at* $\sqrt{s} = 8$ *TeV*, Eur. Phys. J. **C75** (2015) 120, arXiv: 1408.3179 [hep-ex].

[202] G. Aad et al., *Performance of the ATLAS Trigger System in 2010*, Eur. Phys. J. **C72** (2012) 1849, arXiv: 1110.1530 [hep-ex].

[203] M. Aaboud et al., *Performance of the ATLAS Trigger System in 2015*, Eur. Phys. J. **C77** (2017) 317, arXiv: 1611.09661 [hep-ex].

[204] T. A. collaboration, *Electron efficiency measurements with the ATLAS detector using the 2015 LHC proton-proton collision data*, (2016).

[205] 'Photon identification in 2015 ATLAS data', tech. rep. ATL-PHYS-PUB-2016-014, CERN, 2016, URL: https://cds.cern.ch/record/2203125.

[206] G. Aad et al., *Muon reconstruction performance of the ATLAS detector in proton?proton collision data at* $\sqrt{s}$ *=13 TeV*, Eur. Phys. J. **C76** (2016) 292, arXiv: 1603.05598 [hep-ex].

[207] M. Aaboud et al., *Jet energy scale measurements and their systematic uncertainties in proton-proton collisions at* $\sqrt{s} = 13$ *TeV with the ATLAS detector*, Phys. Rev. **D96** (2017) 072002, arXiv: 1703.09665 [hep-ex].

[208] M. Aaboud et al., *Measurements of b-jet tagging efficiency with the ATLAS detector using* $t\bar{t}$ *events at* $\sqrt{s} = 13$ *TeV*, (2018), arXiv: 1805.01845 [hep-ex].

[209] M. Cacciari, G. P. Salam and G. Soyez, *FastJet User Manual*, Eur. Phys. J. **C72** (2012) 1896, arXiv: 1111.6097 [hep-ph].

[210] 'Measurement of large radius jet mass reconstruction performance at $\sqrt{s} = 8$ TeV using the ATLAS detector', tech. rep. ATLAS-CONF-2016-008, CERN, 2016, URL: https://cds.cern.ch/record/2139642.

[211] D. Krohn, J. Thaler and L.-T. Wang, *Jet Trimming*, JHEP **02** (2010) 084, arXiv: 0912.1342 [hep-ph].

[212] ATLAS Collaboration, *Luminosity determination in pp collisions at* $\sqrt{s} = 8$ *TeV using the ATLAS detector at the LHC*, Eur. Phys. J. C **76** (2016) 653, arXiv: 1608.03953 [hep-ex].

[213] *Top group's MC12 Samples For 2012 Data Analyses*, URL: https://twiki.cern.ch/twiki/bin/view/AtlasProtected/TopMC12.

[214] *Top group's MC12a samples list*, URL: https://twiki.cern.ch/twiki/bin/view/AtlasProtected/AtlasProductionGroupMC12a.

[215] S. Agostinelli et al., *GEANT4: A Simulation toolkit*, Nucl. Instrum. Meth. **A506** (2003) 250.

[216] *Top group's MC12 CommonNTUP tags*, URL: https://twiki.cern.ch/twiki/bin/viewauth/AtlasProtected/CommonNTUPTags.

[217] S. Frixione, P. Nason and C. Oleari, *Matching NLO QCD computations with Parton Shower simulations: the POWHEG method*, JHEP **11** (2007) 070, arXiv: 0709.2092 [hep-ph].

[218] P. Nason, *A New method for combining NLO QCD with shower Monte Carlo algorithms*, JHEP **11** (2004) 040, arXiv: hep-ph/0409146 [hep-ph].

[219] S. Frixione, P. Nason and G. Ridolfi, *A Positive-weight next-to-leading-order Monte Carlo for heavy flavour hadroproduction*, JHEP **09** (2007) 126, arXiv: 0707.3088 [hep-ph].

[220] H.-L. Lai, M. Guzzi, J. Huston, Z. Li, P. M. Nadolsky et al., *New parton distributions for collider physics*, Phys.Rev. **D82** (2010) 074024, arXiv: 1007.2241 [hep-ph].

[221] T. Sjostrand, S. Mrenna and P. Z. Skands, *PYTHIA 6.4 Physics and Manual*, JHEP **05** (2006) 026, arXiv: hep-ph/0603175 [hep-ph].

[222] ATLAS Collaboration, *ATLAS tunes of* PYTHIA *6 and Pythia 8 for MC11*, ATL-PHYS-PUB-2011-009, 2011, URL: https://cds.cern.ch/record/1363300.

[223] M. Aliev, H. Lacker, U. Langenfeld, S. Moch, P. Uwer et al., *HATHOR: HAdronic Top and Heavy quarks crOss section calculatoR*, Comput.Phys.Commun. **182** (2011) 1034, arXiv: 1007.1327 [hep-ph].

[224] M. Beneke, P. Falgari, S. Klein and C. Schwinn, *Hadronic top-quark pair production with NNLL threshold resummation*, Nucl.Phys. **B855** (2012) 695, arXiv: 1109.1536 [hep-ph].

[225] M. Czakon and A. Mitov, *NNLO corrections to top pair production at hadron colliders: the quark-gluon reaction*, JHEP **1301** (2013) 080, arXiv: 1210.6832 [hep-ph].

[226] M. Czakon and A. Mitov, *NNLO corrections to top-pair production at hadron colliders: the all-fermionic scattering channels*, JHEP **1212** (2012) 054, arXiv: 1207.0236 [hep-ph].

[227] P. Baernreuther, M. Czakon and A. Mitov, *Percent Level Precision Physics at the Tevatron: First Genuine NNLO QCD Corrections to $q\bar{q} \to t\bar{t} + X$*, Phys.Rev.Lett. **109** (2012) 132001, arXiv: 1204.5201 [hep-ph].

[228] M. Cacciari, M. Czakon, M. Mangano, A. Mitov and P. Nason, *Top-pair production at hadron colliders with next-to-next-to-leading logarithmic soft-gluon resummation*, Phys.Lett. **B710** (2012) 612, arXiv: 1111.5869 [hep-ph].

[229] M. Czakon and A. Mitov, *Top++: A Program for the Calculation of the Top-Pair Cross-Section at Hadron Colliders*, (2011), arXiv: 1112.5675 [hep-ph].

[230] A. D. Martin, W. J. Stirling, R. S. Thorne and G. Watt, *Parton distributions for the LHC*, Eur. Phys. J. **C63** (2009) 189, arXiv: 0901.0002 [hep-ph].

[231] A. Martin, W. Stirling, R. Thorne and G. Watt, *Uncertainties on alpha(S) in global PDF analyses and implications for predicted hadronic cross sections*, Eur.Phys.J. **C64** (2009) 653, arXiv: 0905.3531 [hep-ph].

[232] R. D. Ball, V. Bertone, S. Carrazza, C. S. Deans, L. Del Debbio et al., *Parton distributions with LHC data*, Nucl.Phys. **B867** (2013) 244, arXiv: 1207.1303 [hep-ph].

[233] M. Botje et al., *The PDF4LHC Working Group Interim Recommendations*, (2011), arXiv: 1101.0538 [hep-ph].

[234] A. D. Martin, W. J. Stirling, R. S. Thorne and G. Watt, *Heavy-quark mass dependence in global PDF analyses and 3- and 4-flavour parton distributions*, Eur. Phys. J. **C70** (2010) 51, arXiv: 1007.2624 [hep-ph].

[235] J. Bellm et al., *Herwig 7.0/Herwig++ 3.0 release note*, Eur. Phys. J. **C76** (2016) 196, arXiv: 1512.01178 [hep-ph].

[236] J. M. Butterworth, J. R. Forshaw and M. H. Seymour, *Multiparton interactions in photoproduction at HERA*, Z. Phys. **C72** (1996) 637, arXiv: hep-ph/9601371 [hep-ph].

[237] *Measurement of lepton differential distributions and the top quark mass in tt production in pp collisions at $\sqrt{8}$ TeV with the ATLAS detector*, URL: https://cds.cern.ch/record/2210834/files/ATL-COM-PHYS-2016-1206.pdf.

[238] D. Geerts, 'Estimation of uncertainties on the heavy flavour content of W+jets events generated by AlpGen for top quark analyses in ATLAS', tech. rep. ATL-COM-PHYS-2013-876, A new version with more statistics and improved results has been posted on February 26th, 2014. (The old results are still available in appendix D.): CERN, 2013, URL: https://cds.cern.ch/record/1558629.

[239] K. Becker et al., 'Estimation of Fake Lepton Background for Top Analyses Using the $\sqrt{s} = 8$ TeV Dataset', tech. rep. ATL-COM-PHYS-2013-1100, CERN, 2013, URL: https://cds.cern.ch/record/1571043.

[240] B. Acharya et al., 'Object selection and calibration, background estimations and MC samples for top quark analyses using the full 2012 data set', tech. rep. ATL-COM-PHYS-2013-1016, CERN, 2013, URL: https://cds.cern.ch/record/1563201.

[241] ATLAS Collaboration, *Electron performance measurements with the ATLAS detector using the 2010 LHC proton–proton collision data*, Eur. Phys. J. C **72** (2012) 1909, arXiv: 1110.3174 [hep-ex].

[242] ATLAS Collaboration,
Measurement of the muon reconstruction performance of the ATLAS detector using 2011 and 2012 LHC proton–proton collision data,
Eur. Phys. J. C **74** (2014) 3130, arXiv: 1407.3935 [hep-ex].

[243] ATLAS Collaboration, *Topological cell clustering in the ATLAS calorimeters and its performance in LHC Run 1*, (2016),
arXiv: 1603.02934 [hep-ex].

[244] J. Pinfold et al., *Evaluation of the local hadronic calibration with combined beam-test data for the endcap and forward calorimeters of ATLAS in the pseudorapidity region 2.5 ¡ —eta— ¡ 4.0*,
Nucl. Instrum. Meth. **A693** (2012) 74.

[245] M. Cacciari and G. P. Salam,
Dispelling the N^3 myth for the k_t jet-finder,
Phys. Lett. **B641** (2006) 57, arXiv: hep-ph/0512210 [hep-ph].

[246] ATLAS Collaboration, *A measurement of the calorimeter response to single hadrons and determination of the jet energy scale uncertainty using LHC Run-1 pp-collision data with the ATLAS detector*,
Eur. Phys. J. C **77** (2017) 26, arXiv: 1607.08842 [hep-ex].

[247] ATLAS Collaboration,
Performance of b-Jet Identification in the ATLAS Experiment,
JINST **11** (2016) P04008, arXiv: 1512.01094 [hep-ex].

[248] ATLAS Collaboration, *Measurements of top-quark pair differential cross-sections in the lepton+jets channel in pp collisions at $\sqrt{s} = 8$ TeV using the ATLAS detector*, Eur. Phys. J. C **76** (2016) 538,
arXiv: 1511.04716 [hep-ex].

[249] ATLAS Collaboration,
Measurement of the W boson polarisation in $t\bar{t}$ events from pp collisions at $\sqrt{s} = 8$ TeV in the lepton+jets channel with ATLAS,
(2016), arXiv: 1612.02577 [hep-ex].

[250] *Top group systematic reocmmendations*, URL: https://twiki.cern.ch/twiki/bin/view/AtlasProtected/TopSystematics2012.

[251] C. Patrignani et al., *Review of Particle Physics*,
Chin. Phys. **C40** (2016) 100001.

[252] P. Fernandez, J. Fuster, A. Irles, R. Moles and M. Vos,
Measurement of the top-quark pole mass using tt+1jet events collected with the ATLAS experiment in 7 TeV pp collisions, (2014),
URL: https://cds.cern.ch/record/1647176.

[253] *Measurement of the top-quark pole mass using tt+1jet events collected with the ATLAS experiment in 7 TeV pp collisions*,
URL: https://cds.cern.ch/record/1647176/files/ATL-COM-PHYS-2014-086.pdf.

[254] ATLAS Collaboration, *Measurement of the top quark mass with the template method in the $t\bar{t} \to$ lepton + jets channel using ATLAS data*,
Eur. Phys. J. C **72** (2012) 2046, arXiv: 1203.5755 [hep-ex].

[255] *Particle level objects and pseudo-top-quark definitions*, URL: https://twiki.cern.ch/twiki/bin/view/LHCPhysics/ParticleLevelTopDefinitions.

[256] R. Corke and T. Sjostrand, *Improved Parton Showers at Large Transverse Momenta*, Eur. Phys. J. **C69** (2010) 1, arXiv: 1003.2384 [hep-ph].

[257] G. D'Agostini, *A Multidimensional unfolding method based on Bayes' theorem*, Nucl. Instrum. Meth. **A362** (1995) 487.

[258] ATLAS Collaboration, *Determination of the jet energy scale and resolution at ATLAS using Z/γ-jet events in data at $\sqrt{s} = 8$ TeV*, ATLAS-CONF-2015-057, 2015, URL: https://cds.cern.ch/record/2059846.

[259] ATLAS Collaboration, *Monte Carlo Calibration and Combination of In-situ Measurements of Jet Energy Scale, Jet Energy Resolution and Jet Mass in ATLAS*, ATLAS-CONF-2015-037, 2015, URL: https://cds.cern.ch/record/2044941.

[260] ATLAS Collaboration, *Data-driven determination of the energy scale and resolution of jets reconstructed in the ATLAS calorimeters using dijet and multijet events at $\sqrt{s} = 8$ TeV*, ATLAS-CONF-2015-017, 2015, URL: https://cds.cern.ch/record/2008678.

[261] ATLAS Collaboration, *Calibration of the performance of b-tagging for c and light-flavour jets in the 2012 ATLAS data*, ATLAS-CONF-2014-046, 2014, URL: https://cds.cern.ch/record/1741020.

[262] ATLAS Collaboration, *Calibration of b-tagging using dileptonic top pair events in a combinatorial likelihood approach with the ATLAS experiment*, ATLAS-CONF-2014-004, 2014, URL: https://cds.cern.ch/record/1664335.

[263] ATLAS Collaboration, *Electron reconstruction and identification efficiency measurements with the ATLAS detector using the 2011 LHC proton–proton collision data*, Eur. Phys. J. C **74** (2014) 2941, arXiv: 1404.2240 [hep-ex].

[264] ATLAS Collaboration, *Muon reconstruction efficiency and momentum resolution of the ATLAS experiment in proton–proton collisions at $\sqrt{s} = 7$ TeV in 2010*, Eur. Phys. J. C **74** (2014) 3034, arXiv: 1404.4562 [hep-ex].

[265] ATLAS Collaboration, *Performance of Missing Transverse Momentum Reconstruction in ATLAS studied in Proton–Proton Collisions recorded in 2012 at $\sqrt{s} = 8$ TeV*, ATLAS-CONF-2013-082, 2013, URL: https://cds.cern.ch/record/1570993.

[266] ATLAS Collaboration, *Performance of missing transverse momentum reconstruction in proton–proton collisions at $\sqrt{s} = 7$ TeV with ATLAS*, Eur. Phys. J. C **72** (2012) 1844, arXiv: 1108.5602 [hep-ex].

[267] P. Marquard, A. V. Smirnov, V. A. Smirnov and M. Steinhauser, *Quark Mass Relations to Four-Loop Order in Perturbative QCD*, Phys. Rev. Lett. **114** (2015) 142002, arXiv: 1502.01030 [hep-ph].

[268] K. Melnikov, A. Scharf and M. Schulze, *Top quark pair production in association with a jet: QCD corrections and jet radiation in top quark decays*, Phys. Rev. **D85** (2012) 054002, arXiv: 1111.4991 [hep-ph].

[269] V. S. Fadin, V. A. Khoze and A. D. Martin, *How suppressed are the radiative interference effects in heavy instable particle production?*, Phys. Lett. **B320** (1994) 141, arXiv: hep-ph/9309234 [hep-ph].

[270] V. S. Fadin, V. A. Khoze and A. D. Martin, *Interference radiative phenomena in the production of heavy unstable particles*, Phys. Rev. **D49** (1994) 2247.

[271] A. Denner, S. Dittmaier, S. Kallweit and S. Pozzorini, *NLO QCD corrections to off-shell top-antitop production with leptonic decays at hadron colliders*, JHEP **10** (2012) 110, arXiv: 1207.5018 [hep-ph].

[272] G. Aad et al., *Measurement of the $t\bar{t}$ production cross-section using $e\mu$ events with b-tagged jets in pp collisions at $\sqrt{s}$ = 7 and 8* TeV *with the ATLAS detector*, Eur. Phys. J. **C74** (2014) 3109, [Addendum: Eur. Phys. J.C76,no.11,642(2016)], arXiv: 1406.5375 [hep-ex].

[273] M. Czakon, P. Fiedler, D. Heymes and A. Mitov, 'Measurement of the Pole Mass of the Top Quark using Differential $t\bar{t}$ Cross Sections in $p\bar{p}$ Collisions at $\sqrt{s}$ = 1.96 TeV', 2016, URL: http://lss.fnal.gov/archive/2016/conf/fermilab-conf-16-383-ppd.pdf.

[274] V. Khachatryan et al., *Measurement of the t-tbar production cross section in the e-mu channel in proton-proton collisions at sqrt(s) = 7 and 8 TeV*, JHEP **08** (2016) 029, arXiv: 1603.02303 [hep-ex].

[275] V. M. Abazov et al., *Measurement of the inclusive $t\bar{t}$ production cross section in $p\bar{p}$ collisions at $\sqrt{s} = 1.96$ TeV and determination of the top quark pole mass*, Phys. Rev. **D94** (2016) 092004, arXiv: 1605.06168 [hep-ex].

[276] A. Hocker and V. Kartvelishvili, *SVD approach to data unfolding*, Nucl. Instrum. Meth. **A372** (1996) 469, arXiv: hep-ph/9509307 [hep-ph].

[277] *Studies of the sensitivity to the parton distribution functions and the top quark mass of leptonic differential cross sections in tt production at $\sqrt{8}$ TeV*, URL: https://cds.cern.ch/record/2125717/files/ATL-COM-PHYS-2016-043.pdf.